Nonlinear Systems and Complexity
Series Editor: Albert C. J. Luo

Hernán González-Aguilar
Edgardo Ugalde *Editors*

Nonlinear Dynamics New Directions

Models and Applications

Springer

Nonlinear Systems and Complexity

Volume 12

Series Editor
Albert C. J. Luo
Southern Illinois University
Edwardsville
Illinois
USA

Nonlinear Systems and Complexity provides a place to systematically summarize recent developments, applications, and overall advance in all aspects of nonlinearity, chaos, and complexity as part of the established research literature, beyond the novel and recent findings published in primary journals. The aims of the book series are to publish theories and techniques in nonlinear systems and complexity; stimulate more research interest on nonlinearity, synchronization, and complexity in nonlinear science; and fast-scatter the new knowledge to scientists, engineers, and students in the corresponding fields. Books in this series will focus on the recent developments, findings and progress on theories, principles, methodology, computational techniques in nonlinear systems and mathematics with engineering applications. The Series establishes highly relevant monographs on wide ranging topics covering fundamental advances and new applications in the field. Topical areas include, but are not limited to: Nonlinear dynamics Complexity, nonlinearity, and chaos Computational methods for nonlinear systems Stability, bifurcation, chaos and fractals in engineering Nonlinear chemical and biological phenomena Fractional dynamics and applications Discontinuity, synchronization and control

More information about this series at http://www.springer.com/series/11433

Hernán González-Aguilar • Edgardo Ugalde
Editors

Nonlinear Dynamics New Directions

Models and Applications

Springer

Editors
Hernán González-Aguilar
Autonomous University of San Luis Potosí
San Luis Potosi
Mexico

Edgardo Ugalde
Autonomous University of San Luis Potosí
San Luis Potosi
Mexico

ISSN 2195-9994 ISSN 2196-0003 (electronic)
ISBN 978-3-319-09863-0 ISBN 978-3-319-09864-7 (eBook)
DOI 10.1007/978-3-319-09864-7
Springer Cham Heidelberg New York Dordrecht London

Library of Congress Control Number: 2014951913

Printed on acid-free paper

Springer is part of Springer Science+Business Media (www.springer.com)

Preface

The idea of this book arose during the meeting held in honor of Professor Valentin Afraimovich in Guanajuato, Mexico, in May 2010. The meeting took place in the "Centro de Investigación en Matemáticas," one of the finest places to do mathematics. During the meeting, we had the opportunity not only to share our passion for nonlinear dynamics but also to discuss its foundations and the emerging applications mainly in biology. It was also the occasion to share and celebrate the life experiences of the magnificent person, Valentin Afraimovich. The book covers all scientific aspects of the meeting. For an account of its human aspects, we have Lev Tsrimling's photo gallery. We are awaiting a convincing translation of Micha Ravinovich's poetic work.

This two-volume book covers part of the vast spectrum of interests of Professor Afraimovich, which ranges from fractal analysis to very specific applications of the theory of dynamical systems to biology. The first volume of this book is devoted to fundamental aspects and includes a number of important and new contributions as well as some review articles which emphasize new development prospects. The second volume contains mostly new applications of the theory of dynamical systems to both engineering and biology.

The authors contributing to these two volumes, all of them academically related to Professor Afraimovich, are among the most prominent specialists in nonlinear dynamics. The topics addressed in these two volumes include a rigorous treatment of fluctuation in dynamical systems, topics in fractal analysis, studies of the transient dynamics in biological networks, synchronization in lasers, and control of chaotic systems, among others.

We are very happy to have finally completed this compilation and we thank all the contributors from the bottom of our hearts. We also thank all the agencies which contributed to finance the 2010 meeting, in particular, FENOMEC-UNAM, CONACyT, CIMAT, and UASLP. If despite of our effort, some mistakes remained, we are accountable for it.

San Luis Potosí

Edgardo Ugalde
Hernán González-Aguilar

Contents

Contributors

Igor Belykh Department of Mathematics and Statistics and Neuroscience Institute, Georgia State University, Atlanta, GA, USA

A. S. Dmitrichev Nonlinear Dynamics Department, Institute of Applied Physics of the Russian Academy of Sciences, Nizhny Novgorod, Russia

Alexander Gonchenko Department of Calculated Mathematics and Cybernetics, Nizhny Novgorod State University, Nizhny Novgorod, Russia

Sergey Gonchenko Research Institute of Applied Mathematics and Cybernetics, Nizhny Novgorod State University, Nizhny Novgorod, Russia

Martin Hasler School of Computer and Communication Sciences, Ecole Polytechnique Fédérale de Lausanne (EPFL), Lausanne, Switzerland

Sijo K. Joseph Nonlinear Dynamics, Chaos and Complex Systems Group, Departamento de Física, Universidad Rey Juan Carlos, Móstoles, Madrid, Spain

D. V. Kasatkin Nonlinear Dynamics Department, Institute of Applied Physics of the Russian Academy of Sciences, Nizhny Novgorod, Russia

Xavier Leoncini Centre de Physique Théorique, Aix-Marseille Université, Marseille cedex, France

Ming-Chia Li Department of Applied Mathematics & Center of Mathematical Modeling and Scientific Computing, National Chiao Tung University, Hsinchu, Taiwan

V. I. Nekorkin Nonlinear Dynamics Department, Institute of Applied Physics of the Russian Academy of Sciences, Nizhny Novgorod, Russia

Alexander N. Pisarchik Centro de Investigaciones en Optica, Leon, Guanajuato, Mexico

Mikhail Rabinovich BioCircuits Institute, University of California San Diego, La Jolla, CA, USA

Flavio R. Ruiz-Oliveras Centro de Investigaciones en Optica, Leon, Guanajuato, Mexico

Miguel A. F. Sanjuán Nonlinear Dynamics, Chaos and Complex Systems Group, Departamento de Física, Universidad Rey Juan Carlos, Móstoles, Madrid, Spain

Maurizio Serva Dipartimento di Matematica, Università dell'Aquila, L'Aquila, Italy

Andrey Shilnikov Department of Computational Mathematics and Cybernetics, Lobachevsky State University of Nizhni Novgorod, Nizhni Novgorod, Russia

Oleg Stenkin Research Institute of Applied Mathematics and Cybernetics, Nizhny Novgorod State University, Nizhny Novgorod, Russia

Irma Tristan Instituto de Investigacion en Comunicacion Optica, Universidad Autonoma de San Luis Potosi, San Luis Potosi, Mexico

Dimitri Volchenkov Cognitive Interaction Technology-Center of Excellence, Universit-t Bielefeld, Roma, Italy

Dipartimento di Scienze Economiche ed Aziendali, Università di Cagliari, Bielefeld, Germany

Jeremy Wojcik Applied Technology Associates, Albuquerque, NM, USA

Patterns of Synchrony in Neuronal Networks: The Role of Synaptic Inputs

Igor Belykh and Martin Hasler

Dedicated to Valentin S. Afraimovich on the occasion of his 65th birthday

Abstract We study the role of network architecture and synaptic inputs in the formation of synchronous clusters in synaptically coupled networks of bursting neurons. Through analysis and numerics, we show that the stability of the completely synchronous state, representing the largest cluster, only depends on the number of synaptic inputs each neuron receives, independent from all other details of the network topology. We also give a simple combinatorial algorithm that finds synchronous clusters from the network topology. We demonstrate that networks with a certain degree of internal symmetries are likely to have cluster decompositions with relatively large clusters, leading potentially to cluster synchronization at the mesoscale network level. We address the asymptotic stability of cluster synchronization in excitatory networks of bursting neurons and derive explicit thresholds for the coupling strength that guarantees stable cluster synchronization.

1 Introduction

Brain networks have an hierarchy of different levels, ranging from the microscale via the mesoscale to the macroscale. The microscale is represented by individual neurons and their local synaptic connections. The mesoscale level involves a network of columns and minicolumns, connecting populations of neurons. At the macroscale, large numbers of neuronal populations are arranged into large-scale

I. Belykh (✉)
Department of Mathematics and Statistics and Neuroscience Institute, Georgia State University, 30 Pryor Street, Atlanta, GA 30303, USA
e-mail: ibelykh@gsu.edu

M. Hasler
School of Computer and Communication Sciences, Ecole Polytechnique Fédérale de Lausanne (EPFL), Station 14, 1015 Lausanne, Switzerland
e-mail: martin.hasler@epfl.ch

H. González-Aguilar, E. Ugalde (eds.), *Nonlinear Dynamics New Directions,* Nonlinear Systems and Complexity 12, DOI 10.1007/978-3-319-09864-7_1

patterns of anatomical connectivity [1]. The three scale levels determine the functional properties of individual neurons and neuronal networks. As a result, patterns of cooperative neuronal activity also possess multilevel microscopic, mesoscopic, and macroscopic properties. Individual neurons and their dynamics represent the microscale level; cooperative rhythms of neuronal subpopulations define the mesoscale level, and large-scale patterns of activity, such as an average mean-field dynamics or synchronization, correspond to the macroscale.

Recently, a great deal of attention has been paid to algebraic, statistical, and graph theoretical properties of networks and their relationship to the dynamical properties of the underlying network (see, for example, [2–16] and the references therein). The most important questions about dynamical networks are those of the interplay between network topology and dynamics: How does network structure affect dynamical properties and information capabilities of networks? Can a dynamical partition of a biological network be inferred from purely topological criteria? Until recently, most studies were concerned with the patterns defined by a local microscale network structure or with the macroscopic large-scale patterns of activity such as the mean-field dynamics and synchronization. However, the interest has now shifted toward the analysis of cooperative rhythms in subpopulations defined by the mesoscopic modular structure of the network [10]. Different approaches to extracting dynamical properties from topological and modular structures in complex networks of different nature were recently proposed [11–13].

The simplest macroscopic rhythm in neuronal networks is synchronization; when all neurons fire in unison. Synchronized neuronal firing has been suggested as particularly relevant for neuronal signal transmission and coding. While its involvement in cortical processing is somewhat controversial, the presence of synchronization has been shown in special areas such as the olfactory system or the hippocampal region [17]. Model studies of neuronal synchronization can be separated in those where spiking, relaxation oscillator-type models are used, and bursting models are employed [18–30]. Bursting occurs when neuron activity alternates, on a slow-time scale, between a quiescent state and fast repetitive spiking. There has been much work on mechanisms that produce such bursting [31–38]. In contrast to coupled spiking neurons, whose synchronous dynamics is relatively simple, interacting bursting neurons may exhibit different forms of synchrony; including synchronization of individual spikes, burst synchronization when only the envelopes of the spikes synchronize, and complete synchrony [23, 25, 27]. Typically, burst synchronization arises at a low-coupling strength whereas complete synchrony, which involves both burst and spike synchronization regimes, requires a stronger coupling. Models of interacting bursting neurons often use one of the two different forms of coupling, depending on whether the synapse is electrical or chemical. In the first case, the coupling through gap junctions is linear and directly dependent on the difference of the membrane potentials. In the second case, the coupling is pulsatile and often modeled as a static sigmoidal nonlinear input-output function with a threshold and saturation [53]. The emergence of neuronal synchronization heavily depends on the intrinsic properties of the individual neurons and the type of synaptic coupling and its network topology

[20–30]. This problem was intensively studied for linearly coupled networks of bursting neurons [20, 25], and more generally, of limit-cycle and chaotic oscillators [4–9]. In particular, it has been shown that synchrony in such networks strongly depends on the structure and size of the network. In contrast with linearly (electrically) coupled bursting neurons, the stability of synchronization in pulse- (synaptically) coupled networks only depends on the number of signals each neuron receives, independent from all other details of the network topology [27]. In this chapter, we review this result [27] and give additional details of the proof.

Other important examples of cooperative rhythms are clusters of synchrony [39–41, 43–45], when the neuronal network splits into subpopulations, called clusters, such that all neurons within one cluster fire in perfect synchrony. The existence of clusters of perfect synchrony is strictly defined by the symmetries of the neuronal network [42–45], and therefore by a symmetric modular structure of the network. A symmetry of a coupled cell network is defined as a permutation of the cells that preserves all internal dynamics and all couplings. The stability of synchronous clusters in networks of bursting neurons is defined by different factors such as the type of bursting in the individual neuron model and the neuronal connections among and within the clusters.

In this chapter, we also study the emergence of stable synchronous clusters in synaptically coupled networks as a mesoscale phenomenon. We use our recent results [46] to show how to effectively find clusters defined by subnetworks' mesoscopic architecture and symmetries, and derive the conditions on their stability using the Lyapunov function method. We also demonstrate that the same cluster synchronization regimes may have distinct mesoscopic and macroscopic properties. More precisely, we study the existence and stability of synchronous clusters in excitatory networks of Hindmarsh–Rose (HR) neurons. We implement the concept of minimal balanced coloring [43–45] into a combinatorial algorithm for finding synchronous clusters. The core of the minimal balanced coloring concept is that every cluster of synchrony corresponds to a coloring of the network cells in which two cells have the same color if and only if their dynamical variables are equal (completely synchronized). It is important to emphasize that the vertex coloring [43–45] used in this is *different* from the one defined in graph theory. Graph theory introduces a coloring of a graph as an assignment of colors to the vertices, one color to each vertex, so that adjacent vertices are assigned different colors [47]. However, two adjacent cells from our cluster partition may have the same color as long as their dynamics are described by the same differential equations, up to a permutation of the variables [43].

We use progressive refinement of the coloring map [43–45] to identify clusters in regular and random networks and come to a natural conclusion that random networks rarely exhibit clusters due to the lack of symmetrical network substructures. We also prove the stability of specific clusters in regular lattices of HR neurons, starting with the proof of complete synchronization in globally and densely synaptically coupled excitatory HR neurons that exhibit square-wave bursters. To the best of our knowledge, synchronization of *synaptically* coupled square-wave bursters has not previously been proven, and this chapter, following our recent work [46], presents the

first proof of this kind. In fact, the well developed theory of weakly coupled oscillators had previously been applied to prove synchronization of elliptic bursters [23] that synchronize at very weak coupling strengths, comparable to a small parameter in the individual neuron system. At the same time, square-wave bursters are notorious for their resistance to synchronization [27] and require a strong synaptic coupling, therefore the reduction to phase models cannot be applied. These two types of bursting were first identified by Rinzel [31, 35]. Square-wave bursting was named after the shape of the voltage trace during a burst which resembles a square wave due to fast transitions between the quiescent state and fast repetitive spiking. Similarly, elliptic bursting received its name due to the shape of the voltage trace that looks like a half-ellipse [35].

The layout of this chapter is as follows. First, in Sect. 2, we introduce the HR neuron model as an individual unit of the network. We analyze its dynamics to find the regions of parameters corresponding to square-wave bursting. Then, we present and discuss the network model. In Sect. 3, we prove that the onset of complete synchrony in a network with any coupling topology admitting complete synchronization is ensured by one single condition, defined by the number of synaptic inputs. To prove the stability of synchronization, we construct a Lyapunov function for the difference variables that allows us to analyze the synchronization properties of the networks without resorting to computer simulation. In Sect. 4, we present the algorithm for finding possible synchronous clusters and apply it to specific networks. We also prove the stability of clusters in regular networks where each cluster of cells is driven by the same driving neurons. Finally, in Sect. 5, a brief discussion of the obtained results is given.

2 The Model and Problem Statement

2.1 Single Cell: HR Model and Its Dynamics

We start off with the HR neuron model [48] which represents a class of phenomenological models of spiking and bursting neurons. Without direct relation to concrete physiological mechanisms, these models aim at reproducing the characteristic features of the bursting behavior. To the extent that the assumptions underlying the phenomenological models are sufficiently general, these models may be used to explain generic bifurcation scenarios that can also be observed in the more realistic models.

The HR model is well-known for its chaotic behavior and different types of bursting [22, 27, 49–51]. The model takes the form

$$\begin{cases} \dot{x} &= y + ax^2 - x^3 - z + I \\ \dot{y} &= 1 - dx^2 - y \\ \dot{z} &= \mu(b(x - x_0) - z), \end{cases} \tag{1}$$

where x represents the membrane potential, and variables y and z take into account the transport of ions across the membrane through fast and slow ion channels, respectively. Fast variable y describes the rate of change of the fast (e.g., sodium) current. Slow variable z controls the speed of variation of the slow (e.g., potassium) current. This speed is in turn controlled by a small parameter μ. Parameter I describes an external current that enters the neuron. Parameters a and d (b and x_0) describe activation and inactivation of the fast (slow) ion channel. The presence of the small parameter μ in the z-equation makes the system (1) slow-fast, where the (x, y)-equations and z-equation represent fast "spiking" and slow "bursting" subsystems, respectively.

For the sake of simplicity, the original HR model (1) with the redundant set of parameters can be transformed, using the substitution $(y, z) \to (1-y, 1+I+z)$, $d = a + \alpha, c = -1 - I - bx_0$, into the form

$$\begin{cases} \dot{x} &= ax^2 - x^3 - y - z, \\ \dot{y} &= (a+\alpha)x^2 - y, \\ \dot{z} &= \mu(bx + c - z). \end{cases} \tag{2}$$

The model (2) can exhibit different types of bursting that have different impacts on the stability of the synchronous solution. Therefore, we shall first study the dynamics of the individual model (2) and determine the regions of parameters where square-wave bursting exists. A detailed numerical analysis of bifurcations in the original HR model (1) was recently performed [50, 51].

Readers who are willing to accept the results of this subsection without proof can proceed without loss of continuity to the description of the network model in the next subsection.

We use the standard decomposition of the system (2) into fast and slow subsystems. The fast (x, y)-system has the nullcline $z = f(x) \equiv -\alpha x^2 - x^3$, obtained from solving the system of equations $0 = ax^2 - x^3 - y - z$ and $0 = (a+\alpha)x^2 - y$. The nullcline $z = f(x)$ has two critical points $x_{C1} = -2\alpha/3$ and $x_{C2} = 0$ that correspond to two knees of the graph (see Fig. 1). For simplicity, we shall limit our attention to positive values of parameter α. The generalization to $\alpha < 0$ is straightforward. For $b > \alpha^2/3$ the nullcline of the slow z-equation $z = g(x) \equiv bx + c$ crosses the graph of $f(x)$ at a single point x_e such that the system (2) displays a unique equilibrium point $E(x_e, y_e, z_e)$.

The types of bursting that can exist in the system (2) are defined by the z-parameter sequences of phase portraits of the fast system:

$$\begin{cases} \dot{x} &= ax^2 - x^3 - y - z, \\ \dot{y} &= (a+\alpha)x^2 - y, \quad z = \text{const} \end{cases} \tag{3}$$

derived from (2) for $\mu = 0$. This represents the usual adiabatic approach in which the fast system accounts for the fast dynamics (3), and variations of z describe the slow dynamics. Here, the parameters of the fast system a and α determine the types of possible bursting behavior in the full system (2).

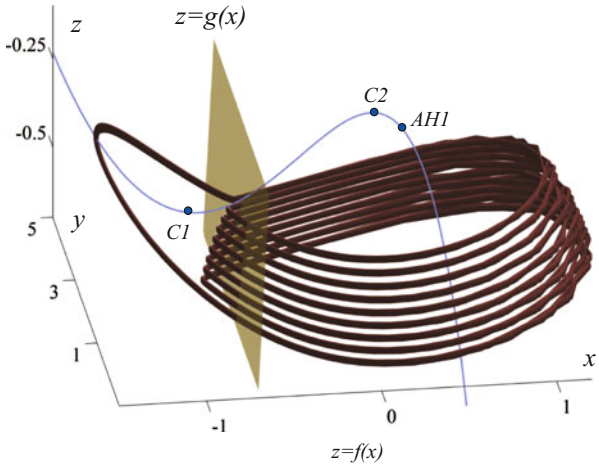

Fig. 1 Square-wave burster of the HR model (2). Parameters $a = 2.8$, $\alpha = 1.6$, $c = 5$, $b = 9$, $\mu = 0.001$. The right stable branch of the fast nullcline $z = f(x)$ contains two points $AH1$ and $AH2$ corresponding to supercritical Andronov–Hopf bifurcations. The second point $AH2$ with $x_{AH2} \approx 1.666$ lies on a much lower part of the nullcline and is not shown

I. Fast System The x-nullcline of the fast system (3) is the curve

$$n_x : \; y = ax^2 - x^3 - z \tag{4}$$

and the y-nullcline is

$$n_y : \; y = (a + \alpha)x^2. \tag{5}$$

Coinciding with the points of intersection between the graphs of (4) and (5), equilibria of the system (3) are determined by the solutions of the equation

$$z = f(x) \equiv -\alpha x^2 - x^3. \tag{6}$$

Hence, for $-\frac{4}{27}\alpha^3 \equiv z_c < z < 0$, $\alpha > 0$ the system (3) has three equilibrium points $N_1(x_1, y_1)$, $O(x_0, y_0)$, and $N_2(x_2, y_2)$, where x_0 and $x_{1,2}$ are the roots of Eq. (6), ordered such that $x_1 < -\frac{2}{3}\alpha < x_0 < 0 < x_2$, and $y_i = (a + \alpha)x_i^2$, $i = 0, 1, 2$. Their stability is defined by the characteristic equation:

$$s^2 - \sigma(x_i)s - f'(x_i) = 0, \; i = 0, 1, 2, \tag{7}$$

where the divergence $\sigma = -(1 - 2ax + 3x^2)$ and the slope $f' = -2\alpha x - 3x^2$. Thus, O is a saddle and N_1 and N_2 are stable nodes or foci. The divergence of the two-dimensional vector field of the fast system (3) changes sign so that

$$\sigma(x) > 0 \text{ for } x_{AH1} < x < x_{AH2}$$
$$\sigma(x) < 0 \text{ for } \; x < x_{AH1}, \;\; x > x_{AH2},$$

where the values $x_{AH1,AH2} = (a\sqrt{a^2 - 3})/3$ correspond to a pair of Andronov–Hopf bifurcations of the equilibrium point N_2 where $\sigma(x_2 = x_{AH1,AH2}) = 0$.

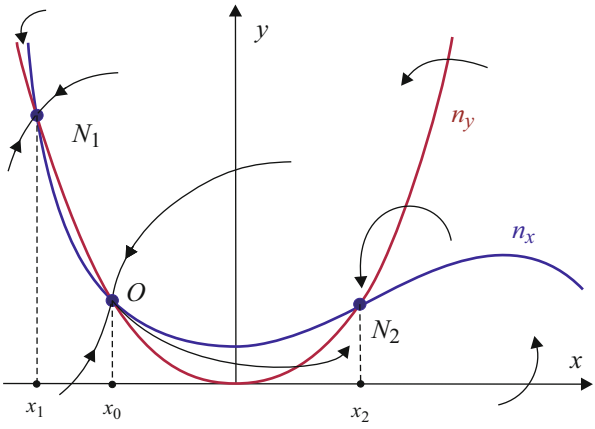

Fig. 2 Nullclines n_x and n_y of the fast system (3). Increasing (*decreasing*) z shifts the cubic nullcine n_x down (*up*). For $-\frac{4}{27}\alpha^3 \equiv z_c < z < 0$, there are three equilibrium points N_1, O, and N_2. While z changes, the three points trace out the left, middle, and right branches of the nullcline $z = f(x)$ of the full system (2), respectively (cf. Fig. 1). Further increase (*decrease*) of z makes the saddle O and the equilibrium point N_2 (N_1) disappear

Using explicit formulas given by Bautin [52], we calculate the first Lyapunov coefficient for the Andronov–Hopf bifurcation of the equilibrium $N_2(x_2, y_2)$ as follows

$$L_1 = -\frac{\pi}{4}|f'(x_2)|^{-3/2}(3 + 2\alpha a). \tag{8}$$

This value is negative for $\alpha > -3a/2$ which is true for any positive values of a and α. Hence, as z decreases for x_{AH1} (or increases for x_{AH2}), the equilibrium N_2 undergoes a supercritical Andronov–Hopf bifurcation such that a unique stable cycle appears softly from N_2.

Using the nullclines n_x and n_y together with the flows shown in Fig. 2, we can deduce the following general properties of the vector field.

Property 2.1 All trajectories of the system (3) leave the region $\{y < 0\}$.

Property 2.2 The system has the absorbing domain $Ab = \{|x| < |x_p|,\ 0 \le y \le y_p\}$, where $y_p = (a+\alpha)x_p^2$ and x_p is either the largest root of equation $x^3 - ax^2 + z = 0$, or the coordinate of the equilibrium point N_1.

Property 2.3 For $x_0 < x_{AH1}$ the limit cycles of the system (3) can only encircle the equilibrium point N_2, i.e., the fast HR model can not produce cycles encircling only equilibrium point N_1, nor can it have cycles enclosing all three equilibrium points. This property follows from the orientation of the vector field as cycles encircling either the equilibrium N_1, or all three equilibria would have to wind against the vector field (cf. the vector field around N_1).

Property 2.4 A homoclinic orbit of O may exist only in the region $x > x_0$ as it is constrained by the vector field, similar to Property 2.3.

II. Square-Wave Bursting According to the above analysis, the behavior of the fast system is essentially different for $a \le \sqrt{3}$ and $a > \sqrt{3}$.

Region 1: $a \leq \sqrt{3}$. As the divergence $\sigma(x) \leq 0$ everywhere, the fast system has no cycles. The equilibrium points N_1 and N_2 are stable, and the stable manifold of the saddle O (when it exists) divides the (x, y) plane into the basins of attraction of N_1 and N_2. As a result, the dynamics of the full system (2) is qualitatively similar to that of the FitzHugh–Nagumo system. That is, with a proper location of the slow nullcline $z = g(x)$, intersecting the middle branch of the fast nullcline $z = f(x)$, the system has an unstable equilibrium encircled by a stable relaxation oscillator-type cycle defining the simplest form of bursting.

Region 2 $a > \sqrt{3}$. The equilibrium point N_2 of the fast system undergoes a supercritical Andronov–Hopf bifurcation for $x_2 = x_{AH1}$, and the homoclinic orbit of the saddle O is always stable (the corresponding saddle value is negative). In this case, the dynamics of the fast system is as follows. For $z < z_{AH2}$ the equilibrium point N_2 is globally stable. For $z_{AH2} < z < z_c$ there exists a stable cycle encircling the unstable equilibrium point N_2. For $z_c < z < z_h$ the unstable manifold W^u of the saddle O consists of two separatrices so that one of them approaches the stable cycle and the other is attracted by the stable equilibrium point N_1. At $z = z_h$ the stable cycle turns into a homoclinic loop, and for $z > z_h$ the separatrices of O change their arrangement so that all trajectories of the system (3), except the stable manifold of O and the unstable equilibrium point N_2, approach the stable equilibrium N_1. The result is a spiking manifold that is composed of the limit cycles of the fast system. Its upper edge is defined by the homoclinic bifurcation at $z = z_h$. Depending on the location of the slow nullcline $z = g(x)$, intersecting the middle branch of the fast nullcline $f(x)$, the full system can generate either square-wave bursting (see. Fig. 1) or tonic spiking. In the Izhikevich classification, [35] this scenario describes the mechanism of formation of the fold/homoclinic burster which is referred to as being square-wave bursting due to the voltage amplitude profile [35]. Bifurcations and complicated sets associated with the transition from tonic spiking into square-wave bursting in various neuronal models have been extensively studied [32, 34, 36–38].

In the following, we will concentrate on the parameters from region 2 where the individual HR model (2) can generate square-wave bursting. Hereafter, the parameters are chosen and fixed as follows: $a = 2.8$, $\alpha = 1.6$, $c = 5$, $b = 9$, $\mu = 0.001$.

2.2 Network of Synaptically Coupled Neurons

Consider now a network of n synaptically coupled HR models (2). The equations of motion read:

$$\begin{cases} \dot{x}_i = ax_i^2 - x_i^3 - y_i - z_i + g_s(V_s - x_i) \sum\limits_{j=1}^{n} c_{ij} \Gamma(x_j), \\ \dot{y}_i = (a + \alpha)x_i^2 - y_i, \\ \dot{z}_i = \mu(bx_i + c - z_i), \ i, j = \overline{1, n}. \end{cases} \tag{9}$$

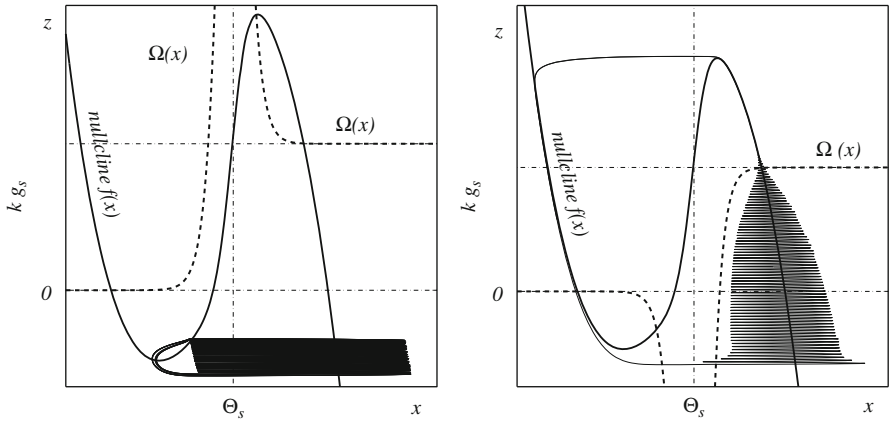

Fig. 3 The function $\Omega(x)$ and the corresponding synchronous bursting. Globally coupled HR neurons ($k = n - 1$, $\lambda = 10$) (*left*). Ring of locally coupled HR neurons ($k = 2$, $\lambda = 10$) (*right*)

Here, each neuron is represented by the HR model (2), and the neurons are identical. The synapses are fast and instantaneous, i.e., time delays and internal synaptic variables are ignored. The parameter g_s is the synaptic coupling strength. The reversal potential $V_s > x_i(t)$ for all x_i and all times t, i.e., the synapse is excitatory. The synaptic coupling function is modeled by the sigmoidal nonlinear input-output function $\Gamma(x_j) = 1/[1 + \exp\{-\lambda(x_j - \Theta_s)\}]$. This oft-used coupling form was called fast threshold modulation by Somers and Kopell [53]. The threshold Θ_s is chosen such that every spike in the single neuron burst can reach the threshold (see Fig. 3). Hereafter, $\Theta_s = -0.25$ and $V_s = 2$.

In (9), $\mathbf{C} = (c_{ij})$ is the $n \times n$ connectivity matrix: $c_{ij} = 1$ if neuron i receives synaptic input from neuron j, $c_{ij} = 0$ otherwise, and $c_{ii} = 0$. Matrix $\mathbf{C}$ can be asymmetric such that both mutual and unidirectional couplings are allowed. We require the connectivity matrix $\mathbf{C}$ to have at least some rows with equal row-sums $k_i = \sum_{j=1}^{n} c_{ij}, i = 1, \ldots, n$. This requirement is a necessary condition for the existence of synchronous clusters of neurons whose states are equal. The existence of clusters yields a decomposition of the network (9) into the disjoint subsets of vertices (neurons) $V = V_1 \cup \ldots \cup V_d$, $V_\gamma \cap V_\nu = \emptyset$ given by the equalities of the neuron states. If the decomposition is flow-invariant with respect to the vector field of the system (9), then the corresponding linear subspace $M(d)$ is invariant and defines d synchronous clusters.

3 Complete Synchronization in the Network

The section reports a surprising find regarding the synchronization of pulse-coupled networks of bursting neurons [27]. We study the stability of full complete synchronization in networks of HR neurons (9) where each neuron receives signals from k others, where k is uniform for all neurons. In the following, we demonstrate that all that matters for the onset of complete synchrony is the number of signals, k, received by each neuron. This is independent of all other details of the network structure. More precisely, the synchronization threshold is inversely proportional to the number of incoming signals k. This criterion applies to a neuronal network with *any* coupling topology admitting complete synchrony.

For this property to be true, we require matrix $\mathbf{C}$ to have equal row-sums $k = \sum_{j=1}^{n} c_{ij}, i = 1, \ldots, n$. This requirement is a necessary condition for the existence of the synchronous solution, namely the invariance of hyperplane $M(1) = \{\xi_1(t) = \xi_2(t) = \ldots = \xi_n(t)\}$, $\xi_i = (x_i, y_i, z_i)$, $i = \overline{1,n}$. In fact, the equal row-sum property implies a network where each cell has the same number k of inputs from other neurons. Note that this k-row sum matrix $\mathbf{C}$ can be asymmetric such that directed networks with the same node in-degree k are also allowed.

Synchronous behavior on the manifold $M(1)$ is generated by the self-coupled system:

$$\begin{cases} \dot{x} = ax^2 - x^3 - y - z + kg_s(V_s - x)\Gamma(x), \\ \dot{y} = (a + \alpha)x^2 - y, \\ \dot{z} = \mu(bx + c - z). \end{cases} \tag{10}$$

Consequently, the synchronous behavior differs from the behavior of the uncoupled neuron and depends on the coupling strength g_s. The analysis of the slow-fast individual HR system, performed in Sect. 2, carries over to the self-coupled system. The main difference is that the fast subsystem of the self-coupled system undergoes Andronov–Hopf bifurcations at new points $x^{\text{self}}_{AH1,AH2} = (a\sqrt{a^2 - 3(kg_s + 1)})/3$. Hence, increasing the coupling g_s makes the points x_{AH1} and x_{AH2} move toward each other along the fast nullcline $f(x)$ of the self-coupled system (cf. Figs. 1 and 3). Hence, for $kg_s = a^2/3 - 1$ the two points merge together such that for $kg_s > a^2/3 - 1$ there is no oscillatory (spiking) dynamics on the right branch of the fast nullcline as the Andronov–Hopf points have disappeared. Thus, there is no square bursting for $kg_s > a^2/3 - 1$, and the synchronous dynamics defined by the self-coupled system (10) is of relaxation oscillator-type.

We begin by deriving the variational equations for the transverse stability of the synchronization manifold $M(1)$.

Adding and subtracting an additional term $g_s(V_s - x_i)\sum_{j=1}^{n} c_{ij}\Gamma(x_i) = kg_s(V_s - x_i)$ $\Gamma(x_i)$ from the x-equation of system (9), yields

$$\begin{cases} \dot{x}_i = ax_i^2 - x_i^3 - y_i - z_i + kg_s(V_s - x_i)\Gamma(x_i) + g_s(V_s - x_i)\sum\limits_{j=1}^{n} c_{ij}\left(\Gamma(x_j) - \Gamma(x_i)\right), \\ \dot{y}_i = (a+\alpha)x_i^2 - y_i, \\ \dot{z}_i = \mu(bx_i + c - z_i),\ i, j = \overline{1,n}. \end{cases} \tag{11}$$

Introducing the differences between the neural oscillator coordinates $X_{12} = x_2 - x_1$, $Y_{12} = y_2 - y_1$, $Z_{12} = z_2 - z_1$ in the limit when these differences are infinitesimal, we derive the stability equations for the transverse perturbations to the synchronization manifold $M(1)$ [27]:

$$\begin{cases} \dot{X}_{ij} = & (2ax - 3x^2)X_{ij} - Y_{ij} - Z_{ij} - kg_s\Gamma(x)X_{ij} + \\ & +g_s(V_s - x)\Gamma_x'(x)\left(kX_{ij} + \sum\limits_{h=1}^{n}\left\{c_{jh}X_{jh} - c_{ih}X_{ih}\right\}\right), \\ \dot{Y}_{ij} = & 2(a+\alpha)xX_{ij} - Y_{ij}, \\ \dot{Z}_{ij} = & \mu(bX_{ij} - Z_{ij}). \end{cases} \tag{12}$$

The derivatives are calculated at the point $X_{ij} = 0, Y_{ij} = 0, Z_{ij} = 0$, and $\{x(t), y(t), z(t)\}$ corresponds to the synchronous bursting solution defined via system (10). The first coupling term $S_1 = -kg_s\Gamma(x)X_{ij}$ accounts for the number of inputs k. At the same time, the contribution of the second coupling term $S_2 = g_s(V_s - x)\Gamma_x'(x)(\cdot)$ depends on the coupling configuration. Note that the term $\sum_{h=1}^{n}\left\{c_{jh}\xi_{jh} - c_{ih}\xi_{ih}\right\}$ is the same as for linear coupling [6]. In terms of the original variables x_i, the corresponding coupling matrix $\mathbf{G} = \mathbf{C} - k\mathbf{I}$ is the Laplacian of the connected graph, except for a sign change. It is well-known that $\mathbf{G}$ has one zero eigenvalue γ_1 and all other eigenvalues have nonpositive real parts. If the coupling is mutual, $\mathbf{G}$ is symmetric and all eigenvalues are real. For simplicity, suppose that the eigenvalue γ_2 with the largest real part is simple. Then, applying the linear transformation that diagonalizes $\mathbf{G}$ to Eq. (12), we obtain the stability equation for the most unstable transverse mode:

$$\begin{aligned} \dot{X} &= (2ax - 3x^2)X - Y - Z - \Omega(x)Z, \\ \dot{Y} &= 2(a+\alpha)xX - Y, \\ \dot{\zeta} &= \mu(bX - Z), \end{aligned} \tag{13}$$

where $\Omega(x) = kg_s\Gamma(x) - g_s(V_s - x)\Gamma_x'(x)(k + \gamma_2)$. System (13) is an analog of the Master Stability function [6] for synaptically coupled networks (9). If γ_2 is not simple, then we can write similar equations to system (13) for the vectors spanning the corresponding blocks in the Jordan normal form of $\mathbf{G}$. The stability discussion, however, is essentially the same. Consider now its application to basic network configurations.

3.1 Globally Coupled Networks

In this case, the second largest eigenvalue $\gamma_2 = -n$ and $k = n - 1$. Consequently, the function $\Omega(x)$ becomes

$$\begin{aligned}\Omega(x) &= kg_s\Gamma(x) + g_s(V_s - x)\Gamma'_x(x)\\ &= \frac{kg_s}{1+\exp\{-\lambda(x-\Theta_s)\}} + g_s(V_s - x)\frac{\lambda\exp\{-\lambda(x-\Theta_s)\}}{(1+\exp\{-\lambda(x-\Theta_s)\})^2}\end{aligned} \tag{14}$$

The function $\Gamma(x)$ together with its derivative $\Gamma'_x(x)$ is nonnegative, and $(V_s - x)$ is always positive (the synapses are excitatory). Therefore, $\Omega(x)$ is always nonnegative and the coupling term $-\Omega(x)X$ aims at stabilizing the zero equilibrium of system (13); corresponding to the synchronous solution. The function $\Omega(x)$ strongly depends on whether the membrane potential $x(t)$ exceeds the threshold Θ_s or not (see Fig. 3). In fact, for a sufficiently large λ ensuring a bell-shape graph $\Omega(x)$ [46], kg_s is a lower bound of $\Omega(x)$ in the region $x(t) > \Theta_s$ and strongly contributes to the stability. At the same time, when $x(t)$ is below Θ_s, the first term in $\Omega(x)$ rapidly decreases to zero, and the second coupling term becomes decisive in a small region close to $x = \Theta_s$. This region is defined by the parameter λ. For our results concerning the stability of synchronization, it is also necessary to assume that λ is only moderately large. Our stability approach does not carry over to the case where the function $\Gamma(x)$ is approaching the Heaviside function when λ approaches infinity. In fact, the bounds of Theorem 1 on the sufficient coupling strength become too conservative when λ approaches infinity. At the same time, to prove synchronization of bursters, we do not require μ to be a singular perturbation parameter. Applying the Lyapunov function method to the stability of system (13) with the function (14), we prove the following theorem that synchronization in the globally coupled network can be made stable, provided that the coupling g_s is sufficiently strong.

Theorem 1 *Complete synchronization in the globally coupled network* (9) *with the number of synaptic inputs* $k = n - 1$ *is locally stable if the coupling* g_s *exceeds the critical value*

$$g_s^* = \max\{D_1, D_2, D_3\}, \quad \text{where} \tag{15}$$

$$\begin{aligned}&D_1 = \tfrac{a^2}{3k}, \quad D_2 = \tfrac{(a-\alpha)^2}{4k(3-\beta(a+\alpha)^2)} + \tfrac{1}{4k\beta}, \quad \beta < 3/(a+\alpha)^2,\\ &D_3 = \tfrac{p(1+e^{-\lambda(b-\Theta_s)})^2}{\beta[k(1+e^{-\lambda(b-\Theta_s)})+(V_s-b)\lambda e^{-\lambda(b-\Theta_s)}]}, \quad b = \tfrac{(a-\alpha)-\sqrt{(a-\alpha)^2+(3/\beta-(a+\alpha)^2)}}{2(3-\beta(a+\alpha)^2)}\\ &\text{for } a \geq \alpha: \ p = \tfrac{1}{4} \text{ and } \quad \text{for } a < \alpha: \ p = \tfrac{1}{4} + \tfrac{\beta(a-\alpha)^2}{4(3-\beta(a+\alpha)^2)}.\end{aligned} \tag{16}$$

Proof Consider the Lyapunov function

$$\Phi = X^2/2 + \beta Y^2/2 + \frac{1}{2\mu b}Z^2, \tag{17}$$

where β is a positive auxiliary parameter to be defined.

The derivative of the Lyapunov function (17) with respect to the variational Eqs. (13) and (14) is calculated as follows

$$\dot{\Phi} = -\left\{AX^2 - BXY + \beta Y^2 + Z^2/b\right\}, \tag{18}$$

where $A = [3x^2 - 2ax + \Omega(x)]$ and $B = (2\beta(a+\alpha)x - 1)$.

Our goal is to prove the negative definiteness of the quadratic form $\dot{\Phi}$ and to obtain conditions under which solutions of the variational Eq. (13) and (14) converge to 0 as $t \to \infty$, and its trivial equilibrium, corresponding to the synchronization manifold of system (9), is locally asymptotically stable.

The quadratic form $\dot{\Phi}$ is negative definite as long as the quadratic form

$$W = -\left\{AX^2 - BXY + \beta Y^2\right\}$$

is negative.

Applying Sylvester's criterion for the negative definiteness of the quadratic form W, we obtain the following two conditions.

Condition I: $A > 0$.

Part 1 If $x \geq \Theta_s$ then the condition $A > 0$ is true if $3x^2 - 2ax + kg_s > 0$. Here, we have taken the lowest bound (kg_s) of the function $\Omega(x)$ in the region $x \geq \Theta_s$ (cf. Fig. 3). The roots of the quadratic equation are $x^r_{1,2} = \left(a \pm \sqrt{a^2 - 3kg_s}\right)/3$. Therefore, this equation has no solutions for

$$g_s > \frac{a^2}{3k}. \tag{19}$$

Part 2 For $x \leq \Theta_s$ and for the given $\Theta_s = -0.25$, A is always positive.

Condition II. The second condition of Sylvester's criterion is $\beta A - B^2/4 > 0$. This leads to the inequality

$$Q(x) \equiv \varphi(x) + \Omega(x) > 0, \quad \text{where} \tag{20}$$

$\varphi(x) = \beta(3 - \beta(a+\alpha)^2)x^2 - \beta(a-\alpha)x - 1/4$.

The function $\Omega(x)$ is nonnegative for any $x(t)$ while the parabola $\varphi(x)$ can be negative in some interval of $x(t)$. To satisfy the condition (20), we should increase the values of the function Ω by increasing the coupling g_s such that the superposition of the two functions becomes positive.

First of all, we require $(3 - \beta(a+\alpha)^2) > 0$ to keep the parabola $\varphi(x)$ concave up. This constrains the choice of the auxiliary parameter β. As the region of parameters where square-wave bursters can exist in the individual HR model (2) is defined by the condition $\{a \geq \sqrt{3}\}$ (Region 2), we have to choose $\beta < 1$ for synchronization of square-wave bursters.

The roots of the parabola $\varphi(x)$ are

$$x^r_{1,2} = \frac{(a-\alpha) \pm \sqrt{(a-\alpha)^2 + (3/\beta - (a+\alpha)^2)}}{2(3-\beta(a+\alpha)^2)}$$

such that the function $\varphi(x)$ is positive outside the region $[x^r_1, x^r_2]$.

We derive the conditions for Eq. (20) in two steps, considering two parts of the bursting solution (10): $x \geq \Theta_s$ and $x < \Theta_s$.

Part 1. $x \geq \Theta_s$.

As before, we take the lowest bound (kg_s) of $\Omega(x)$ in the region $x \geq \Theta_s$ such that the condition (20) becomes

$$(3-\beta(a+\alpha)^2)x^2 - (a-\alpha)x - \frac{1}{4\beta} + kg_s > 0.$$

This is true under the conditions

$$g_s > g^*_s = \left[\frac{(a-\alpha)^2}{4k(3-\beta(a+\alpha)^2)} + \frac{1}{4k\beta}\right], \quad \beta < 3/(a+\alpha)^2 \tag{21}$$

Part 2 $x < \Theta_s$.

The minimum of the parabola $\varphi(x)$ is reached at $x^* = \frac{a-\alpha}{2(3-\beta(a+\alpha)^2)}$. If $a < \alpha$ then x^* lies in the region $x < \Theta_s < 0$ and the minimum of the function φ is $\varphi(x^*) \equiv -m = -1/4 - \frac{\beta(a-\alpha)^2}{4(3-\beta(a+\alpha)^2)}$. If $a > \alpha$ then the minimum value of $\varphi(x)$ in the region $x < \Theta_s < 0$ becomes

$$\varphi(\Theta_s) = \beta(3-\beta(a+\alpha)^2)\Theta_s^2 + \beta(a-\alpha)|\Theta_s| - 1/4.$$

Therefore, we take $\varphi(\Theta_s) = -1/4$ as the ultimate bound for the case $a > \alpha$.

To compensate these negative mimimum values of $\varphi(x)$, we should make the coupling strength g_s sufficiently strong such that the minimum value of the positive function $\beta\Omega(x)$ in the interval $[x^r_2, \Theta_s]$ is greater than $-m$ and $-1/4$ for $a < \alpha$ and $a > \alpha$, respectively.

The function $\Omega(x)$ reaches its minimum at the left endpoint of the interval $[x^r_2, \Theta_s]$

$$b = x^r_2 = \frac{(a-\alpha) - \sqrt{(a-\alpha)^2 + (3/\beta - (a+\alpha)^2)}}{2(3-\beta(a+\alpha)^2)}.$$

Hence, the stability condition (20) for the region $x < \Theta_s$ becomes

$$\begin{aligned} g_s > \quad & g^*_s = \frac{p(1+e^{-\lambda(b-\Theta_s)})^2}{\beta[k(1+e^{-\lambda(b-\Theta_s)})+(V_s-b)\lambda e^{-\lambda(b-\Theta_s)}]}, \\ & p = m \ \text{ for } \ a < \alpha; \ \ p = 1/4 \ \text{ for } \ a > \alpha; \ \ \beta < 3/(a+\alpha)^2. \end{aligned} \tag{22}$$

Combining the conditions (19), (21), and (22), we obtain an upper bound for the negative definiteness of the quadratic form $\dot{\Phi}$ and come to the conditions of the Theorem. ■

Remark 1 Condition for D_3 in Theorem 1 gives a large overestimate. This is due to the simplifications made in estimating the positiveness of the function $Q(x)$. To obtain a tighter bound for the coupling threshold g_s^* that would replace the constant D_3, we should resolve the transcendental Eq. (20) with respect to g_s

$$\begin{aligned} Q(x) &= \beta(3-\beta(a+\alpha)^2)x^2-\beta(a-\alpha)x-1/4+\beta\frac{g_s^*}{1+e^{-\lambda(U-\Theta_s)}}+ \\ &\quad +\beta k g_s^*(V_s-U)\frac{\lambda e^{-\lambda(U-\Theta_s)}}{(1+e^{-\lambda(U-\Theta_s)})^2}=0, \end{aligned} \tag{23}$$

taking into account the condition $\beta < 3/(a+\alpha)^2$. We shall find the solution of Eq. (23) only in the region $x < \Theta_s$. In fact, the bound D_2 (cf. Theorem 1) for the region $x > \Theta_s$ is close to an optimum.

One can see that the Eq. (23) has a unique solution with respect to g_s^* in the region $x < \Theta_s$ that can be found numerically. Therefore, we can formally substitute D_3 in Theorem 4.1 by $D_3^{\text{new}} = g_s^{\text{cr}}$, where g_s^{cr} is the solution of Eq. (23) in the region $x < \Theta_s$. Note that for a relatively sharp saturating coupling function (λ is relatively large), the constant D_3 (or the corresponding D_3^{new}) often dominates over D_1 and D_2.

Remark 2 The analysis shows that the major part of the quiescent (slow) mode of the synchronous solution, where the contribution of $\Omega(x)$ is negligible, lies in a stable zone $x < x_1^r$, where function $\varphi(x)$ is positive. Here, the derivative of the Lyapunov function is always negative, i.e., where the solutions of the individual systems converge to each other. On the other hand, the part of the bursting solution that is the most difficult to synchronize, favorably lies in the region $x(t) \geq \Theta_s$, where the contribution of $\Omega(x) = kg_s$ is strong and depends on k. This property will reappear for the densely and sparsely networks later in the text.

Theorem 1 guarantees the stability of the synchronized solution, where the solution could be an equilibrium, a limit cycle-defining periodic bursting, or a chaotic attractor-corresponding to a chaotic bursting rhythm. The type of the synchronous dynamics is determined by the self-coupled system (10), possessing the additional coupling-dependent term. Let us calculate the synchronization threshold g_s^* (15) with D_3^{new} for the simplest two-neuron globally coupled network (9) with $k = 1$ and parameters of the individual HR model (2) given in Fig. 1. The auxiliary parameter β is chosen from the condition $\beta < 3/(a+\alpha)^2$ and set equal to 0.14. Therefore, the upper synchronization bounds D_1 and D_2 calculated from (15), become $D_1 = 2.61$ and $D_2 = 2.7$. The bound D_3^{new} that we calculate from the transcendental equation ($Q(x) = 0$) (23) becomes $g_s = D_3^{\text{new}} = 2.94$. Therefore, the final upper bound is $g_s^* = \max\{D_1, D_2, D_3^{\text{new}}\} = 2.94$. Numerical simulation shows that complete synchronization arises in the system (9) at a relatively strong coupling $g_s^* = 1.28$. Our bound $g_s^* = 2.94$ clearly gives an overestimate as it comes from sufficient conditions of stability, however it is consistent with nontrivial synchronous behavior.

3.2 Densely Coupled Networks

We define a densely coupled network (9) as a network (9) for which the eigenvalue γ_2 of $\mathbf{G}$ is close to $-k$. For example, for a ring of $2K$-nearest neighbor mutually-coupled neurons, $\gamma_2 = -4\sum_{l=1}^{K} \sin^2 \frac{l\pi}{n}$ [54] with $n = 10$, $K = 4$, and $k = 2K = 8$, we obtain $\gamma_2 \approx -7.976$. Consequently, the function $\Omega(x)$ becomes close to $kg_s\Gamma(x)$. Therefore, if k is sufficiently large, the bound for the synchronization threshold is close to that for globally coupled networks. In particular, the following theorem holds.

Theorem 2 *An upper bound for the coupling threshold that guarantees local stability of synchronization in the (dense) network* (9) *with the eigenvalue* γ_2 *of* $\mathbf{G}$ *smaller than or equal to* $-k$ *is*

$$g_s^* = \max\{D_1, D_2, D_3^{\text{dense}}\}, \quad \text{where} \tag{24}$$

constants D_1 *and* D_2 *are given in the condition* (15) *of Theorem* 1. *Here, the new constant* $D_3^{\text{dense}} = \frac{p(1+e^{-\lambda(b-\Theta_s)})^2}{\beta[k(1+e^{-\lambda(b-\Theta_s)})-(k+\gamma_2)(V_s-b)\lambda e^{-\lambda(b-\Theta_s)}]}$, *and parameters* p, b, *and* β *are given in* (15).

Proof The proof is identical to that of Theorem 1 except for the change of function $\Omega^{\text{dense}}(x) = kg_s\Gamma(x) - (k+\gamma_2)g_s(V_s - x)\Gamma'_x(x)(k+\gamma_2)$. ■

Remark 3 Note that the second term $-(k+\gamma_2)g_s(V_s - x)\Gamma'_x(x)$ in the denominator of D_3^{dense} is positive as long as $-\gamma_2 > k$ and therefore contributes to lowering the coupling threshold g_s^*. This term, however, is small compared to the first term in the denominator that is decisive for the stability and directly proportional to the number of synaptic inputs k. Consequently, the coupling threshold g_s^* is inversely proportional to k, as in the globally coupled networks.

3.3 Intermediately and Sparsely Coupled Networks

When the number of links between the neurons in a network is small, the eigenvalue γ_2 is also small such that the second term in $\Omega(x)$, $-g_s(k+\gamma_2)(V_s - x)\Gamma'_x(x)$ no longer favors the stability. Consequently, the function $\Omega(x)$ takes negative values in the region close to the threshold Θ_s and defines the instability zone, where the coupling desynchronizes the neurons. At the same time, the stability zone is defined by the first term in Ω, $kg_s\Gamma(x)$, which is bounded from below by kg_s in the region $x(t) \geq \Theta_s$ (cf. Fig. 3 (right)). Strictly speaking, while we are no longer able to prove that the systems synchronize within the framework of the Lyapunov function method, the slow-fast structure of the self-coupled system (10), defining the synchronous solution, yields the following. The excitatory coupling raises the x-nullcline $f(x) = -\alpha x^2 - x^3 - kg_s(x - V_s)\Gamma(x)$ of system (10) such that the right-branch attractor

corresponding to spiking gradually moves to the right from the threshold $x = \Theta_s$. Finally, it leaves the zone where $\Omega(x)$ is negative (cf. Fig. 3 (right)), provided g_s is large enough. Note that the raising of the nullcline and the shift of the attractor are also governed by kg_s (cf. Eq. (10)). In the singular perturbation limit ($\mu \to 0$), the synchronous trajectory traverses the instability region via fast jumps from the quiescent mode to repetitive spiking, and spends almost all its time in the stability regions. As in the case of the global coupling, the first stability zone corresponding to a major part of the slow motion along the left branch of $f(x)$ is always stable, whereas the stability of the second zone corresponding to spiking is defined by kg_s. Hence, once again we see that the synchronization threshold in sparsely and intermediately connected networks is also inversely proportional to k.

3.4 Arbitrary Network Topology: What Matters for Synchronization

Collecting all the considered coupling topologies and the conditions of Theorems 1 and 2, we come to the following assertion [27].

Statement 1 *The synchronization threshold estimate*

$$g_s^* = g_s^{(n=2)}/k, \tag{25}$$

is valid for the networks (9) *with any coupling configuration (whether global or local, regular or random, mutual or unidirectional) under the constraint that each neuron has the same number of inputs k. In* (25)*, $g_s^{(n=2)}$ is a constant corresponding to the synchronization coupling threshold between two mutually coupled HR neurons ($k = 1$).*

Remark 4 The constant $g_s^{(n=2)}$ comes from sufficient conditions and therefore gives an overestimate for the real coupling strength that leads to complete synchronization of two HR neurons: 2.94 predicted versus 1.285 actual for the above mentioned parameters and $\lambda = 10$. However, using the numerically obtained $g_s^{(n=2)}$, we can predict the threshold g_s^*, for any k, from (25), as shown in the numerical examples below.

Remark 5 The synchronization threshold in locally synaptically coupled networks is constant; $g_s^* = g_s^{(n=2)}/2$ for mutually nearest-neighbor coupled neurons, and does not depend on the number of neurons n. This is in sharp contrast with linearly coupled networks where the coupling required for stable synchronization has a quadratic dependence on n [9].

In support of this claim, we determine numerically the threshold for complete synchronization as a function of k for various coupling configurations (local, intermediate and global), and compare it to the value predicted by Eq. (25). For $g_s^{(n=2)}$, the value from simulation of two mutually coupled HR neurons was used. This value is $g_s^{(n=2)} = 1.285$ for $\lambda = 10$ and $g_s^{(n=2)} = 1.139$ for $\lambda = 50$. It can be seen from

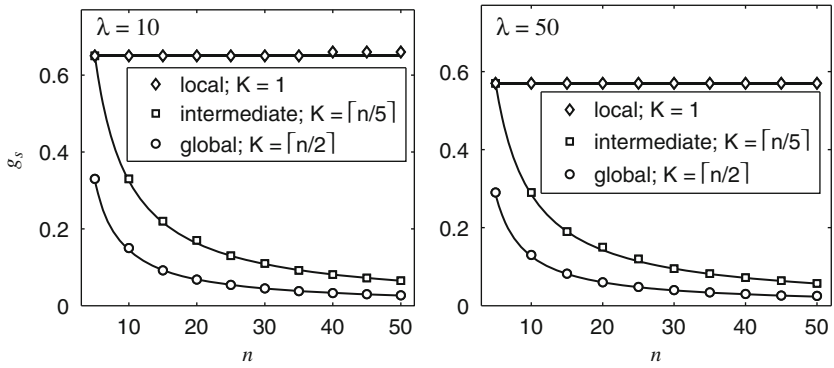

Fig. 4 Synchronization thresholds g_s^* in a ring of 2 K-nearest neighbor coupled HR neurons as functions of n for various coupling configurations (different K). Markers: Simulation results. Solid line: Prediction of Eq. (25)

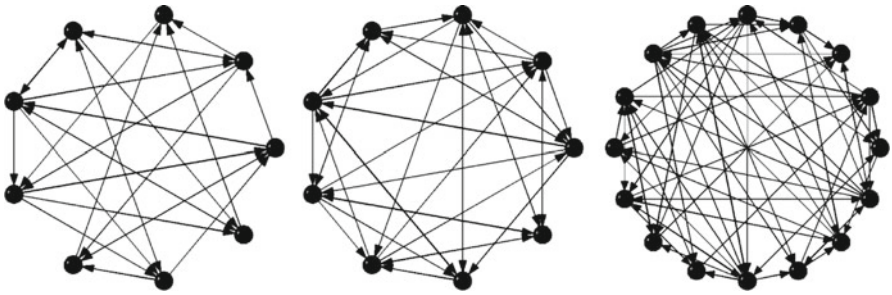

Fig. 5 Ten networks of each type, (*left*): $n = 9$, $k = 3$; (*middle*): $n = 9$, $k = 4$; (*right*): $n = 16$, $k = 4$ were generated randomly. The synchronization threshold for networks of type (**a**): $g_s^* = 0.429$ for $\lambda = 10$, and $g_s^* = 0.380$ for $\lambda = 50$; and of types (**b**) and (**c**): $g_s^* = 0.322$ for $\lambda = 10$, and $g_s = 0.285$ for $\lambda = 50$. All the calculated thresholds coincide perfectly with $g_s^{(n=2)}/k$

Fig. 4 that the deviation of the data from the fitted curve is very small indeed. Note that even for large λ, when the synaptic function $\Gamma(x_i)$ approaches the Heaviside function, the estimate (25) gives an excellent numerical prediction (cf. Fig. 4 (right)).

To illustrate the power of condition (25) even further we have simulated—in addition to the regular, mutually coupled networks from Fig. 4—a series of randomly generated *unidirectionally* coupled networks of HR neurons with uniform number of synapses as those shown in Fig. 5. For all simulated networks, numerical results are nearly identical to the analytical predictions of Eq. (25).

Finally, we have tested robustness of the synchronization with respect to a mismatch in the synaptic strengths. We have simulated networks of 20 neurons for the local, intermediate and global cases, introducing a mismatch in the synaptic strengths around the average g_s. Perfect synchronization is no longer possible in these cases, due to the absence of the synchronization manifold, and there is always an error in the synchronization. However, for a given value of g_s this error falls rapidly and

then remains constant when g_s is further increased. This point can be seen as the coupling threshold for the approximate synchronization. In all simulated cases this value is nearly identical to the synchronization threshold without mismatch as shown in Fig. 4. The synchronization has been verified to be robust for mismatches in g_s of up to 5%.

The derivation of condition (25) mainly relies on two properties of the coupled system: (i) the spiking state, which is most resistant to synchronization, encircles the right branch of the fast nullcline $f(x)$, where the contribution of coupling is strong; (ii) the quiescent state, which is easy to synchronize, belongs to the left branch of $f(x)$. These properties are typical for square-wave and parabolic bursters, whose formation involves the two branches of $f(x)$. Consequently, the synchronization condition (25) is not restricted to the HR neuron, but is applicable to other Hodgkin-Huxley-type neurons, exhibiting square-wave and parabolic bursters. For example, two Sherman models displaying square-wave bursting for the standard parameters [20], synchronize at $g_s^{(n=2)} = 0.25$ when synaptically coupled with $\Theta_s = -40$, $V_s = -10$, and $\lambda = 50$. The synchronization thresholds in a larger network (9) of the Sherman models correspond to the values predicted by $g_s^{(n=2)}/k$.

This completes our study of stable complete synchronization in the network (9) with any coupling configuration admitting synchronization. In the next section, we consider the existence and stability of synchronous clusters in the network (9).

4 Clusters of Synchrony

4.1 Existence of Synchronous Clusters

Synchronous clusters exist if the graph vertices have a corresponding balanced coloring [43–45]. Every cluster of synchrony corresponds to a coloring of the graph vertices in which two vertices have the same color if and only if their states are equal (completely synchronized). Vertices colored in this way create a coloring map.

Definition 1 A coloring of the vertices is balanced, if each vertex of color i gets the same number of inputs from the vertices of color j, for all i and j.

That is, we color the vertices from the cluster decomposition V according to the following rule. We assign the same color to vertices (neurons) if their coordinates in the corresponding linear subspace $M(d)$ are equal. Coloring is balanced if all cells with the same color receive equal number of inputs from cells of a given color. The linear subspace $M(d)$ is flow-invariant if and only if the chosen coloring is balanced [43].

Definition 2 A minimal balanced coloring is a balanced coloring with the minimal number of colors.

Note that the above coloring differs from the classical definition used in graph theory. Indeed, graph theory defines a coloring of a graph as an assignment of colors to the vertices, one color to each vertex, so that adjacent vertices are assigned

different colors. The minimum integer k for which a graph is k-colorable is called the chromatic number [47]. However, our cluster partition and the associated balanced coloring allow two adjacent cells (vertices) to have the same color, provided that the two cells are input isomorphic [42], i.e., their dynamics are described by the same differential equations, up to a permutation of the variables [43].

In the following we use this concept to identify partitions with minimum number of clusters in networks (9) with regular and random structures. Finding a minimal balanced coloring in a given complex network is a nontrivial task. In this subsection, we propose a simple combinatorial algorithm that finds the minimal balanced coloring, and therefore identifies the largest synchronous clusters in the given (complex) network. In the next subsection, we address the stability of the clusters.

We shall first establish a few properties of balanced colorings before introducing an algorithm that allows finding a minimal balanced coloring.

Definition 3 A coloring C_2 is a refinement of a coloring C_1 if two vertices that have the same color in C_2 have the same color also in C_1.

Remark 6

a) We do not distinguish colorings where the subsets of vertices with the same color are the same, but the colors are different.
b) Any coloring is a refinement of the coloring where all vertices have the same color.
c) The coloring where all vertices have a different color is balanced and it is a refinement of any other coloring.
d) The set V_{1m} of vertices with color c_{1m} in C_1 is a union of sets V_{2p}, where V_{2p} is the set of all vertices with the same color c_{2p} in C_2.
e) If C_2 is a refinement of C_1, and C_1 is a refinement of C_2, the two colorings are the same (modulo the colors, cf. Remark 6a)).

We now introduce a special refinement in view of balancing.

Definition 4 The input driven refinement C_2 of a coloring C_1 is obtained as follows. Consider all vertices that have color c_m in C_1. Color them with the same color c_{mj} if they have the same number of inputs from all vertices of the same color $c_{m'}$ in C_1, for every color $c_{m'}$.

Property 4.1

a) Either the input driven refinement C_2 of C_1 has more colors than C_1 or C_2 is equal to C_1 (modulo the colors) and balanced.
b) Suppose that a balanced coloring C_2 is a refinement of a (not necessarily balanced) coloring C_1. Let C_3 be the input driven refinement of C_1. Then C_2 is also a refinement of C_3.

Proof Property 4.1a) follows immediately from Definition 4. For the proof of Property 4.1b) suppose that two vertices v and w have the same color in C_2. We have to show that they also have the same color in C_3. Since C_2 is a refinement of C_1, v and

w also have the same color in C_1. Now consider the set V_{2p} that have the color c_{2p} in C_2. Again, they must also have the same color in C_1. Furthermore, since C_2 is a balanced coloring, the number of inputs from V_{2p} to v is the same as the number of inputs from V_{2p} to w. This is true for any color c_{2p} of C_2. Now consider the set V_{1m} of vertices that have color c_{1m}. Then according to the above remark, V_{1m} is a union of sets V_{2p}. From each of the sets V_{2p} there is the same number of inputs to the vertices v and w and therefore there is also the same number of inputs from V_{1m} to v and w. As this holds for any color c_{1m}, by the construction of C_3, v and w must have the same color in C_3. ■

Property 4.1 and Remark 6a suggest the following algorithm to obtain a minimal balanced coloring:

Algorithm for Finding Synchronous Clusters *Initialization: Start with the coloring where all vertices are colored with the same color.*
Repeat: Replace the current coloring with the input driven refinement of the current coloring until no new refinement is obtained.

The following property follows immediately from Property 4.1.

Property 4.2

a) The algorithm stops in a finite number of steps. The maximum number of steps is the number of vertices in the graph.
b) The coloring, obtained when the algorithm stops, is balanced.

Corollary 4.1 Given a directed graph, the minimal balanced coloring is unique and it is obtained by the above algorithm.

Proof According to Property 4.1b) any balanced coloring C_b is a refinement of all colorings obtained during the execution of the algorithm. It is in particular a refinement of the balanced coloring $C_{\min}$ obtained when the algorithm stops. Therefore, $C_{\min}$ is minimal. Furthermore, if there was another minimal balanced coloring C_m, it would also have to be a refinement of $C_{\min}$. But since C_m is minimal, it must be equal to $C_{\min}$ (modulo the colors). ■

We have applied our combinatorial algorithm to a number of regular and random networks. Three of them are shown in Figs. 6 and 7. The application of our algorithm has shown that random networks generated with uniform probability per link appearance rarely have clusters of synchrony, whereas pseudorandom networks (cf. Fig. 6 (right)) may have a hidden subnetwork modular structure that yields clusters of synchrony.

The stability of clusters in networks of bursting neurons (9) depends on various factors, including the individual neuron dynamics and network topology. In the next section, we prove the stability of specific clusters of synchrony in networks (9). The stability conditions for irregular cluster configurations are often tedious and will be reported elsewhere.

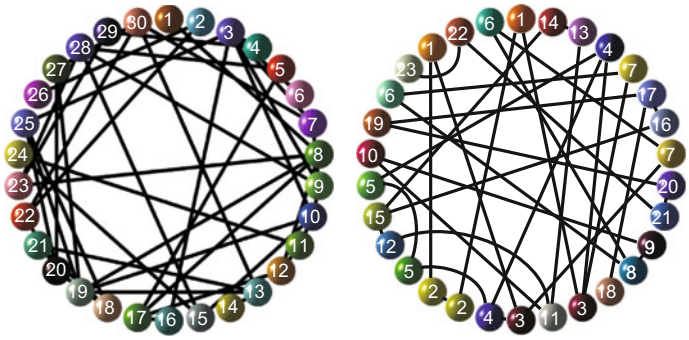

Fig. 6 Clusters of synchrony in random networks of 30 neurons. (*Left*): Network generated by randomly choosing a link between any two nodes with probability $p = 0.045$. There are 30 independent clusters, each represented by one distinct neuron. Neurons do not form clusters of synchrony due to the lack of symmetry. (*Right*): Random network with 23 clusters. Links are generated with uneven probabilities. Note clusters formed by vertices with the same index

4.2 Stability of Clusters in Multi-Layer Networks

We use the pyramidal-shape network of Fig. 7 as a representative example of multi-layer networks where the cells from each layer receive a common input from the same driving neurons. The network of Fig. 7 with uniform symmetrical connections has a four-color partition, corresponding to four clusters of synchrony that are defined by $M(4) = \{\xi_2(t) = \xi_3(t), \xi_4(t) = \xi_5(t) = \xi_6, \xi_7(t) = \xi_8(t) = \xi_9(t) = \xi_{10}(t)\}$, $\xi_i = (x_i, y_i, z_i)$.

In the following, we derive stability conditions for the four clusters in the network (2) with the above four-layer structure. The stability Eqs. (2) for the transverse perturbations to the linear invariant manifold $M(4)$ take the form

$$\begin{aligned}
\dot{X}_{c2} &= (2ax_{c2} - 3x_{c2}^2)X_{c2} - Y_{c2} - Z_{c2} - g_s\left[\Gamma(x_{c1}) + 3\Gamma(x_{c3})\right]X_{c2} \\
\dot{Y}_{c2} &= 2(a+\alpha)x_{c2}X_{c2} - Y_{c2} \\
\dot{Z}_{c2} &= \mu(bX_{c2} - Z_{c2}) \\
\dot{X}_{c3} &= (2ax_{c3} - 3x_{c3}^2)X_{c3} - Y_{c3} - Z_{c3} - g_s\left[2\Gamma(x_{c2}) + 4\Gamma(x_{c4})\right]X_{c3} \\
\dot{Y}_{c3} &= 2(a+\alpha)x_{c3}X_{c3} - Y_{c3} \\
\dot{Z}_{c3} &= \mu(bX_{c3} - Z_{c3}) \\
\dot{X}_{c4} &= (2ax_{c4} - 3x_{c4}^2)X_{c4} - Y_{c4} - Z_{c4} - 3g_s\Gamma(x_{c3})X_{c4} \\
\dot{Y}_{c4} &= 2(a+\alpha)x_{c4}X_{c4} - Y_{c4} \\
\dot{Z}_{c4} &= \mu(bX_{c4} - Z_{c4})
\end{aligned} \tag{26}$$

Here, $\{X_{c2}, Y_{c2}, Z_{c2}\}$, $\{X_{c3}, Y_{c3}, Z_{c3}\}$ and $\{X_{c4}, Y_{c4}, Z_{c4}\}$ are infinitesimal differences between the coordinates of the neurons from clusters $\{C2 : \xi_2 = \xi_3\}$, $\{C3 : \xi_4 =$

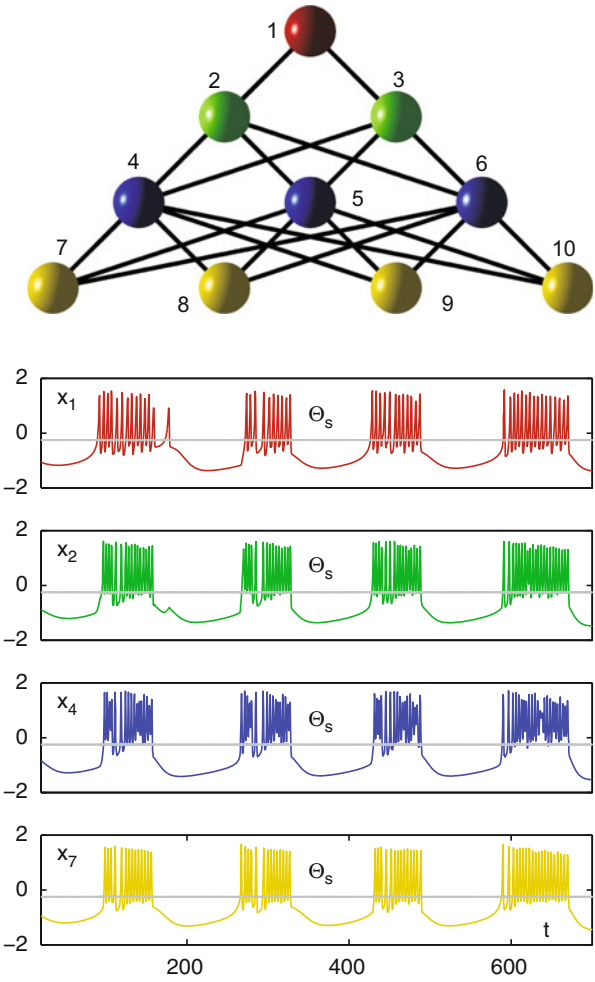

Fig. 7 Multi-layer network with symmetrical connections (*top*). Cells with the same color belong to the same cluster. Time-series of four synchronous clusters. Note that the time-series are synchronized at the level of bursts but there is spike asynchrony between the clusters. Neurons within the clusters are synchronized completely

$\xi_5 = \xi_6\}$, and $\{C4 : \xi_7 = \xi_8 = \xi_9 = \xi_{10}\}$, respectively. The first cluster $C1$ is represented by one, unsynchronized neuron from layer 1. Technically, we should have considered the difference stability equations for any pair of neurons from the same cluster. However, due to the layer-structure of the network in which each neuron from a given cluster receives inputs from the same neurons, these stability equations are identical and can be replaced by a system of only three stability equations for each cluster. In (26), the variables (x_{ci}), $i = 1, .., 4$ are governed by the system (10) with the number of inputs $k_i = 2, 4, 6, 3$, respectively.

System (26) is an analog of the Master Stability (MS) function [6] for the stability of the cluster synchronization. MS functions of this kind are usually analyzed numerically. Completely rigorous derivation of an upper bound for the coupling threshold sufficient for cluster synchronization is complicated as the X stability equation of

each cluster is also driven by neurons from other clusters. To get around this difficulty, we make the following simplification. Numerical simulations show that when cluster synchronization takes place and neurons split into clusters of perfect synchrony, all neurons of the network also become synchronized at the level of bursts but there is no spike synchrony among the clusters (see Fig. 7). As a result, the network behavior possesses two distinct mesoscopic and macroscopic properties: synchronization within the clusters representing the mesoscale and burst synchronization of the entire network at the macroscale. Burst synchronization implies that all the neurons start and cease bursting at the same time instant. Consequently, the variables defining the four clusters of perfect synchrony: x_{c1}, x_{c2}, x_{c3}, and x_{c4} cannot be equal. However, the corresponding synaptic functions $\Gamma(x_{c1})$, $\Gamma(x_{c2})$, $\Gamma(x_{c3})$, and $\Gamma(x_{c4})$ become approximatively equal as the neurons states cross the synaptic threshold Θ_s and therefore activate the synaptic functions $\Gamma(x_{ci})$ at approximatively same times. Using this approximation that $\Gamma(x_{c1}) = \Gamma(x_{c2}) = \Gamma(x_{c3}) = \Gamma(x_{c4})$, we can transform the stability Eq. (26) as follows:

$$\begin{aligned}
\dot{X}_{c2} &= (2ax_{c2} - 3x_{c2}^2)X_{c2} - Y_{c2} - Z_{c2} - 4g_s\Gamma(x_{c2})X_{c2} \\
\dot{Y}_{c2} &= 2(a+\alpha)x_{c2}X_{c2} - Y_{c2} \\
\dot{Z}_{c2} &= \mu(bX_{c2} - Z_{c2}) \\
\dot{X}_{c3} &= (2ax_{c3} - 3x_{c3}^2)X_{c3} - Y_{c3} - Z_{c3} - 6g_s\Gamma(x_{c3})X_{c3} \\
\dot{Y}_{c3} &= 2(a+\alpha)x_{c3}X_{c3} - Y_{c3} \\
\dot{Z}_{c3} &= \mu(bX_{c3} - Z_{c3}) \\
\dot{X}_{c4} &= (2ax_{c4} - 3x_{c4}^2)X_{c4} - Y_{c4} - Z_{c4} - 3g_s\Gamma(x_{c4})X_{c4} \\
\dot{Y}_{c4} &= 2(a+\alpha)x_{c4}X_{c4} - Y_{c4} \\
\dot{Z}_{c4} &= \mu(bX_{c4} - Z_{c4})
\end{aligned} \tag{27}$$

Note that three subsystems for the stability of clusters $C2$, $C3$, and $C4$ are independent. The new stability system (27) is stabilized as long as its weakest subsystem, corresponding to the cluster $C4$ that receives the fewest number of inputs, becomes stable. This statement can be verified by constructing a Lyapunov function similar to the function (17), written for all nine coordinates of the system (27) and showing that its derivative splits into three independent quadratic forms. Each quadratic form corresponds to the stability of each cluster, and the negativeness of the form corresponding to the cluster $C4$ with the fewest number of inputs ensures the negativeness of the other two quadratic forms. For the sake of brevity, we have omitted this proof. In short, the linear invariant manifold $M(4)$ defining the cluster partition is locally stable as long as the origin of the following system is stable

$$\begin{aligned}
\dot{X}_{c4} &= (2ax_{c4} - 3x_{c4}^2)X_{c4} - Y_{c4} - Z_{c4} - 3g_s\Gamma(x_{c4})X_{c4} \\
\dot{Y}_{c4} &= 2(a+\alpha)x_{c4}X_{c4} - Y_{c4} \\
\dot{Z}_{c4} &= \mu(bX_{c4} - Z_{c4}).
\end{aligned} \tag{28}$$

Statement 2 *Under the numerically validated approximation that* $\Gamma(x_{c1}) = \Gamma(x_{c2}) = \Gamma(x_{c3}) = \Gamma(x_{c4})$ *in the regime of cluster synchronization, an upper bound for the coupling threshold that guarantees local stability of cluster synchronization in the network* (2) *with the structure of Fig.* 7 *becomes*

$$g_s^* = \max\{2D_1/3, 2D_2/3, D_3^{\text{cl}}\}, \quad \text{where} \tag{29}$$

constants D_1 *and* D_2 *are given in the condition* (15) *of Theorem* 1 *with* $k = 1$. *Here, the new constant* $D_3^{\text{cl}} = \frac{p}{3\beta}(1 + e^{-\lambda(b-\Theta_s)})$, *and parameters* p, b, *and* β *are given in* (15).

Proof. The stability system (28) is similar to the variational Eqs. (13)–(14) for the stability of complete synchronization in the simplest globally coupled two-neuron network (2) with $k = 1$. Use the Lyapunov function (17) and follow the steps of the proof of Theorem 1, replacing the function $\Omega(x)$ with $3g_s\Gamma(x)$. Note that the lowest bound of $3g_s\Gamma(x)$ in the region $x \geq \Theta_s$ is $3/2$. Therefore, Conditions I and II (Part I) of the above proof yield the bounds $2D_1/3$ and $2D_2/3$. The stability condition (20) for the part of the synchronous trajectory $x_{c4} < \Theta_s$ turns into $g_s = D_3^{\text{cl}} = \frac{p}{3\beta}(1 + e^{-\lambda(b-\Theta_s)})$. □

Note that the obtained bound (29) is not completely rigorous as opposed to the rigorous bounds for complete synchronization derived in Theorems 1 and 2. The above approximation only holds to a certain degree of precision and comes from numerical simulations. However, it clearly shows that the stability of cluster synchronization in the multi-layer network (2) is determined by the stability of the cluster with the smallest number of inputs. In our case, this is cluster $C4$, representing layer 4 of the network in which the neurons receive three inputs.

5 Conclusions

Networks of synaptically coupled neurons have very different synchronization properties from linearly (gap-junction) coupled neurons. In the case of identical neurons with identical excitatory coupling functions and coupling constants, complete synchronization is only possible when each neuron receives the same number of inputs from other neurons [27]. In this case, we have shown that the single condition (25) ensures the onset of complete synchronization in networks of synaptically coupled bursting neurons (9) with any coupling topology in which each neuron receives signals from k others. The synchronization condition depends on the number of inputs k and *not* on the connectivity matrix. This condition carries over to burst synchronization when the neurons are nonidentical and the synaptic connections are heterogeneous, provided that the total input, each neuron receives, is roughly the same. Burst synchronization occurs when the envelopes of the spikes synchronize, but there is no synchrony among the spikes.

The equal k constraint is often invalid for biologically relevant networks with a complex structure where the number of inputs is not necessarily constant, but if k is uniform for a group of neurons, synchronization within this cluster of neurons can

occur. The possible cluster decompositions of the network can be identified from the network topology alone through a so-called balanced coloring of the vertices [43–45]. Among the balanced colorings there is a unique coloring that uses the minimal number of colors, corresponding to a cluster decomposition with the smallest number of clusters, and therefore to the largest clusters. With sufficiently strong coupling, the neurons within these clusters synchronize. We have given a simple algorithm that finds this cluster decomposition from the network topology. Networks with a certain degree of internal symmetries are likely to have cluster decompositions with relatively large clusters, leading potentially to synchronization at mesoscale, whereas random graphs rarely admit clusters composed of more than two or three neurons. We have also addressed the important question of the (local) asymptotic stability of cluster synchronization. This property depends not only on the network topology, but also on the neuron models themselves. We have concentrated on the HR model in the range of parameters where square-wave bursting takes place. We have given an explicit rigorous threshold for the coupling strength that guarantees the asymptotic stability of local synchronization in globally and densely coupled neurons. We have then used a similar stability argument to establish thresholds for the stability of cluster synchronization in well-structured networks where each cluster receives the same inputs from other neurons. Our analysis demonstrates that the stability of the cluster synchronization in the entire network is determined by the stability of the cluster composed of two or more neurons with the smallest number of inputs.

The synaptic strengths in biologically relevant networks with a complex structure can change as a result of pre- and postsynaptic neuron activity. This may result in temporally approximate cluster synchronization when the total input to groups of neurons becomes color balanced only for a specific interval of time. The proposed algorithm promises to allow finding temporal clusters of synchrony in networks with time-varying synapses. Its extension to adaptive networks with the ability to privilege clusters of synchrony is a subject of separate study.

Acknowledgment This work was supported by the National Science Foundation under Grant DMS-1009744, the GSU Brains and Behavior program, and RFFI Grants N 2100-065268 and N 09-01-00498-a (to I.B.).

References

1. Sporns, O.: Brain connectivity. Scholarpedia **2**(10), 4695 (2007)
2. Watts, D.J., Strogatz, S.H.: Collective dynamics of ‘small-world’ networks. Nature **393**, 440–442 (1998)
3. Strogatz, S.H.: Exploring complex networks. Nature **410**(6825), 268–276 (2001)
4. Afraimovich, V.S., Verichev, N.N., Rabinovich, M.I.: Stochastic synchronization of oscillations in dissipative systems. Izv. Vuzov. Radiofiz. **29**, 795 (1986)
5. Pecora, L.M., Carroll, T.L.: Synchronization in chaotic systems. Phys. Rev. Lett. **64**(8), 821–824 (1990)
6. Pecora, L.M., Carroll, T.L.: Master stability functions for synchronized coupled systems. Phys. Rev. Lett. **80**(10), 2109 (1998)

7. Barahona, M., Pecora, L.M.: Synchronization in small-world systems. Phys. Rev. Lett. **89**(5), 054101 (2002)
8. Nishikawa, T., Motter, A.E., Lai, Y.-C., Hoppensteadt, F.C.: Heterogeneity in oscillator networks: Are smaller worlds easier to synchronize? Phys. Rev. Lett. **91**(1), 014101 (2003)
9. Belykh, V.N., Belykh, I.V., Hasler, M.: Connection graph stability method for synchronized coupled chaotic systems. Physica (Amsterdam) **195D**, 159 (2004)
10. Almendral, J., Leyva, I., Daqing, L., Sendina-Nadal, I., Shlomo, H., Boccaletti, S.: Dynamics of overlapping structures in modular networks. Phys. Rev. E **82**, 016115 (2010)
11. Rodriguez-Caso, C., Corominas-Murtra, B., Sole, R.V.: On the basic computational structure of gene regulatory networks. Mol. Biosyst. **5**(12), 1617–1629 (2009)
12. Newman, M.E.: Modularity and community structure in networks. Proc. Natl. Acad. Sci. USA **103**(23), 8577–8582 (2006)
13. Boccaletti, S., Latora, V., Moreno, Y., Chavez, M., Hwang, D.-U.: Complex networks: Structure and dynamics. Phys. Rep. **424**(4–5), 175–308 (2006)
14. Afraimovich, V.S., Bunimovich, L.A.: Dynamical networks: Interplay of topology, interactions and local dynamics. Nonlinearity **20**(7), 1761 (2007)
15. Afraimovich, V.S., Zhigulin, V.P., Rabinovich, M.I.: On the origin of reproducible sequential activity in neural circuits. Chaos **14**(4), 1123–1129 (2004)
16. Afraimovich, V.S., Yong, T., Muezzinoglu, M.K., Rabinovich, M.I.: Nonlinear dynamics of emotion-cognition interaction: When emotion does not destroy cognition? Bull Math. Biol. **73**(2), 266–284 (2011)
17. Gray, C.M., Singer, W.: Stimulus-specific neuronal oscillations in orientation columns of cat visual cortex. Proc. Natl. Acad. Sci. USA **86**(5), 1698–1702 (1989). (Bazhenov, M., Stopfer, M., Rabinovich, M.I., Huerta, R., Abarbanel, H.D.I., Sejnowski, T.J., and Laurent, G.: Neuron **30**, 553 (2001); Mehta, M. R., Lee, A. K. , and Wilson, M. A.: Nature **417**, 741 (2002))
18. Ermentrout, G.B., Kopell, N.: Parabolic bursting in an excitable system coupled with a slow oscillation. SIAM J. Appl. Math. **46**(2) 233–253 (1986)
19. Sherman, A., Rinzel, J.: Rhythmogenic effects of weak electrotonic coupling in neuronal models. Proc. Natl. Acad. Sci. USA **89**(6), 2471–2474 (1994)
20. Sherman, A.: Anti-phase, asymmetric and aperiodic oscillations in excitable cells–I. Coupled bursters. Bull. Math. Biol. **56**, 811–835 (1994)
21. Terman, D., Wang, D.: Global competition and local cooperation in a network of neural oscillators. Phys. (Amsterdam) **81D**, 148–176 (1995)
22. Rabinovich, M.I., Torres, J.J., Varona, P., Huerta, R., Weidman, P.: Origin of coherent structures in a discrete chaotic medium. Phys. Rev E **60**, R1130–R1133 (1999)
23. Izhikevich, E.M.: Synchronization of Elliptic Bursters. SIAM Rev. **43**, 315–344 (2001)
24. Rubin, J., Terman, D.: Synchronized bursts and loss of synchrony among heterogeneous conditional oscillators. SIAM J. Appl. Dyn. Sys. **1**, 146 (2002)
25. Dhamala, M., Jirsa, V.K., Ding, M.: Enhancement of neural synchrony by time delay. Phys. Rev. Lett. **92**, 074104 (2004)
26. de Vries, G., Sherman, A.: Beyond synchronization: Modulatory and emergent effects of coupling in square-wave bursting. In: Coombes, S., Bressloff, P.C. (eds.) Bursting: The Genesis of Rhythm in the Nervous System, pp. 243–272. World Scientific Publishing, London (2005)
27. Belykh, I., de Lange, E., Hasler, M.: Synchronization of bursting neurons: what matters in the network topology. Phys. Rev. Lett. **94**(18), 188101 (2005)
28. Belykh, I., Shilnikov, A.: When weak inhibition synchronizes strongly desynchronizing networks of bursting neurons. Phys. Rev. Lett. **101**(7), 078102 (2008)
29. Shilnikov, A., Gordon, R., Belykh, I.: Polyrhythmic synchronization in bursting networking motifs. Chaos **18**(3), 037120 (2008)
30. Jalil, S., Belykh, I., Shilnikov, A.: Fast reciprocal inhibition can synchronize bursting neurons. Phys. Rev. E **81**, R045201 (2010)
31. Rinzel, J.: Lecture Notes in Biomathematics, vol. 71, pp. 251–291. Springer, Berlin (1987)
32. Terman, D.: Chaotic spikes arising from a model of bursting in excitable membranes. SIAM J. Appl. Math. **51**, 1418 (1991)

33. Bertram, R., Butte, M.J., Kiemel, T., Sherman, A.: Topological and phenomenological classification of bursting oscillations. Bull. Math. Biol. **57**(3), 413–439 (1995)
34. Belykh, V.N., Belykh, I.V., Colding-Joergensen, M., Mosekilde, E.: Homoclinic bifurcations leading to bursting oscillations in cell models. Eur. Phys. J. E **3**(3), 205–219 (2000)
35. Izhikevich, E.M.: Neural excitability, spiking, and bursting. Int. J. Bifurc. Chaos **10**, 1171–1266 (2000)
36. Shilnikov, A., Cymbalyuk, G.: Transition between tonic spiking and bursting in a neuron model via the blue-sky catastrophe. Phys. Rev. Lett. **94**(4), 048101 (2005)
37. Shilnikov, A., Calabrese, R., Cymbalyuk, G.: Mechanism of bistability: Tonic spiking and bursting in a neuron model. Phys. Rev. E **71**, 056214 (2005)
38. Frohlich, F., Bazhenov, M.: Coexistence of tonic firing and bursting in cortical neurons. Phys. Rev. E **74**, 031922 (2006)
39. Pogromsky, A.Yu., Nijmeijer, H.: Cooperative oscillatory behavior of mutually coupled dynamical systems. IEEE Trans. Circuits Syst., I: Fundam. Theory Appl. **48**(2), 152 (2001).
40. Belykh, V., Belykh, I., Hasler, M.: Hierarchy and stability of partially synchronous oscillations of diffusively coupled dynamical systems. Phys. Rev. E **62**, 6332–6345 (2000)
41. Belykh, I., Belykh, V., Nevidin, K., Hasler, M.: Persistent clusters in lattices of coupled nonidentical chaotic systems. Chaos **13**(1), 165–178 (2003)
42. Stewart, I., Golubitsky, M., Pivato, M.: Symmetry groupoids and patterns of synchrony in coupled cell networks. SIAM J. Appl. Dynam. Sys. **2**(4), 609–646 (2003)
43. Golubitsky, M., Stewart, I., Torok, A.: Patterns of synchrony in coupled cell networks with multiple arrows. SIAM J. Appl. Dynam. Sys. **4**(1), 78–100 (2005)
44. Golubitsky, M., Stewart, I.: Nonlinear dynamics of networks: The groupoid formalism. Bull. Am. Math. Soc. **43**, 305–364 (2006)
45. Wang, Y., Golubitsky, M.: Two-color patterns of synchrony in lattice dynamical systems. Nonlinearity **18**, 631-657 (2005)
46. Belykh, I., Hasler, M.: Mesoscale and clusters of synchrony in networks of bursting neurons. Chaos **21**(1), 016106 (2011)
47. Bollobas, B.: Modern Graph Theory. Springer, New York (1998)
48. Hindmarsh, J.L., Rose, M.: A model of neuronal bursting using three coupled first order differential equations. Proc. R Soc. Lond. B Biol. Sci. **221**(1222), 87–102 (1984)
49. Wang, X.-J.: Genesis of bursting oscillations in the Hindmarsh-Rose model and homoclinicity to a chaotic saddle. Physica (Amsterdam) **62D**, 263 (1993)
50. Shilnikov, A.L., Kolomiets, M.L.: Methods of the qualitative theory for the Hindmarsh–Rose model: A case study. Int. J. Bifurc. Chaos **18**(8) 1 (2008)
51. Storace, M., Linaro, D., de Lange, E.: The Hindmarsh-Rose neuron model: bifurcation analysis and piecewise-linear approximations. Chaos **18**(3), 033128 (2008)
52. Bautin, N.N.: Behavior of Dynamical Systems Near the Boundary of Stability. Nauka Publ. House, Moscow (1984)
53. Somers, D., Kopell, N.: Rapid synchronization through fast threshold modulation. Biol. Cybern. **68**, 393–407 (1993)
54. Wang, X.F., Chen, G.: Synchronization in scale free dynamical networks: Robustness and fragility. IEEE Trans. Circuits Syst. I Fundam. Theory Appl. **49**(1), 54–62 (2002)

On Topological and Hyperbolic Properties of Systems with Homoclinic Tangencies

Sergey Gonchenko, Alexander Gonchenko and Ming-Chia Li

Abstract We study dynamical properties of a set Λ of trajectories from a small neighbourhood of a non-transversal Poincaré homoclinic orbit. We show that this problem has no univalent solution, as it takes place in the case of a transversal homoclinic orbit. Here different situations are possible, depending on the character of the homoclinic tangency, when Λ is trivial or contains topological (hyperbolic) horseshoes. In this chapter we find certain conditions for existence of both types of dynamics and give a description (in term of the symbolic dynamics) of the corresponding non-trivial hyperbolic subsets from Λ.

1 Introduction

Homoclinic orbit or *Poincaré homoclinic orbit* is an orbit that is bi-asymptotic to a saddle periodic trajectory. Thus, any such orbit belongs to the intersection of the invariant stable W^s and unstable W^u manifolds of the corresponding periodic orbit. Depending on transversality or non-transversality of the intersection, the homoclinic orbit is called *transversal* or *non-transversal*. In the latter case, one says also about *homoclinic tangency*.

The existence of transversal Poincaré homoclinic orbits is considered as the universal criterium of chaos. The point is that even the set Λ_1 of orbits entirely lying in a small neighbourhood of a transversal homoclinic orbit has a non-trivial structure:

S. Gonchenko (✉)
Research Institute of Applied Mathematics and Cybernetics,
Nizhny Novgorod State University, Nizhny Novgorod, Russia
e-mail: gonchenko@pochta.ru

A. Gonchenko
Department of Calculated Mathematics and Cybernetics,
Nizhny Novgorod State University, Nizhny Novgorod, Russia
e-mail: agonchenko@mail.ru

M.-Chia Li
Department of Applied Mathematics & Center of Mathematical Modeling and Scientific Computing, National Chiao Tung University, 300 Hsinchu, Taiwan
e-mail: mcli@math.ncue.edu.tw

H. González-Aguilar, E. Ugalde (eds.), *Nonlinear Dynamics New Directions,*
Nonlinear Systems and Complexity 12, DOI 10.1007/978-3-319-09864-7_2

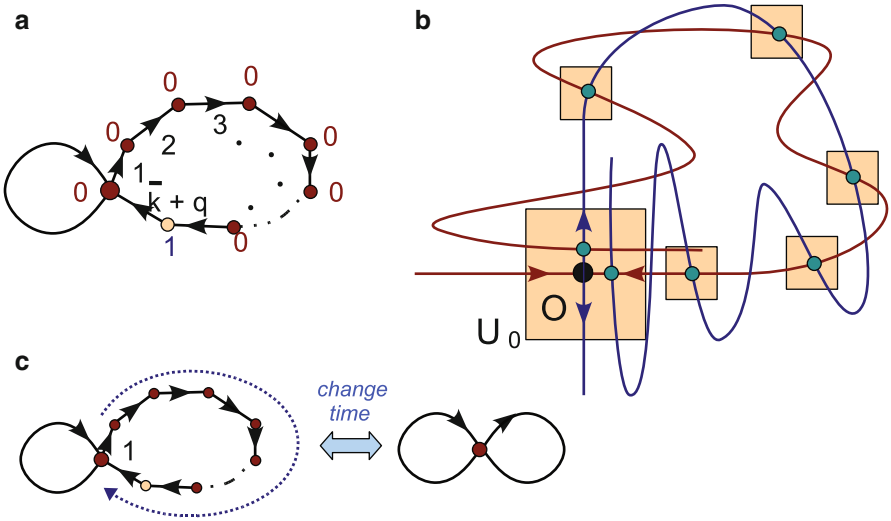

Fig. 1 **a** The graph of the Markov chain $\mathcal{B}_2^{\bar{k}+q}$ related to the symbolic description of Λ_1. **b** A neighbourhood of a transversal homoclinic orbit: $\bar{k}$ can be interpreted as a minimal number of iterations of the diffeomorphism under which orbits of Λ_1 can stay in U_0; and q is a number of neighbourhoods (*small squares*) surrounding those points of Γ_1 which do not belong to U_0. **c** Suspensions over $\mathcal{B}_2^{\bar{k}+q}$ and $\mathcal{B}_2$ are equivalent [3]

it contains infinitely (countable) many periodic and homoclinic orbits, continuum of Poisson stable orbits, etc. Nevertheless, the set Λ_1 can be described completely in terms of the symbolic dynamics, [33]. Namely, let f be a diffeomorphism having a transversal homoclinic orbit Γ_1 to a saddle fixed point O (see Fig. 1). Then the following result, *Shilnikov theorem* [33], takes place:

- *The set Λ_1 is a locally maximal uniformly hyperbolic invariant set on which a diffeomorphism is topologically conjugate to a subsystem $\mathcal{B}_2^{\bar{k}+q}$ of the Bernoulli shift $\mathcal{B}_2$ with two symbols, where $\mathcal{B}_2^{\bar{k}+q}$ is given by the Markov chain of* Fig. 1a *and $\bar{k}, q$ are integers indicated in* Fig. 1b.

Evidently, this result covers also the flow case: then one can consider the set Λ_1 as an invariant set for the Poincaré map of a local section to the corresponding saddle periodic trajectory. However, if we consider Λ_1 as the set of flow orbits, then the result sounds simpler:

- *Λ_1 is topologically equivalent to a suspension over $\mathcal{B}_2$.*

Note that the notion of suspension over a topological Markov chain was introduced in [3]. It generalizes the standard notation of suspension over a map and is convenient for description of flow dynamics (in particular, for classification of critical sets of Morse–Smale systems [2, 3]).

In the case of homoclinic tangency, the corresponding problem (of a description of the orbit structure near a non-transversal homoclinic orbit) becomes much more

complicated. Moreover, it cannot be principally solved namely as the problem of "complete description", especially when nearby systems are considered. The point is that arbitrarily small smooth perturbations of any system with a (quadratic) homoclinic tangency can lead to the appearance of homoclinic and periodic orbits of any orders of degeneracy, see [17, 18, 20, 22].

One of the problems of such a type, namely, *the study of topological and hyperbolic properties of systems with homoclinic tangencies*, is the subject of the present chapter. Hyperbolic properties of systems with quadratic homoclinic tangencies were studied first in the paper [5] of N.K. Gavrilov and L.P. Shilnikov and, afterwards, in a series of papers, e.g. [7, 8, 11]. See also the special issue [16] devoted to homoclinic tangencies. Homoclinic tangencies of arbitrary finite orders were studied in papers [6, 11] in which the main attention was given to detecting non-trivial hyperbolic subsets. Note also that certain conditions for the existence of topological horseshoes near homoclinic tangencies were established in [26, 29] for two-dimensional dissipative diffeomorphisms.

In this chapter, see also [24], we extend these results to multidimensional diffeomorphisms (not necessarily dissipative) having homoclinic tangencies to saddle periodic orbits with one-dimensional unstable invariant manifolds.

We assume throughout the paper the following set-up. Let f be an $(m+1)$-dimensional C^r-diffeomorphism, $r \geq 2$, having a hyperbolic fixed point O with multipliers $\lambda_1, \ldots, \lambda_m, \gamma$ such that

$$0 < |\lambda_m| \leq \cdots \leq |\lambda_2| \leq |\lambda_1| < 1 < |\gamma|. \tag{1}$$

We consider the quantity $\sigma \equiv |\lambda_1||\gamma|$ which is called the *saddle value*. Our main assumption is $\sigma \neq 1$ and we consider two different general cases:[1]

(1) the *sectionally dissipative case* when $\sigma < 1$ and
(2) the *sectionally saddle case* when $\sigma > 1$.

We assume also that f has a homoclinic orbit Γ_0 to O for which m-dimensional stable W^s and one-dimensional unstable W^u invariant manifolds of O are tangent and this tangency can be *arbitrary*.

Let U be a small neighbourhood of the contour $O \cup \Gamma_0$. It can be represented as a union of a small neighbourhood U_0 of the point O with a number of small neighbourhood of those points of Γ_0 which do not belong to U_0, as in Fig. 1b. Let Λ be the set of orbits (of f) entirely lying in U.

Our main problem is the study of both topological and hyperbolic properties of Λ. We will keep the following standard terminology.

Definition 1 *We say that*

(i) f possesses a trivial dynamics near Γ_0 if $\Lambda = O \cup \{\Gamma\}$, where $\{\Gamma\}$ is a set of homoclinic orbits to O;

[1] Note that the case $\sigma = 1$ (i.e. O is a neutral saddle) is very specific and we do not consider it here. We only refer the reader to papers [9, 12, 21] in which various cases of neutral saddles ($\sigma = 1$) with homoclinic tangencies were analysed; see also papers [10, 14, 15] in which area-preserving maps were considered.

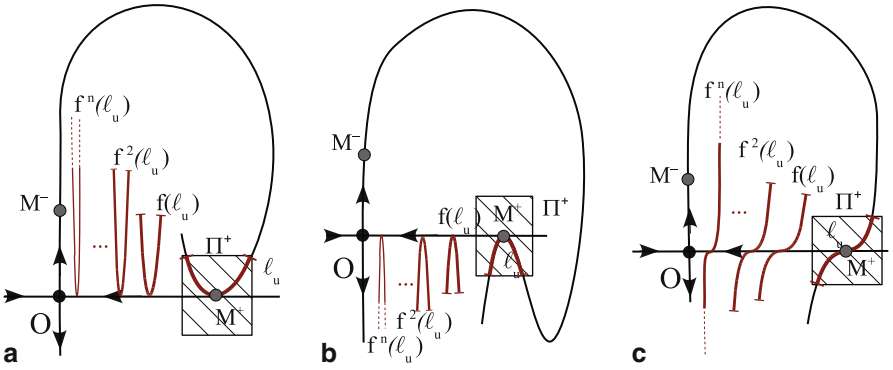

Fig. 2 Homoclinic tangencies. **a** One-sided "from above". **b** One-sided "from below". **c** Topological crossing

(ii) f has a topological horseshoe if Λ contains an f-invariant subset $\tilde{\Lambda}$ such that $f|_{\tilde{\Lambda}}$ is topologically semi-conjugate to a subshift of finite type with positive topological entropy;

(iii) f has a hyperbolic horseshoe if $\tilde{\Lambda}$ from (ii) is uniformly hyperbolic and a topological conjugacy (instead the semi-conjugacy) takes place.

Let M^+ and M^- be a pair of points of Γ_0 such that $M^+ \in W^s_{loc} \cap U_0$, $M^- \in W^u_{loc} \cap U_0$. Let Π^+ and Π^- be sufficiently small neighbourhoods of the points M^+ and M^-, respectively, and let $M^+ = f^q(M^-)$ for some integer positive q. Denote the map $f|U_0$ as T_0 and the map $f^q|\Pi^-$ as T_1 (thus, $T_1(M^-) = M^+$). The map T_0 is called the *local map*, because it is defined in a small neighbourhood of O; while, the map T_1 is called the *global map*, because it acts along a global piece of the orbit Γ_0.

Definition 2 *The homoclinic tangency is* isolated *if, for some Π^+, the point M^+ is the unique intersection point of $l_u = T_1(W^u_{loc} \cap \Pi^-) \cap \Pi^+$ and W^s_{loc}. We say that the (isolated) homoclinic tangency is* one-sided *if W^s_{loc} divides Π^+ onto two half-parts and the curve l_u belongs as whole to the closure of exactly the one half of Π^+, otherwise, the tangency is called* topological crossing. *We say that a one-sided tangency is* from below, *if the point M^- is not an accumulation point of the curves $T_0^i(l_u), i = 0, 1, \ldots$, i.e.*

$$M^- \notin \overline{\bigcup\nolimits_{i\geq 0}\{T_0^i(l_u)\}}; \tag{2}$$

and is from above *otherwise. See* Fig. 2 *for an illustration.*[2]

We need to say that the problem under consideration (on a structure of the set Λ of orbits near a non-transversal homoclinic orbit) is sharply different in many aspects

[2] Note that if $\gamma < 0$, then condition (2) can hold only when W^s_{loc} contains l_u. Thus, in this case, any isolated one-sided tangency is, in fact, a tangency "from above". On the other hand, if $\gamma > 0$, condition (2) allows a big variety of non-isolated tangencies.

from the corresponding problem (the so-called Poincaré–Birkhoff problem) for the case of transversal homoclinic orbit.

First, it does not allow a single (univalent) answer (like the Shilnikov theorem): we select two very different situations when the set Λ has a *trivial structure* and when Λ contains *infinitely many horseshoes*, in a sense of Definition 1.

Second, under the weakest assumptions, related only to geometrical properties of the homoclinic tangency, see Definition 2, we can establish the corresponding classification results for the sectionally dissipative case $\sigma < 1$ (see Theorem 1) or for the two-dimensional case $\sigma > 1$ (which is reduced to the case $\sigma < 1$ for f^{-1}), see Proposition 2. Furthermore, we render concrete the problem by means of additional general assumptions under conditions A, B, C and D in Sect. 3). Conditions A–C define the so-called *simple homoclinic tangency* and D defines an order of this tangency. Importantly, for simple homoclinic tangencies with $\sigma > 1$, we can establish quite readable classification results, see Theorems 2 and 3. However, for non-simple homoclinic tangencies with $\sigma > 1$, even for quadratic ones, we have no hope for a similar classification; see Sect. 4.1. Instead, it was shown in [6, 24] that, in the case of simple homoclinic tangencies of finite orders, a quite detailed description of non-trivial hyperbolic invariant subsets from Λ can be achieved. We collect the corresponding (hyperbolic) results in Sect. 5, see Theorems 4 and 5 and their specifications: Proposition 5 for the case $\sigma < 1$ and Proposition 6 for the case $\sigma > 1$. By "a quite detailed description", we mean that for some dense subset of systems with homoclinic tangency this description (given by Theorem 5) becomes complete; we prove this fact in Sect. 5.1, see also Proposition 7.

2 Topological Horseshoes in the Sectionally Dissipative Case

Note, at first, that condition (2) in the sectionally dissipative case ($\sigma < 1$) can be regarded to a certain criterion of trivial dynamics that the following result shows.

Theorem 1 *Let f have a homoclinic tangency to O and $\sigma < 1$. Then*

1. *If the tangency satisfies condition (2) (in particular, when the tangency is "from below"), then f possesses the trivial dynamics near Γ_0.*
2. *Otherwise, i.e. when condition (2) is not fulfilled (but, again, $\sigma < 1$), f has infinitely many topological horseshoes near Γ_0.*

The proof is given in Sect. 6, see also [24]. Note that the two-dimensional case was analysed in [29, 26]. Nevertheless, it is necessary to note that the main geometric idea of the proof is quite simple that Fig. 3 reflects where the corresponding illustrations (in dimension 2) are shown.

Indeed, the problem under consideration allows a geometric interpretations as follows. In Π^+ and Π^- there exist infinitely many ($m+1$-dimensional) disjoint strips $\sigma_k^0 \subset \Pi^+$ and $\sigma_k^1 \subset \Pi^-$, $k = k_1, k_1+1, \ldots$, such that $\sigma_k^0 = T_0^{-k}(\Pi^-) \cap \Pi^+$ and $\sigma_k^1 = T_0^k(\Pi^+) \cap \Pi^- = T_0^k \sigma_k^0$. Thus, only iterations under f of points from Π^+

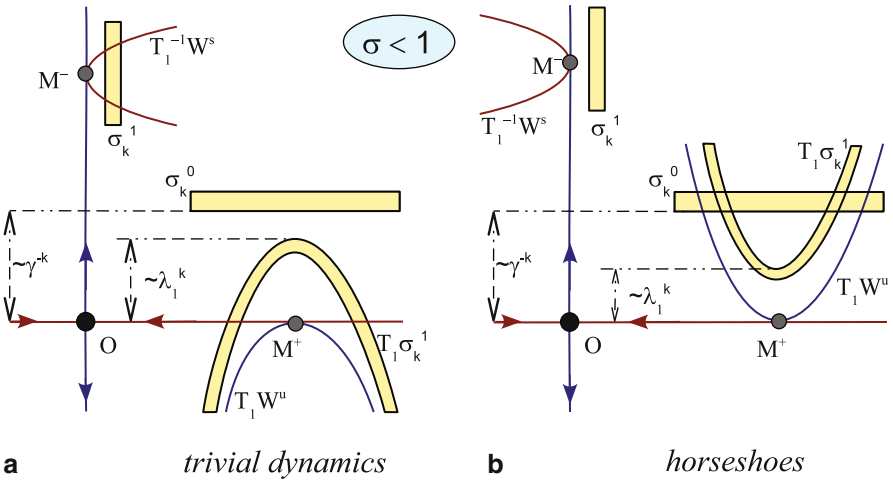

Fig. 3 The strips σ_k^0 and σ_k^1 are posed on the distances of order γ^{-k} from W^s_{loc} and λ_1^k from W^u_{loc}, respectively. By a geometry of the tangency, the image of σ_k^1 under the global map T_1 is a horseshoe $T_1(\sigma_k^1)$ whose top is posed on a distance $\sim \lambda_1^k$ from W^s_{loc}. Since $\lambda_1^k \ll \gamma^{-k}$, we have: **a** $T_1(\sigma_k^1) \cap \sigma_k^0 = \emptyset$ in the case of tangency "from below". **b** The return map $T_k \equiv T_1 T_0^k : \sigma_k^0 \to \Pi^+$ is similar to a Smale horseshoe map in the case of tangency "from above"

which belong to the strips σ_k^0 can reach Π^-. In turn, the image of the strip σ_k^1 under the global map T_1 is a horseshoe-shaped figure $T_1(\sigma_k^1) \subset \Pi^+$ (below we will use term "horseshoe $T_1(\sigma_k^1)$" namely in this, geometrical, sense). Therefore, infinitely many first return maps $T_k = T_1 T_0^k : \sigma_k^0 \to \Pi^+$, $k = \bar{k}, \bar{k}+1$, are defined here. If the tangency is "from below" all these maps possess a trivial dynamics, see Fig. 3a. However, in the case of tangency "from above" (or topological crossing), all these maps act, topologically, as Smale horseshoe maps, see Fig. 3b. Therefore, we can say, in the latter case, about existence of infinitely many *geometrical* Smale horseshoes.

Although within the hypothesis of Theorem 1 we can not say directly on hyperbolic properties of these topological horseshoes, one can apply some indirect facts, like the Katok theorem [30], in order to deduce the following.

Proposition 1 *In the case 2 of Theorem 1 the set Λ contains infinitely many hyperbolic horseshoes in sense of Definition 1.*[3]

Indeed, by Theorem 1, we get that the restriction to each topological horseshoe has positive topological entropy. The latter means that there are some orbits with positive first Lyapunov exponent. These orbits have other Lyapunov exponents to

[3] For example in the case of tangency "from above", the topological (geometrical) horseshoe of map T_k (for every value of k from an infinite sequence of integers) contains an T_k-invariant subset Δ_k such that the system $T_k|\Delta_k$ is uniformly hyperbolic and topologically conjugate to a subshift of finite type with positive topological entropy.

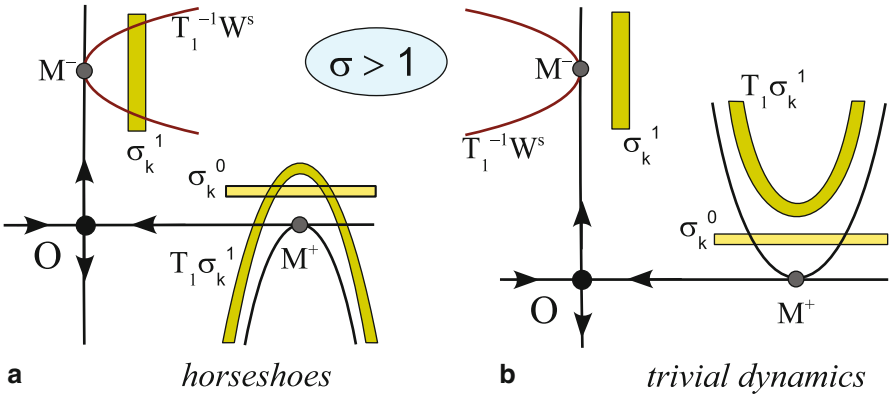

Fig. 4 Geometry of strips and horseshoes in the case $\sigma > 1$

be negative, due to the sectional dissipation that implies the absence of such orbits having zero second Lyapunov exponent.[4]

Thus, in the sectionally dissipative case, relation (2) provides the *necessary condition* for the existence of trivial dynamics near a homoclinic tangency. It is not the case when $\sigma > 1$. In particular, we can see principal differences in geometry between the cases $\sigma < 1$ and $\sigma > 1$ even in dimension two (compare Figs. 3 and 4). However, Theorem 1 can be directly applied to this 2dim case for $\sigma > 1$, since we can here consider f^{-1} instead f. Then the following condition

$$M^+ \notin \overline{\bigcup_{i\geq 0}\{T_0^{-i}(l_s)\}}, \tag{3}$$

where the curve $l_s \subset \Pi^-$ is defined as $l_s = T_1^{-1}(W^s_{loc} \cap \Pi^+) \cap \Pi^-$, plays role of the condition(2). Thus, we obtain

Proposition 2 *Let f be two-dimensional and $\sigma > 1$. Then*

1) *If condition (3) holds, then f possesses a trivial dynamics near Γ_0.*
2) *Otherwise, i.e. when (3) is not valid (but, again, $\sigma > 1$), then f has infinitely many topological horseshoes near Γ_0 every of which contains a hyperbolic horseshoe in sense of Definition 1.*

Unfortunately, this approach is not suitable for multidimensional case with $\sigma > 1$ since $\dim W^u(O) > 1$ for f^{-1} and it is not the case under consideration. Moreover, as we will see below, in this case we need, by necessity, an additional specification of the homoclinic tangency, since only geometrical properties are not sufficient even for deriving certain classification results like Theorem 1. However, an analogous specification is required especially (even for the case $\sigma < 1$), if we want to know

[4] We thank D. Turaev who attracted our attention to the interesting fact that the Katok theorem can be directly applied to the sectionally dissipative case. See also [35].

more. question relates to hyperbolic properties. Indeed, the hyperbolic horseshoes from Corollary 1 are not specified. We do not know whether the first return maps $T_1 T_0^i : \sigma_i^0 \to \sigma_i^0$ are hyperbolic. In order to get more information, we need to make more assumptions (see conditions A–D below).

3 The Definition of a Simple Homoclinic Tangency

Let the multipliers $\lambda_1, \dots, \lambda_m, \gamma$ of O are ordered as in (1). We call *leading* (or weak) those multipliers that are equal to $|\lambda_1|$ by the absolute value. Accordingly, the other stable multipliers (less than $|\lambda_1|$ by modulus) are called *non-leading* (or strong stable). We consider the following general condition:

A) the leading stable multipliers of O are simple.
Accordingly, two different types of saddle fixed (periodic) points are defined. Namely,

A1) the point O is a *saddle*, i.e. the multiplier λ_1 is real and $|\lambda_1| > |\lambda_j|$ for $j = 2, \dots, m$;

A2) the point O is a *saddle-focus*, i.e. λ_1 and λ_2 are complex conjugate, $\lambda_1 = \lambda e^{i\psi}, \lambda_2 = \lambda e^{-i\psi}, 0 < \lambda < 1, 0 < \psi < \pi$ and $\lambda > |\lambda_j|$ for $j = 3, \dots, m$.

When the point O has also non-leading stable multipliers we need more assumptions related to the homoclinic tangency. Recall some necessary facts.

First, if Condition A holds, the manifold $W^s_{loc}(O)$ contains a C^r-smooth *strong stable manifold* W^{ss}_{loc} which touches at O the eigenspace of Df corresponding to the non-leading multipliers λ_i (thus, the W^{ss}_{loc} has dimension $(m-1)$ or $(m-2)$ when, respectively, A1 or A2 holds). Moreover, it is well-known (see e.g. [25, 34]) that W^s_{loc} is foliated by the C^r *strong stable foliation* F^{ss} containing W^{ss}_{loc} as the leaf.

Note also that the manifold $W^u(O)$ is a part of the so-called *extended unstable manifold* $W^{ue}(O)$ (see, for example, [25, 34]). It is a smooth (at least $C^{1+\epsilon}$) invariant manifold which is tangent, at O, to the eigenspace of Df corresponding to the unstable and the leading stable multipliers, thus, W^{ue} is two- or three-dimensional if O is a saddle or a saddle focus, respectively. Although, the manifold W^{ue} is not defined uniquely, any two such manifolds contain W^u_{loc} and are tangent to each other at the points of W^u_{loc}. Thus, at the homoclinic point $M^- \in W^u_{loc}$ the tangent space to W^{ue}, denoted as $\mathcal{T}_{M^-} W^{ue}$ is defined uniquely. Since $M^+ = T_1(M^-)$, we can extend W^{ue} up to the homoclinic point M^+. Denote the tangent space to W^{ue} at M^+ as $\mathcal{T}_{M^+} W^{ue}$. Evidently, $\mathcal{T}_{M^+} W^{ue} = DT_1\,(\mathcal{T}_{M^-} W^{ue}))$, where DT_1 denotes the differential of the global map $T_1 \equiv f^q : \Pi^- \to \Pi^+$ at the point M^-.

We introduce the following general conditions: *the off strong stable manifold condition*

B) $M^+ \notin W^{ss}_{loc}$
and *subtransversality condition*

C) $\mathcal{T}_{M^+} W^{ue}$ is transversal to $F^{ss}(M^+)$ at M^+, where $F^{ss}(M^+)$ is the leaf of the foliation F^{ss} containing the point M^+.

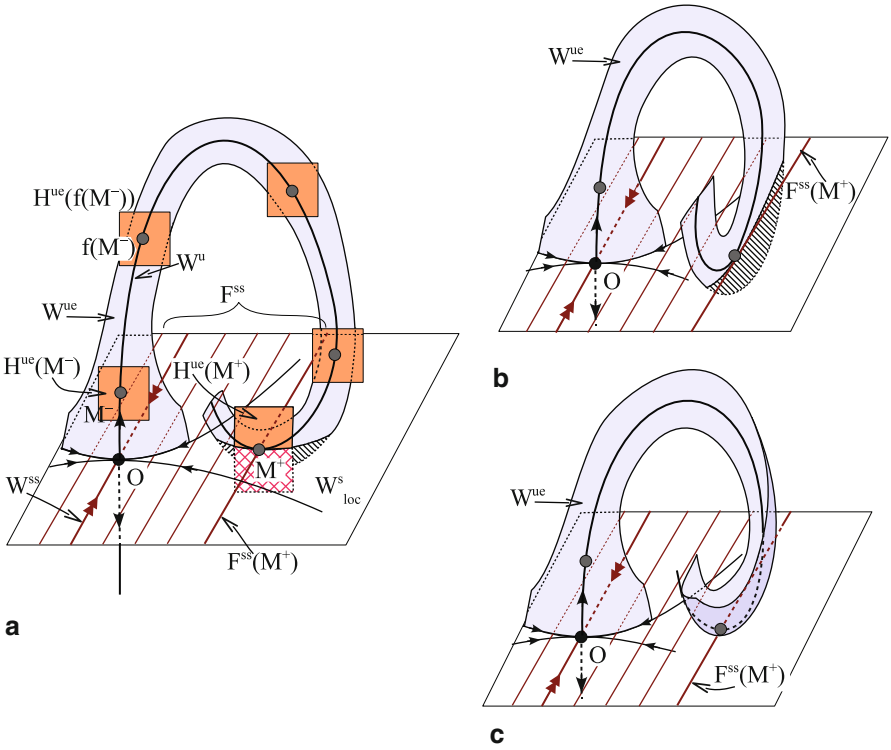

Fig. 5 Examples of three-dimensional diffeomorphisms with simple (**a**), and non-simple (**b**)–(**c**) homoclinic tangencies

An example of three-dimensional diffeomorphism satisfying the conditions A1, B and C is shown in Fig. 5a. Main cases where C is violated (while A1 and B are kept) are illustrated in Fig. 5b and c. Here, either $\mathcal{T}_{M^+} W^{ue}$ is transversal to W^s_{loc} but touches $F^{ss}(M^+)$ at M^+, as in case (b), or $\mathcal{T}_{M^+} W^{ue}$ belongs to W^s_{loc} (i.e., any surface $T_1(W^{ue})$ touches W^s_{loc} at M^+), as in case (c).

Definition 3 *A homoclinic tangency satisfying conditions A–C is called* simple.

We can also adapt this definition to homoclinic tangencies of finite orders as follows.

Definition 4 Let f be a C^r-diffeomorphism under consideration and n be an integer such that $2 \le n \le r$. Then we say that the homoclinic tangency at M^+ is of order n if there exists local (near M^+) C^r-coordinates $(\xi_1, \ldots, \xi_m, \eta)$ in which W^s_{loc} has the equation $\eta = 0$ and a piece of W^u containing M^+ can be written (in the parameter form) as follows

$$\xi_i = b_i \alpha + O(\alpha^2),\ (i = 1, \ldots, m),\ \eta = g(\alpha), \tag{4}$$

where $g(\alpha)$ is C^r and

$$g(0) = \frac{dg(0)}{d\alpha} = \cdots = \frac{d^{n-1}g(0)}{d\alpha^{n-1}} = 0, \frac{d^n g(0)}{d\alpha^n} = n!, \quad d \neq 0, \tag{5}$$

where α is a parameter varying near zero, b_i and d are constants and $\sum |b_i| \neq 0$. If all derivatives $d^i g(0)/d\alpha^i$ vanish for $i = 0, \ldots, s$, where $s \geq r$, then we say that the tangency is of indefinite order.

By definition, tangencies of even orders are one-sided, while, tangencies of odd orders correspond to the topological crossings. Tangencies of some small orders have special notations: *quadratic* for $n = 2$, *cubic* for $n = 3$, *quadric* for $n = 4$. Note that a type of the tangency can depend on coordinate changes. For instance, even a quadratic tangency can be transformed into a tangency of indefinite order under C^1-change of coordinates.[5]

We introduce the following condition:

D) the manifolds $W^s(O)$ and $W^u(O)$ have the tangency of a finite order $n \geq 2$ at the homoclinic point M^+.

Since f is diffeomorphism, condition D implies that $W^s(O)$ and $W^u(O)$ have tangency of order n at any point of Γ_0. Note that, in the real analytical case, the condition D holds always in that sense that any possible homoclinic tangency can be only of finite order here (except for infinitely degenerate cases when $W^s(O)$ and $W^u(O)$ coincide).

By Definition 3, a homoclinic tangency satisfying conditions A–D should be labeled as *simple homoclinic tangency of order n*. Note that notation of simple quadratic homoclinic tangency was introduced in [19] which is, in fact, a certain variant of the so-called quasi-transversal homoclinic intersection, [31].

Note that conditions A–C have very important dynamical sense. Namely, when these conditions hold the corresponding diffeomorphism f has, see [34, 36],

- *A global smooth invariant center manifold W^c which contains the orbits O and Γ_0 as well as all orbits entirely lying in U.*

This manifold is normally-hyperbolic (in sense of [25]), since f is exponentially contracting along transversal to W^c directions which correspond, at O, to the u-directions. Therefore, $\dim W^c = 2$ or $\dim W^c = 3$ depending on A1 or A2 holds and, thus, the problem under consideration allows the so-called *dimension reduction* to $\dim = 2$ or $\dim = 3$, respectively. Therefore, it has a certain sense to single out this type of homoclinic tangencies, i.e. *the simple homoclinic tangencies*.

However, an insufficient smoothness of W^c (only $C^{1+\epsilon}$, the same as for W^{ue}) "destroys" the condition D in the restricted system $f|W^c$. Therefore, when this condition is principally important (see Sect. 5) we should work with the initial multidimensional system (even in the sectionally dissipative case $\sigma < 1$). On the other hand,

[5] Therefore, in problems of such type, it is not reasonable to use a C^1-linearization (which, by the way, does not always exist in the multidimensional case). This can lead to non-repairable mistakes in the proofs or to absurd results, and, in the best case, only very rough topological properties can be established [32, 4].

the condition D is hardly controlled one (for specific systems) and, therefore, it is reasonable to assume that only its topological variant takes place, i.e. the homoclinic tangency is *simple one-sided* or *simple topological crossing* (here, "simple" means again that conditions A–C are fulfilled). In this case one can obtain certain meaningful results related to the existence of horseshoes (topological or even hyperbolic) in the case $\sigma > 1$. See Sect. 4.

3.1 On a Coordinate Expression of the Simple Homoclinic Tangency

We will use in U_0 local coordinates in which the saddle map T_0 takes the so-called *main normal form* or *normal form of the first order*. This form is very convenient for calculations and, in contrast to the linear form, exists always. Thus, the following result holds.

Lemma 1 [13, 8, 34]. *Let f be C^r ($r \geq 2$) and O have multipliers $\lambda_1, \ldots, \lambda_m, \gamma$ satisfying (1). Then the map $T_0 = f|U_0$ can be written, in some C^r-coordinates (x, u, y) on U, as follows:*

$$(\bar{x}, \bar{u}, \bar{y}) = \left(\hat{A}x + h_1(x, u, y), \hat{B}u + h_2(x, u, y), \gamma y + h_3(x, u, y)\right), \tag{6}$$

where eigenvalues of the matrix $\hat{A}$ are equal to $|\lambda_1|$ by absolute values, whereas, eigenvalues of $\hat{B}$ are all smaller. Besides, the functions h_1, h_2, h_3 satisfy conditions

$$\begin{aligned} &h_1(0, 0, y) \equiv 0,\ h_2(0, 0, y) \equiv 0,\ h_3(x, y, 0) \equiv 0, \\ &h_1(x, u, 0) \equiv 0,\ h_3(0, 0, y) \equiv 0, \\ &\frac{\partial h_1}{\partial x}|_{x=0,u=0} \equiv 0,\ \ \frac{\partial h_2}{\partial x}|_{x=0,u=0} \equiv 0\ \ \frac{\partial h_3}{\partial y}|_{y=0} \equiv 0. \end{aligned} \tag{7}$$

Remark 1 The proof of Lemma 1 is based on the so-called "Afraimovich changes of variables" [1]. In turn, these changes generalize the method by E.A. Leontovich for construction of finitely-smooth normal forms of two-dimensional flows near saddle equilibria [27, 28]. See also [21, 34] for a modern treatment of this theory.

If condition A holds, we have in Lemma 1 that either $x \in \mathbb{R}^1$ and $\hat{A} = \lambda_1$ in case A1; or $x \in \mathbb{R}^2$ and $\hat{A}_2 = \lambda \begin{pmatrix} \cos\psi & -\sin\psi \\ \sin\psi & \cos\psi \end{pmatrix}$ in case A2.

Using the main normal form one can easily calculate any iterations T_0^k, especially, when k is large that the following result shows.

Lemma 2 [13, 8, 34] *Let* $(x_k, u_k, y_k) = T_0^k(x_0, u_0, y_0)$. *When the local map* T_0 *is written in form* (6) *and identities* (7) *hold, the following relations take place for all large* k*:*

$$\begin{aligned} x_k \ - \ \hat{A}^k x_0 \ &= \ \hat{\lambda}^k \xi_k(x_0, u_0, y_k), \\ u_k \ &= \ \hat{\lambda}^k \hat{\xi}_k(x_0, u_0, y_k), \\ y_0 \ - \ \gamma^{-k} y_k \ &= \ \hat{\gamma}^{-k} \eta_k(x_0, u_0, y_k) \end{aligned} \tag{8}$$

where $\hat{\lambda}$ *and* $\hat{\gamma}$ *are some constants such that* $0 < \hat{\lambda} < |\lambda_1|$, $\hat{\gamma} > |\gamma|$ *and functions* $\xi_k, \eta_k, \hat{\xi}_k, \hat{\eta}_k$ *are uniformly bounded for all* k*, along with the derivatives up to order* $(r-2)$. *The derivatives of orders* $(r-1)$ *and* r *are estimated as follows* $\|x_k, u_k\|_{C^{r-1}} = o(|\lambda_1|^k)$, $\|y_0\|_{C^{r-1}} = o(|\gamma|^{-k})$ *and* $\|x_k, u_k, y_0\|_{C^r} = o(1)_{k\to\infty}$.

In the coordinates of Lemma 1, the manifolds $W^s_{loc}(O)$, $W^u_{loc}(O)$ as well as W^{ss}_{loc} are straightened, i.e. they have the following equations:

$$W^s_{loc}(O) \ - \ \{y = 0\}, \ \ W^u_{loc}(O) \ - \ \{(x, u) = 0\}, \ \ W^{ss}_{loc} \ - \ \{x = 0, y = 0\}.$$

Hence, we can write that $M^+ = (x^+, u^+, 0)$ and $M^-(0, 0, y^-)$, where $y^- > 0$. If condition B holds, then $\|x^+\| \neq 0$. In case A1, since $x \in \mathbb{R}^1$ (and $u \in \mathbb{R}^{m-1}$), it means that $x^+ \neq 0$ and we assume that $x^+ > 0$ here.

Define the neighbourhoods Π^+ and Π^- of M^+ and M^-, respectively, as follows

$$\Pi^+ = \{\|(x - x^+, u - u^+)\| \le \varepsilon_0, |y| \le \varepsilon_0\}, \ \ \Pi^- = \{\|(x, u)\| \le \varepsilon_1, |y - y^-| \le \varepsilon_1\}, \tag{9}$$

where $\varepsilon_0 > 0, \varepsilon_1 > 0$ are sufficiently small and $T_0\Pi^+ \cap \Pi^+ = \emptyset$, $T_0^{-1}\Pi^- \cap \Pi^- = \emptyset$.

The global map $T_1 \equiv f^q : \Pi^- \to \Pi^+$ can be written as follows

$$(\bar{x} - x^+, \bar{u} - u^+) \ = \ F(x_1, u_1, y_1 - y^-), \ \ \bar{y} \ = \ G(x_1, u_1, y_1 - y^-), \tag{10}$$

where C^r-functions F and G are defined on Π^- and $F(0) = 0, G(0) = 0$ as well as $G_y(0) = 0$. Then we can write the map T_1 in the following form

$$\begin{aligned} &(\bar{x} - x^+, \bar{u} - u^+) = ax + \hat{a}u + b(y - y^-) + O\left(\|(x, u)\|^2 + (y - y^-)^2\right), \\ &\bar{y} = cx + \hat{c}u + \varphi(y - y^-) + O\left(\|(x, u)\|^2 + \|(x, u)\||y - y^-|\right), \end{aligned} \tag{11}$$

where $\varphi(0) = 0$ and $\varphi'(0) = 0$, since the curve $T_1(W^u_{loc})$ touches W^s_{loc} at the point M^+, and

$$\det \begin{pmatrix} a & \hat{a} & b \\ c & \hat{c} & 0 \end{pmatrix} \ \neq \ 0. \tag{12}$$

If condition D holds, then

$$\varphi(y - y^-) \ \equiv \ d(y - y^-)^n + o\left((y - y^-)^n\right) \ \text{ and } \ d \neq 0. \tag{13}$$

Note also that, in the coordinates of Lemma 1, the foliation F^{ss} has a form $\{x = const, y = 0\}$ and the tangent space $\mathcal{T}_M W^{ue}$ to W^{ue} at any point $M \in W^u_{loc}$ is the plane $u = 0$. Then condition C means, by (11), that the planes $\mathcal{T}_{M^+} W^{ue}$: $\{(\bar{x} - x^+, \bar{u} - u^+) = ax + b(y - y^-), \quad \bar{y} = cx\}$ and $F^{ss}(M^+)$: $\left\{\bar{x} = x^+, \bar{y} = 0\right\}$ are transversal (here, $\mathcal{T}_{M^+} W^{ue}$ is given in a parameter form where x and $(y - y^-)$ are parameters). It means that the system $(0, u - u^+) = ax + b(y - y^-), 0 = cx$ has a unique solution. Thus, condition C reads as

$$b_1 \neq 0, \quad c \neq 0 \ \text{ in case A1} \tag{14}$$

or as

$$b_1^2 + b_2^2 \neq 0, \quad c_1^2 + c_2^2 \neq 0 \ \text{ in case A2.} \tag{15}$$

Note that Fig. 5b and c correspond to the case A1 with $b_1 = 0$ and $c = 0$, respectively.

4 On Simple Homoclinic Tangencies in the Sectionally Saddle Case

In this section we consider, essentially, the multidimensional sectionally saddle case $\sigma > 1$. Concerning a type of the homoclinic tangencies, we assume in this section that they are *isolated and one-sided*.

Then f can possess both trivial and non-trivial dynamics near Γ_0 depending on type of the tangency.

Remark 2 In the case of topological intersection, infinitely many topological horseshoes near the homoclinic tangency always exist. It follows from the fact that the system $f|\Lambda$ is *semi-conjugate* to $\mathcal{B}_2^{\bar{k}+q}$ (compare with the Shilnikov theorem from Introduction). However, even in this case, if conditions A1, B and C hold (i.e. O is a saddle and the tangency is simple), infinitely many *hyperbolic horseshoes* (in the sense of Definition 1) exist. This fact follows directly from the Katok theory, since the problem allows reduction to dim = 2 in this situation. Note that in [11] certain classes of systems with simple homoclinic tangencies of odd order are described for which $f|\Lambda$ is *topologically conjugate* to $\mathcal{B}^2_{\bar{k}+q}$ and all orbits of Λ, except Γ_0, are of saddle type.

We introduce the so-called "index of one-sided tangency" ν_0 that can take values $+1$ or -1 and is defined as follows. Consider the piece $T_1(W^u_{loc}) \cap \Pi^+$ of $W^u(O)$ which, by (11), has the equation

$$(\bar{x} - x^+, \bar{u} - u^+) = b\alpha + O\left(\alpha^2\right), \quad \bar{y} = \varphi(\alpha), \tag{16}$$

written in the parametric form, where $\alpha = y - y^-$ is a parameter. Since $\varphi(0) = 0, \varphi'(0) = 0$, the curve (16) touches the plane $\bar{y} = 0$ at $\alpha = 0$. Let this tangency be

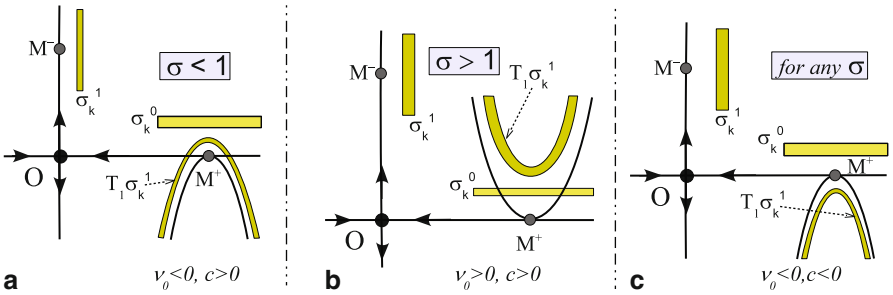

Fig. 6 Examples of simple homoclinic tangencies with trivial dynamics for $\lambda_1 > 0, \gamma > 0$

one-sided, then we define

$$\nu_0 \;=\; \text{sign}\,\varphi(\xi) \;\text{ at }\xi \neq 0.$$

Thus, if $\gamma > 0$ the homoclinic tangency (one-sided and isolated) is "from below" if $\nu_0 = -1$ and it is "from above" if $\nu_0 = +1$. If $\gamma < 0$ the value of index ν_0 depends on a choice of homoclinic points in such a way that, for example, $\nu_0(M^+) = -\nu_0(f(M^+))$; it means that we can always take such pairs of the homoclinic points that $\nu_0 = +1$. Note that if the tangency is of even order, then $\nu_0 \;=\; \text{sign}\; d$ that follows directly from (13).

Theorem 2 [Simple homoclinic tangencies with trivial dynamics]
Let f have a one-sided homoclinic tangency satisfying A1, B and C and one of the following conditions: (1) $\sigma < 1$ and $\gamma > 0, \nu_0 < 0$; (2) $\sigma > 1$ and $\lambda_1 > 0, c\nu_0 > 0$ or 3) $\lambda_1 > 0, \gamma > 0, c < 0, \nu_0 < 0$ (independently on σ).

Then f possesses trivial dynamics near Γ_0, i.e. $\Lambda = O \cup \Gamma_0$.

Proof Item 1 of the theorem is a partial case of Theorem 1, see Fig. 6a.

Consider item 2 of the theorem.

Since A1 holds, the map T_0, by Lemma 1, takes the form

$$(\bar{x}, \bar{u}, \bar{y}) \;=\; \left(\lambda_1 x + h_1(x,u,y), \hat{B}u + h_2(x,u,y), \gamma y + h_3(x,u,y)\right), \qquad (17)$$

where $x, y \in \mathbb{R}^1$, $u \in \mathbb{R}^{m-1}$ and the matrix $\hat{B}$ has eigenvalues $\lambda_2, \ldots, \lambda_m$. Then, by Lemma 2, map T_0^k can be written in the following cross-form (compare with (8))

$$x_k \;=\; \lambda_1^k x_0 \left(1 + O([\hat{\lambda}/\lambda_1]^k)\right), u_k = O\left(\hat{\lambda}^k\right), \;\; y_0 \;=\; \gamma^{-k} y_k (1 + O\left([\hat{\gamma}/\gamma]^{-k}\right)). \qquad (18)$$

Using (11) we can write the first return map $T_k = T_1 T_0^k : \sigma_k^0 \mapsto \Pi^+$ as follows

$$\begin{aligned}(\bar{x}_0 - x^+, \bar{u}_0 - u^+) &= b(y_1 - y^-) + O\left(|\lambda_1|^k \|(x_0,u_0)\| + (y_1 - y^-)^2\right),\\ \bar{y}_0 &= c_1 \lambda_1^k x_0 + \varphi(y_1 - y^-) + O\left(\tilde{\lambda}^k \|(x_0,u_0)\| + |\lambda_1^k| \|(x_0,u_0)\| |y_1 - y^-|\right),\end{aligned} \qquad (19)$$

where $x_0, y_0, y_1 \in \mathbb{R}^1, u_0 \in \mathbb{R}^{m-1}$. Let $\bar{y}_0$ be the y-coordinate of a point inside some strip $\sigma_j^0 \subset \Pi^+$. Then we can write, by (18), that $\bar{y}_0 = \gamma^{-j}\bar{y}_1 + O(\tilde{\gamma}^{-j})$. Introduce the coordinates $\xi = x_0 - x^+, \hat{\xi} = u_0 - u^+$ and $\eta = y_1 - y^-$. Then we can write the second equation of (19) in the form

$$\gamma^{-j}\left(y^- + \bar{\eta} + O([\hat{\gamma}/\gamma]^{-j}\right) \;=\; c_1\lambda_1^k\left(x^+ + O(|\xi| + |\eta|) + O([\hat{\lambda}/\lambda]^j)\right) + \varphi(\eta). \tag{20}$$

Since $\xi, \hat{\xi}, \eta$ are small, $x^+ > 0, y^- > 0$ as well as $\lambda_1 > 0$ and $c_1\nu_0 > 0$, Eq. (20) can have solutions only in the case $|\gamma|^{-j} \geq \lambda_1^k$. Since $|\lambda_1\gamma| > 1$, this inequality can be fulfilled if only $k \gg j$. Thus, any horseshoe $T_1(\sigma_k^1)$ can intersect only those strips σ_j^0 whose numbers are strictly less than k, see Fig. 6b. It implies that some forward iteration of any point from Π^+ must leave U. Thus, only two orbits, O and Γ_0, will always stay in U which implies that the dynamics is trivial.

In the case $\lambda_1 > 0, \gamma > 0, c_1 < 0, \nu_0 < 0$, Eq. (20) has no solutions at all, independently on σ. It means that the horseshoes $T_1(\sigma_k^1)$ do not intersect any strip σ_i^0, see Fig. 6c, i.e. the dynamics is trivial. This completes item (3) of the theorem.

Theorem 3 [Simple one-sided tangencies with non-trivial dynamics at $\sigma > 1$] *Let f have a one-sided homoclinic tangency satisfying conditions A–C and let $\sigma > 1$. Then the set $\Lambda(f)$ contains infinitely many topological horseshoes in the following cases:*

(1) *the point O is a saddle-focus, i.e. conditions A2 holds;* (2) *the point O is a saddle, i.e. A1 holds, and the combination $\lambda_1 > 0, \nu_0 > 0$ of the signs takes no place.*

Proof In the case of *item 1* of the theorem, we have, by Lemma 1, that the local map T_0 has the form

$$(\bar{x}, \bar{u}, \bar{y}) = \left(\lambda R_\psi x + h_1(x, u, y), \hat{B}u + h_2(x, u, y), \gamma y + h_3(x, u, y)\right),$$

where $x = (x_1, x_2)$ and R_ψ is the rotation matrix (on the angle ψ). The global map T_1 has now form (11), where $c = (c_1, c_2)$ and $c_1^2 + c_2^2 \neq 0$ by the condition C and $\varphi(s)$ is a function of fixed sign at $s \neq 0$ because the homoclinic tangency is one-sided.

Consider the first return map $T_k = T_1T_0^k : \sigma_k^0 \mapsto \Pi^+$ which can be written now as

$$\begin{aligned}
&(\bar{x} - x^+, \bar{u} - u^+) = (b_1, b_2)^\intercal(y - y^-) + O\left(\lambda^k\|(x, u)\| + (y - y^-)^2\right),\\
&\bar{y} = \lambda^k\left((c_1\cos k\psi + c_2\sin k\psi)x_1 + (c_2\cos k\psi - c_1\sin k\psi)x_2\right)\\
&\qquad + \varphi(y - y^-) + +O\left(\tilde{\lambda}^k\|(x, u)\| + \lambda^k\|(x, u)\||y - y^-|\right).
\end{aligned} \tag{21}$$

Let us show that, for infinitely many values of k, these maps T_k are, geometrically, Smale horseshoe maps. Introduce new x-coordinates as $\xi_1 = x_1 - x_1^+, \xi_2 = x_2 - x_2^+$. Then the second equation from (21) can be written as

$$\begin{aligned}
\bar{y} = \lambda^k\left(\hat{C}\cos(k\psi + \theta) + O(\|\xi\|)\right) + \varphi(y - y^-)\\
+O\left(\tilde{\lambda}^k\|(\xi, u)\| + \lambda^k\|(\xi, u)\||y - y^-|\right),
\end{aligned} \tag{22}$$

where $\hat{C} = \sqrt{(c_1^2 + c_2^2)((x_1^+)^2 + (x_2^+)^2)}$ and $\theta \in [0, 2\pi)$ is an angle such that $\cos\theta = (c_1 x_1^+ + c_2 x_2^+)\hat{C}^{-1}$, $\cos\theta = (c_2 x_1^+ - c_1 x_2^+)\hat{C}^{-1}$.

Note that $\hat{C} > 0$, since the conditions B and C imply, respectively, that $(x_1^+)^2 + (x_2^+)^2 \neq 0$ and $c_1^2 + c_2^2 \neq 0$.

Let $\varphi(s) \geq 0$ and $\gamma > 0$, for the sake of definiteness. Then $\bar{y}$ from (22) can run values from $\bar{y}_{min} = \lambda^k(\hat{C}\cos(k\psi + \theta) + O(\|\xi\|))$ till $\bar{y}_{max} = \max\varphi(s)_{|s|\leq\varepsilon_1} + O(\lambda^k)$. However, values of the coordinate y on the strip σ_k^0 satisfy the inequality

$$\gamma^{-k}(y^- - \varepsilon_1) < y < \gamma^{-k}(y^- + \varepsilon_1).$$

Evidently, there are such $\delta_0 > 0$ and $\delta_1 > 0$ that (i) $\bar{y}_{max} > \delta_0$ for all sufficiently large k and (ii) for any ψ, since $\hat{C} > 0$ and $\|\xi\|$ is small, there are infinitely many such k that $(\hat{C}\cos(k\psi + \theta) + O(\|\xi\|)) < -\delta_1$. Thus, the first return map $T_1 T^k$ for such values of k transforms the strip σ_k^0 into the horseshoe $T_k(\sigma_k^0)$ such that its top is posed below σ_k^0 (and even below W^s_{loc}) and the horseshoe intersects σ_k^0 forming (at least) two connected components. Thus, f possesses, in this case, infinitely many geometrical Smale horseshoes. Other cases are considered analogously.

Consider *item 2* of the theorem. Since $A1$ holds, the map $T_k = T_1 T_0^k : \sigma_k^0 \mapsto \Pi^+$ can be written now as

$$\begin{aligned}(\bar{x} - x^+, \bar{u} - u^+) &= (b_1, b_2)^\intercal (y - y^-) + O\left(|\lambda_1|^k \|(x,u)\| + (y - y^-)^2\right),\\ \bar{y} &= c\lambda_1^k x + \varphi(y - y^-) + O\left(\tilde{\lambda}^k \|(x,u)\| + |\lambda_1|^k \|(x,u)\| |y - y^-|\right).\end{aligned} \tag{23}$$

Denote $\xi = x - x^+$. Then the second equation from (23) is rewritten as

$$\bar{y} = c\lambda_1^k \left(x^+ + O(|\xi|) + O([\tilde{\lambda}/\lambda_1]^k)\right) + \varphi(y - y^-). \tag{24}$$

Consider the model equation $\gamma^{-k} y^- = c\lambda_1^k x^+ + \varphi(s)$ where $s \in [-\varepsilon_1, \varepsilon_1]$ and for some $\hat{\delta} > 0$, $\varphi(s) \in [0, \hat{\delta}]$ or $\varphi(s) \in [-\hat{\delta}, 0]$ and $\nu_0 = \mathrm{sign}\varphi(s)_{s\neq 0}$. Since $|\lambda_1\gamma| > 1$, this equation has no solution (with respect to s) only in the case where $\lambda_1 > 0$ and $c\nu_0 > 0$. In other cases, at least two solutions exist.

It gives us the desired result.

4.1 On the Necessity of Conditions A and C for the Existence/Absence of Topological Horseshoes

Note that, in the sectionally dissipative case $\sigma < 1$, as we can see from Theorem 1, conditions A, B and C play only a role of auxiliary conditions which help to establish certain hyperbolic properties. However, in the sectionally saddle case $\sigma > 1$, these conditions become necessary even for the topological horseshoe property. If they are violated, then the corresponding system can possess either trivial dynamics or horseshoes depending on new characteristics of the corresponding (non-simple) homoclinic tangency. We illustrate this fact by means of considering a three-dimensional model below.

Let g_0 be a three-dimensional diffeomorphism having a saddle fixed point $\hat{O}$ with multipliers $\lambda_1, \lambda_2, \gamma$, where $0 < \lambda_2 < \lambda_1 < 1 < \gamma$ and $\lambda_1\gamma > 1$, and a homoclinic orbit $\hat{\Gamma}_0$ at whose points the manifolds $W^u(\hat{O})$ and $W^s(\hat{O})$ have a quadratic tangency. We assume also that this homoclinic tangency is not simple, the local map T_0 is linear and the global map T_1 is of model form. We take T_0 in the linear form $(\bar{x}, \bar{u}, \bar{y}) = (\lambda_1 x, \lambda_2 u, \gamma y)$ and T_1 in the following form

$$(\bar{x}_0 - x^+, \bar{u}_0 - u^+, \bar{y}_0) = \big(b_1(y - y^-), a_{21}x, \hat{c}u + d(y - y^-)^2\big), \tag{25}$$

where $b_1 a_{21}\hat{c} \neq 0$, since the map T_1 should be diffeomorphism. We see that condition C is violated in this case: the model map T_1 corresponds to the case where $c = 0$ in (11), i.e. (14) is not valid here. We assume, for more definiteness, that $d < 0$, i.e. the quadratic homoclinic tangency is "from below". We assume also that $u^+ > 0$ in the given example.

Proposition 3 *The following dynamical properties of g_0 hold.*

(i) *If $\hat{c} < 0$, then $\Lambda(g_0)$ is trivial, i.e. $\Lambda(g_0) = \hat{O} \cup \hat{\Gamma}_0$.*
(ii) *If $\hat{c} > 0$ and $\lambda_2\gamma < 1$, then $\Lambda(g_0)$ is trivial, i.e. $\Lambda(g_0) = \hat{O} \cup \hat{G}_0$.*
(iii) *If $\hat{c} > 0$ and $\lambda_2\gamma > 1$, then $\Lambda(g_0)$ contains infinitely many geometrical Smale horseshoes.*

Proof Since the corresponding results have an independent interest and the proof consists mainly in direct calculations, we analyse the problem under consideration in more detail than before. Since T_0 is linear, the equations of $W^s_{loc}(O)$ and $W^u_{loc}(O)$ are $y = 0$ and $(x = 0, u = 0)$, respectively. We choose a pair of homoclinic points: $M^+(x^+, u^+, 0) \in W^s_{loc}$ and $M^-(0, 0, y^-) \in W^u_{loc}$ assuming that $u^+ > 0, y^- > 0$. We consider sufficiently small rectangle neighbourhoods $\Pi^+ = \{|x - x^+| \le \varepsilon_0, |u - u^+| \le \varepsilon_0, |y| \le \varepsilon_0)\}$ and $\Pi^- = \{|x| \le \varepsilon_1, |u| \le \varepsilon_1, |y - y^-| \le \varepsilon_1)\}$ of the points M^+ and M^-, respectively, such that $T_0(\Pi^+) \cap \Pi^+ = \emptyset$ and $T_0^{-1}(\Pi^-) \cap \Pi^- = \emptyset$. Note that (for any $\varepsilon_{0,1} > 0$) there exist points on Π^+ whose iterations under T_0 reach Π^-. The set of such initial points on Π^+ consists from countable many disjoint strips $\sigma^0_k, k = \bar{k}, \bar{k}+1, \ldots$ Accordingly, a countable many disjoint strips $\sigma^1_k, k = \bar{k}, \bar{k}+1, \ldots$ exists on Π^- such that $\sigma^1_k = T_0^k(\sigma^0_k)$. Note also that the strips σ^0_k and σ^1_k are defined as $\sigma^0_k = \Pi^+ \cap T_0^{-k}(\Pi^-)$ and $\sigma^1_k = \Pi^- \cap T_0^k(\Pi^+)$. In the case under consideration, since the map T_0^k can be written in the form

$$x_k = \lambda_1^k x_0,\ u_k = \lambda_2^k u_0,\ y_0 = \gamma^{-k} y_k\,, \tag{26}$$

we can write exact formulas for the strips:

$$\sigma^0_k = \{(x, u, y) \| x - x^+| \le \varepsilon_0, |u - u^+| \le \varepsilon_0, |y - \gamma^{-k} y^-| \le \gamma^{-k}\varepsilon_1\}, \tag{27}$$

$$\sigma^1_k = \{(x, u, y) \| x - \lambda_1^k x^+| \le \lambda_1^k\varepsilon_0, |u - \lambda_2^k u^+| \le \lambda_2^k\varepsilon_0, |y - y^-| \le \varepsilon_1\}. \tag{28}$$

For the sake of definiteness, we will denote coordinates x, u, y of points in Π^+ as x_0, u_0, y_0 and in Π^- as x_1, u_1, y_1. Now we take the strip σ^1_k and consider its image, horseshoe $T_1(\sigma^1_k)$, under the global map T_1.

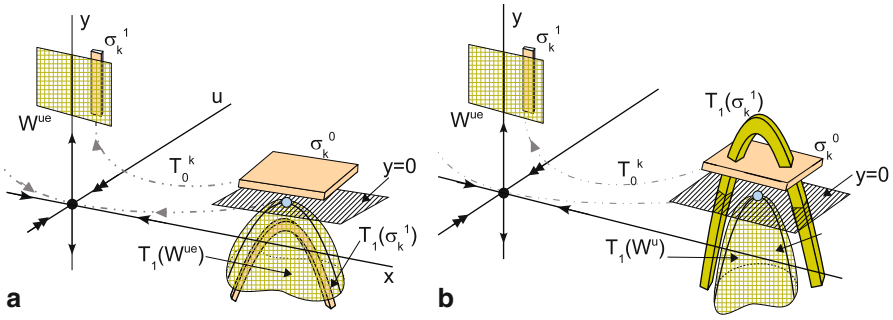

Fig. 7 Examples of homoclinic tangencies with $c = 0$ in the sectionally saddle case $\sigma > 1$: **a** The dynamics is trivial; **b** Smale horseshoes exist

By (25), we obtain that $T_1(\sigma_k^1)$ is a 3D-figure in Π^+ which can be given in the coordinate form as follows

$$(x_0 - x^+, u_0 - u^+, y_0) = \left(b_1(y_1 - y^-), a_{21}x_1,\ \hat{c}u_1 + d(y - y^-)^2\right), \tag{29}$$

where the coordinates (x_1, u_1, y_1) run values along σ_k^1, see formula (28).

Consider now *item (i)*, $\hat{c} < 0$, of Proposition 3 and show that here $T_1(\sigma_k^1) \cap \sigma_j^0 = \emptyset$ for all sufficiently large k and j. Suppose, however, that $T_1(\sigma_k^1) \cap \sigma_j^0 \neq \emptyset$ for some k and j. Then, evidently, by virtue of (27), (28) and (29), the equation

$$\gamma^{-j}\eta = \hat{c}\lambda_2^k\xi + dz^2 \tag{30}$$

has solutions with respect to $\eta \in [y^- - \varepsilon_1, y^- + \varepsilon_1]$ when (ξ, z) run values from the domain $(|\xi - u^+| \leq \varepsilon_0, |z| \leq \varepsilon_1)$. Note that since $u^+ > 0, y^- > 0$ such η and ξ take only positive values for sufficiently small $\varepsilon_{0,1}$. Then, since $d < 0, \lambda_2 > 0, \gamma > 0$, Eq. (30) can have solutions only in that case where

$$\gamma^{-j}\eta - \hat{c}\lambda_2^k\xi \leq 0. \tag{31}$$

However, since $\hat{c} < 0$, the latter inequality is not valid for any $j, k \geq \bar{k}$. It implies that the horseshoes $T_1(\sigma_k^1)$ and strips σ_j^0 do not intersect each other in this case. Geometrically, it follows from the fact that in the case $\hat{c} < 0$ the strips σ_j^0 and the horseshoes $T_1(\sigma_k^1)$ are posed in Π^+ on different sides from a plane $W_{loc}^s : y = 0$, see Fig. 7a. Hence, the diffeomorphism g_0 has a trivial dynamics here: $\Lambda(g_0) = \hat{O} \cup \hat{\Gamma}_0$. Consider now <col1>item (ii), $\hat{c} > 0$ and $\lambda_2\gamma < 1$, of Proposition 3. Again we obtain that if $T_1(\sigma_k^1) \cap \sigma_j^0 \neq \emptyset$, then the inequality (31) has solutions. Since $\gamma^{-1} > \lambda_2$ in this case, the Eq. (30) can have solutions only if $j > k$. It follows that $T_1(\sigma_k^1) \cap \sigma_k^0 = \emptyset$, i.e. g_0 has no (topological) horseshoes in U, and, moreover, $\Lambda(g_0) = \hat{O} \cup \hat{\Gamma}_0$ here. Consider now *item (iii)*, $\hat{c} > 0$ and $\lambda_2\gamma > 1$, of Proposition 3. We obtain from (29) and (28) that the horseshoe $T_1(\sigma_k^1)$ has a top with coordinate $y_0^{top} \sim \hat{c}\lambda_2^k u^+$ and its bottom (i.e. T_1-image of the top and bottom of the strip σ_k^1) has coordinate $y_0^{bot} \sim d\varepsilon_1^2 + \hat{c}\lambda_2^k u^+$. Since $\lambda_2\gamma > 1$ we have that $y_0^{top} > \gamma^{-k}(y^- + \varepsilon_1)$, i.e. the

top of the horseshoe $T_1(\sigma_k^1)$ is posed above the strip σ_k^0. Since $d < 0$ we have that $y_0^{bot} < 0$ for sufficiently large k, i.e. the bottom of $T_1(\sigma_k^1)$ is posed below the strip σ_k^0. Thus, the first return maps $T_k = T_1 T_0^k$ for all sufficiently large k are in this case, topologically, Smale horseshoe maps. This completes the proof.

5 Hyperbolic Properties of Diffeomorphisms with Simple Homoclinic Tangencies of Finite Order

We assume now that f satisfies conditions A)–D). Then reformulating Theorem 2 we select class of simple homoclinic tangencies of finite order. Namely, Theorem 2 implies the following result

Proposition 4 *Let a diffeomorphism f satisfying conditions A–D with even n be such that 1) either $\gamma > 0, d < 0$ in the case $\sigma < 1$; 2) or $\lambda_1 > 0, cd > 0$ in the case $\sigma > 1$; 3) or $\lambda_1 > 0, \gamma > 0, c < 0, d < 0$ independently on σ. Then f possesses trivial dynamics near Γ_0, i.e. $\Lambda = O \cup \Gamma_0$.*

Other diffeomorphisms under consideration will contain non-trivial hyperbolic subsets inside Λ. The corresponding results were proved in [5, 6, 11] and [24]. Therefore, we give here only some review of results.

Among the diffeomorphisms with hyperbolic subsets we select first those which admits a complete description of Λ. Namely, let f satisfy conditions A1, B, C and D with $\gamma > 0, \lambda_1 > 0, c < 0$ and also $d > 0$ when n is even. We bring such diffeomorphisms to the *complete class*.

In this case the geometry of the strips σ_k^0 and horseshoes $T_1(\sigma_i^1)$ for all possible $i, k \geq \bar{k}$ is of such type as in Fig. 8: all strips and horseshoes intersect "regularly". As it was shown still in [5, 6], such a geometry implies a non-uniform hyperbolicity: all orbits of Λ, except for Γ_0, are of saddle type and the set Λ can be described completely in terms of the symbolic dynamics.

If n is odd (the tangency if like cubic), then Λ can be identified with $\mathcal{B}_2^{\bar{k}+q}$ as in the case of transversal homoclinic orbit. If n is even, the set Λ is described now by means of the topological Bernoulli scheme (shift) $\mathcal{B}_3$ with three symbols. Namely, let $\mathcal{B}_3^{\bar{k}+q}$ be a subsystem of $\mathcal{B}_3$ which contains all bi-infinite sequences of form

$$(\ldots, 0, \alpha_i, \overbrace{0, 0, \ldots 0, 1}^{j_i+q}, \overbrace{0, 0, \ldots, 0, \alpha_{i+1}}^{j_{i+1}+q}, 0, \ldots), \tag{32}$$

where $\alpha_i \in \{1, 2\}$ and $j_i \geq \bar{k}$ for all i.[6] We identify in $\mathcal{B}_3^{\bar{k}+q}$ two homoclinic orbits $\omega_1 = (\ldots, 0, \ldots, 0, 1, 0, \ldots, 0, \ldots)$ and $\omega_2 = (\ldots, 0, \ldots, 0, 2, 0, \ldots, 0, \ldots)$ and let $\hat{\omega}$ be the glued orbit. We denote the resulting factor-system as $\hat{\mathcal{B}}_3^{\bar{k}+q}$.

[6] We include also sequences with $j_i = \infty$ or $j_{i+1} = \infty$. Then such sequences contain infinite strings from zeros either on the left or, respectively, right end and correspond either α- or ω-asymptotic orbit to the fixed point $(\ldots, 0, \ldots, 0, \ldots)$.

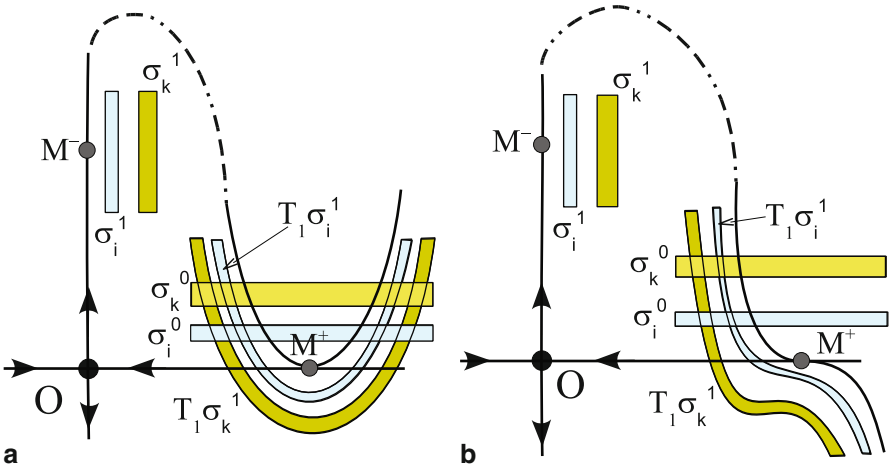

Fig. 8 Homoclinic tangencies for diffeomorphisms from the complete class. **a** The order of tangency n is even and the corresponding homoclinic tangency is "from above", i.e. $d > 0$ and $\gamma > 0$, and the horseshoes $T_1\sigma_k^1$ are posed under $T_1(W^u_{loc})$, i.e. $c < 0$ and $\lambda_1 > 0$. **b** n is odd and $\gamma > 0, \lambda_1 > 0$ and $c < 0$

Theorem 4 *Let f belong to the complete class. Then there exists such $\bar{k}$ that all orbits from the set Λ, except for Γ_0, are of saddle type and the system $f|_\Lambda$ is topologically conjugate either to $\mathcal{B}_2^{\bar{k}+q}$ for odd n or $\hat{\mathcal{B}}_3^{\bar{k}+q}$ for even n.*

Note that we do not require here that the saddle value σ is less or greater than 1. Therefore, the structure of the set $\Lambda(f)$ for systems from the complete class is the same for all cases of the sectionally dissipative, saddle or neutral ($\sigma = 1$) ones.

In the remaining cases (except for diffeomorphisms of trivial and complete classes), the set Λ does not allow, in general, the complete description. Moreover, as it is shown in [17–20], Λ can contain periodic and homoclinic orbits of any orders of degeneracy (including homoclinic and heteroclinic tangencies of indefinite orders). Nevertheless, we can observe here certain elements of hyperbolicity and, moreover, we are able to give a description of hyperbolic subsets by means of methods of the symbolic dynamics like it was done for diffeomorphisms of complete class.

However, while for diffeomorphisms of the complete class, all strips σ_i^0 and horseshoes $T_1(\sigma_j^1)$ have regular intersections, in other cases we have both to detect regular intersections and remove, from a description, all irregular and empty ones. As result, we obtain some sufficient conditions (in form of inequalities, see below) which provide the existence of certain (non-uniformly) hyperbolic subsets.

Formally speaking, we consider in this section such diffeomorphisms which satisfy conditions A–D but are not diffeomorphisms with trivial and complete description. We will call them as diffeomorphisms *with partial description*.[7]

[7] Thus, the diffeomorphisms with partial description in the main case $\sigma \neq 1$ are such that conditions A–D are valid and the following combinations of signs of the parameters λ_1, γ, c and d are excluded:

Let $\Omega_2^{\bar{k}+q}$ be such a subsystem of $\mathcal{B}_2^{\bar{k}+q}$ which contains the fixed point $\hat{O}$, the homoclinic orbit $\hat{\omega} = (\dots, 0, \dots, 0, 1, 0, \dots, 0, \dots)$ and all such orbits of form (32), where $\alpha_i = 1$ for any i and the following estimates hold for any successive integers $\bar{k} \le j_i \le \infty$ and $\bar{k} \le j_{i+1} \le \infty$

(H1) $|\gamma^{-j_{i+1}} y^- - c\lambda_1^{j_i} x_1^+| > S_{\bar{k}}(j_i, j_{i+1})$ in the case A1;

(H2) $|\gamma^{-j_{i+1}} y^- - Q\cos(j_i\psi + \omega)\cdot\lambda^{j_i}| > S_{\bar{k}}(j_i, j_{i+1})$ in the case A2;

where

$$S_{\bar{k}}(j_i, j_{i+1}) = \nu\left(|\lambda_1|^{j_i} + |\gamma|^{-j_{i+1}}\right)\cdot\left(|\lambda_1|^{\bar{k}/n} + |\gamma|^{-\bar{k}/n}\right),$$
$$Q = \left[(c_1x_1^+ + c_2x_2^+)^2 + (c_1x_2^+ - c_2x_1^+)^2\right]^{1/2}, \quad \omega = \arccos\frac{c_1x_1^+ + c_2x_2^+}{Q} \tag{33}$$

and ν is some positive constant independent of $\bar{k}$, j_i and j_{i+1}.

Let $\hat{\Omega}_3^{\bar{k}+q}$ be such a subsystem of $\hat{\mathcal{B}}_3^{\bar{k}+q}$ which contains the fixed point $\hat{O}$ the homoclinic orbit $\hat{\omega}$ and all such orbits of form (32) for which the following estimates hold

(H3) $d\left[\gamma^{-j_{i+1}} y^- - c_1\lambda_1^{j_i} x_1^+\right] > S_{\bar{k}}(j_i, j_{i+1})$ in the case A1;

(H4) $d\left[\gamma^{-j_{i+1}} y^- - Q\cos(j_i\psi + \omega)\cdot\lambda^{j_i}\right] > S_{\bar{k}}(j_i, j_{i+1})$ in the case A2;

Theorem 5 [6, 24] *Let f be a diffeomorphism with partial description. Then there is a closed invariant subset $\tilde{\Lambda}_{\bar{k}+q} \subset \Lambda$ such that* (i) *$\tilde{\Lambda}_{\bar{k}+q}$ contains the orbits O and Γ_0;* (ii) *all orbits of $\tilde{\Lambda}_{\bar{k}+q}$, except for Γ_0, are of saddle type;* (iii) *the system $f|\tilde{\Lambda}_{\bar{k}+q}$ is conjugate either to $\Omega_2^{\bar{k}+q}$ for odd n or to $\tilde{\Omega}_3^{\bar{k}+q}$ for even n.*

One can deduce certain simple consequences from this theorem on the existence of Smale horseshoes in the first return maps. For the sake of definiteness, we consider case of even order n (like quadratic) of the tangency. Then it follows directly from Theorem 5 that

- If the estimates H3 or H4 hold for $j_i = j_{i+1} = k$, then the first return map $T_k \equiv T_1T_0^k : \sigma_k^0 \to \sigma_k^0$ has in σ_k^0 a Smale horseshoe, i.e. a closed invariant hyperbolic set Ω_{k+q} such that the system $T^k|\Omega_{k+q}$ is topologically conjugate to $\mathcal{B}_2$.

In the sectionally dissipative case $\sigma < 1$, we have that $|\lambda_1|^k \ll |\gamma|^{-k}$. Then both the inequalities (H3) and (H4) with sufficiently large $j_i = j_{i+1} = k$ can be rewritten as follows $d\gamma^{-k}y^- > 0$. Since $y^- > 0$, it implies the following result.

(1) those ones which correspond to the trivial class, i.e. n is even and (i) $\gamma > 0, d < 0$ if $\sigma < 1$, (ii) $\lambda_1 > 0, dc > 0$ if $\sigma > 1$; and (2) those ones which correspond to the complete class, i.e (iii) $\gamma > 0, \lambda_1 > 0, c < 0, d > 0$ with even n and (iv) $\gamma > 0, \lambda_1 > 0, c < 0$ with odd n.

Proposition 5 *Let f satisfy conditions A–D with even n and $\sigma < 1$, and let the case $\gamma > 0, d < 0$ be excluded. Then, f has infinitely many Smale horseshoes Ω_{k+q}, where $k \geq \bar{k}$ and k run all integers if $\gamma > 0$ or all odd (even) integers if $\gamma < 0, d < 0$ ($\gamma < 0, d > 0$).*

In the sectionally saddle case $\sigma > 1$, we have, conversely, that $|\gamma|^{-k} \ll |\lambda_1|^k$. Then, for sufficiently large $\bar{k}$, the inequalities (H3) and (H4), for $j_i = j_{i+1} = k \geq \bar{k}$, take, respectively, the following forms

$$dc_1 x_1^+ \lambda_1^k < 0 \tag{34}$$

and

$$-dQ\cos(k\psi + \omega) > \nu(\bar{k}) > 0, \tag{35}$$

where $\nu(\bar{k}) \to 0$ as $\bar{k} \to \infty$. (Note that we can not write in (35) simply "> 0" since values of $\cos(k\psi + \omega)$ are not uniformly bounded from zero when ψ/π is irrational).

The inequality (34) has no solutions only in the case $\lambda_1 > 0, dc_1 > 0$, i.e. for diffeomorphisms with trivial dynamics. Since $Q > 0$ and $\psi \neq 0, \pi$, the inequality (35) has always infinitely many integer solutions. Thus, we obtain the following.

Proposition 6 *Let f satisfy conditions A–D with even n and $\sigma > 1$, and let the case $\lambda_1 > 0, dc_1 > 0$ be excluded. Then, f has infinitely many Smale horseshoes Ω_{k+q}, where $k \geq \bar{k}$ and k run all integers such that the inequalities (34) in case A1 or (35) in case A2 hold.*

5.1 Invariants θ and τ and a Complete Description of $\tilde{\Lambda}_{\bar{k}}$

Note that the inequalities H1–H4 generally define an "infinite net" of the strips and horseshoes which have regular (hyperbolic) intersections. Naturally, conditions H1–H4 are only sufficient. However, using them we describe quite large (non-uniformly) hyperbolic subsets $\tilde{\Lambda}_{\bar{k}+q} \subset \Lambda$. Moreover, for some dense subset of systems with homoclinic tangency, $\tilde{\Lambda}_{\bar{k}+q}$ can provide a complete description for Λ, i.e. $\Lambda = \tilde{\Lambda}_{\bar{k}+q}$.

In this section we will prove the corresponding result for the case where O is a saddle, i.e. condition A1 holds.

Consider the following inequality

$$|d| \left| \gamma^{-j_{i+1}} y^- - c_1 \lambda_1^{j_i} x_1^+ \right| \leq S_{\bar{k}}(j_i, j_{i+1}). \tag{36}$$

By geometric constructions (see [6, 24]), integer solutions (j_i, j_{i+1}) of this inequality include *all* numbers of those strips and horseshoes which can intersect non-hyperbolically. By (33), the inequality (36) is equivalent to the following system of inequalities

$$\gamma^{-j_{i+1}}(y^- - \rho_{\bar{k}}) \leq \lambda_1^{j_i}(cx^+ + \rho_{\bar{k}}), \quad \gamma^{-j_{i+1}}(y^- + \rho_{\bar{k}}) \geq \lambda_1^{j_i}(cx^+ - \rho_{\bar{k}}), \tag{37}$$

where

$$\rho_{\bar{k}} = \frac{\nu}{|d|}\left(|\lambda_1|^{\bar{k}/n} + |\gamma|^{-\bar{k}/n}\right).$$

If both sides of the inequalities (37) are of the same sign (that can be always fulfilled for diffeomorphisms with partial description), we take the logarithm of them.

As result, we obtain the following double inequalities

$$\epsilon^2_{\bar{k}} \;\le\; j_{i+1} - j_i\theta + \tau \;\le\; \epsilon^1_{\bar{k}}, \tag{38}$$

where

$$\theta = -\frac{\ln|\lambda_1|}{\ln|\gamma|}, \quad \tau = \frac{1}{\ln|\gamma|}\ln\frac{|cx^+|}{y^-}$$

and

$$\epsilon^1_{\bar{k}} = \frac{1}{\ln|\gamma|}\ln\left(\frac{1+\rho_{\bar{k}}|cx^+|^{-1}}{1-\rho_{\bar{k}}(y^-)^{-1}}\right), \quad \epsilon^2_{\bar{k}} = \frac{1}{\ln|\gamma|}\ln\left(\frac{1-\rho_{\bar{k}}|cx^+|^{-1}}{1+\rho_{\bar{k}}(y^-)^{-1}}\right),$$

Now we assume that the following condition holds:

S1) θ is rational, i.e. $\theta = r/s$ for some relatively prime natural r and s, and the number $s\tau$ is not integer.

Then the straight line $j - i\theta + \tau = 0$ is posed, in the (i, j)-plane, on a finite distance (depending on θ and τ) from points of the integer lattice. This means that the inequality (38) has no integer solutions for sufficiently large $\bar{k}$. In turn, it implies that all orbits of $\Lambda_{\bar{k}+q}$, except for Γ_0, are of saddle type.

In the case of odd n we have that if there is some non-saddle orbit in $\Lambda_{\bar{k}+q}$, then the inequality opposite to H1, i.e. again inequality (36), has to be fulfilled for at least one pair j_i, j_{i+1}.

Thus, the following result takes place.[8]

Proposition 7 *Let f be a diffeomorphism with partial description satisfying conditions A1, B, C, D, $\sigma \neq 1$ and S1. Then there is such $\bar{k}_1 = \bar{k}_1(\theta, \tau)$, where $\bar{k}_1 \to \infty$ as $s \to \infty$ or $s\tau$ tends to an integer, that all orbits of $\Lambda_{\bar{k}_1+q}$, except for Γ_0, are of saddle type and $f|\Lambda_{\bar{k}_1+q}$ is conjugate either to $\Omega_2^{\bar{k}+q}$ for odd n or to $\tilde{\Omega}_3^{\bar{k}+q}$ for even n.*

6 Proof of Theorem 1

Here we assume only that a diffeomorphism f has a homoclinic tangency of the invariant manifolds of a saddle fixed point O with multipliers $\lambda_1, \ldots, \lambda_m, \gamma$ ordered by the rule (1) and such that $\sigma \equiv |\lambda_1||\gamma| < 1$. In the case under consideration, by

[8] This result was proved also in [6] for the sectionally dissipative case $\sigma < 1$.

Lemma 1, we can write the local map T_0 in the following form

$$\bar{x} \;=\; \mathcal{A}, x + \hat{h}_1(x, y), \quad \bar{y} = \gamma y + h_3(x, y),$$

where $x \in \mathbb{R}^m$, $y \in \mathbb{R}^1$, $\mathcal{A}$–$(m \times m)$-matrix with eigenvalues $\lambda_1, \ldots, \lambda_m$. This form of T_0 can be considered as form (6) with identities (7), where $\mathcal{A} = \text{diag}\ (\hat{A}, \hat{B})$, $\hat{h}_1 = (h_1, h_2)$ and $x_{new} = (x, u)$. Then, by (10), the global map T_1 takes the form

$$\begin{aligned} &\bar{x} - x^+ = F(x, y - y^-), \\ &\bar{y} \;=\; G(x, y - y^-) \equiv cx + \varphi(y - y^-) + O(\|x\|^2 + \|x\||y - y^-|) \end{aligned} \tag{39}$$

where $(x, y) \in \Pi^-$, $(\bar{x}, \bar{y}) \in \Pi^+$, $F(0, 0) = 0, G(0, 0) = 0$ and $\varphi(0) = \varphi'(0) = 0$. If the homoclinic tangency is isolated, then $\varphi \neq 0$ at $y \neq y^-$. Besides, in the case of one-sided tangency, we have that either $\varphi \geq 0$ (the tangency "from above") or $\varphi \leq 0$ (the tangency "from below" if also $\gamma > 0$); in the case of topological intersection, we have that either $s\varphi(s) \geq 0$ (the tangency like "$y = x^3$") or $s\varphi(s) \leq 0$ (the tangency like "$y = -x^3$"), where $s = (y - y^-)$.

Again, by Lemma 2, the map T_0^k can be written in the following cross-form (compare with (8))

$$x_k \;-\; \mathcal{A}^k x_0 \;=\; \hat{\lambda}^k \tilde{\xi}_k(x_0, y_k), \quad y_0 \;-\; \gamma^{-k} y_k \;=\; \hat{\gamma}^{-k} \tilde{\eta}_k(x_0, y_k) \tag{40}$$

Proof [of item 1 of Theorem 1] Take some strip $\sigma_k^1 \subset \Pi^-$. Suppose that the corresponding horseshoe $T_1(\sigma_k^1)$ has non-empty intersection with a strip σ_i^0. Then, by (40) and (39), the equation

$$\gamma^{-i} \bar{y} \left(1 + O([\hat{\gamma}/\gamma]^{-i})\right) = \alpha_k(x, y) + \varphi(y - y^-), \tag{41}$$

has a solution with respect to $\bar{y}$ (for some (x, y)). Note that the following estimate $\|\alpha_k\| < \tilde{\lambda}^k$ holds for sufficiently large k, where $\tilde{\lambda} = |\lambda_1| + \delta$ and $\delta \geq 0$ is a sufficiently small constant such that, in any case, $|\tilde{\lambda}\gamma| < 1$.

Let the homoclinic tangency satisfy the condition (2). If $\gamma > 0$ (the main case), it means that $\varphi(y_1 - y^-) \leq 0$. Then the Eq. (41) can have a solution if only

$$\gamma^{-i} \bar{y} \left(1 + O([\hat{\gamma}/\gamma]^{-i})\right) - \alpha_k(x, y) \leq 0.$$

Since $\gamma > 0$, $\|\alpha_k\| < \tilde{\lambda}^k$ and $|\tilde{\lambda}\gamma| < 1$, the inequality above can hold only in the case where $i \gg k$. Thus, any horseshoe $T_1(\sigma_k^1)$ can intersect only those strips σ_i^0 whose numbers are much bigger than k, see Fig. 9a. In turn, the horseshoe $T_1(\sigma_i^1)$, again, can intersect only some strip σ_j^0 with $j > i$, etc. It implies that some backward iteration of any point from Π^+ must leave U. Thus, only two orbits, O and Γ_0, will stay always in U.

If $\gamma < 0$, the condition (2) imply the identity $\varphi(y_1 - y^-) \equiv 0$. Evidently, Eq. (41) can have a solution in this case again only for $i \gg k$.

Proof [of item 2 of Theorem 1] Consider first the case of one-sided tangency "from above". If $\gamma < 0$ we can always choose such homoclinic points M^- and M^+ that

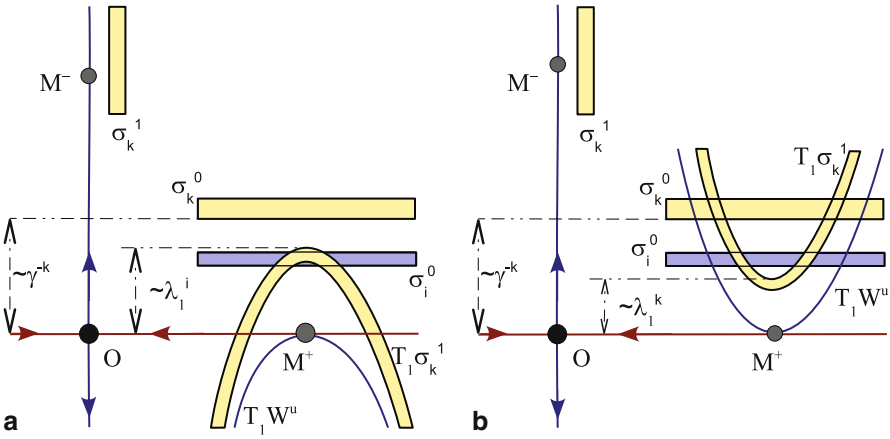

Fig. 9 A horseshoe geometry in the case $\sigma < 1$ for homoclinic tangencies **a** from below and **b** from above

$T_1(W^u)$ touches W^u_{loc} from above (if it not the case for a given point M^+, we take the point $T_0(M^+)$). Then, by condition $\varphi \geq 0$ and $\varphi > 0$ if $y_1 \neq y^-$, we have that the curve $T_1(W^u) : x_0 - x^+ = F(0, y_1 - y^-)$, $y_0 = \varphi(y_1 - y^-)$ will intersect all the strips σ^0_k with sufficiently large k (even k if $\gamma < 0$) at least two connected components. (Note that the vector $\hat{l} = F_y(0, 0)$ is non-zero, since T_1 is diffeomorphism). The strips σ^0_k are posed on distance $\rho_k \geq |\gamma|^{-k}(y^- - \varepsilon_1)$ from the plane $y_0 = 0$. While, the strips σ^0_k are posed from the line $x = 0$ on the distance of order $\tilde{\lambda}^k$. The latter means that the horseshoes $T_1(\sigma^1_k)$ will be posed from $T_1 W^u_{loc}$ on the distance of order $\tilde{\lambda}^k$. Since $\tilde{\lambda}^k \ll |\gamma|^{-k}$, it follows that the strips σ^0_k with sufficiently large k will intersect own horseshoes $T_1(\sigma^1_k)$ along at least two connected components (the same as they intersect the curve $T_1 W^u_{loc}$). See Fig. 9b.

Concerning the case of topological intersection, we note that the curve $T_1 W^u_{loc}$ intersect infinitely many strips σ^0_k. In turn, strips σ^1_j accumulate to W^u_{loc}. It implies that infinitely many strips σ^0_k and horseshoes $T_1(\sigma^1_j)$ for all sufficiently large k and j are mutually intersect.

Acknowledgements The authors thank M. Malkin and D. Turaev for very fruitful discussions. AG and SG have been partially supported by the Russian Scientific Foundation Grant 14-41-00044 and the grants of RFBR No.13-01-00589, 13-01-97028-povolzhye and 14-01-00344. ML was partially supported by a NSC research grant.

References

1. Afraimovich, V.S.: On smooth changes of variables. Methods of Qualitative Theory of Differential Equations, Gorky State University, pp. 10–21 (1984) (in Russian)
2. Afraimovich, V.S., Shilnikov, L.P.: On singular orbits of dynamical systems. Uspekhi Math. Nauk **27**(3), 189–190 (1972)

3. Afraimovich, V.S., Shilnikov, L.P.: On critical sets of Morse–Smale systems. Trans. Mosc. Math Soc. **28**, 179–212 (1973)
4. Afraimovich, V., Young, T.: Multipliers of homoclinic tangencies and a theorem of Gonchenko and Shilnikov on area preserving maps. Int. J. Bifurc. Chaos **15**(11), 3589–3594 (2005)
5. Gavrilov, N.K., Shilnikov, L.P.: On three-dimensional dynamical systems close to systems with a structurally unstable homoclinic curve, Part 1. Math. USSR Sb. **17**, 467–485 (1972) (Part 2, Math. USSR Sb. **19**, 139–156 (1973))
6. Gonchenko, S.V.: Non-trivial hyperbolic subsets of multidimensional systems with a non-transversal homoclinic curve. Methods of Qualitative Theory of Differential Equations. Gorky State University, pp. 89–102 (1984) (in Russian)
7. Gonchenko, S.V.: Dynamics and moduli of Ω-conjugacy of 4D-diffeomorphisms with a structurally unstable homoclinic orbit to a saddle-focus fixed point. Am. Math. Soc. Transl. **200**(2), 107–134 (2000)
8. Gonchenko, S.V.: Dynamical systems with homoclinic tangencies, Ω-moduli and bifurcations. Doctor of Physics and Mathematical Sciences Thesis, Nizhny Novgorod, p. 300 (2004) (in Russian)
9. Gonchenko, S.V., Gonchenko, V.S.: On bifurcations of birth of closed invariant curves in the case of two-dimensional diffeomorphisms with homoclinic tangencies . Proc. Math. Steklov Inst. **244**, 80–105 (2004)
10. Gonchenko, M.S., Gonchenko, S.V.: On cascades of elliptic periodic points in two-dimensional symplectic maps with homoclinic tangencies. Reg. Chaot. Dyn. **14**(1), 116–136 (2009)
11. Gonchenko, S.V., Shilnikov, L.P.: On dynamical systems with structurally unstable homoclinic curves. Sov. Math. Dokl. **33**, 234–238 (1986)
12. Gonchenko, S.V., Shilnikov, L.P.: Arithmetic properties of topological invariants of systems with a structurally unstable homoclinic trajectory. J. Ukr. Math. **39**, 21–28 (1987)
13. Gonchenko, S.V., Shilnikov, L.P.: On moduli of systems with a nontransversal Poincaré homoclinic orbit. Russ. Acad. Sci. Izv. Math. **41**(3), 417–445 (1993)
14. Gonchenko, S.V., Shilnikov, L.P.: On two-dimensional area-preserving mappings with homoclinic tangencies. Russ. Acad. Sci. Dokl. Math. **63**(3), 395–399 (2001)
15. Gonchenko, S.V., Shilnikov, L.P.: On two-dimensional area-preserving maps with homoclinic tangencies that have infinitely many generic elliptic periodic points. Notes of S.-Peterburg. Branch of Math. Steklov Inst. (POMI) **300**, 155–166 (2003)
16. Gonchenko, S.V., Shilnikov, L.P.: Homoclinic tangencies. Thematic issue: Moscow-Izhevsk, p. 524 (2007) (in Russian)
17. Gonchenko, S.V., Turaev, D.V., Shilnikov, L.P.: On models with a structurally unstable homoclinic curve. Sov. Math. Dokl. **44**(2), 422–426 (1992)
18. Gonchenko, S.V., Shilnikov, L.P., Turaev, D.V.: On models with non-rough Poincaré homoclinic curves. Phys. D **62**(1–4), 1–14 (1993)
19. Gonchenko, S.V., Turaev, D.V., Shilnikov, L.P.: Dynamical phenomena in multi-dimensional systems with a non-rough Poincaré homoclinic curve. Russ. Acad. Sci. Dokl. Math. **47**(3), 410–415 (1993)
20. Gonchenko, S.V., Turaev, D.V., Shilnikov, L.P.: Homoclinic tangencies of any order in Newhouse regions. J. Math. Sci. **105**, 1738–1778 (2001)
21. Gonchenko, S.V., Meiss, J.D., Ovsyannikov, I.I.: Chaotic dynamics of three-dimensional Henon maps that originate from a homoclinic bifurcation. Regul. Chaot. Dyn. **11**(2), 191–212 (2006)
22. Gonchenko, S., Shilnikov, L., Turaev, D.: Homoclinic tangencies of arbitrarily high orders in conservative and dissipative two-dimensional maps.Nonlinearity **20**, 241–275 (2007)
23. Gonchenko, S.V., Shilnikov, L.P., Turaev, D.V.: On dynamical properties of multidimensional diffeomorphisms from Newhouse regions. Nonlinearity **21**(5), 923–972 (2008)
24. Gonchenko, S., Li, M.-C., Malkin, M.: On hyperbolic dynamics of multidimensional systems with homoclinic tangencies of arbitrary orders. (to appear)
25. Hirsch, M.W., Pugh, C.C., Shub, M.: Invariant Manifolds. Lecture Notes in Mathematics, vol. 583. Springer, Berlin (1977)

26. Homburg, A.J., Weiss, H.: A geometric criterion for positive topological entropy II: Homoclinic tangencies. Commun. Math. Phys. **208**, 267–273 (1999)
27. Leontovich, E.A.: On a birth of limit cycles from a separatrix loop. Sov. Math. Dokl. **78**(4), 641–644 (1951)
28. Leontovich, E.A.: Birth of limit cycles from a separatrix loop of a saddle of a planar system in the case of zero saddle value. Preprint VINITI, p. 114 (1988) (in Russian)
29. Ivanov, B.F.: Towards existence of closed trajectories in a neighbourhood of a homoclinic curve. J. Diff. Eq. **15**(3), 548–550 (1979) (in Russian)
30. Katok, A.: Lyapunov exponents, entropy and periodic orbits for diffeomorphisms. IHES Publ. Math. **51**, 137–173 (1980)
31. Newhouse, S.E, Palis, J., Takens, F.: Bifurcations and stability of families of diffeomorphisms. IHES Publ. Math. **57**, 5–72 (1984)
32. Rayskin, V.: Homoclinic tangencies in $\mathbb{R}^n$. Discret. Contin. Dyn. Syst. **12**(3), 465–480 (2005)
33. Shilnikov, L.P.: On a Poincaré–Birkhoff problem. Math. USSR Sb. **3**, 91–102 (1967)
34. Shilnikov, L.P., Shilnikov, A.L., Turaev, D.V., Chua, L.O.: Methods of Qualitative Theory in Nonlinear Dynamics, Part I. World Scientific, Singapore (1998) (Part II, 2001)
35. Shilnikov, L.P., Shilnikov, A.L., Turaev, D.V.: On some mathematical topics in classical synchronization. A tutorial. Int. J. Bifurc. Chaos **14**(7), 2143–2160 (2004)
36. Turaev, D.V.: On dimension of non-local bifurcational problems. Int. J. Bifurc. Chaos **6**, 919–948 (1996)

Homoclinic Ω-Explosion: Hyperbolicity Intervals and Their Bifurcation Boundaries

Sergey Gonchenko and Oleg Stenkin

Abstract It has been established by Gavrilov and Shilnikov (Math USSR Sb 17:467–485, 1972) that at the bifurcation boundary, separating Morse–Smale systems from systems with complicated dynamics, there are systems with homoclinic tangencies. Moreover, when crossing this boundary, infinitely many periodic orbits appear immediately, just by "explosion." Newhouse and Palis (Asterisque 31:44–140, 1976) have shown that in this case, there are infinitely many intervals of values of the splitting parameter corresponding to hyperbolic systems. In the present chapter, we show that such hyperbolicity intervals have natural bifurcation boundaries, so that the phenomenon of homoclinic Ω-explosion gains, in a sense, complete description in the case of 2D diffeomorphisms.

1 Introduction

"Homoclinic Ω-explosion" is, undoubtedly, one of those dynamical phenomena that causes always a great interest for specialists on nonlinear dynamics. The essence of it is based on the fact that the system under consideration possesses a simple dynamics up to some (bifurcation) moment, and the dynamics becomes immediately complicated, just after. In other words, at the homoclinic Ω-explosion, the system itself belongs to a boundary of Morse–Smale systems and the transition through this boundary has the nature of an "explosion"—infinitely many periodic orbits appear immediately. We notice that such a scenario of chaos development is typical for many specific systems.

It should be noted that, for the first time, global bifurcations like homoclinic Ω-explosion were discovered and studied by L. P. Shilnikov. So, in his paper [1], see also [2], a global bifurcation was studied for a system having a saddle–saddle equilibrium

S. Gonchenko (✉) · O. Stenkin
Research Institute of Applied Mathematics and Cybernetics,
Nizhny Novgorod State University, Nizhny Novgorod, Russia
e-mail: gosv100@uic.nnov.ru

O. Stenkin
e-mail: ostenkin@mail.ru

H. González-Aguilar, E. Ugalde (eds.), *Nonlinear Dynamics New Directions,*
Nonlinear Systems and Complexity 12, DOI 10.1007/978-3-319-09864-7_3

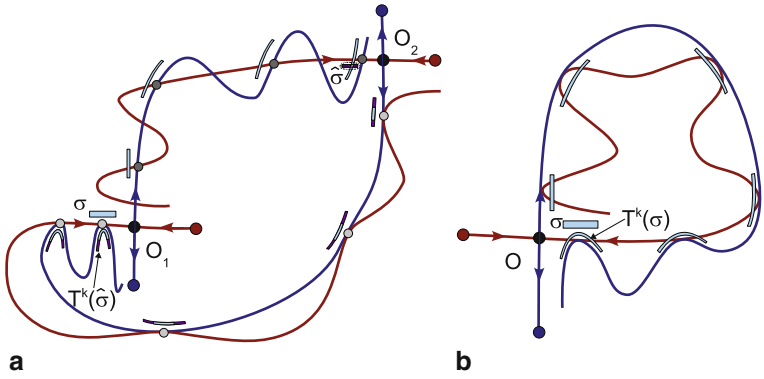

Fig. 1 Examples of 2D diffeomorphisms with heteroclinic (**a**) and homoclinic (**b**) tangencies belonging to a boundary between Morse–Smale systems and systems with (infinitely) many periodic orbits

with several homoclinic loops. Recall that for dimension 3, nonhyperbolic points with eigenvalues $\lambda_2 < \lambda_1 < 0, \gamma = 0$ and $\lambda_2 < 0, \lambda_1 = 0, \gamma > 0$ are called, respectively, *saddle-node* and *saddle–saddle*. Note that a saddle–saddle can have, in contrast to a saddle-node, several homoclinic loops and, in general, it is a codimension one phenomenon. However, if only one homoclinic loop of a saddle–saddle exists, dynamics is trivial and not more than one (saddle) limit cycle can be born here [3]. It not the case when several homoclinic loops exist: then, if the equilibrium disappears, a closed invariant hyperbolic set (a horseshoe bouquet) appears whose orbits are coded by means of p symbols, where p is the number of loops [1, 2].

Strictly speaking, the term "Ω-explosion" was introduced by J. Palis in the paper [4] in which he, in fact, has justified necessity of the "no cycles" condition for Ω-stability of dynamical systems, i.e., structural stability on the set of nonwandering orbits. In Fig. 1a, an example of 2D diffeomorphism is shown that has such a "cycle"—containing saddle fixed points O_1 and O_2 and two heteroclinic orbits, one of which is nontransversal (at whose points $W^u(O_2)$ and $W^s(O_1)$ have a quadratic tangency). Moreover, the nonwandering set of this map is hyperbolic and consists only of a finite number of periodic points (saddle, sinks, and sources). However, if the tangency splits, the nonwandering set becomes immediately infinite: in particular, infinitely many periodic and homoclinic orbits appear.

In Fig. 1b, another situation is shown when a 2D diffeomorphism has a quadratic homoclinic tangency "from below." It belongs also to the boundary of Morse–Smale systems. However, the exit to this boundary means that the nonwandering set becomes nonhyperbolic, since the homoclinic orbit itself is nonwandering. When crossing this boundary, a "rich collection" of global bifurcations can be observed and, as a whole, the corresponding bifurcation phenomenon is called the *homoclinic Ω-explosion*. In comparison, in the case of the cycle from Fig. 1a, one can say about *heteroclinic Ω-explosion*. We can see a certain difference between these two cases (which, if desire, can be considered as a definition): in the first, heteroclinic case, the nonwandering

set is not changed when entering the boundary; whereas, in the homoclinic case, a (finite) number of new nonhyperbolic nonwandering orbits appears. Evidently, the Shilnikov's bifurcations of homoclinic bouquet of saddle–saddle are related to the second (homoclinic) case.

In the present chapter, we study dynamical phenomena appearing namely at the homoclinic Ω-explosion in the case of 2D diffeomorphisms. The first results with respect to this topic were obtained by N. K. Gavrilov and L. P. Shilnikov in the paper [5]: here, the existence of Ω-accessibility from the Morse–Smale systems to systems with homoclinic tangencies was proved; a description in terms of symbolic dynamics for nontrivial hyperbolic subsets was given (including those born by Ω-explosion), etc. Analogous results were obtained in the paper of N. K. Gavrilov [6] for 2D diffeomorphisms with nontransversal heteroclinic cycles, see also [7, 8]. We note that in the paper [9] by S. Newhouse and J. Palis, one quite interesting and most popular result from the theory of homoclinic Ω-explosion, the so-called Theorem on Hyperbolicity Intervals, was established (see Theorem 1 below). Also known are ceratin extensions, see e.g., [10–13], and the most complete (and multidimensional) variant of this theorem was proved in the paper [14] by O. V. Sten'kin and L. P. Shilnikov.

In the present chapter, we give some review of the mentioned results, see Sects. 2 and 3, and prove new ones. In particular, we prove Theorem 3 in Sect. 4 about exact bifurcation boundaries of the hyperbolicity intervals in the case of the "global homoclinic Ω-explosion."

2 Three Classes of Quadratic Homoclinic Tangencies

Let f be a C^r-smooth ($r \geq 3$) 2D diffeomorphism satisfying the following conditions:

(A) f has a saddle fixed point O with multipliers λ and γ where $0 < |\lambda| < 1 < |\gamma|$;
(B) *the saddle value* $\sigma \equiv |\lambda\gamma|$ is less than 1; [1]
(C) f has a nontransversal homoclinic orbit Γ at points of which the invariant stable $W^s(O)$ and unstable $W^u(O)$ manifolds of O have a quadratic tangency (see Fig. 2a).

Diffeomorphisms that are C^r-close to f and have close to Γ a nontransversal homoclinic orbit compose a locally connected codimension one surface $\mathcal{H}$ in the space of C^r-smooth 2D diffeomorphisms.

Let U be a small neighborhood of $O \cup \Gamma_0$. It consists of a small disk U_0 containing O and a number of small disks surrounding those points of Γ_0 that do not lie in U_0 (see Fig. 2b). Denote as $N \equiv N(f)$, the set of orbits of f entirely lying in U.

[1] Evidently, the case $\sigma > 1$ is reduced to the case under consideration for f^{-1}. Thus, only the case $\sigma = 1$ is not in our competence; however, it is very specific and requires a special consideration (see, for example, [15, 16]).

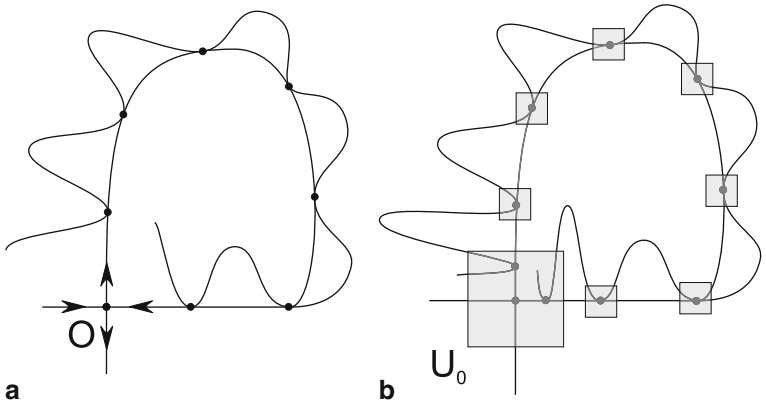

Fig. 2

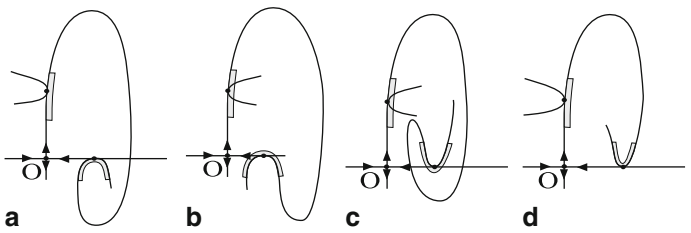

Fig. 3 Various types of planar diffeomorphisms with quadratic homoclinic tangencies

According to [5], homoclinic tangencies satisfying conditions (A)–(C) are divided into three classes depending on the structure of N. For homoclinic tangencies of the first class, the set N is trivial: $N = O \cup \Gamma$. For homoclinic tangencies of the second and third classes, the set N contains nontrivial hyperbolic subsets. However in the case of tangencies of the second class, the set N allows always a complete description in terms of symbolic dynamics, and $N(f)$ is not changed at varying f inside $\mathcal{H}$ (i.e., when the homoclinic tangency does not split). Unlike this, diffeomorphisms with homoclinic tangencies of the third class are Ω-unstable in $\mathcal{H}$.[2]

In Fig. 3, four main types of homoclinic tangencies for planar diffeomorphisms with $\lambda > 0, \gamma > 0$ are shown. The cases (a) and (b) correspond to so-called tangencies "from below" which are, in fact, tangencies of *the first class*. Third and fourth figures correspond to tangencies "from above" which are homoclinic tangencies either of *the second class*—Fig. 3c, or of *the third class*—Fig. 3d.

[2] Moreover, they possess Ω-moduli, i.e., continuous invariants of topological conjugacy on the set of nonwandering orbits. It means that any change of value of an Ω-modulus leads to a bifurcation of an orbit (periodic, homoclinic, etc) from the set $N(f)$. As it was established in [19], the Gavrilov–Shilnikov invariant, $\theta = -\ln|\lambda|/\ln|\gamma|$ introduced in [5], is the principal Ω-modulus here.

In this chapter, we consider mainly homoclinic tangencies of the first class. However, in order to describe more precisely qualitative (geometric) properties of such systems, we need a certain information about their analytical properties. Below we give necessary facts, including also recent results, from [17]; see also the book [18].

Consider the map $T_0 \equiv f|U_0$ which is called the *local map*. We can use such C^r-coordinates (x, y) in U_0 in which the map T_0 has the following form [17, 19]:[3]

$$\bar{x} = \lambda x + f(x, y)x^2 y, \ \bar{y} = \gamma y + g(x, y)xy^2. \tag{1}$$

In these local coordinates in U_0, the point O is in the origin, $O(0, 0)$, and the local stable and unstable manifolds $W^s_{\text{loc}}(O)$ and $W^u_{\text{loc}}(O)$ have equations $y = 0$ and $x = 0$, respectively. Choose in U_0, a pair of homoclinic points $M^+(x^+, 0) \in W^s_{loc}$ and $M^-(0, y^-) \in W^u_{loc}$ of the orbit Γ. We assume, without loss of generality, that $x^+ > 0$ and $y^- > 0$. Let Π^+ and Π^- be sufficiently small neighborhoods of the points M^+ and M^- such that $T_0(\Pi^+) \cap \Pi^+ = \emptyset$ and $T_0^{-1}(\Pi^-) \cap \Pi^- = \emptyset$. Since M^+ and M^- are points of the same orbit Γ, a positive integer q exists such that $f^q(M^-) = M^+$. Consider the so-called *global map* $T_1 \equiv f^q|_{\Pi^-} : \Pi^- \to \Pi^+$ which can be written in the local coordinates (1) in the following form:

$$\begin{aligned} \bar{x} - x^+ &= ax + b(y - y^-) + O(x^2 + (y - y^-)^2), \\ \bar{y} &= cx + d(y - y^-)^2 + O(x^2 + |y - y^-|^3 + |x||y - y^-|). \end{aligned} \tag{2}$$

Here, $bc \neq 0$ since T_1 is a diffeomorphism and $d \neq 0$ since by condition C, the curves $T_1(W^u_{\text{loc}})$ and W^s_{loc} are tangent at the point M^+ and this tangency is quadratic.

Now we can characterize homoclinic tangencies of Fig. 3 (at $\lambda > 0$ and $\gamma > 0$) in terms of coefficients of the global map T_1. Figure 3a corresponds to the case $c < 0, d < 0$, Fig. 3b-$c > 0, d < 0$, Fig. 3c-$c < 0, d > 0$, and Fig. 3d-$c > 0, d > 0$.

One of the main advantages of the normal form (1) consists of the fact that in these coordinates, the map T_0^k for any sufficiently large k, can be represented in a form which is asymptotically close to the corresponding form for the linear map $\tilde{T}_0$: $\bar{x} = \lambda x, \ \bar{y} = \gamma y$. In the latter case, the relation $(x_k, y_k) = \tilde{T}_0^k(x_0, y_0)$ can be written either as $x_k = \lambda^k x_0, \ y_k = \gamma^k y_0$ or in the *cross-form* $x_k = \lambda^{-k} x_0, \ y_0 = \gamma^{-k} y_k$. If T_0 is written in normal form (1), then the corresponding cross-form for the map $T_0^k : (x_0, y_0) \mapsto (x_k, y_k)$ is as follows, [17, 20]:

$$x_k = \lambda^k x_0 + |\lambda|^k |\gamma|^{-k} \phi_{k1}(x_0, y_k), \quad y_0 = \gamma^{-k} y_k + |\gamma|^{-2k} \phi_{k2}(x_0, y_k). \tag{3}$$

Here, the functions ϕ_{k1} and ϕ_{k2} are uniformly bounded in k along with all derivatives up to order $(r - 2)$; the derivatives of x_k and y_0 of order $(r - 1)$ have orders $O(\lambda^k)$ and $O(\gamma^{-k})$, respectively; the derivatives of order r tend to 0 as $k \to \infty$.

Evidently, any orbit of N (except for O) has to intersect Π^+ and Π^-. However, the set of points in Π^+ iterations which (by T_0) reach Π^- consist of infinitely many

[3] The existence of such coordinates was proved in [17]. Note that analogous C^{r-1}-coordinates was found in [19]. The form (1) of a saddle map is called the *main normal form* or *normal form of the first order*: such a form exists for any multidimensional saddle map, [17].

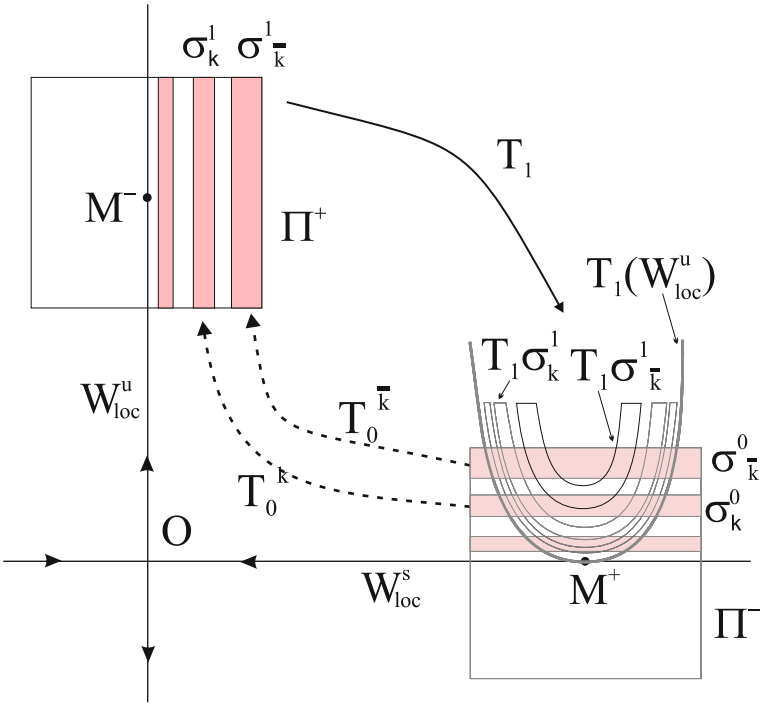

Fig. 4 Strips and horseshoes

strips $\sigma_k^0 \equiv \Pi^+ \cap T_0^{-k}\Pi^-$ accumulating at $W^s_{loc} \cap \Pi^+$ as $k \to \infty$. Their images under maps T_0^k and the strips $\sigma_k^1 \equiv T_0^k(\sigma_k^0)$, belong to Π^- and accumulate to $W^u_{loc} \cap \Pi^-$ as $k \to \infty$. In turn, it means, by (2), that images $T_1\sigma_k^1$ of the strips σ_k^1 have a horseshoe-shaped form and accumulate to the "parabola" $T_1 W^u_{\rm loc}$ as $k \to \infty$. See Fig. 4 for reference.

It is clear from above geometry constructions that orbits of N must have points in Π^+ belonging to intersections of the horseshoes $T_1\sigma_i^1$ and strips σ_j^0 for all possible $i, j \geq \bar{k}$, where $\bar{k}$ is some sufficiently large integer.[4] Therefore, the structure of the set N should essentially depend on geometrical properties of these intersections.

Various types of such intersections are shown in Fig. 5a: the horseshoe $T_1\sigma_i^1$ has a regular intersection with the strip σ_j^0, irregular one with σ_k^0, and empty intersection with σ_l^0. Figure 5b illustrates a definition of the so-called *regular intersection* of the horseshoe and strip. In this case (see [21]),

[4] The number $\bar{k}$ is chosen, in principle, depending on sizes of Π^+ and Π^i and it equals the minimal index "i" of the strips σ_i^0 and σ_i^1 from these neighborhoods. That is, the strips with index $\bar{k}$ are "border": they form the boundary, the so-called "special neighborhood" from U, [8, 24] (so that, for example, Π^+ does not contain points which reach Π^- for a number of iterations (by T_0) less than $\bar{k}$), see Fig. 4.

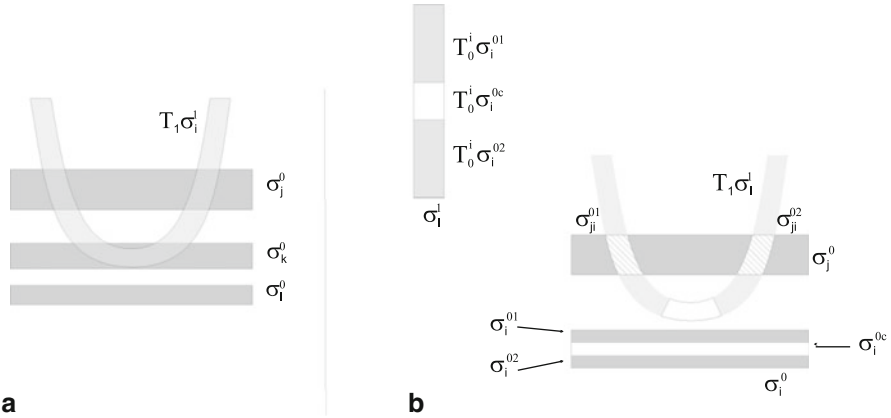

Fig. 5

1. the set $T_1\sigma_i^1 \cap \sigma_j^0$ consists of two connected components: σ_{ji}^{01} and σ_{ji}^{02} and
2. the maps $T_1T_0^i$ defined onto the corresponding preimages in σ_i^0, i.e., σ_i^{01} and σ_i^{02} are saddle in sense of [22, 23] (roughly speaking, they exponentially expand in the y-direction and contract in the x-direction).

We note that certain conditions for intersections of the horseshoes and strips were established in [5, 24]. So, if the inequality,

$$d\left[\gamma^{-j}y^- - c\lambda^i x^+\right] > S_{\bar{k}}(i,j) \tag{4}$$

holds, where $S_{\bar{k}}(i,j) = S_1(|\lambda|^i + |\gamma|^{-j})|\gamma|^{-\bar{k}/2}$, $i, j \geq \bar{k}$ and S_1 is a positive constant independent of i, j, and $\bar{k}$, then the intersection of the horseshoe $T_1\sigma_i^1$ with the strip σ_j^0 is regular.

On the other hand, the inequality

$$d[\gamma^{-j}y^- - c\lambda^i x^+] < -S_{\bar{k}}(i,j) \tag{5}$$

implies that $T_1\sigma_i^1 \cap \sigma_j^0 = \emptyset$.

Then, using only the inequalities (4) and (5), one can easily understand a principal structure of the set $N(f)$ for diffeomorphisms of Fig. 3: here $\lambda > 0, \gamma > 0$.

In the cases (a) and (b), related to $d < 0$, the set $N(f)$ has a trivial structure. Indeed, if $c < 0, d < 0$, then the inequality (5) holds always: here all horseshoes are posed from below the axis x (see Fig. 6a), i.e., their points leave U under forward iterations of f. If $c > 0$ and $d < 0$, since $|\lambda\gamma| < 1$, it follows from (5) that if $T_1\sigma_i^1 \cap \sigma_j^0 \neq \emptyset$, then $j \gg i$, see Fig. 6b. This evidently implies that $N = O \cup \Gamma$.

However, in the cases (c) and (d) of Fig. 3 (corresponding to $d > 0$), the set $N(f)$ has a nontrivial structure. In particular, the inequality (4) holds here for all sufficiently large $i = j$. This means that f has infinitely many *Smale horseshoes* $\Omega_i, i = \bar{k}, \bar{k}+1, \ldots$. Unlike other hyperbolic subsets, we select Ω_j as such invariant

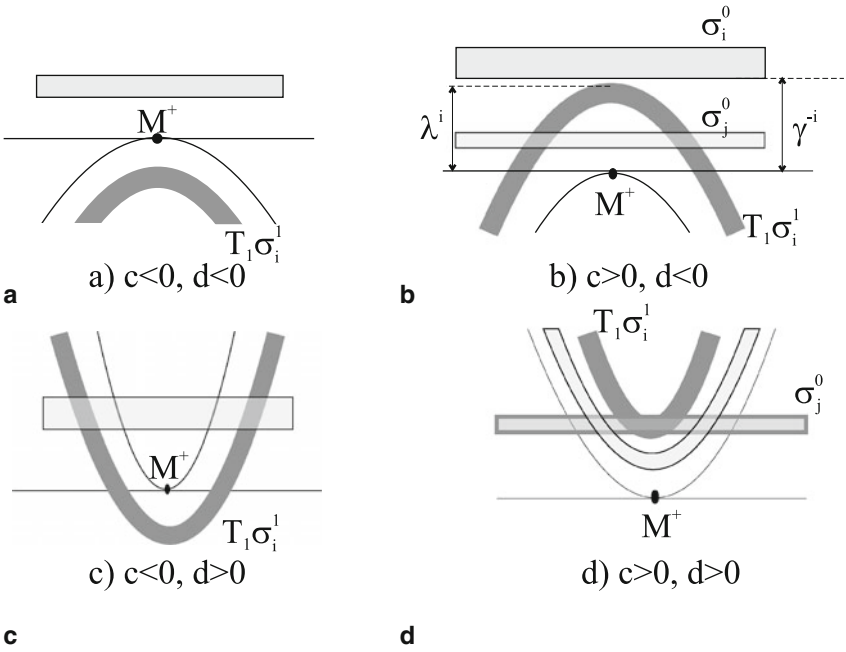

Fig. 6

set that its points in σ_j^0 are invariant under the first return map $T_j = T_1 T_0^j$ and the system $T_j|\Omega_j$ is conjugate to the topological Bernoulli scheme (shift) from two symbols. Thus, Ω_j is the usual Smale horseshoe for the map T_j.

We note also that in the case of homoclinic tangency of the second class (i.e., $\lambda > 0, \gamma > 0, c < 0, d > 0$), the inequality (4) is fulfilled for all sufficiently large i and j. It means that all the strips and horseshoes intersect regularly and, hence, all orbits of $N(f)$, except for Γ, are saddle and the set $N(f)$ allows a complete description in terms of symbolic dynamics [5].

3 Homoclinic Ω-Explosion—A Review of Results

We assume here that f satisfies conditions (A)–(C) as well as the condition (D) which is described as follows:

(D) Γ is a homoclinic orbit of the first class.

Thus, relations $\gamma > 0$ and $d < 0$ form here. Then, depending on the signs of the coefficients λ and c, we can select three different types of homoclinic tangencies: (i) $\lambda > 0, c > 0$, (ii) $\lambda > 0, c < 0$, and (iii) $\lambda < 0$ (here the sign of c is not important). Examples of the corresponding homoclinic tangencies in the case of planar diffeomorphisms are shown in Fig. 7a, b and d. Note that diffeomorphisms

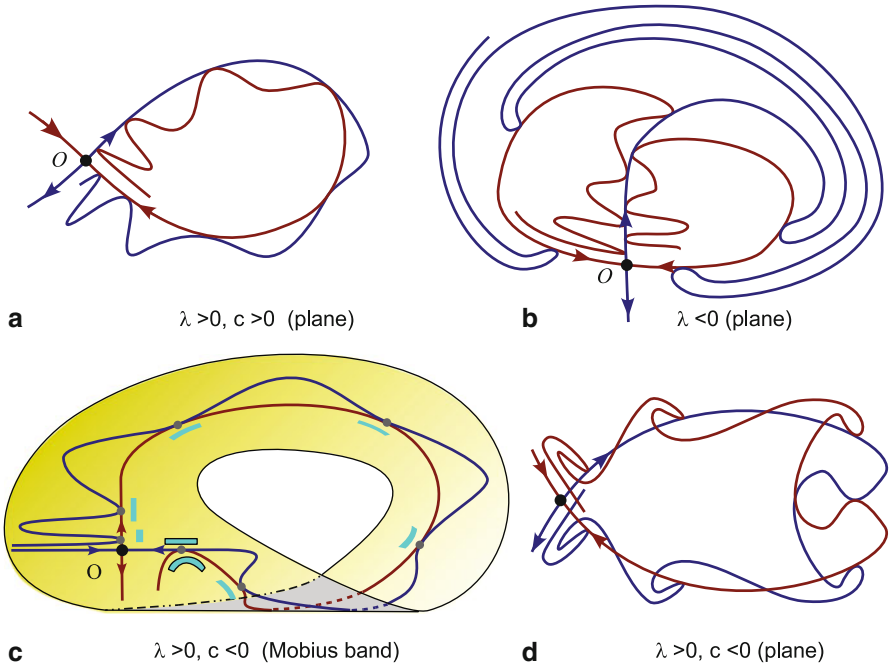

Fig. 7 A global picture for homoclinic tangencies of the first class

(of the plane) in the cases (a) $\lambda > 0, c > 0$ and (b) $\lambda < 0$ can belong to a boundary of the Morse–Smale systems. However, the case (d) $\lambda > 0, c < 0$ of the homoclinic tangency without other homoclinic points is impossible for planar diffeomorphisms, although it is realized for diffeomorphisms of nonorientable manifolds—see Fig. 7c where an example of the corresponding diffeomorphism of the Möbius band is shown.

Now we embed f into a one-parameter family f_μ such that

(E) $f_0 = f$ and the family f_μ is transversal at $\mu = 0$ to a bifurcation surface (of codimension one) $\mathcal{H}_1$ of the diffeomorphisms of the first class.

Note that the corresponding local and global maps for the diffeomorphisms f_μ will depend (smoothly) on μ. However, for the local map $T_0 = T_{0\mu}$, formulae (1) and (3) will take place again where we have to assume that all functions depend (implicitly) on μ, e.g., $\lambda = \lambda(\mu), \gamma = \gamma(\mu)$. The global map $T_1 = T_{1\mu}$, by condition (E), can be written now as follows:

$$\begin{aligned} \bar{x} - x^+ &= ax + b(y - y^-) + O(x^2 + (y - y^-)^2), \\ \bar{y} &= \mu + cx + d(y - y^-)^2 + O(x^2 + |y - y^-|^3 + |x||y - y^-|). \end{aligned} \tag{6}$$

Here in general, all coefficients a, b, c, d as well as x^+ and y^- depend (smoothly) on μ. The equations of the local stable and unstable invariant manifolds of the point O_μ

have, as before, a form $y = 0$ and $x = 0$, respectively. However, the global piece $T_{1\mu}(W^u_{loc}) \cap \Pi^+$ of the unstable manifold of O_μ has, by (6):

$$y = \mu + \frac{d}{b^2}(x - x^+)^2 + O\left((x - x^+)^3\right). \tag{7}$$

It is seen that μ is the parameter which splits generally the invariant manifolds of O_μ with respect to the homoclinic point M^+.

Now, the same as at the homoclinic tangency (for $\mu = 0$), we are able to deduce certain conditions for intersections of the strips and horseshoes (as it was done in [5], for example). For the case where f_0 is a diffeomorphism of the first class, following conditions were found in [14]:

(i) let $\mu > 0$, $i, j \geq k(\mu)$ and the following inequality holds

$$\gamma^{-j} y^- - c\lambda^i x^+ - \mu < \delta_k \left(|\lambda|^i + \gamma^{-j}\right), \tag{8}$$

where $\delta_k = S_2 \gamma^{-k/2}$, $S_2 > 0$ is a constant and $k(\mu) \sim -\ln \mu / \ln \gamma$ (i.e., $\mu \sim \gamma^{-k}$), then the intersection of the horseshoe $T_{1\mu}\sigma^1_i$ with the strip σ^0_j is regular;[5]

(ii) the inequality

$$\gamma^{-j} y^- - c\lambda^i x^+ - \mu > -\delta_k \left(|\lambda|^i + \gamma^{-j}\right) \tag{9}$$

implies that $T_{1\mu}\sigma^1_i \cap \sigma^0_j = \emptyset$.

Let N_μ be the set of orbits of f_μ which belong entirely to U. Evidently, the structure of the set N_μ is sharply changed at transition of values of μ through $\mu = 0$. Indeed, N_μ is trivial, if $\mu \leq 0$:

$$N_\mu = \begin{cases} N_\mu = O \ \text{ if } \ \mu < 0, \\ N_\mu = O \cup \Gamma \ \text{ if } \ \mu = 0. \end{cases}$$

Since $d < 0$, the curves $T_{1\mu}(W^u_{loc})$ and W^s_{loc} do not intersect at $\mu < 0$, quadratically touch each other at $\mu = 0$, and intersect transversally at two points

$$M^+_\alpha = \left(x^+ + (-1)^\alpha b\sqrt{-\frac{\mu}{d}} + O(\mu),\ 0\right), \ \ \alpha = 1, 2$$

at $\mu > 0$ (see formula (7)). Thus, Γ splits into two transversal homoclinic orbits $\Gamma_{1\mu}$ and $\Gamma_{2\mu}$ at $\mu > 0$. Accordingly, the set N_μ has at $\mu > 0$, a nontrivial structure.

[5] Note that the minimal number $k(\mu)$ of the strips is chosen here to be depending on μ (in particular, $k(\mu) \to +\infty$ as $\mu \to 0$). It follows from the fact that if $i < k(\mu)$, then the condition $T_{1\mu}\sigma^1_i \cap \sigma^0_j \neq \emptyset$ means that $j > i$. Therefore, $N(f_\mu)$ does not contain those orbits which intersect the strips $\sigma^{0,1}_i$ with numbers $i < k(\mu)$; it means that all such strips can be "eliminated from" the initial neighborhoods Π^+ and Π^- and, thus, one can consider smaller neighborhoods of $O \cup \Gamma$, the so-called "special neighbourhoods," see [14] for more detail.

Moreover, as it was discovered already in [5], at transition of values of μ through $\mu = 0$ (from negative to positive values), a countable set of Smale horseshoes Ω_i appear immediately, "by explosion," that is, for all integers $i \geq k_0(\mu)$ where $k_0(\mu) \to \infty$ as $\mu \to +0$, the horseshoes $T_{1\mu}(\sigma_i^1)$ and strips σ_i^0 intersect regularly.

However, we have to note that the corresponding *global bifurcation*[6] can take place either in the cases where $c > 0$ for planar diffeomorphisms f_0 such as in Fig. 7a and b or in the cases where $c < 0$ for diffeomorphisms of nonorientable manifolds such as in Fig. 7c.

3.1 Hyperbolicity Intervals

Consider a subsystem B_3^n of the topological Bernoulli shift with three symbols $\{0, 1, 2\}$ which satisfy the following conditions: (1) B_3^n has no orbits containing at least two neighboring nonzero symbols; and (2) for any orbit of B_3^n, the length of any complete segment of zeros is not less than n.

Theorem 1 [9, 14] **[Theorem on Hyperbolicity Intervals]**
Let f_μ be a one-parameter family of 2D diffeomorphisms satisfying conditions (A)–(E). *Then for any $\mu_0 > 0$, there is a countable sequence of open (and nonintersecting) intervals $\Delta_k \subset (0, \mu_0)$ such that at $\mu \in \Delta_k$, all orbits from N_μ are saddle and the system $f_\mu | N_\mu$ is topologically conjugate to B_3^{k+q}.*

This theorem goes back to what was established in [14]. Below we recall principal moments of the proof.

A Scheme of Proving Theorem 1 Let $N_k(\mu)$ be such a subset of $N_\mu = N(f_\mu)$ that contains the saddle O_μ and all those orbits which intersect Π^+ at points belonging to W^s_{loc} or the strips σ_i^0 with $i \geq k$.

For more definiteness, let Π^+ and Π^- be the rectangles

$$\Pi^+ = \{(x_0, y_0) \mid \ |x_0 - x^+| \leq \varepsilon_0, |y_0| \leq \varepsilon_0\},$$
$$\Pi^- = \{(x_1, y_1) \mid \ |x_1| \leq \varepsilon_1, |y_1 - y^-| \leq \varepsilon_1\}$$

with sufficiently small positive ε_0 and ε_1. Then, by (3), the strips $\sigma_k^0 \subset \Pi^+$ and $\sigma_k^1 \subset \Pi^-$, $k = \bar{k}, \bar{k}+1, \ldots$, are given as follows

$$\sigma_k^0 = \left\{(x_0, y_0) \mid \ |x_0 - x^+| \leq \varepsilon_0, |y_0 - \gamma^{-k} y^-| \leq |\gamma^{-k}| \left(\varepsilon_1 + O(\gamma^{-k})\right)\right\},$$
$$\sigma_k^1 = \left\{(x_1, y_1) \mid \ |x_1 - \lambda^k x^+| \leq |\lambda^k| \left(\varepsilon_0 + O(\gamma^{-k})\right), |y_1 - y^-| \leq \varepsilon_1\right\}.$$

[6] It can easily be seen from Fig. 7d that if a planar diffeomorphism has a homoclinic tangency with $c < 0$, then other homoclinic orbits necessarily exist. Therefore, here takes place the so-called *local Ω-explosion*, i.e., the sharp change in the structure of nonwandering orbits from some subdomain of the phase space. Although this case can be described in the same way as the global Ω-explosion, it is not so interesting and, therefore, we do not consider it especially.

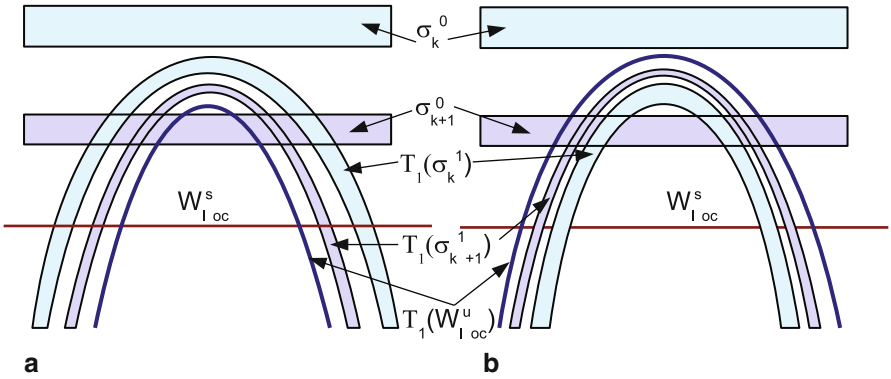

Fig. 8 Toward a geometry of the strips and horseshoes for $\mu \in \Delta_{k+1}$ for the cases **a** $c > 0, \lambda > 0$ and **b** $c < 0, \lambda > 0$

We consider, for more definiteness, the case $\lambda > 0, \gamma > 0, c > 0, d < 0$ and assume first that $\mu > 0$, such that the following inequality holds:

$$\mu + c\lambda^k(x^+ + \varepsilon_0) < \gamma^{-k}(y^- - \varepsilon_1). \tag{10}$$

In this case, the horseshoe $T_{1\mu}\sigma_k^1$ lies from below the own strip σ_k^0 and, accordingly, it can intersect only the strips σ_j^0 with numbers $j > k$. By the geometry, the horseshoes $T_{1\mu}\sigma_j^1$ with $j > k$ are not also intersected with the strip σ_k^0 (see Fig. 8a).

Next we take μ satisfying the following inequality:

$$\mu > \gamma^{-(k+1)}(y^- + \varepsilon_1). \tag{11}$$

In this case, the parabola $T_{1\mu}(W^u_{loc})$ intersects all the strips σ_i^0 with numbers $i \geq k+1$. Besides, all the horseshoes $T_1\sigma_j^1$ and strips σ_i^0 with numbers $i, j \geq k+1$ are also intersected, see see Fig. 8a. Moreover, as it was shown in [14], all these intersections are regular. It implies that for all μ satisfying (11), the set $N_{k+1}(\mu)$ is a uniformly hyperbolic set topologically conjugated with B_3^{k+q+1}.

On the other hand, the set N_μ will coincide with $N_{k+1}(\mu)$ for μ satisfying inequality (10). Thus, we obtain that for μ belonging to the interval h_{k+1},

$$\gamma^{-(k+1)}(y^- + \varepsilon_1) < \mu < \gamma^{-k}(y^- - \varepsilon_1) - c\lambda^k(x^+ + \varepsilon_0)$$

the set N_μ is hyperbolic and conjugate to B_3^{k+q+1} (by construction, $h_{k+1} \subset \Delta_{k+1}$). Note that the interval h_{k+1} is not empty for sufficiently large k. Indeed, its length $\ell(h_{k+1}) = \gamma^{-k}\left[(y^- - \varepsilon_1)(1 - \gamma^{-1}) - c\lambda^k\gamma^k(x^+ + \varepsilon_0)\right]$ is a value of order γ^{-k} for large k, since $\gamma > 1, \lambda\gamma < 1$, and $\varepsilon_0, \varepsilon_1$ are sufficiently small.

In principle, the case $c < 0$ is analyzed analogously. However, the upper boundary of the interval h_{k+1} is defined now from the condition $T_{1\mu}(W^u_{loc}) \cap \sigma_k^0 = \emptyset$; the lower boundary of h_{k+1} is found from the fact that a hyperbolic dynamics "is organized"

on the strips σ_i^0 with $i \geq k+1$ (see Fig. 8b). The corresponding conditions (similar to the inequalities (10) and (11)) are written as:

$$\gamma^{-(k+1)}(y^- + \varepsilon_1) + |c|\lambda^{k+1}(x^+ + \varepsilon_0) < \mu < \gamma^{-k}(y^- - \varepsilon_1), \tag{12}$$

that gives the estimate $\ell(h_{k+1}) = \gamma^{-k}\left(y^-(1-\gamma^{-1}) - \varepsilon_1(1+\gamma^{-1}) + \ldots\right)$. □

3.1.1 Prevalence of Hyperbolicity

In the paper [14], the following refined formulae for boundaries of the intervals $h_{k+1} = (\mu_{k+1}^1, \mu_{k+1}^2)$ were obtained: in the case $c > 0$,

$$\mu_{k+1}^1 = \gamma^{-(k+1)}y^-(1+\ldots), \;\; \mu_{k+1}^2 = \gamma^{-k}y^-(1 - \frac{cx^+}{y^-}(\lambda\gamma)^k + \ldots), \tag{13}$$

and in the case $c < 0$,

$$\mu_{k+1}^1 = \gamma^{-(k+1)}y^-(1 + \gamma\frac{|c|x^+}{y^-}(\lambda\gamma)^k + \ldots), \;\; \mu_{k+1}^2 = \gamma^{-k}y^-(1+\ldots), \tag{14}$$

where the dots stand for terms of order $o(|\lambda\gamma|^k)$. In these formulae, in contrast to (10–12), there is no explicit dependence of boundary values on ε_0 and ε_1. It allows to establish certain invariant results on measure of hyperbolicity that we explain below.

We call as the *relative measure of hyperbolicity* the following value

$$\nu = \lim_{\mu\to 0}\frac{m(\mathrm{Hyp})}{\mu},$$

where $\mathrm{Hyp} = \left\{\hat{\mu} : \hat{\mu} \in (0,\mu),\; f_{\hat{\mu}} \text{ is hyperbolic}\right\}$ and m is the Lebesgue measure. It follows from (13) and (14) that

$$\ell(\Delta_{k+1}) = \gamma^{-k}\left(1-\gamma^{-1}\right)y^-\left(1+O(|\lambda\gamma|^k)\right).$$

We take the interval $I_{k+1} = (0,\mu)$ with $\mu_{k+1}^1 < \mu < \mu_{k+1}^2$ which contains all hyperbolicity intervals Δ_i for $i \geq k+1$. We find from (13) and (14) that

$$m(\mathrm{Hyp}) \cap I_{k+1} \geq \sum_{i=k+1}^{\infty}\ell(\Delta_i) \;=\; \gamma^{-k}y^-(1+\epsilon_k),$$

where $\epsilon_k \to 0$ as $k \to \infty$. Then we obtain that

$$\nu = \lim_{k\to\infty}\frac{m(\mathrm{Hyp}) \cap I_{k+1}}{\ell(I_{k+1})} = 1.$$

This result from [11, 14], known as *prevalence of hyperbolicity*, goes back, in fact, to the papers of Newhouse and others [9, 10] in which, however, the measure of bifurcation sets was estimated.

4 On Boundaries of Hyperbolicity Intervals by the Global Ω-Explosion

Formulae (13) and (14) give a useful information on a structure and position of the hyperbolicity intervals. However, they do not answer questions on *exact* boundaries of the intervals Δ_k. In particular, a question on a bifurcation character of the boundary points has the definite interest, since it relates to the study of global bifurcations which lead to the creation/destruction of uniformly hyperbolic sets.

In this section, we consider one-parameter families f_μ of 2D C^r-smooth ($r \geq 3$) diffeomorphisms satisfying conditions (A)–(E) and such that

(F) the diffeomorphism f_0 belongs to a boundary of the Morse–Smale systems.

Thus, we will study transitions through $\mu = 0$ corresponding to the so-called *global Ω-explosion*. Requiring the condition (F) (along with (A)–(E)), we select essentially, the following three main cases (here always $\gamma > 0, d < 0$):

(1) f_0 is a planar diffeomorphism with $\lambda > 0, c > 0$ (here also, $bc < 0$, since the global map T_1 is orientable); see an example in Fig. 7a;
(2) f_0 is a diffeomorphism of a nonorientable manifold with $\lambda > 0, c < 0$ (here $bc > 0$, since T_1 is a nonorientable map); see an example in Fig. 7c;
(3) f_0 is a planar diffeomorphism with $\lambda < 0, c > 0$; see an example in Fig. 7b.[7]

By Theorem 1, all diffeomorphisms of the first class at $\mu \in \Delta_k$ are Ω-conjugate, i.e., they are conjugate in the restriction onto N_μ which is here a uniformly hyperbolic closed invariant set. However, if one considers not only orbits from N_μ but also all close ones, i.e., one studies hyperbolic sets from point of view of *local topological conjugacy*, then one can see that the sets N_μ are different. Moreover, we can distinct these hyperbolic sets by their *border points*.

Recall some definitions.

Definition 1 Let Λ be an invariant closed hyperbolic set for a 2D map. A saddle periodic point $P \in \Lambda$ is said to be *s-border* (resp., *u-border*) if any sufficiently small neighborhood of P is divided by $W^s_{loc}(P)$ (resp., $W^u_{loc}(P)$) into two disks, one of which does not contain points of Λ, while the other does contain. If P is both s-border and u-border, the point P is said to be (s,u)-*border*.

[7] Here we assume that c is positive only for the sake of definiteness: it can be always realized for the appropriate choosing of a pair of homoclinic points. Indeed, take a pair of points $M^{+\prime} = T_0(M^+)$ and $M^-(0, y^-)$ instead $M^+(x^+, 0)$ and $M^-(0, y^-)$. Then it is easy to check that $x^{+\prime} = -\lambda x^+, b' = b\lambda, c' = c\gamma$ for the new global map $T_1' = T_0 T_1 : \Pi^- \to T_0(\Pi^+)$. Making the coordinate change $x \mapsto -x, y \mapsto y$, we obtain that $x^{+\prime} = |\lambda| x^+, b' = -b\lambda, c' = -c\gamma$, that is, the "new c" will have the opposite sign than the "old" one (making the change $x \mapsto -x$, we arrive to our agreement that the coordinates x^+ and y^- of choosing homoclinic points must be positive).

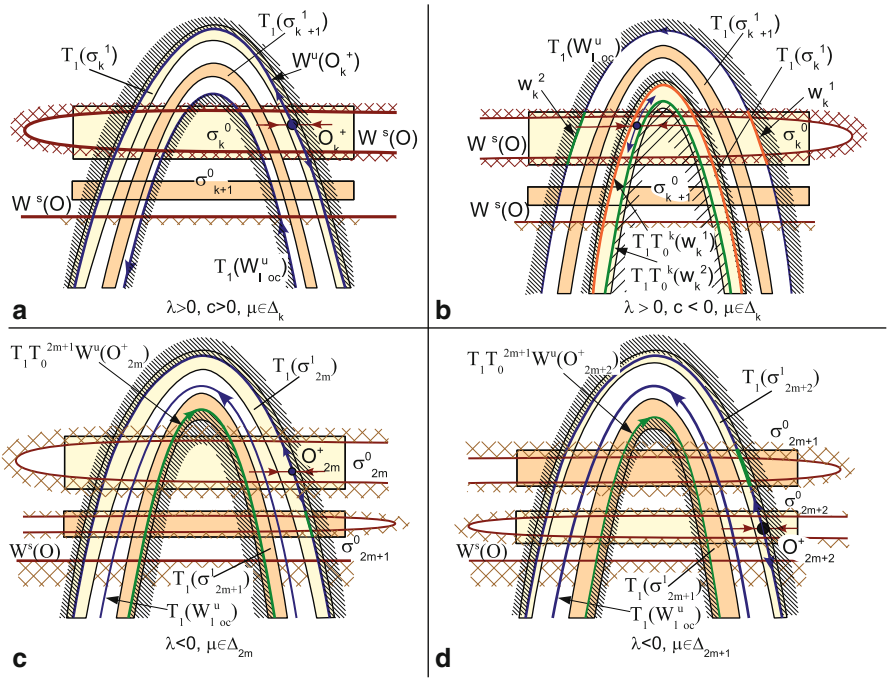

Fig. 9 We mark by a hatching that side of the corresponding invariant manifold of a border point where nonwandering points are absent

The notation of border periodic points was introduced in the paper by Grines [25], where it was shown that the border points are topological invariants of transitive hyperbolic sets.

Concerning our hyperbolic set N_μ for $\mu \in \Delta_k$, we note that it contains infinitely many Smale horseshoes Ω_j. Let O_j^+ and O_j^- be fixed points in Ω_j, i.e., the fixed points of the first return map T_j, such that O_j^+ (resp., O_j^-) has the positive (resp., negative) unstable multiplier. Then the following result holds:

Theorem 2 (Border Points for Hyperbolic Sets at Ω-Explosion)
Let $\mu \in \Delta_k$. Then N_μ has border periodic orbits as follows:

(1) in the case $\lambda > 0, c > 0$, the point O is (s,u)-border and O_k^+ is u-border;
(2) in the case $\lambda > 0, c < 0$, the point O is (s,u)-border;
(3) in the case $\lambda < 0, c > 0$, the point O is s-border and (i) the point $O_{2\,m}^+$ is u-border if $\mu \in \Delta_{2\,m}$ or (ii) the point $O_{2\,m+2}^+$ is u-border, if $\mu \in \Delta_{2\,m+1}$.

The statement of this theorem should be clear from Fig. 9 in which basic geometrical constructions for the hyperbolic sets H_μ are shown.

Evidently, the corresponding invariant manifolds of border points play an important role in bifurcations of birth and crisis of hyperbolic invariant sets. In any

case, the first and last bifurcations at creation/destruction of hyperbolicity should be connected with the appearance homoclinic or heteroclinic tangencies between stable and unstable manifolds of s-border and u-border points. The following result can be considered as a concrete realization of this observation for the global Ω-explosion.

Theorem 3 (On Exact Boundaries of Hyperbolicity Intervals) *Let f_μ be a one-parameter family of C^r-smooth, ($r \geq 3$), 2D diffeomorphisms satisfying conditions* (A)–(F) *and $\Delta_k = (\mu_k^*, \mu_k^{**})$ be the hyperbolicity interval for sufficiently large k. Then $\mu = \mu_k^*$ and $\mu = \mu_k^{**}$ correspond to codimension 1 global bifurcations of the following types:*

Case (1) *At $\mu = \mu_k^*$, a quadratic homoclinic tangency of the second class appears that is "the last" one for the curves $T_1(W^u_{loc}(O))$ and $W^s(O) \cap \sigma_k^0$, see* Fig. 10a. *If $\lambda^2\gamma^3 < 1$, a quadratic heteroclinic tangency, which is "the first" one for the curves $W^u(O_k^+)$ and $W^s(O) \cap \sigma_{k-1}^0$, appears at $\mu = \mu_k^{**}$, see* Fig. 10b. *If $\lambda^2\gamma^3 > 1$, at $\mu = \mu_k^{**}$, a fixed saddle-node point $\tilde{O}_{k-1}$ is born for the first return map T_{k-1}.*

Case (2) *Values $\mu = \mu_k^*$ and $\mu = \mu_k^{**}$ correspond to the appearance in f_μ quadratic homoclinic tangencies of the saddle O_μ: at $\mu = \mu_k^*$, the corresponding tangency is of the second class ("the last tangency" on the strip σ_k^0), see* Fig. 11a*; at $\mu = \mu_k^{**}$, the corresponding tangency is of the first class ("the first" one on the strip σ_{k-1}^0), see* Fig. 11b.

Case (3) (i) *Let $k = 2m$. At $\mu = \mu_{2m}^*$, the invariant manifolds $W^s(O)$ and $W^u(O_{2m}^+)$ have a quadratic tangency which is "the last" one on the strip σ_{2m}^0, see* Fig. 12a; *at $\mu = \mu_{2m}^{**}$, the manifolds $W^s(O)$ and $W^u(O_{2m}^+)$ have a quadratic tangency which is "the first" one on the strip σ_{2m-1}^0 at $\mu = \mu_{2m}^{**}$, see* Fig. 12b.

(ii) *Let $k = 2m + 1$. At $\mu = \mu_{2m+1}^*$, the invariant manifolds $W^s(O)$ and $W^u(O_{2m+2}^+)$ have a quadratic tangency which is "the last" one on the strip σ_{2m+1}^0, see* Fig. 13a. *If $\lambda^2\gamma^3 < 1$, then at $\mu = \mu_{2m+1}^{**}$, the manifolds $W^s(O)$ and $W^u(O_{2m+2}^+)$ have a quadratic tangency which is the "first" on the strip σ_{2m}^0, see* Fig. 13b. *If $\lambda^2\gamma^3 > 1$, then at $\mu = \mu_{2m+1}^{**}$, the map T_{2m} has a saddle-node $\tilde{O}_{2m}$.*

Remark 1 One can say that the moment $\mu = \mu_k^*$ corresponds to *the last bifurcation* at the formation of the hyperbolic set $N_k = N(f_\mu)$.[8] In the cases (2) and 3(i) as well as in the cases (1) and 3(ii) with $\lambda^2\gamma^3 < 1$, the moment $\mu = \mu_k^{**}$ corresponds to *the first bifurcation* leading to a breakdown of hyperbolicity (in other words, μ_k^* is the crisis bifurcation value for the hyperbolic set $N(f_\mu)$). However, the situation is certainly different for the cases (1) and 3(ii) with $\lambda^2\gamma^3 > 1$. Here, at $\mu = \mu_k^{**}$, a periodic saddle-node orbit is born to be far from the pointed-out hyperbolic set N_k. That is, nothing has happened with this set (now it is a subset $N_k \subset N(f_\mu)$): it exists yet certain time as a basic hyperbolic set till the same moment, denote it as $\mu = \mu_k^{het}$, when the first heteroclinic tangency appears between the manifolds $W^u(O_k^+)$ and $W^s(O) \cap \sigma_{k-1}^0$, see Fig. 10a. Evidently, namely this value $\mu = \mu_k^{het}$ must be considered as the crisis one for N_k.

[8] An analog is the well-known "last bifurcation" in the Hénon family after which the nonwandering set becomes hyperbolic.

Remark 2 If $\lambda^2\gamma^3 > 1$ (for the cases (1) and (3)), then $\mu_k^{het} - \mu_k^{**} = \nu_k$, where $\nu_k > 0$ is a value of order λ^k (for example, it follows from formulae (18) and (19) below that $\nu_k = cx^+(\lambda^{-1}-1)\lambda^k + o(\lambda^k)$). On the other hand, as well-known (see e.g., [18, 21]), the length of the bifurcation interval $B_k = [\mu_k^{sn}, \mu_k^{sh}]$ for the first return map $T_{k-1}(\mu)$ is a value of order $\gamma^{-2(k-1)}$. Here, at $\mu = \mu_{k-1}^{sn} = \mu_k^{**}$, a saddle-node fixed point appears at $T_{k-1}(\mu)$ and $\mu = \mu_{k-1}^{sh}$ corresponding to the last (homoclinic) bifurcations after which $T_{k-1}(\mu)$ becomes hyperbolic (its nonwandering set is the Smale horseshoe Ω_{k-1}). Since $\gamma^{-2k} \ll \lambda^k$ here (the inequality $\lambda\gamma^{3/2} > 1$ implies that $\lambda\gamma^2 > 1$), we obtain that $\mu_k^{het} > \mu_k^{sh}$. Then, for $\mu = \mu_k^{het}$, the diffeomorphism f_μ has simultaneously two hyperbolic basic sets, N_k and Ω_{k-1} and "cycle", since $W^u(N_k) \cap W^s(\Omega_k) \neq \emptyset$ for $\mu \geq \mu_k^{het}$ and $W^u(\Omega_k) \cap W^s(N_k) \neq \emptyset$ for $\mu \geq \mu_k^{**}$. Will correspond in this case to the bifurcation moment of the heteroclinic Ω-explosion (in the Palis sense [4]). That is, at $\mu = \mu_k^{het}$, the diffeomorphism f_μ has two hyperbolic basic sets, N_k and Ω_{k-1} and "Palis-cycle," since $W^u(O_k^+)$ touches $W^s(O) \cap \sigma_{k-1}^0$. Thus, the bifurcation at $\mu = \mu_k^{het}$ has always the important meaning. If $\lambda^2\gamma^3 < 1$, then the set $N(f_\mu)$ "softly bifurcates" at $\mu_k^{het} = \mu_k^{**}$—small fragments of nonwandering orbits having points in the strip σ_{k-1}^0 appear gradually. If $\lambda^2\gamma^3 > 1$, the moment $\mu = \mu_k^{het}$ corresponds to the "hard collision" of two hyperbolic basic sets, N_k and Ω_{k-1}.

Remark 3 The boundary $\mu = \mu_k^*$ is "exact." However, we do not prove (in this chapter) that the set N_k at $\mu = \mu_k^*$ is nonuniformly hyperbolic, i.e., all its orbits are saddle, except for exactly one orbit (homoclinic in the cases (1) and (2) or heteroclinic in the case (3)). This fact can be proved by using new "cone technique" for nonuniformly hyperbolic systems, see e.g., [26, 27].

4.1 The Proof of Theorem 3

Case (1): $\lambda > 0, \gamma > 0, d < 0, c > 0$. By Theorem 2, the first and last bifurcations at creation/destruction of the hyperbolic set N_μ have to be connected, respectively, with the appearance of the first and last tangencies between the manifolds $W^s(O)$ and $W^u(O)$ or $W^u(O_k^+)$. Therefore, the appearance at $\mu = \mu_k^*$, a homoclinic tangency of the second class between $W^s(O)$ and $W^u(O)$, looks to be quite evident, see Fig. 10a. Indeed, the piece $T_1(W_{loc}^u) \cap \sigma_k^0$ of $W^u(O)$ is the lower one in Π^+ from all unstable manifolds (of points of N_μ). On the other hand, one of two connected components $T_0^{-k}(T_1^{-1}W_{loc}^s(O)) \cap \sigma_k^0$ is the upper invariant curve from all stable manifolds (of points from N_μ). Accordingly, the homoclinic tangency of these curves is the "last one" at the creation of the hyperbolicity of the set N_μ. This tangency can be evidently interpreted as the homoclinic tangency of the second class for the manifolds $W_{loc}^s(O)$ and $T_1T_0^kT_1(W_{loc}^u)$.

At increasing μ, the top of $W^u(O)$ (and hence, the top of the horseshoe $T_1(\sigma_i^1)$) is moved up. In this case, one can see a priori two different variants reaching the boundary $\mu = \mu_k^{**}$ of the interval $\Delta_k(\mu)$. The first one is connected with the appearance in

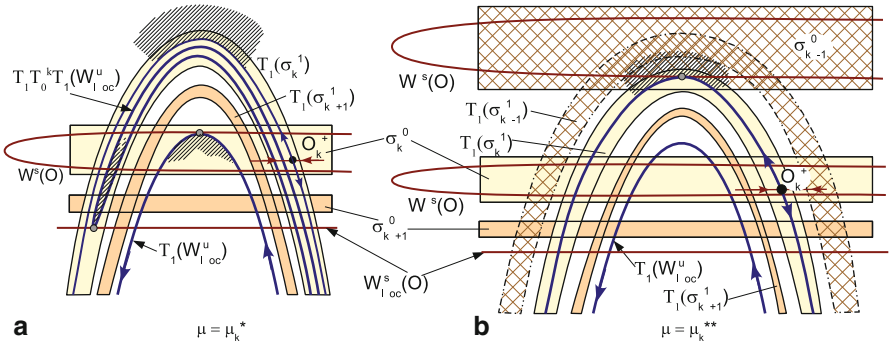

Fig. 10 Case (1). **a** At $\mu = \mu_k^*$ the curves $W^s_{loc}(O)$ and $T_1 T_0^k T_1(W^u_{loc})$ touch each other. **b** A moment $\mu = \mu_k^{het}$ (the same, $\mu = \mu_k^{**}$ at $\lambda\gamma^{3/2} < 1$) is shown when a heteroclinic tangency (first one in σ^0_{k-1}) between $W^u(O_k^+)$ and $W^s(O) \cap \sigma^0_{k-1}$ appears (the corresponding heteroclinic cycle has a type of a cycle from Fig. 1a

σ^0_{k-1}, a quadratic heteroclinic tangency of the manifolds $W^u(O_k^+)$ and $W^s(O)$. Moreover, in this case, a nontransversal heteroclinic cycle is created to be the same type as the cycle from Fig. 1a and hence, a transition through such a tangency is accompanied by the heteroclinic Ω-explosion leading to the appearance of infinitely many nonwandering orbits intersecting the strip σ^0_{k-1}. In the second variant, at $\mu = \mu_k^{**}$, a saddle-node fixed point is born at the first return map $T_{k-1} = T_1 T_0^{k-1}$. In Fig. 10b, a moment of creation of a heteroclinic tangency between $W^u(O_k^+)$ and $W^s(O)$ is shown. However, it is not clear even here—does the first return map $T_{k-1} = T_1 T_0^{k-1}$ have periodic orbits or not? In any case, we see in Fig. 10b that $T_1(\sigma^1_{k-1}) \cap \sigma^0_{k-1} \neq \emptyset$.

Thus, we need to clarify what possibility (and when) is realized here. For this goal, we estimate both values of μ at which a tangency between $W^u(O_k)$ and $W^s(O)$ appears and a saddle-node fixed point is born in T_{k-1}.

Let $y_1 = \varphi_1(x_1)$ and $y_0 = \varphi_0(x_0)$ be the lower traces of the stable manifold $W^s(O)$ on the strips σ^1_{k-1} and σ^0_{k-1}, respectively. We find from (6) that the curve $T_1^{-1} W^s(O)$ has in Π^- the following equation:

$$x_1 = -\frac{d}{c}(y_1 - y^-)^2 - \frac{\mu}{c} + \dots \tag{15}$$

Since $\gamma^{-k} y^-(1 + \dots) < \mu < \gamma^{-k-1} y^-(1 + \dots)$ at $\mu \in \Delta_k$ and $x_1 = O(\lambda^k)$ for points on σ^1_{k-1}, we obtain from (15) that the curve $y_1 = \varphi_1(x_1)$ has the equation

$$y_1 = y^- - \sqrt{\frac{\mu}{|d|}}(1 + \dots).$$

Then we deduce from (3) that the curve $y_0 = \varphi_0(x_0)$ on σ^0_{k-1} has such equation

$$y_0 = \gamma^{-k+1} y^- - \gamma^{-k+1} \sqrt{\frac{\mu}{|d|}}(1 + \dots). \tag{16}$$

We obtain from (3) and (6) the following formula for the coordinate y of the top of the manifold $W^u(O_k^+)$:

$$y_{\max} = \mu + cx^+\lambda^k(1 + \ldots). \tag{17}$$

Denote as μ_{tan}, that value of μ at which f_μ has a nontransversal heteroclinic cycle such as in Fig. 10b. We obtain from (16)–(17) that

$$\mu_{tan} = \gamma^{-(k-1)}y^- - cx^+\lambda^k - \gamma^{-3(k-1)/2}\sqrt{\frac{y^-}{|d|}}(1 + \ldots). \tag{18}$$

On the other hand, the saddle-node appears in σ_{k-1}^0 at $\mu = \mu_{k-1}^{+1}$, where

$$\mu_{k-1}^{+1} = \gamma^{-(k-1)}y^- - cx^+\lambda^{k-1} + \frac{1}{4d}\gamma^{-2(k-1)}(1 + \ldots), \tag{19}$$

(see e.g., [18, 21, 28]). Since $\lambda < \gamma^{-1}$, it follows from (18)–(19) that $\mu_{tan} > \mu_{k-1}^{+1}$ only in the case where $\lambda^k\gamma^{3k/2} > 1$, that is at $\lambda^2\gamma^3 > 1$.

Case (2): $\lambda > 0, \gamma > 0, c < 0, d < 0$. If $\mu = 0$, the curve $T_1^{-1}(W_{loc}^s(O))$ does not intersect with the strips $\sigma_i^1 \subset \Pi^-$. However, at $\mu \in \Delta_k$, this curve will intersect the strips σ_i^1 with numbers $i = m(k), m(k)+1, \ldots$, where $m(k) \sim k\cdot(-\ln\gamma/\ln\lambda) \ll k$, along two curves of the form

$$|x_1 - \lambda^i x^+| \le \lambda^i\varepsilon_1, y_1 - y^- = \pm\sqrt{-\frac{\mu}{|d|}}(1 + \ldots). \tag{20}$$

Indeed, the curve $T_1^{-1}W^s(O) \cap \Pi^-$ has the Eq. (15). Since μ is a value of order γ^{-k} at $\mu \in \Delta_k$ (see (13) and (14)), formula (20) takes place for such i that $\lambda^i < \gamma^{-k}$, i.e., for $i \ge m(k)$.

By Theorem 2, the hyperbolic set N_μ at $\mu \in \Delta_k$ has only one border point O which is (s,u)-border here. Therefore, the values $\mu = \mu_k^*$ and $\mu = \mu_k^{**}$ correspond to homoclinic tangencies (of the first and second class, respectively) to the point O. In Fig. 11, the corresponding bifurcation moments are shown. In Fig.11a, the lower in Π^+ piece of $W^u(O)$ (one of the two curves $T_1T_0^kT_1(W_{loc}^u)$) touches the upper piece of $W^s(O) \cap \sigma_k^0$. This tangency is of the second class, evidently (the same as in Fig. 10a). In Fig. 11b otherwise, the upper in Π^+ piece of $W^u(O)$ (it is $T_1(W_{loc}^u)$) touches the lower piece of $W^s(O) \cap \sigma_{k-1}^0$. This tangency (of the first class) has, evidently, the same type as the initial one at $\mu = 0$.

Case (3) $\lambda < 0, \gamma > 0, c > 0, d < 0$. Since λ is negative here, the point O is not more u-border but it is s-border as for all other cases under consideration.

(i) Let $\mu \in \Delta_{2\,m}$. By Theorem 2, the point $O_{2\,m}^+$ is u-border here. It means that a connected piece $W^u(O_{2\,m}^+) \cap T_1(\sigma_{2\,m}^1)$ containing the point $O_{2\,m}^+$ is the upper trace in Π^+ of unstable manifolds (for points of N_μ). Accordingly, the lower trace is one of the curves $T_1T_0^{2\,m+1}(W^u(O_{2\,m}^+))$ in the horseshoe $T_1(\sigma_{2\,m+1}^1)$. Note that the horseshoe $T_1(\sigma_{2\,m-1}^1)$ is posed from below the own strip $\sigma_{2\,m-1}^0$, see Fig. 12b. Therefore, the values $\mu = \mu_k^*$ and $\mu = \mu_k^{**}$ should correspond to heteroclinic tangencies of the

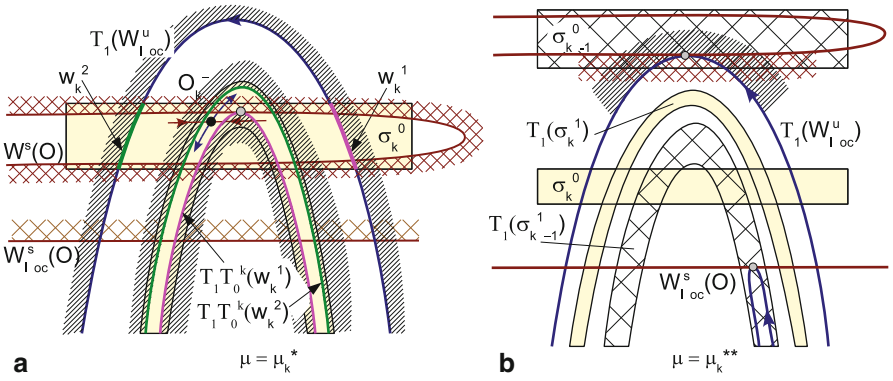

Fig. 11 Case (2). **a** The moment $\mu = \mu_k^*$ is shown when a homoclinic tangency occurs (between the curves $W^s(O) \cap \sigma_k^0$ and $T_1 T_0^k T_1(W^u_{loc})$). This is a tangency of the second class and, after its splitting, the set N_μ becomes hyperbolic. **b** The moment $\mu = \mu_k^{**}$ is shown when the curves $T_1(W^u_{loc})$ and $W^s(O) \cap \sigma^0_{k-1}$ touch each other at the first time

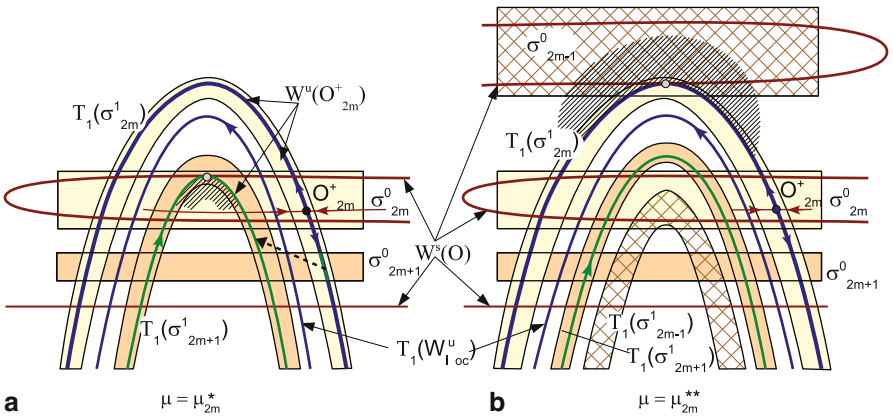

Fig. 12 Case 3(i). **a** At $\mu = \mu_k^*$, a heteroclinic tangency (between the curves $W^s(O) \cap \sigma^0_{2\,m}$ and $T_1 T_0^{2\,m-1} T_1(W^u(O^+_{2\,m}))$) appears to be "last" in $\sigma^0_{2\,m}$. **b** At $\mu = \mu_k^{**}$, the curves $T_1(W^u(O^+_{2\,m}))$ and $W^s(O) \cap \sigma^0_{2\,m-1}$ touch (at the first time)

manifolds $W^u(O^+_{2\,m})$ and $W^s(O)$, respectively, "the last" one on $\sigma^0_{2\,m}$ (Fig. 12a) and "the first" one on $\sigma^0_{2\,m-1}$ (Fig. 12b).

(ii) Let $\mu \in \Delta_{2\,m+1}$. By Theorem 2, the point $O^+_{2\,m+2}$ is u-border here. Thus, the manifold $W^u(O^+_{2\,m+2})$ forms in the horseshoes $T_1(\sigma^1_{2\,m+2})$ and $T_1(\sigma^1_{2\,m+1})$—both the upper and the lower in Π^+ traces of unstable manifolds of orbits from N_μ. The value $\mu = \mu^*_{2\,m+1}$ corresponds to the heteroclinic tangencies of the manifolds $W^u(O^+_{2\,m+2})$ and $W^s(O)$ which is "the last" one in $\sigma^0_{2\,m+1}$, see Fig. 13a. Note that the horseshoe $T_1(\sigma^1_{2\,m})$ can also intersect the own strip $\sigma^0_{2\,m}$. Therefore (the same as in the case $\lambda > 0, c > 0$), the value $\mu = \mu^{**}_{2\,m+1}$ at $\lambda^2\gamma^3 > 1$ corresponds to the saddle-node

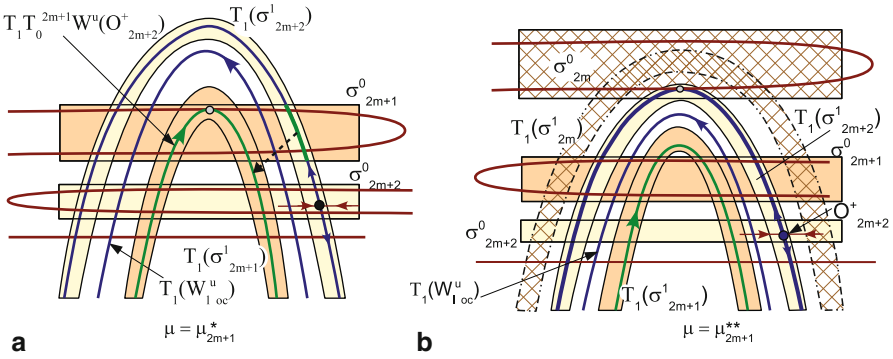

Fig. 13 Case 3(ii). **a** At $\mu = \mu^*_{2\,m+1}$, a heteroclinic tangency (between the curves $W^s(O) \cap \sigma^0_{2\,m+1}$ and $T_1 T_0^{2\,m+2} T_1(W^u(O^+_{2\,m+2}))$) appears to be "last" in $\sigma^0_{2\,m+1}$. **b** At $\mu = \mu^{**}_{2\,m+1}$, the curves $T_1(W^u(O^+_{2\,m+2}))$ and $W^s(O) \cap \sigma^0_{2\,m}$ touch (at the first time)

bifurcation in the first return map $T_{2\,m} : \sigma^0_{2\,m} \to \sigma^0_{2\,m}$. If $\lambda^2\gamma^3 < 1$, then the value $\mu = \mu^{**}_{2\,m+1} \equiv \mu^{het}_{2\,m+1}$ corresponds to the heteroclinic tangency of the manifolds $W^u(O^+_{2\,m+2})$ and $W^s(O)$ which is "the first" one in $\sigma^0_{2\,m}$, see Fig. 13b.

It completes the proof. □

Acknowledgments The authors thank D. Turaev for fruitful discussions. This research was carried out within the framework of the Russian Federation Government grant, contract No.11.G34.31.0039. The paper was supported also in part by grants of RFBR No.10-01-00429, No.11-01-00001, and No.11-01-97017-povoljie.

References

1. Shilnikov, L.P.: On a new type of bifurcations in multidimensional dynamical systems. Sov. Math. Dokl. **182**(1), 53–56 (1969)
2. Afraimovich, V.S., Shilnikov, L.P.: On accesible transitions from Morse–Smale systems to systems with many periodic motions. Russ. Acad. Sci. Izv. Math. **38**(6), 1248–1288 (1974)
3. Shilnikov L.P.: On birth of periodic orbits from an orbit bi-asymptotic to a saddle–saddle equilibrium. Sov. Math. Dokl. **170**(1), 49–52 (1966)
4. Palis, J.: A note on Ω-stability. Global Analysis. Proceedings of Symposia in Pure Mathematics, vol. 14, pp. 221–222. American Mathematical Society, Providence (1970)
5. Gavrilov N.K., Shilnikov, L.P.: On three-dimensional dynamical systems close to systems with a structurally unstable homoclinic curve. Part 1, Math. USSR Sb. **17**, 467–485 (1972); Part 2, Math. USSR Sb. **19**, 139–156 (1973)
6. Gavrilov, N.K.: On three-dimensional dynamical systems having a structurally unstable homoclinic contour. Sov. Math. Notes **14**(5), 687–696 (1973)
7. Gonchenko, S.V.: Moduli of Ω-conjugacy of two-dimensional diffeomorphisms with a nontransversal heteroclinic cycle. Russ. Math. Sb. **187**(9), 3–24 (1996)
8. Gonchenko, S.V., Shilnikov, L.P., Turaev, D.V.: On Newhouse regions of two-dimensional diffeomorphisms close to a diffeomorphism with a nontransversal heteroclinic cycle. Proc. Steklov Inst. Math. **216**, 70–118 (1997)

9. Newhouse, S., Palis, J.: Cycles and bifurcation theory. Asterisque **31**, 44–140 (1976)
10. Palis, J., Takens, F.: Cycles and measure of bifurcation sets for two dimensional diffeomorphisms. Invent. Math. **82**, 397–422 (1985)
11. Palis, J., Takens, F.: Hyperbolicity and the creation of homoclinic orbit. Ann. Math. **125**, 337–374 (1987)
12. Palis, J., Takens, F.: Hyperbolicity and the Creation of Homoclinic Orbit. Cambridge Studies in Advanced Mathematics, vol. 35. Cambridge University Press, Cambridge (1993)
13. Alligood, K., Sander, E., Yorke, J.: Explosions: Global bifurcations at heteroclinic tangencies. Ergod. Theory Dyn. Syst. **22**, 953–972 (2002)
14. Stenkin, O.V., Shilnikov, L.P.: Homoclinic Ω-explosion and hyperbolicity domains. Russ. Math. Sb. **189**(4), 125–144 (1998)
15. Gonchenko, S.V., Shilnikov, L.P.: Arithmetic properties of topological invariants of systems with a structurally unstable homoclinic trajectory. Ukr. Math. J. **39**, 21–28 (1987)
16. Gonchenko, S.V., Gonchenko, V.S.: On bifurcations of birth of closed invariant curves in the case of two-dimensional diffeomorphisms with homoclinic tangencies. Proc. Math. Steklov Inst. **244**, 80–105 (2004)
17. Gonchenko, S.V., Shilnikov, L.P., Turaev, D.V.: On dynamical properties of multidimensional diffeomorphisms from Newhouse regions. I. Nonlinearity **21**, 923–972 (2008)
18. Gonchenko, S.V., Shilnikov, L.P.: Homoclinic tangencies. Thematic issue: Moscow-Izhevsk 524 p. (in Russian) (2007)
19. Gonchenko, S.V., Shilnikov, L.P.: Invariants of Ω-conjugacy of diffeomorphisms with a nontransversal homoclinic orbit. Ukr. Math. J. **42**(2), 134–140 (1990)
20. Gonchenko, S.V., Shilnikov, L.P.: On moduli of systems with a nontransversal Poincaré homoclinic orbit. Russ. Acad. Sci. Izv. Math. **41**(3), 417–445 (1993)
21. Gonchenko, S.V., Sten'kin, O.V., Turaev, D.V.: Complexity of homoclinic bifurcations and Ω-moduli. Int. J. Bifurc. Chaos **6**(6), 969–989 (1996)
22. Shilnikov, L.P.: On a Poincaré-Birkhoff problem. Math. USSR Sb. **3**, 91–102 (1967)
23. Shilnikov, L.P., Shilnikov, A.L., Turaev, D.V., Chua, L.O.: Methods of qualitative theory in nonlinear dynamics. World Scientific, Singapore, Part I (1998), Part II (2001)
24. Gonchenko, S.V.: Nontrivial hyperbolic subsets of multidimensional systems with a nontransversal homoclinic curve. In: Methods of Qualitative Theory of Differential Equations, pp. 89–102. Gorky State University, Yekaterinberg (in Russian) (1984)
25. Grines, V.Z.: On topological conjugacy of diffeomorphisms of a two-manifold on one-dimensional basic sets. Part I, Trudy Moskov. Mat. Obšč. **32**, 35–60 (1975); Part II, Trudy Moskov. Mat. Obšč. **34**, 243–252 (1977)
26. Enrich, H.: A heteroclinic bifurcation of Anosov diffeomorphisms. Ergod. Theory Dyn. Syst. **18**, 567–608 (1998)
27. Hoensch, U.A.: Some hyperbolic results for Henon-like diffeomorphisms. Nonlinearity **21**, 587–611 (2008)
28. Gonchenko, S.V., Turaev, D.V., Shilnikov, L.P.: Homoclinic tangencies of any order in Newhouse regions. J. Math. Sci. **105**, 1738–1778 (2001)

Self-Organized Regularity in Long-Range Systems

Xavier Leoncini

Abstract Dynamics of many-body long-range interacting systems are investigated. Using the XY-Hamiltonian mean-field model as a case study, we show that regular trajectories, associated with invariant tori of the single-particle dynamics emerge as the number of particles is increased. Moreover, the construction of stationary solutions as well as studies of the maximal Lyapunov exponent of the systems show the same trend towards integrability. This feature provides a dynamical interpretation of the emergence of long-lasting out-of-equilibrium regimes observed generically in long-range systems. Extensions beyond the mean-field system are considered and display similar features.

1 Introduction

Dynamics of many body systems interacting through two-body long-range interactions defines a long-standing problem, with many potential domains of applications. In such systems, each constituent is under the influence of all other microscopic actors, resulting in a complex dynamical picture. These systems cover a broad spectrum of physical interactions most notably because of the long-range nature of the gravitational and coulomb interaction, but not restricting to these we find long-range interactions in fluid mechanics for instance in Stokes flows (see for instance [1] for some of its consequences) or in two-dimensional Eulerian flows between vortices [2, 3], we find them also in systems dealing with wave-particle interactions in plasma physics [4] or the free-electron-lasers [5] and the list is not exhaustive. These studies also extend to cross-disciplinary fields, most notably in biological and social sciences, where an intricate network of mutual interactions between agents has to be accommodated for [6]. A system is considered long-range when the two-body interaction potential $V(r)$ decays as $V(r) \sim r^{-\alpha}$ with $\alpha \leq d$, where d is the embedded dimension. We may have also instances where we do not see any decay such as $V(r) \sim \log(r)$ for point vortices on a plane or cases where we have $\alpha = 0$,

X. Leoncini (✉)
Centre de Physique Théorique, Aix-Marseille Université, Campus de Luminy,
Case 907 - 13288 Marseille cedex 9, France
e-mail: Xavier.Leoncini@cpt.univ-mrs.fr

H. González-Aguilar, E. Ugalde (eds.), *Nonlinear Dynamics New Directions,*
Nonlinear Systems and Complexity 12, DOI 10.1007/978-3-319-09864-7_4

as for instance, for mean field situations. The study of these systems with a large number of constituents within the statistical physics framework still is problematic. Indeed, the energy is generally nonextensive and even if the coupling constant is renormalized to restore extensiveness, additivity is not. This leads to the possibility of ensemble nonequivalence, such as negative specific heat in the microcanonical one, as well as other problems [7, 8]. From the dynamical perspective, long-range interacting Hamiltonian systems display as well some ubiquitous features. Through an initial violent relaxation, the system relaxes toward a quasi-stationary state (QSS) whose lifetime diverges with system size, implying a very slow relaxation toward equilibrium. A paradigmatic representative of long-range interactions, sharing the mean field viewpoint, is the so called Hamiltonian mean field (HMF) model, which describes the mean field evolution of N $XY-$spins (rotators). In the limit of infinite system size the discrete HMF model becomes a Vlasov equation for the evolution of the single particle distribution function [9]. This leads to a statistical based treatment within the Lynden-Bell formalism displaying some fermion properties [9, 10]. More recently, the HMF stationary states have been constructed by using a formal analogy with a set of uncoupled pendula [11].

This formal analogy represented an important step in understanding of the dynamical properties of the QSS in the HMF model, beyond the statistical and kinetic (Vlasov) approaches. Indeed, it has been shown that the actual microscopic dynamics in the magnetized stationary state is regular and explicitly known and thus explained the abundance of emerging regular orbits observed in [12].

In this chapter, we shall review different results obtained in this framework of long-range interacting systems displaying microscopic low dimensional dynamics and the rise of regularity. In the first part, we shall discuss the construction of stationary states in the HMF model and its consequence on regularity and dynamics. A special emphasis will be made on the so-called statistical equilibrium distribution and for which we shall display some Poincaré sections, monitor the fluctuations, and compute some finite time Lyapunov exponents. We shall then move on to other systems beyond the mean field approach displaying similar feature.

2 Regular Motion

In this section, we recall the mechanisms giving rise of microscopic regular motion in these long-range systems. As a starting point, we consider the now paradigmatic HMF model which corresponds to an $XY-$model with mean field interactions. We first start with reminding some of the thermodynamical properties of the system and display some numerical investigations.

2.1 The Hamiltonian Mean Field (HMF) Model

This model was introduced in [13–15] as a one-dimensional model comprising the first Fourier term of interacting gravitational sheets. It is formally equivalent to a mean-field $XY-$model, yet it also bears many similarities with the problem of self-consistent wave–particle interactions discussed in [16], and the possibility to describe the phenomenon of collective atomic recoil laser has been discussed in [17]. Its N-body Hamiltonian form, which corresponds to the mean field XY model with ferromagnetic interactions, writes

$$H = \sum_{i=1}^{N} \left[\frac{p_i^2}{2} + \frac{1}{2N} \sum_{j=1}^{N} 1 - \cos\left(q_i - q_j\right) \right], \tag{1}$$

where p_i and q_i are respectively the (canonically conjugate) momentum and position of particle (rotor) i. The Hamiltonian (1) displays a peculiar feature, namely a renormalization of the coupling constant inversely proportional to the size of the system. This feature known as the Kac prescription, is necessary in order to recover an extensive system (at least in the regime of low energies). For a discussion on extensiveness and additivity in these type of system, we refer the reader to the very detailed review [8] and references therein. To get a grasp of the model we first start with its thermodynamical properties.

2.1.1 Equilibrium Statistical Properties

To monitor the equilibrium properties it is convenient to define an order parameter, the "magnetization" as the norm of the vector

$$\mathbf{M} = \frac{1}{N} \left(\sum \cos q_i, \sum \sin q_i \right) = M\,(\cos\varphi,\ \sin\varphi). \tag{2}$$

Note that, due to the translation symmetry displayed in (1), the phase φ has no special value and M is the order parameter. It has been shown (see for instance [8]) that for the HMF model, we had equivalence between ensembles, meaning the microcanonical one and the canonical one were giving rise to the same properties, and no negative specific heat could be expected. It is then easier to deal with the canonical one. In this setting we can extract from the partition function (see [15]) that the one-particle distribution function at thermal equilibrium writes

$$\rho(p,q) = \sqrt{\frac{2\pi}{\beta}} \frac{1}{I_0(\beta M)} \exp\left(-\beta \left(\frac{p^2}{2} - M\cos q \right) \right), \tag{3}$$

with M[1] solution of the implicit equation

$$M = \frac{I_1(\beta M)}{I_0(\beta M)}, \tag{4}$$

[1] We do not differentiate between the observable M and its statistical average $\langle M \rangle$, for simplicity in notations, except when needed

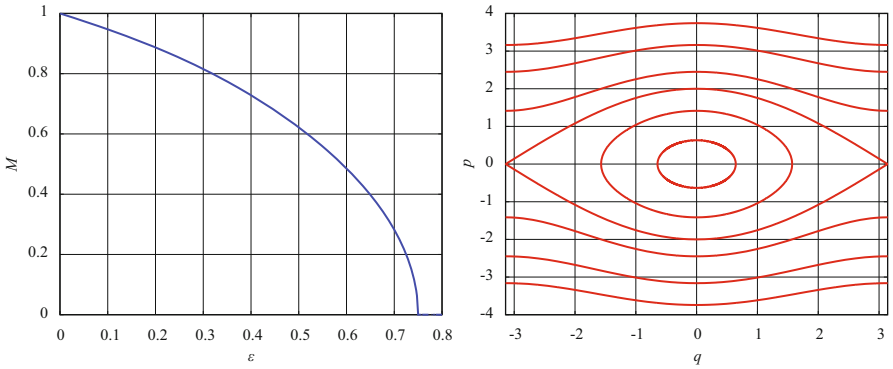

Fig. 1 *Left*: Equilibrium magnetization versus density of energy of the HMF model: A second-order phase transition is observed at $\varepsilon_c = 0.75$ ($T_c = 0.5$). *Right*: Phase portrait of a pendulum with $m = 1$

where I_0 and I_1 are the modified Bessel function of the first kind of orders 0 and 1 and β is the inverse of the temperature T. Given the form of the Hamiltonian we can develop the cosine and rewrite it as

$$H = N\left(\frac{1}{N}\sum_i \frac{p_i^2}{2} + \frac{1}{2} - \frac{M^2}{2}\right). \tag{5}$$

Thus, we can then easily compute the average density of energy per particle as

$$\varepsilon = \frac{T}{2} + \frac{1}{2}(1 - M^2). \tag{6}$$

The implicit Eq. (4) can easily be solved, the results are displayed in Fig. 1. One observes a second-order phase transition occurring at $\varepsilon_c = 0.75$.

2.1.2 Microscopic Dynamics

Studying the dynamics of Hamiltonian systems with a large number of degree of freedom and its connection to equilibrium statistical mechanics has been a long-standing problem. The relaxation to statistical equilibrium has been under scrutiny ever since the pioneering work of Fermi and the FPU problem [18]. Moreover, since the advent of powerful computers and for specific systems within a class of initial conditions, integrating numerically Hamiltonian dynamics has proven to be competitive in regards to Monte Carlo schemes for the study of statistical properties (see for instance [19]). The main assumption made in these studies was that, since the system admitted only a few conserved quantities for generic initial conditions, once the dimensions of phase space were large enough, microscopic Hamiltonian chaos should be at play and be sufficiently strong to provide the foundation for the statistical approach within the microcanonical ensemble.

Following the same strategy, we may wonder what occurs when dealing with long-range systems. As a first requirement, let us write the equation of motion:

$$\dot{p}_i = -\frac{1}{N}\sum_j \sin(q_i - q_j),$$
$$\dot{q}_i = p_i,$$

where the dot denotes the time derivative. Developing the sine term, the equations of motion for the particles are then rewritten in the form

$$\begin{cases} \dot{p}_i &= -M\ \sin(q_i - \varphi) \\ \dot{q}_i &= p_i \end{cases} \tag{7}$$

The form (7) is somehow reminiscent of the dynamics of a pendulum. We though have to remember that the magnetization M and its phase φ are actually global collective quantities depending on all the particles positions (2).

2.1.3 Regular Stationary States

Now let us imagine that starting from a given initial condition, the system of coupled rotators has eventually settled down to an intermediate quasi-equilibrium and assume that in the $N \to \infty$ limit the magnetization M of the XY-HMF model is converging to a constant. Then the equations of motion (7) would imply that the system formally reduces to an infinite set of uncoupled pendula. Let us see if we can start from there and let us consider the Hamiltonian of N independent pendula

$$H = \sum_{i=1}^{N} \frac{p_i^2}{2} + m(1 - \cos q_i)\,. \tag{8}$$

We shall use the fact that system (8) is integrable and construct a subset of solutions which are stationary for (1) in the thermodynamic limit [11, 20]. Note that a similar approach was used in [21] for other purposes.

Given the Hamiltonian (8), we know that each pendulum i is confined on a specific torus of the pendulum phase portrait depicted in Fig 1. To build a stationary state we naturally consider the ergodic measure on the torus which originate from the pendulum motion and time averages. The dynamics is though nonlinear making this measure quite impractical. Since the dynamics is integrable and periodic on a torus, it is easier to change coordinates and perform a canonical transformation to the action-angle variables (I, θ) of the system (see for instance [22]). Then for one pendulum, we obtain $H_m = H_m(I)$, with

$$\dot{I} = 0 \tag{9}$$
$$\dot{\theta} = \partial H_m / \partial I = \omega(I), \tag{10}$$

where I and θ stand for the constant action and the angle. The action is a constant of the motion, which is fixed by the initial state the pendulum i. And thus we have

$$\theta(t) = \omega(I)t + \theta(0). \tag{11}$$

For any selected initial condition, as time evolves, θ covers uniformly the circle $[-\pi, \pi[$, while the action I keeps its constant value which we note A_i. The natural ergodic measure is then simple to obtain and reduces hence to

$$\rho_i(I, \theta) = \frac{1}{2\pi}\delta(I - A_i). \tag{12}$$

From this measure (12) we can immediately obtain an ergodic measure for the system of N pendula

$$\rho_E = \prod_{i=1}^{N} \rho_i = \frac{1}{(2\pi)^N} \prod_{i=1}^{N} \delta(I_i - A_i). \tag{13}$$

Going back to a more statistical approach and since particles are identical and noninteracting one can straightforwardly deduce the following expression for the one particle density function (or equivalently an invariant measure of the pendulum system):

$$f(I, \theta) = \frac{g(I)}{2\pi}, \tag{14}$$

where $g(\cdot)$ is for instance a discrete valued function determined by selected N initial conditions. Since we actually have $N = \infty$, it is also possible to consider that $g(\cdot)$ changes smoothly with the action variable.

Should we prefer to work in the original phase space we can then use the $f(I, \theta)$ according to (14) and then perform an "inverse" canonical transformation to obtain an explicit expression for the one particle density function $\tilde{f}(p, q)$ as defined in the original phase space Γ_{pq}. Since it corresponds to an invariant measure, this distribution corresponds to a stationary state of an infinite ensemble of uncoupled pendula.

Now using this distribution we can compute global macroscopic variables as for instance the global magnetization $\mathbf{M}$ as specified by Eq. (2)). Since we have a stationary state corresponding to an invariant measure, the time average of the magnetization coincides with the ergodic-spatial average, we thus have

$$\bar{\mathbf{M}} = \langle \mathbf{M} \rangle = \left(\int \tilde{f}(p, q) \cos q \; dpdq, 0 \right), \tag{15}$$

where the observation that $\tilde{f}$ is even in p and q has been used and $\bar{x}$ denotes a time average while $\langle x \rangle$ a spatial one (statistical one). Note that due to the symmetry of the distribution function (see the tori in Fig. 1) the average of the sine part is zero. We can also express the Eq. (15) using action-angle variables and thus write

$$\bar{\mathbf{M}} = \langle \mathbf{M} \rangle = \left(\frac{1}{2\pi} \int g(I) \cos q(I, \theta) \, dI d\theta, 0 \right). \tag{16}$$

In order to perform the integration over the angle we need the specific details of the coordinate. Regarding the motion of a pendulum we have two type of orbits trapped and nontrapped ones (see Fig. 1). The separatrix separating the two regions has an energy $E = m$. Given these, it is convenient to define $\kappa = \kappa(I) = (E + m)/2\, m$ to characterize the orbit: trapped for $\kappa < 1$ and nontrapped for $\kappa > 1$. This parameter κ is also used to parameter the Jacobi elliptic function, as well as the complete elliptic function of first and second kind. Given these we obtain that trapped orbits (libration) are characterized by:

$$q = 2\sin^{-1}\left[\kappa sn\left(\frac{2K(\kappa)\theta}{\pi}, \kappa\right)\right],$$
$$I = \frac{8}{\pi}\sqrt{m}\left[E(\kappa) - \kappa'^2 K(\kappa)\right],$$

which yields

$$\langle \cos q \rangle = 2\frac{E(\kappa)}{K(\kappa)} - 1. \tag{17}$$

While for the nontrapped ones (rotation) we get

$$q = 2am\left(\frac{2K(1/\kappa)\theta}{\pi}, \kappa^{-1}\right),$$
$$I = \frac{8\kappa}{\pi}\sqrt{m}E(1/\kappa),$$

leading to

$$\langle \cos q \rangle = 1 + \frac{2}{\kappa^2}\left(\frac{E(\kappa^{-1})}{K(\kappa^{-1})} - 1\right), \tag{18}$$

where $< \cdot >= \int_0^{2\pi} \cdot d\theta/(2\pi)$ stands for averaging over the angles. In order to continue our original computation, we have to split our integral in two parts, depending whether the action is lower or higher than the value $I_c = 8\sqrt{m}/\pi$ corresponding to the separatrix. We finally obtain as a final form

$$M = \int_0^{\frac{8}{\pi}\sqrt{m}} g(I)\left(2\frac{E(\kappa)}{K(\kappa)} - 1\right) dI$$
$$+ \int_{\frac{8}{\pi}\sqrt{m}}^{\infty} g(I)\left(1 + \frac{2}{\kappa^2}\left(\frac{E(\kappa^{-1})}{K(\kappa^{-1})} - 1\right)\right) dI. \tag{19}$$

We recall given an initial distribution $\tilde{f}$, then the magnetization (19) stays constant since, by construction $\tilde{f}$ corresponds to an invariant measure.

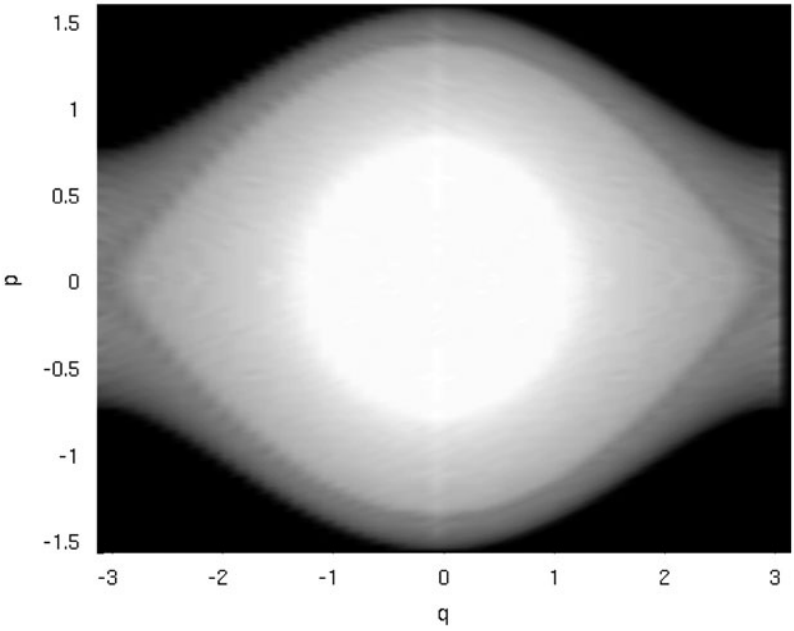

Fig. 2 Stationary distribution $\tilde{f}(p,q)$ obtained with $m = M = 0.5$ and a continuous $g(.)$

We now shall reconnect the model of uncoupled pendula parameterized by the real number m to the XY-HMF interacting rotator imposing a self-consistency constraint:

$$\langle \mathbf{M} \rangle = m. \tag{20}$$

Indeed, let us recall that the equations of motion for the system of pendula are

$$\begin{cases} \dot{p}_i &= -m \ \sin q_i \\ \dot{q}_i &= p_i \end{cases}, \tag{21}$$

hence, if there exists an $\tilde{f}$ for which the constraint given by Eq. (20) is satisfied (with $m \neq 0$ else things are rather trivial), then we have obtained a stationary solution of the system of pendula, which is in turn also stationary solution of the XY-HMF model in the $N \to \infty$ limit (QSS).

As we shall be able to replace m by M in Eq. (21) and recover equations which are formally identical to (7), noting that our choice for the pendulum Hamiltonian implied a constant $\varphi = 0$. It is not so difficult to find a function $g(.)$ and a parameter m which satisfies the constraint Eq. (20) (see [11] for details). A solution which does not correspond to the equilibrium distribution is given by Eq. (3) and corresponding to a value of magnetization $M = 0.5$ and a continuous $g(I)$ is displayed in Fig. 2. One typically recognizes the underlying pendulum phase portrait, with each tori being differently populated according to the function $g(I)$. The nonuniformity of

$\tilde{f}(p,q)$ on each torus arises from the nonlinearity of the transformation $q = q(I,\theta)$, $p = p(I,\theta)$.

As consequence of our analysis, we know that any stationary state of the HMF model will be of the type discussed above, meaning that the microscopic dynamics of its constituent will have an integrable regular motion like a system of uncoupled pendula. Particles of the HMF model have self-created the magnetization which then traps them and dictates their regular motion, in that sense we have some self organized regularity in this model. We shall return on this feature in the following sections. But let us discuss how the magnetization is created and which particle are "confining" (creating magnetization) and which one are "deconfining" the system. Looking back at Eq. (19), we notice that the second part (rotating particles) always has a negative contribution. For the librating particles, the contribution of each particle $< \cos q >$ near the separatrix is close to -1 as they spend most of there time around $q = \pm\pi$. Hence given Eq. (17), only particules with a $\kappa < \kappa_c \approx 0.90891$ contribute constructively (positively) to the magnetization, κ_c being the value for which the equality $2E(\kappa) = K(\kappa)$ holds. We may then consider as a distribution a single torus (for $\kappa < \kappa_c$), for instance for $M = 0.5$ the torus with $\kappa \approx 0.68118$, corresponds to a stationary state of the HMF model. We can go on and add more tori and put different weights on them to construct stationary states and so consider also deconfining tori. Note that we shall not discuss here the stability of these stationary states[2], but these features may certainly prove to be fruitful and give some explanations on possible stabilizing/destabilizing mechanisms. In fact, it has been demonstrated in [23–25] that a necessary (and sufficient) condition for these stationary states to give rise to quasi-stationarity in the finite-N dynamics is that they are *linearly stable*. More precisely, the stationary state described before corresponds to Vlasov equilibria. The analysis of linear stability of this Vlasov equation may reveal which stationary states will generate quasi-stationarity, and action-angle approaches has proved particularly useful in this context [26, 27].

We shall now move on to what happens when considering only a finite number of particles.

2.1.4 Dynamics of the HMF with a Finite Number of Particles

We have shown before that for any stationary state (including equilibrium), the microscopic dynamics of the particles becomes regular. This behavior is somewhat counterintuitive regarding statistical equilibrium. Indeed, in the microcanonical ensemble statistical equilibrium corresponds to a maximal entropy state and in this sense to a maximal disordered state, and it is difficult to imagine such a state being created by regular motion (nonlinear shear may help though). In order to see effectively we shall first consider the dynamics of a finite number of particles which are close to the equilibrium state given by Eq. (3).

[2] Note that even if one accounts for the linear stability criteria, there are still large sets of distributions which shall generate quasi-stationary dynamics.

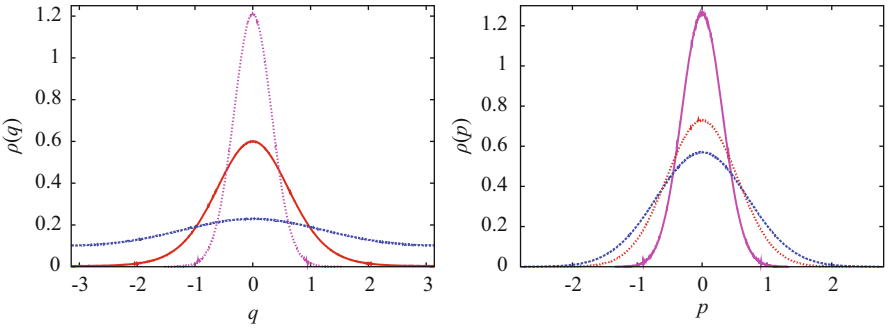

Fig. 3 Equilibrium distribution of q (*top*) and p (*bottom*) obtained from the construction. Histograms are built using 4×10^6 particles and 1000 bins. The different lines from highest maximum to smallest correspond respectively to $T = 0.1$, $T = 0.3$, $T = 0.49$

To build a finite particle number distribution as close as possible to equilibrium we proceed as follows. We consider the equilibrium stationary one particle distribution function and fix the temperature T. We solve the implicit Eq. (4) to get the magnetization M. Then we consider the action-angle coordinates of the pendulum as new variables.

We have

$$\tilde{\rho}(I,\theta) = \tilde{\rho}(I) = \frac{1}{2\pi} \frac{\exp(-\beta H(I))}{\int \exp(-\beta H(I'))dI'}. \tag{22}$$

We then renormalize the distribution function $\tilde{\rho}$ to N[3] and compute progressively its definite integral

$$Z(I) = N \int_0^I \tilde{\rho}(J)dJ, \tag{23}$$

and place a particle (I_k, θ_k) for each $Z(I_k) = k$, where $k \in \{1, \ldots, N\}$ and $\theta_k = \theta_{k-1} + \alpha$, with α incommensurate with π to insure proper uniform sampling (we chose $\alpha = 0.3$ and $\theta_0 = 0$). We then get back in the (p,q) space. The resulting integrated distribution $\rho(q) = \int \rho(p,q)dp$ and $\rho(p) = \int \rho(p,q)dq$, computed using $N = 4 \times 10^6$ and 1000 bins, are displayed in Fig. 3. In fact since we know analytically $\rho(q)$ and $\rho(p)$, we check the accuracy of our computation by measuring the error as $\int |\rho - \rho_{analytic}|$, and for the cases portrayed in Fig. 3, we find that the error oscillate between 0.13 % and 0.3 %, in good agreement with the estimated $1/\sqrt{N}$ error.

We now check the fact that finite size dynamics are "stationary" and we have indeed fluctuations of the magnetization which decrease as $1/\sqrt{N}$ with system size,

[3] Actually due to numerical error we renormalize to $(N + \sqrt{N}/4)\tilde{\rho}$, which is in range with expected typical fluctuations.

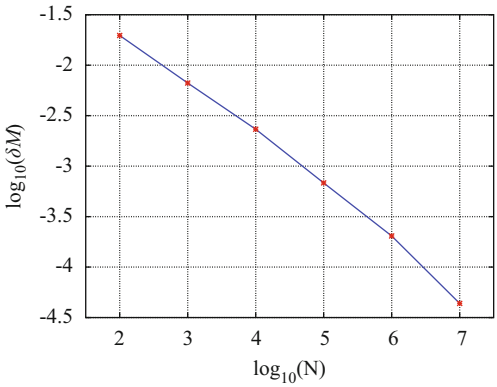

Fig. 4 Standard deviation δM of magnetization fluctuation versus system size for close to equilibrium initial conditions with temperature $T = 0.3$. Simulations are performed up to time $t = 250$, with time step $\delta t = 10^{-2}$ using fifth-order symplectic scheme [28]. Algebraic decay is observed over four decades with a characteristic exponent measured as $\sim 1/2$

giving rise to the integrable dynamics. For this purpose we monitored the evolution of the magnetization for an initial distribution computed with $T = 0.3$ and follows the magnetization of finite N samples versus time by computing the individual trajectories using a fifth order symplectic scheme [28] starting from the equilibrium initial condition obtained for different system sizes. Regarding the initial conditions chosen, we actually computed an initial condition as described earlier with a number of particles $N_1 \gg N$, and we randomly picked N particles from this sample. Results are presented in Fig. 4 and show that the amplitude of fluctuations of M decrease with system size as $1/\sqrt{N}$ as expected. The equation of motions (8) become the equation of an integrable pendulum. This is confirmed by looking at finite samples of trajectories of the system, where the increase of regularity with N appears (see Figs. 5 and 6).

Due to these last results, we decided to investigate the behavior of the Lyapunov exponent for finite N and for initial conditions which are as close as possible as the canonical statistical equilibrium one. Indeed, since the $N \to \infty$ results in an integrable description, this limit may be singular, since earlier studies have suggested that the Lyapunov may actually not vanish in the thermodynamic limit [29, 30]. However, this $N \to \infty$ limit may be singular regarding regularity, and from the dynamical perspective one can imagine the increase of dimensionality of the phase space $d \sim N$, may overcome the decrease of fluctuations observed in M and φ, leaving some space to Hamiltonian chaos and/or Arnold diffusion to develop. In order to check the previous assumptions we decided to compute numerically the Lyapunov exponent arising from finite N dynamics in the HMF-model. Initial conditions are tailored as described previously, meaning that the initial distribution is close to the canonical one-particle equilibrium distribution. A range of temperatures below the critical one ($T_c = 1/2$) is explored, as well as the number of particles is varied from $N = 10^3$ to for some cases $N = 10^7$.

The Lyapunov exponent is computed using the standard method (see [31]), and dynamics are integrated using the leap-frog symplectic scheme[4]. The first scan of

[4] A comparison with higher scheme has been made and gave identical results.

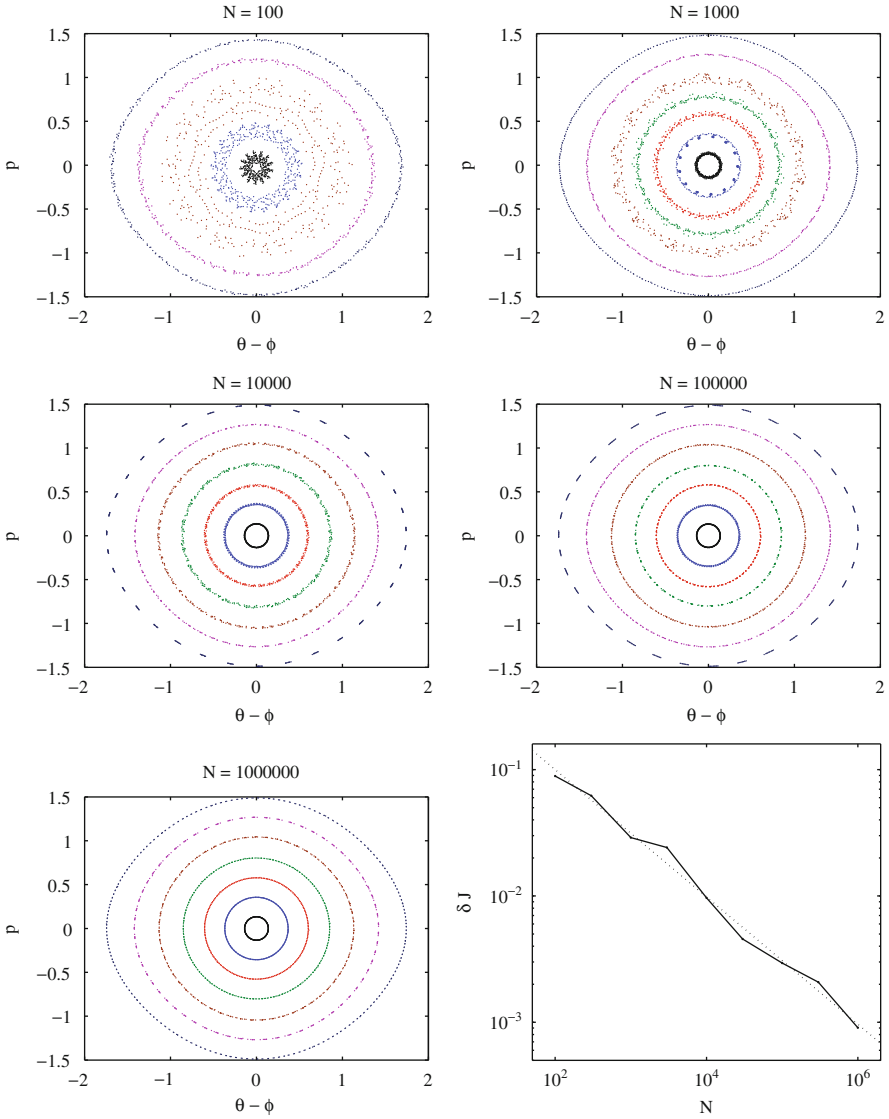

Fig. 5 Samples individual trajectories for different system sizes. Trajectories are computed up to time $t = 1000$ and points are recorded every $\delta t = 2.5$. The initial condition is chosen to be a close to equilibrium configuration with $T = 0.1$ and corresponds to a magnetization $M \approx 0.9$. We notice that contrary to the data displayed in Fig. 5, we have both librating and rotating trajectories. We can notice as well that the trajectories are a little more noisy (note that M is smaller). A clear trend toward regularity is observed. The numerical integration uses the fifth-order optimal symplectic integrator [28] and a time step $\delta t = 0.05$. The width (fluctuations) of a given torus action gives and confirms this trend as a power-law decay close to $1/2$ is observed

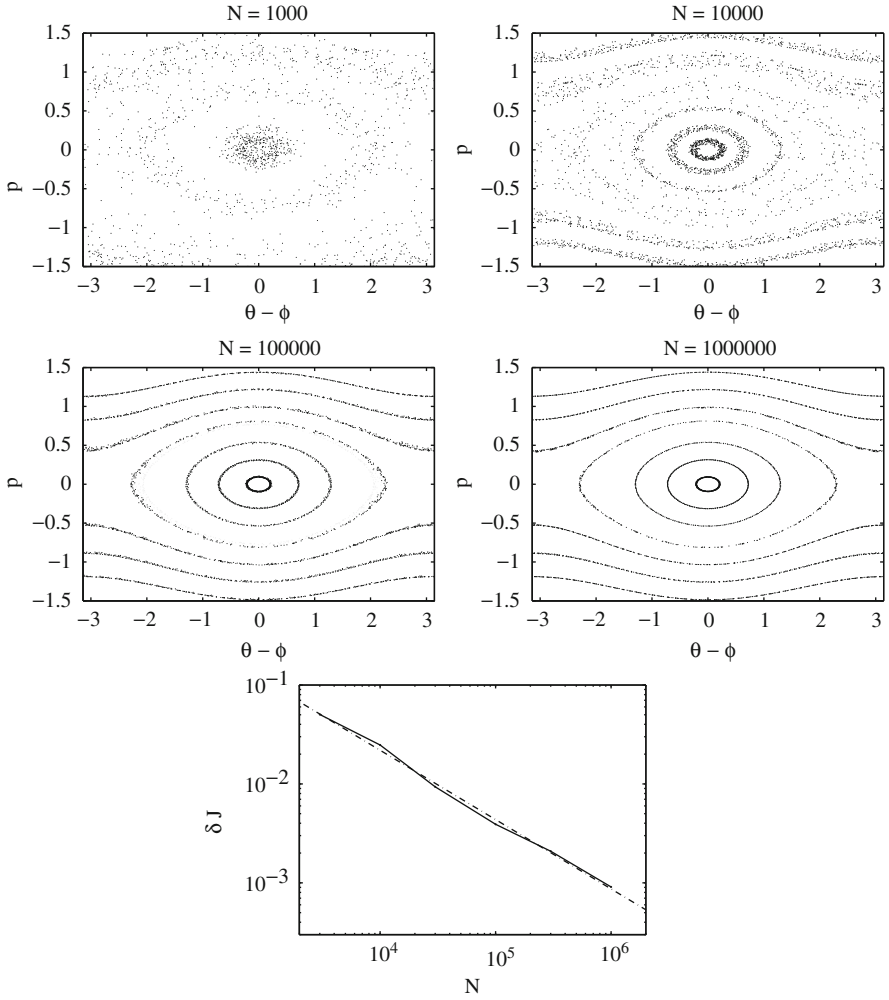

Fig. 6 Same as Fig. 5 but with with $T = 0.49$ and $M \approx 0.19866$. We notice that contrary to the data displayed in Fig. 5, we have both librating and rotating trajectories. We can notice as well that the trajectories are a little more noisy (note that M is smaller)

results is shown in Table 1, where the exponents have been computed using a time step $\delta t = 0.05$ and a total time $t = 2.5 \times 10^4$. Typically one can notice two types of behavior, a decreasing Lyapunov exponent for temperatures below $T < 0.1$ and above $T > 0.4$ and a stable nonzero exponent for $0.1 < T < 0.4$. Scaling laws versus system size are displayed in Fig. 7 for both the decaying regimes. Typically one finds an algebraic decay of the Lyapunov exponent versus system size, indicating a zero Lyapunov exponent in the $N \to \infty$ limit, like what was observed in the nonmagnetized phase above the critical temperature. Moreover, the scaling exponent

Table 1 Lyapunov exponent versus system size for different temperatures. A decay is observed for $T \leq 0.1$ and $T \geq 0.4$ (see Fig. 7)

$N \backslash T$	0.1	0.2	0.3	0.4	0.49
10^3	5.4×10^{-3}	2.2×10^{-2}	0.09	0.17	0.178
10^4	3×10^{-3}	2.4×10^{-2}	0.11	0.15	0.145
10^5	1.5×10^{-3}	2.4×10^{-2}	0.11	0.135	0.126
10^6	8.3×10^{-4}	4.4×10^{-2}	0.10	0.125	0.111
10^7	3.32×10^{-4}	7.1×10^{-2}			0.10

in the regime of low temperatures displays an exponent close to $1/3$, which was as well observed and explained in the high temperature phase.

Regarding the intermediate regime of $0.1 < T < 0.4$, results displaying a stable or growing Lyapunov are somewhat surprising as nothing special happens in this range of temperature regarding thermodynamic properties, and one thus does not expect a different behavior of the Lyapunov exponent. A possible explanation can be inferred when one looks at the distributions displayed in Fig. 3. Indeed, it appears that for this range of temperature few particles are located near the pendulum separatrix. Since equilibrium solutions correspond to a collection of pendulum tori, each being populated according to its ergodic measure [11] we may expect that the finite N sampling is not accurate in this region, leading to hyperbolic dynamics and a nonvanishing Lyapunov exponent. However, if this phenomenon is true, it means that the $\sim N^{-1/3}$ decay observed at small temperature is an artifact of finite N sampling as well, since for the range of N considered no particles are located nearby the separatrix.

In order to check this scenario, we considered as initial conditions a truncated distribution; meaning that we considered initial conditions whose action I_k was less than 99 % of the separatrix value $I_s = 8\sqrt{M}/\pi$. Results for an initial distribution computed at $T = 0.3$ are displayed in Table 2. A drastic reduction of the Lyapunov

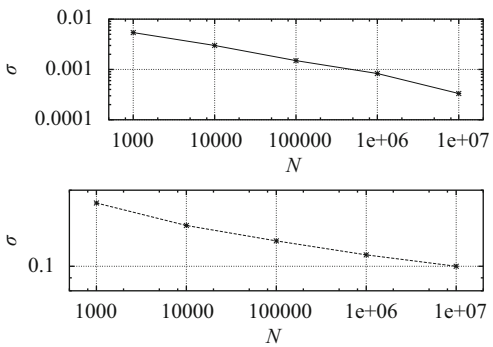

Fig. 7 Maximum Lyapunov exponent σ_N versus system size for initial conditions computed using (22) for temperatures $T = 0.1$ (*upper plot*) and $T = 0.49$ (*lower plot*) . Algebraic decay is observed with a characteristic exponent measured respectively as $\alpha = 0.28$ and $\alpha = 0.06$. Simulations are performed using a leap-frog integration scheme with $\delta t = 0.05$ and are computed up to $t = 2.5 \times 10^4$

Table 2 Lyapunov exponent vs. system size for $T = 0.3$ and a truncated distribution $I < 0.99 * I_s$. A drastic decrease of value of the exponent is observed when comparing to Table 1, first a decay of the exponent versus system size is observed than a stabilization, fluctuations of δM stabilize as well, indicating global oscillations due to the truncation

N	10^3	10^4	10^5
σ	0.0125	7×10^{-3}	7×10^{-3}
δM	5.1×10^{-3}	4.0×10^{-3}	3.9×10^{-3}

exponent is observed, giving a strong indication that it is indeed the particles located near the separatrix which contribute to the Lyapunov exponent. However after a decrease with size, one observes a stabilization of the exponent. Analysis of the behavior of magnetic fluctuations (Table 2) reveals the fact that the truncated distribution is not a stationary solution and a stabilization of the magnetic fluctuations is observed as well, explaining thus the stabilization of the Lyapunov exponent. Note that this stabilization was not observed for initial conditions computed with $T = 0.2$ and a $\sim N^{-1/3}$ was recovered, however we may expect as well a stabilization of the Lyapunov exponent and magnetic fluctuations for larger values of N.

Given the way the initial condition is constructed we can estimate the minimal number of particles N_c needed for at least one to be above the separatrix, as $N_c \approx \left(\frac{1}{4\int_{I_S}^{\infty} \rho(I) dI}\right)^2$. In the light of the results presented in Table 1, the important role of particles located near the separatrix is confirmed. Indeed one can see that for $T = 0.2$ there is a jump in the Lyapunov exponent between $N = 10^5$ and 10^6 which is confirmed by the estimated value of $N_c \approx 9 \times 10^5$. Moreover, for the initial conditions used for the computation of Lyapunov exponents have been prepared using 10^6 particles, from which N particles have been randomly picked. This can also explain why the Lyapunov is more or less stable even for smaller values of N for $T = 0.2$.

From the presented results a scenario emerges from which we speculate (conjecture) that, for all the range of temperature below the critical one and for those which are considered close to initial equilibrium conditions the Lyapunov exponent decays to zero as the number of particles N goes to infinity. We base this speculation on the fact that numerical evidence is found for temperatures above $T = 0.4$, and that from a dynamical point of view the equilibrium solutions are more or less identical besides a change of the values of M and T, that moreover from a statistical physics perspective nothing is really different for $T < 0.4$, and $0.4 < T < T_c$, and finally it is consistent with the fact that stationary solutions in the $N \to \infty$ limit can be mapped to an integrable system of uncoupled pendulum.

For small temperatures $T < 0.2$, we have observed an algebraic decay with an exponent close to $1/3$. However, the calculations of the minimal number of particles N_c for one to be near the separatrix reveals that in this range of temperature, the number of particles needed is beyond our computing power. Finally, in the intermediate range $0.2 < T < 0.4$, we observe a stabilization of the Lyapunov exponent. Looking at the distribution displayed in Fig. 3, we conclude that for this

range of temperatures, we also have a problem of N being too small and not being able to correctly sample the local ergodic measure and anticipate that we should have access to larger values of N and also we will observe a decay of the Lyapunov exponent like for $T > 0.4$. In the same spirit in the low temperature regime, we expect that as N increases, we shall reach the N_c range eventually, which will lead to some stabilization of the Lyapunov exponent like in the intermediate regime, but should we continue to increase N, we will also eventually observe again a decay like for $T > 0.4$. Note though that N_c diverges as $T \to 0$. Last, a Fourier analysis of the time series of the magnetization shows a main peak centered around the natural frequency of the pendulum $\omega_0 = \sqrt{\bar{M}}$, where $\bar{M}$ denotes the time average (equilibrium value) of the magnetization, given the equations of motion (7), we can reasonablly expect that particles trajectories should be similar to those governed by a one and a half degree of freedom Hamiltonian of the perturbed pendulum

$$H = \frac{p^2}{2} - \bar{M}\cos q + \epsilon(N)\cos(q - \omega_0 t + \varphi), \tag{24}$$

with $\epsilon(N) \sim N^{-1/2}$ and φ some constant phase. The behavior of Lyapunov exponent $\lambda(\epsilon)$ of particles residing in the stochastic layer as well as the width $\delta(\epsilon)$ of the layer, with constant ω_0 and $\epsilon \to 0$ had been analyzed in [32]. They found a scaling of the type $\lambda(\epsilon) \sim \epsilon^{1/6}$ and $\delta(\epsilon) \sim \epsilon^{3/4}$, which translates into $\lambda \sim N^{-1/12}$ and $\delta \sim N^{-3/8}$. Since for the HMF we are computing the global Lyapunov exponent, we can assume that only the particles trapped in the stochastic layer contribute to the exponent, which represents a number of particles scaling as some power law of N since the width scales as well as a power law. Now expecting that all trapped particles have a similar contribution to the global Lyapunov exponent we expect a scaling $\sigma(N) \sim \frac{1}{N^{1/12}}$, in relative good agreement with the results depicted in Fig. 7 as $1/12 \approx 0.08$.[5]

Finally, in order to explain the contradiction with earlier result we question the role of the initial condition, and consider what happens when we consider an initial condition with Gaussian distribution in p and q's.

Results for an initial condition with zero mean is displayed in Fig. 8. In the low energy regions, one recovers the same values of the Lyapunov exponent and the algebraic decay with exponent $\sim 1/3$. However, for temperatures closer to the critical region, we can measure different values of the finite time Lyapunov exponent which are orders of magnitude higher and do not display a decay with time. We may explain this by the fact that actually, no decay of fluctuation is observed (Table 3). When looking at the behavior of the magnetization versus time in Fig. 8, one can notice for a short time a similar behavior although on a different scale as the one observed when starting without the initial equilibrium conditions such as a waterbag, namely the "violent relaxation" described in [10], while no particular behavior is observed for the close-to-equilibrium one. Hence, it is likely that the system relaxes to a QSS,

[5] Note that $1/\log(N)$ scalings are also good, and can be explained by the fact that the typical time scale in the separatrix can be estimated from the period of regular motion of the last regular trajectory $T \sim \log(\delta E) \sim \log(\delta M) \sim \log(N)$.

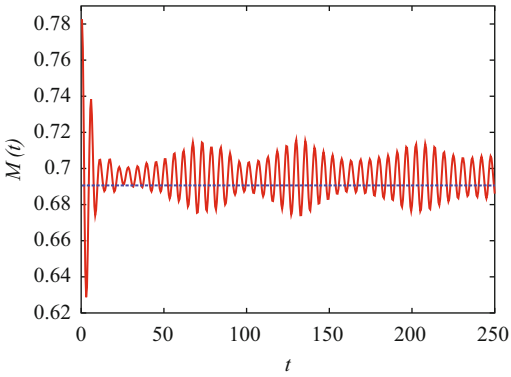

Fig. 8 Magnetization as a function of time for two different initial conditions and a density of energy $\varepsilon = 0.44$ corresponding to a temperature $T = 0.353$. The *red line* corresponds to Gaussian initial conditions in p and q's, while the *blue one* corresponds to a close to canonical equilibrium one. Simulations are run using $N = 10^6$ particles with a time step $\delta t = 0.05$

Table 3 Fluctuations of the magnetization versus system size for Gaussian initial conditions and close to equilibrium ones with density of energy corresponding to a temperature of $T = 0.353$. The behavior vs. N is totally different and the values are of higher magnitude orders. Comparison for fluctuations can be made looking at the results displayed in Fig. 8. The simulations are run with the same parameters and total time $t = 2000$, fluctuations are computed using the second half of the total trajectory

N	10^3	10^4	10^5	10^6
δM_{gauss}	9.8×10^{-3}	4.3×10^{-3}	7.0×10^{-3}	8.3×10^{-3}
δM	8.5×10^{-3}	2.6×10^{-3}	7.7×10^{-4}	8.5×10^{-5}

explaining thus the difference in numerically computed Lyapunov exponents. By tailoring an initial condition very close to the canonical equilibrium distribution, we "fast-forward" in time and circumvent the slow relaxation of the QSS to equilibrium, and obtain different scaling results for the finite time Lyapunov exponent. Since the presented Lyapunov results are numerical, and due to the fact that in the $N = \infty$ limit the dynamics displays multiple ergodic measures, it is difficult to conclude whether the scaling is universal for any initial condition and remains as it is, or should we have performed longer more accurate simulations and/or considered larger sizes.

2.2 Beyond the HMF Model

The results discussed up to now have been obtained in the framework of a mean field system. Discussion regarding the decrease of the interaction with distance as well as the underlying topology is then unclear. The actual distance between particles does not explicitly appear in the HMF potential and since it is a mean field, it is possible

to claim that the observed phase transition is just a trace of a higher embedded dimension; it can be considered very large and a Kosterlitz phase transition for the $XY-$model is already observed on a lattice with close neighbors and a second-order one when we move to three dimensions. It is then important to alleviate the previous potential objections in our findings and consider a more realistic one-dimensional model with long-range couplings.

2.2.1 The $\alpha-$HMF Model

For this purpose, we now focus on the $\alpha-$HMF model [33]. In its long-range version ($\alpha < 1$ as discussed below), this model behaves at equilibrium as the HMF, see for instance [8, 34–36]. We may then ask if the same correspondence applies to the out of equilibrium dynamics. QSSs exist as depicted in [37], but is there still an asymptotic trend toward regularity? How does the spatial organization impact on these features? It was also shown recently that fractional calculus may be a crucial ingredient when dealing with long-range systems [38, 39], and we shall see how this point enters the picture in the considered case.

Let us start by introducing the governing Hamiltonian which can be cast in the form:

$$H = \sum_{i=1}^{N} \left[\frac{p_i^2}{2} + \frac{1}{2\tilde{N}} \sum_{j \neq i}^{N} \frac{1 - \cos\left(q_i - q_j\right)}{\|i - j\|^{\alpha}} \right], \tag{25}$$

where q_i stands for the orientation of the rotor occupying the lattice position i, while p_i labels the conjugate momentum. The quantity $\|i-j\|$ denotes the shortest distance on the circle of perimeter $N-1$, where we have placed our rotators in order to have an isolated system with periodic boundary conditions. The coupling constant between classical rotators decays as a power law of the sites distance. The HMF limit is recovered for $\alpha = 0$. In this context we have also to rescale the potential according to Kac's prescription, it is easy to note that for N even, we have

$$\tilde{N} = \left(\frac{2}{N}\right)^{\alpha} + 2 \sum_{i=1}^{N/2-1} \frac{1}{i^{\alpha}} \tag{26}$$

which guarantees extensiveness of the system (it is mostly useful in the long-range case for $\alpha \leq 1$, but allows as well for comparison when $\alpha > 1$). The equation of motions of element i are derived from the above Hamiltonian and can be written as follows

$$\dot{p}_i = -\sin\left(q_i\right) C_i + \cos\left(q_i\right) S_i = M_i \sin\left(q_i - \varphi_i\right) \tag{27}$$

$$\dot{q}_i = p_i \tag{28}$$

where use has been made of the following global quantities:

$$C_i = \frac{1}{\tilde{N}} \sum_{j \neq i} \frac{\cos q_j}{\|i - j\|^{\alpha}} \tag{29}$$

$$S_i = \frac{1}{\tilde{N}} \sum_{j \neq i} \frac{\sin q_j}{\|i - j\|^{\alpha}}. \tag{30}$$

These identify the two components of what we shall refer to as a local magnetization, whose norm is $M_i = \sqrt{C_i^2 + S_i^2}$, and define a phase $\varphi_i = \arctan(S_i/C_i)$. When doing so, Eq. (27) brings a formal analogy with the HMF setting (Eq. 7). And thus, we notice that each individual $\alpha-$HMF particle obeys a dynamical equation which closely resembles that of a pendulum. This observation represented the starting point of our previous discussions, where stationary states were constructed from the first principles. However, in the present $\alpha-$HMF, due to site localization of the magnetization, this approach is not as straightforward. Anyway, let us first make some preliminary rearrangements in order to overcome this difficulty. First, let us introduce a continuous limit. We can notice that, for large N, and assuming $0 < \alpha < 1$, we have

$$\tilde{N} \approx \frac{2}{1-\alpha}(N/2)^{1-\alpha}. \tag{31}$$

We can then use expression (31) in Eq. (29) and, as $N \to \infty$, introduce the continuous variables $x = i/N$ and $y = j/N$ defined now on a circle of perimeter 1, and after some simple algebra obtain the following Riemann integral

$$C(x) = \frac{1-\alpha}{2^{\alpha}} \oint \frac{\cos(q(y))}{\|x - y\|^{\alpha}} dy, \tag{32}$$

where $\|x - y\|$ represents the minimal distance on a circle of perimeter one. A similar expression can be found for $S(x)$.

In the expression (32) we recognize one of the definitions of a fractional integral $I^{1-\alpha}$ and consequently write

$$C(x) = \frac{1-\alpha}{2^{\alpha}} \Gamma(1-\alpha) I^{1-\alpha}(\cos q(x)). \tag{33}$$

As mentioned, we notice that fractional calculus is indeed a pertinent tool when investigating the dynamics of long-range systems [38, 39].

In this setting of $N = \infty$, the study of the $\alpha-$HMF dynamics corresponds to understanding the evolution of the scalar fields $q(x,t)$ and $p(x,t)$ defined on a circle and which are ruled by the fractional (nonlocal) partial differential equations

$$\frac{\partial q}{\partial t} = p(x,t) \tag{34}$$

$$\frac{\partial p}{\partial t} = \frac{\mu}{2^{\alpha}} \Gamma(\mu) \left(-\sin(q) I^{\mu}(\cos q) + \cos(q) I^{\mu}(\sin q)\right) \tag{35}$$

where $\mu = 1 - \alpha$.

In contrast to the HMF ($\alpha = 0$) model, the spatial organization $q(x)$ matters within the general setting $\alpha > 0$. In order to recover the previous setting, a simple

requirement is to have $C(x) = \langle C \rangle = M$, while imposing as well $I^{\mu}(\sin q) = 0$. This observation is also compatible with the translation invariance along the original lattice, which from the statistical perspective is also likely to lead to such a state [35].

In the infinite N limit, and given Eq. (33), the requirement writes:

$$\frac{dC(x)}{dx} = \mathcal{D}^{\alpha} \cos q = \frac{d^{\alpha} \cos q}{dx^{\alpha}} = 0 \tag{36}$$

where the operator $\mathcal{D}^{\alpha}$ stands for the fractional derivative. Trivial states ($q_i = Cte$) are solutions of this equation as well as for finite N. However, this infinite size limit enables us to compute different solutions. Indeed since $\alpha < 1$, the integral $\int 1/\|x\|^{\alpha} dx$ is defined near 0 and since the function $1/\|x - y\|^{\alpha}$ is smooth, we may cut the integral in Eq. (32) into L pieces

$$C(x) = \frac{1-\alpha}{2^{\alpha}} \sum_{k=0}^{L-1} \int_{k/L}^{(k+1)/L} \frac{\cos q(y)}{\|x - y\|^{\alpha}} \, dy.$$

Now using the regularity of $1/\|x - y\|^{\alpha}$, we formally assume we can extract it from the integral:

$$C(x) \approx \frac{1-\alpha}{2^{\alpha}} \sum_{k=0}^{L-1} \frac{1}{\|x - y_k\|^{\alpha}} \int_{k/L}^{(k+1)/L} \cos q(y) \, dy,$$

with $y_k \in [k/L,(k+1)/L]$[6].

Once this is done the procedure is quite straightforward, meaning that if values of likely a completely discontinuous function $q(x)$ are such so that in any small interval the average of $\cos q(x)$ is constant and equal to the magnetization of the system, meaning a function such that for any k and L

$$\int_{k/L}^{(k+1)/L} \frac{\cos q(y)}{\|x - y\|^{\alpha}} \, dy = Cte = M,$$

we shall have a solution of Eq. (33) and a configuration $q(x)$ which gives $C(x) = M$, a constant function on the circle. In some way, this procedure implies a peculiar spatial organization which returns a constant coarse grained image of the function $\cos q$, equal in turn to M a process reminiscent of homogenization techniques.

The last condition to fully recover the results of the HMF is stationarity, but in some way the work has already been done, indeed we have access to the available stationary distributions of the HMF. Thus, given one of these distributions we can pick up q and p values that have to be placed on the circle as originating from this distribution. If this is the case, the time evolution (Eqs. 34 and 35), can only consist of a local reshuffling on the circle of the actual phase space coordinates. And, since the values are corresponding to a stationary distribution, the reshuffling does not

[6] This approximation can be rigorously justified via a detailed expansion see [36] for details.

change the averaged coarse grained value. We hence obtain a family of stationary solutions of the α-HMF model.

Let us remark that actually, many distinct stationary distributions of the HMF model give identical values of M. It should then be possible to place or mix different distributions in distinct regions of space. In this sense a stationary distribution of the α-HMF model can correspond to either a single stationary distribution of the HMF model which would be set in some spatially scale free form on the circle, or to a collection of such distributions all with the same magnetization and placed in a scale free form in different regions of the circle.

These stationary states for the $\alpha-$HMF model because of their construction, display as well some self-organized regularity and individual dynamics of the particles correspond to pendulum motion. This phenomenon is conditioned by a locally scale free spatial organization. The functions $q(x,t)$ and $p(x,t)$ are thus "very complicated" along the spatial direction, while displaying a regular time evolution and no chaos. In this sense, the systems prefers to have a regular evolution at the price of spatial disorder. This phenomenon should prove to be very interesting to study using the tools of space-time complexity such as the one mentioned in [40] and references therein.

In order to validate this result we consider a finite size sample on the original lattice and see how the regularity emerges. For this purpose we consider the stationary state of the HMF consisting of just one torus with associated magnetization $M = 0.5$ already mentioned earlier. In pendulum action-angle variable we refer hence to a one-particle distribution of the type $f(I,\theta) = \delta(I - I_0)/2\pi$. In order to mimic the spatial disorder that are specific to the stationary state of the α-HMF model, we randomly place on the lattice values of $(p_i,\ q_i)$ picked from the analytically accessible, distribution: in action-angle coordinates, we assign one action and uniformly distribute the angles. The analysis for different values system size N for $\alpha = 0.25$ is by monitoring the distribution actions after a fixed amount of time. Results are displayed in Fig. 9 and show as expected a trend toward the stabilization of such a state as N increases.

It is shown that increasing the value of α, which weakens the coupling strength, implies a more pronounced destabilization of the state, which can be effectively opposed by increasing N. The solutions here constructed are hence stable versus the α-HMF dynamics, provided the continuum limit is being performed and so represent an analytical verification of the existence of stationary states, beyond the original HMF setting.

We have up to now focused our attention on stationary state. Let us now in turn look at the dynamics starting from a given initial condition.

3 Self-Organized Regularity

As mentioned in the introduction and illustrated previously, systems with long-range interactions display peculiar features regarding their dynamics. One of its striking feature, is that starting from a given initial condition the systems undergoes a

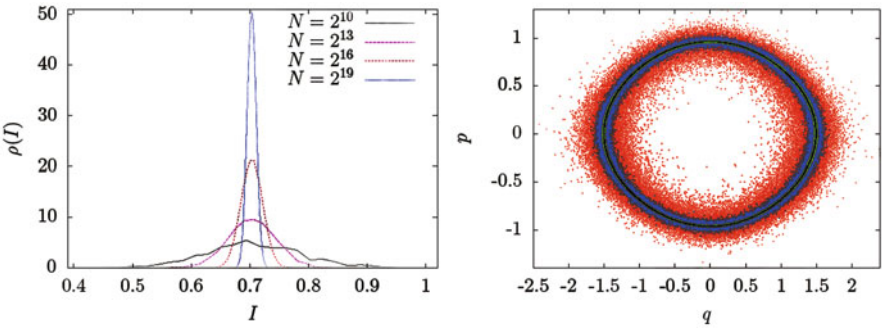

Fig. 9 QSS for the α-HMF model built using a stationary solution of the HMF model corresponding to a one particle PDF of the type $f(I,\theta) = \delta(I - I_0)/2\pi$ (one torus $M = 0.5$). *Top*: The system is evolved via the α-HMF dynamics with $\alpha = 0.25$. The figure displays the resulting distribution of actions I at $t = 200$, for different sizes. *Bottom*: A simple superposition of snapshots relative to different values of α and at final time $t = 200$, with $N = 2^{19}$. $\alpha = 0.75, \alpha = 0.5, \alpha = 0.25$, $\alpha = 0$, correspond respectively to the colors *red*, *blue green and black*. Clearly the thickness of the rings get reduced as $\alpha \to 0$, i.e., when the α-HMF model tends toward its corresponding HMF limit. The integration for both figures uses the fifth order optimal symplectic integrator [28] and a time step $\delta t = 0.05$

so-called violent relaxation toward a QSS, and then displays a slow relaxation toward equilibrium, which actually diverge with the number of constituents (reminiscent of what has been observed in the dynamics of finite samples of steady states). In the previous section, we devoted our study to the dynamics of stationary states, but actually the notion of QSS encompass a wider notion, and time-dependent steady states or quasi-periodic ones are possible [8, 9, 12]. In what follows we shall give some evidence of regularity in all these states at least in certain regions of phase space.

3.1 The HMF Model

We start with the HMF model. In order to study out-of-equilibrium states (stable QSSs in some sense), it is convenient to start with waterbag initial conditions. A waterbag consists of a two-level (0 and some constant) one particle density function $f(p,q)$. Since the violent relaxation has been shown is some cases to be "collisionless," the evolution of f is governed with good approximation by the Vlasov equation, which translates the "advection" in the reduced phase space of the values of f. Choosing a two-level function insures that whatever the initial distribution, the values of f will remain constant and just move in the (p,q) plane. It is this remark that led Lynden-Bell to its classical fermion-like statistical formalism [10] which was used with success for the HMF in predicting out of equilibrium phase transitions when initial conditions are waterbags in [9, 41].

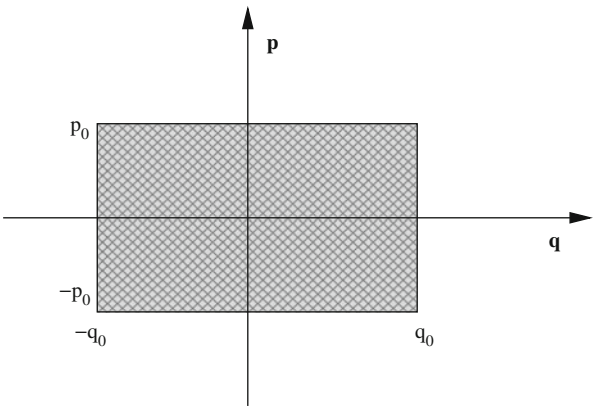

Fig. 10 Visualization of a waterbag initial condition

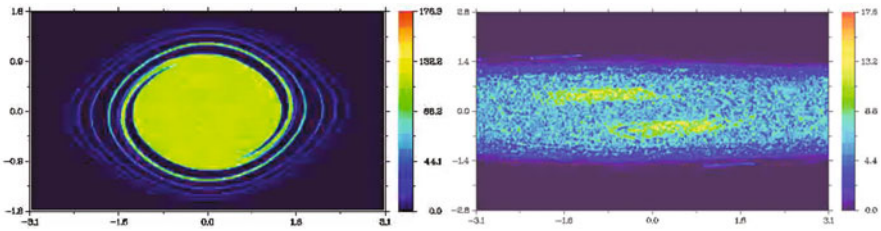

Fig. 11 Possible outcomes starting from a waterbag. *Left*: a magnetized mono-cluster. *Right*: a bi-cluster displaying some weak time average magnetization. Initial conditions are sampled from an initial waterbag (Fig. 10) with $N = 10^5$ particles. Simulations are run up to $t = 1000$ with a time step $\delta t = 0.05$

We shall take the same initial conditions, namely a waterbag which corresponds to a rectangular region in phase space: $f(p,q) = Cte$ if $|p| \leq p_0$ and $|q| \leq q_0$ and zero elsewhere.

This waterbag is convenient as it allows to consider two parameters, namely the initial magnetization

$$M_0 = \sin q_0/q_0 \tag{37}$$

and the density of energy energy

$$\varepsilon = p_0^2/6 + (1 - M_0^2)/2 \tag{38}$$

to characterize it uniquely, keeping in mind that the waterbag is defined on $[-q_0, q_0] \times [-p_0, p_0]$.

As mentioned after a short transient, a QSS sets in. This phenomenon is depicted in Fig. 11 giving rise to two different QSS's with drastically different time averaged magnetizations, and it illustrates an out of equilibrium phase transitions. These states have been analyzed and studied in [9] and have been shown to correspond to specific solutions of the associated Vlasov equation using the Lynden-Bell formalism. In

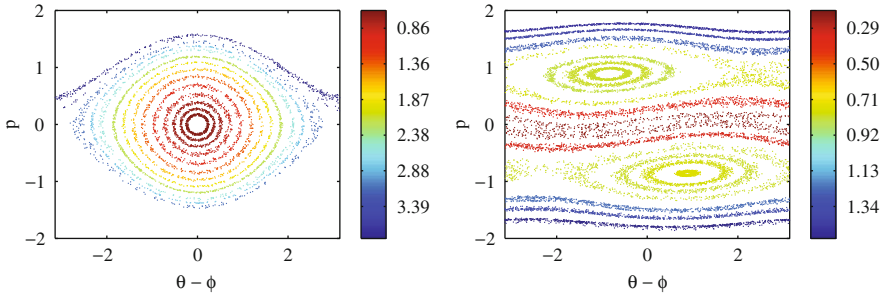

Fig. 12 Poincaré section of the HMF model for configurations below transition $((M0, U) = (0.6, 0.54))$ and above transition $(M0, U) = (0.6, 0.88)$. Simulations realized for $N = 2 \times 10^5$ particles

order to go beyond the description of the one-particle density distribution function, we decided to investigate the phase space of the $N-$body system by computing adapted Poincaré sections. Indeed, when looking at the behavior of the magnetization versus time, (see for instance Fig. 8) we see that long lasting oscillating fluctuations remain (Fig. 12).

Thus, given the equation of motion (7), and the fact that QSS are long lived, we computed the following sections. We consider the time average $\bar{M}$, and record particle positions $(p_i,\ q_i - \varphi)$ in phase space for $M(t) = \bar{M}$ and $dM/dt > 0$. Results for the HMF model for $N = 2\ 10^5$ are displayed in Fig. 11. As one could have expected from the equation of motions (7), in the magnetized QSS phase with $M \neq 0$ the Poincaré section shows a pendulum like phase portrait. The so-called mono-cluster QSS appears to map itself to a collection of pendula. Tori are however like for the equilibrium situations, no thin line and display some dispersion. What is more peculiar is that in the $M \approx 0^+$ regime corresponding to a bi-cluster state in the QSS terminology, the Poincaré section displays as well a phase portrait reminiscent of an integrable one-dimensional Hamiltonian. One possible way to understand the phenomena is to recall that Hamiltonian (1) is invariant by translation. Hence, one can foresee a system with two contra-propagating magnetized phases, which if the resonances are far enough should not interact much.

Finally, we shall discuss the phenomenon of selforganized regularity. In this perspective let us recall the Poincaré section of the bi-cluster state, which displays a system with two resonances. According to the empirical Chirikov criterion, one may expect chaos if these resonance overlap. Let us now suppose that the resonance overlap, the resulting Poincaré section should then display a chaotic sea and islands of regular motion centered on each resonance but with a smaller width. One then recalls the definition of the magnetization, one can expect that only the trapped particles[7] shall contribute to each magnetized cluster. Since chaos reduced the regular region, the magnetization is necessarily smaller and given the equation of motion

[7] Actually only the ones with $\kappa < \kappa_c$.

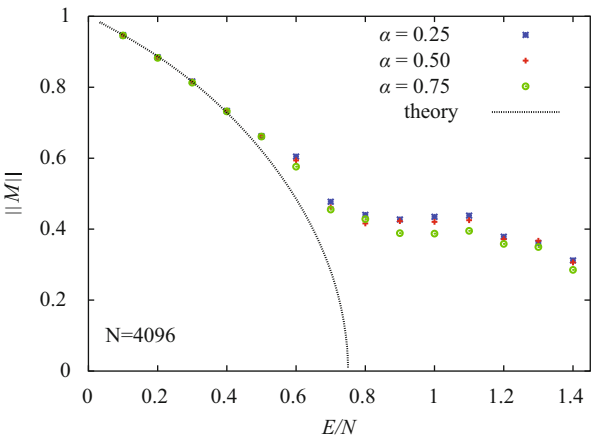

Fig. 13 Magnetization versus energy per particle E/N for different α, for a system made of $N = 4096$ particles. The magnetization values here reported follow from a time average over the window $400 < T < 800$

(7), this implies that the width of the resonance is actually smaller, hence resonances are further apart and the system becomes more regular thus the self-organized into regular microscopic motion at least in some regions of phase space.

3.2 Beyond the Mean Field

In order to discriminate whether or not similar studies can be performed in nonmean field models, we turn back to the $\alpha-$HMF model.

To make this analysis we turn to direct simulations. We initialize the system in $q = 0$ and a Gaussian distribution for the conjugate momenta p [34]. The system state is monitored by estimating the average magnetization amount as a function of the energy, see Fig. 13.

For energies larger than 0.75 one would expect the homogeneous solution to prevail, as dictated by the statistical mechanics calculation. However, the system gets confined into a inhomogeneous state, the residual time averaged, magnetization being large and persistent in time. It is therefore tempting to interpret those states as QSS, and so analyze their associated dynamical features in light of the above conclusions. In particular, we expect the microscopic dynamics to resemble that of a pendulum, bearing some degree of intrinsic regularity. To unravel the phase space characteristics we compute the Poincaré sections, following the recipe in [12, 42] and so visualizing the single particle stroboscopic dynamics, with a rate of acquisition imposed by the self-consistent mean field evolution.

The averages of C_i and S_i refer to the two components of the magnetization per site. The Poincaré sections are drawn by recording the positions p_i and $q_i - \varphi_i$ in phase space each time the equality $M_i = M$ is verified. Results for a specific initial conditions are depicted in Fig. 14, where one hundred trajectories are retained. The phase portrait shares many similarities with that obtained for a simple one and a half

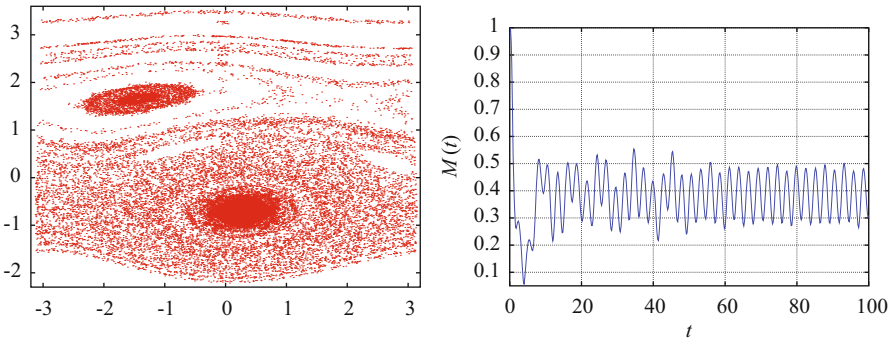

Fig. 14 "Poincaré section" of a QSS for $E/N = 1.2$, $N = 65536$. Initial conditions are Gaussian in p and $q = 0$. The section is computed for $150 < t < 1000$ and $\alpha = 0.25$. In the bottom plot one can see the magnetic fluctuations

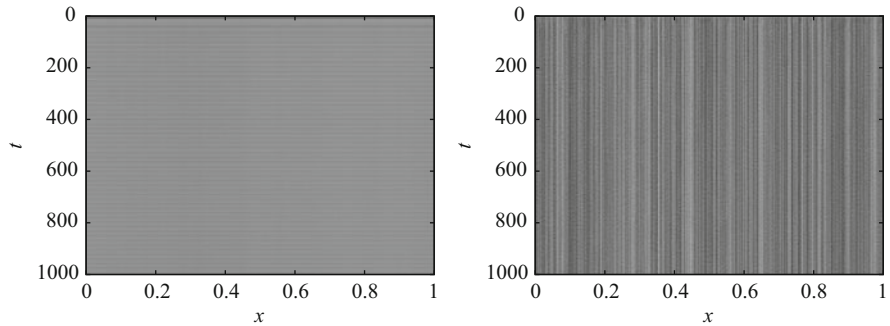

Fig. 15 *Left*: $M(x) = \sqrt{C(x)^2 + S(x)^2}$ as a function of time. *Right*: individual particle's action as a function of time. The system is initialized to get a QSS with $E/N = 1.2$ and $\alpha = 0.25$ (see Fig. 14). Total number of particle is $N = 8192$, $x = i/N$, with $1 \leq i \leq N$. The actions are those of a pendulum corresponding to Eq. (27). $M(x)$ is almost uniform in space, while the individual spatial organization is complex. The time evolution of the actions appears quite regular

degree of freedom Hamiltonian (see for instance [22]), with many resonances and invariant tori. Clearly, and in agreement with the above scenario, a large number of particles exhibit regular dynamics. However as the nature of phase space reveals, these QSSs are steady state of the discrete dynamics, not stationary solutions.

Nevertheless, we set to analyze the spatial organization of the identified steady state to test whether stationary state features are present in this configuration. To this end, we computed the values of the local magnetization $M(x,t) = \sqrt{C(x,t)^2 + S(x,t)^2}$ versus time and estimated an individual action, stemming from a Hamiltonian pendulum, which would give rise to an equation of motion formally identical to the Eq. (27). Results of the analysis are depicted in Fig. 15. One clearly sees that the function $M(x,t)$ is homogeneous and presents a modest dependence on t, thus suggesting that the distribution of $q(x,t)$ is a solution of Eq. (36). The plot

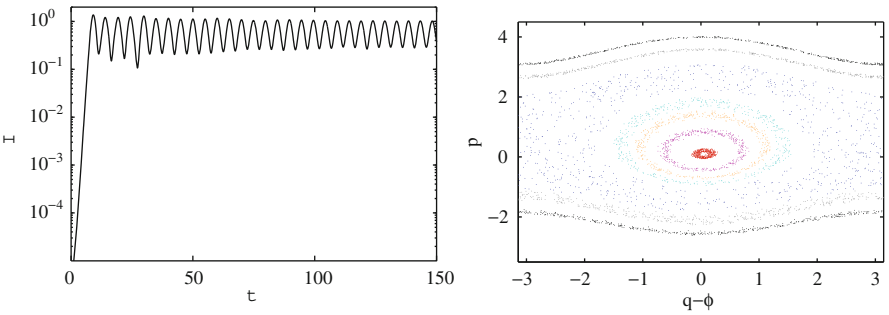

Fig. 16 *Left*: Intensity of the wave versus time. *Right*: Poincaré maps of the particles, once the steady-state oscillating regime has been reached. The system was initiated with random positions for the particles, and a mono-kinetic beam $p_i = \overline{p} = 0$

of action versus time as depicted in Fig. 15, clearly indicates a degree of enhanced spatial complexity, nearby particles not belonging to the same tori. We find in these simulations and in this (N- finite) steady state the same distinctive features of the stationary solutions as depicted earlier. Moreover, we confirm the presence of regions of regular motion in phase space for a QSS arising in this nonmean field situation.

3.2.1 Wave–Particle Interactions

The wave–particle interaction is a very interesting system regarding long-range interactions, since it provides a simple mean field model. Indeed, in its simplest form, one can consider a monochromatic wave interacting with N particles in one dimension. Although it may look like a rough approximation, this approximation is very common to model the dynamics of free electron lasers [43, 44] or of collective atomic recoil lasers [45, 46].

Extensively studied in [16], this wave–particle interaction can be cast in the following Hamiltonian form

$$H_N(\{q_j, p_j\}, \phi, I) = \sum_{j=1}^{N} \frac{p_j^2}{2} + 2\sqrt{\frac{I}{N}} \sum_{j=1}^{N} \cos(q_j - \phi), \tag{39}$$

where q_j is the (normalized) position of the particle, p_j its (normalized) conjugate momentum, I the intensity of the wave, and ϕ its phase. If the dynamics is initiated with $I = 0$, a mono-kinetic beam of particles ($p_j = \overline{p}$) and the particles' position randomly distributed, the wave will typically grow exponentially until it saturates, where it will start oscillating in a quite regular manner (see Fig. 16). As for the particles, the wave amplification relies on their aggregation into a large cluster—the process of "bunching" of the particles (which is actually a trapping by the wave) and of amplification of the wave will develop in a self-consistent way.

Regarding the particles' dynamics, most of them will be trapped by the wave. To confirm this point, we performed Poincaré-like sections, recording the particles' positions in phase space when the wave intensity meets its average value, and this revealed that many particles are actually confined to "tori," although these tori are spoiled by finite-N effects (Fig. 16). However, because of the oscillating behavior of the wave, a chaotic layer has been created around the pendulum separatrix. This behavior is typical of pendula perturbed with a oscillating term, although here this oscillation appeared naturally from the self-consistent interaction.

Thus, if one increases the number of particles coupled to the wave, the particles' trajectories gets more and more regular (not shown here), yet the width of the chaotic sea remains the same. This means that there now exist a set of particles with a strong chaotic behavior, whatever N.

Hence, compared to the HMF and α-HMF model, we observe that the introduction of a new *macroscopic* degree of freedom (the wave) introduced a strong chaotic component to the dynamics. Yet, the oscillations of the wave actually do not destroy all the "tori," in a way similar to the KAM approach which suggests that tori may resist to perturbation of an integrable system.

Let us conclude by mentioning that the infinite-N dynamics of this interaction could be investigated numerically, e.g., using Vlasov codes. This would in particular allow to discriminate the role of finite-N effects and of the wave fluctuations regarding the chaotic nature of this dynamics. Yet, Vlasov codes are themselves limited by the finite grid on which they can be implemented, and one must carefully monitor the possible chaotic effects this grid may induce.

4 Conclusion

To conclude, in this chapter we have studied dynamical properties of Hamiltonian systems with a large number of constituents and interacting through a long-range potential. Conversely, with the more traditional statistical approaches which often assume ergodicity and mixing, we have shown from first principle that stationary states among which thermodynamical equilibrium of paradigm systems implied similar properties as those of a perfect gas, namely regular microscopic trajectories. Beyond mean field approaches the price to pay for this microscopic regularity in time is a complex, self-similar, spatial organization corresponding to the solution of a fractional equation. Hence in this last setting, a possible success of statistical approach lies actually in spatial disorder and not so much on speculated "molecular chaos." When turning to direct numerical investigations, we have identified a series of QSS, which corresponds to steady states, with macroscopic oscillations. Still, such states share many of the features of their stationary counterparts. The importance of these findings are manifold: First, we confirm that QSS do exist in a generalized nonmean field setting [37]. Also, we validate a theoretical method to construct, from first principle, (out of) equilibrium stationary solutions. Finally, and we believe more interestingly and prone to debate, the fact that in long-range

systems stationary states (among which we may of course count the equilibrium) display regular microscopic dynamics allows us to dispose of an enormous amount of information regarding the intimate dynamics of a system frozen in such state. Indeed in contrast to molecular chaos, we recover predictability of the microscopic dynamics, at least for much larger times then originally expected in the context of a finite system. Looking forward, we speculate that the knowledge of the microscopic dynamics can somehow enables one to challenge the second law of thermodynamics by setting up appropriate Maxwell daemons. Note also, that the regularity of the dynamics in the large N limit, induces from a statistical stand point a freezing of the system in a zero dynamical entropy production state, in this frame of mind, we may wonder if minimal entropy production settings could predict final states of these classical long-range interacting systems. As perspectives, work in different settings have to be performed in order to confirm/infirm the proposed trends. In the considered systems, we either had in the mean-field case no space dependent interaction, and in the α-HMF model, the spatial interaction was set up on a one-dimensional lattice with a power-law decreasing coupling constant. The simplest generalizations that come to mind are twofold, what happens when the interaction actually depends on the distance and in a phase space that allows "collisions" [47], the other way is to keep the lattice and focus on its topology and the way the constant of motion is set up, for instance studying the case of diluted complex networks and see how and in which settings the aforementioned features arise [48]. Work is in progress for these two proposed directions, if the results display as well self-organized regularity, one may then tackle systems with higher embedded dimensions, before considering more realistic physical models and potential applications in for instance hot noncollisional plasmas or self-gravitating systems. Another potential perspective is to leave the realm of conservative Hamiltonian systems and see how some of the self-organized regularity translates in setting such as for instance neural networks, and if for instance this phenomenon would imply reaching some kind of global "synchronicity."

Acknowledgements I am grateful to Romain Bachelard for a careful reading of the manuscript, suggesting corrections, references, and extensions to the original text. I am also thankful to him for preparing Figs. 5 and 6. His input was much appreciated. Most of the work presented in this chapter is shared with my coauthors: Duccio Fanelli, Tineke Van den Berg, Stefano Ruffo, Cristel Chandre. I use this occasion to thank them again. Discussions about the possible implications of self-organized regularity first occurred between the author and George M. Zaslavsky, in November 2007, and I take this opportunity to express my gratitude.

References

1. Metzger, B., Nicolas, M., Guazzelli, E.: Falling clouds of particles in viscous fluids. J. Fluid Mech. **580**, 283–301 (2007)
2. Marchioro, C., Pulvirenti, M.: Mathematical theory of uncompressible nonviscous fluids. In: John, F., Marsden, J.E., Sirovich, L. (eds.) Applied Mathematical Science, vol. 96. Springer, New York (1994)

3. Saffman, P.G.: Vortex Dynamics. Cambridge Monographs on Mechanics and Applied Mathematics. Cambridge University Press, Cambridge (1995)
4. Benisti, D., Gremillet, L.: Nonlinear plasma response to a slowly varying electrostatic wave, and application to stimulated Raman scattering. Phys. Plasmas **14**(4), 042304 (2007)
5. Bonifacio, R., Casagrande, F., Cerchioni, G., Souza, L.D., Pierini, P., Piovella, N.: Physics of the high-gain FEL and superradiance. Riv. Del Nuovo Cimento. **13**(9), 1–69 (1990)
6. Dauxois, T., Ruffo, S., Arimondo, E., Wilkens, M. (eds.): Dynamics and Thermodynamics of Systems with Long Range Interactions. Lecture Notes in Physics, vol. 602. Springer-Verlag, Berlin (2002)
7. Pettini, M.: Geometry and Topology in Hamiltonian Dynamics and Statistical Mechanics. Interdisciplinary Applied Mathematics. Springer, New York (2007)
8. Campa, A., Dauxois, T., Ruffo, S.: Statistical mechanics and dynamics of solvable models with long-range interactions. Phys. Rep. **480**, 57–159 (2009)
9. Chavanis, P.H., Ninno, G.D., Fanelli, D., Ruffo, S.: Out of equilibrium phase transitions in mean-field hamiltonian dynamics. In: Chandre, C., Leoncini, X., Zaslavsky, G. (eds.) Chaos, Complexity and Transport, pp. 3–26. World Scientific, Singapore (2008)
10. Lynden-Bell, D.: Statidtical mechanics of violent relaxation in stellar systems. Mon. Not. R. Astron. Soc. **136**, 101–121 (1967)
11. Leoncini, X., Van den Berg, T.L., Fanelli, D.: Out-of-equilibrium solutions in the XY-Hamiltonian mean-field model. Europhys. Lett. **86**(2), 20002 (2009)
12. Bachelard, R., Chandre, C., Fanelli, D., Leoncini, X., Ruffo, S.: Abundance of regular orbits and nonequilibrium phase transitions in the thermodynamic limit for long-range systems. Phys. Rev. Lett. **101**(26), 260603 (2008)
13. Inagaki, S., Konishi, T.: Dynamical stability of a simple model similar to self-gravitating systems. Publ. Astron. Soc. Jpn. **45**, 733–135 (1993)
14. Pichon, C.: Mécanismes de structuration gravitationnelle : Théorie et estimation. Ph.D. thesis, Université Pierre et Marie Curie and Institut d'Astrophysique de Paris (1999)
15. Antoni, M., Ruffo, S.: Clustering and relaxation in Hamiltonian long-range dynamics. Phys. Rev. E **52**(3), 3261 (1995)
16. Elskens, Y., Escande, D.F.: Microscopic Dynamics of Plasmas and Chaos. IoP, Bristol (2002)
17. Bachelard, R., Manos, T., de Buyl, P., Staniscia, F., Cataliotti, F.S., Ninno, G.D., Fanelli, D., Piovella, N.: Experimental perspectives for systems based on long-range interactions. J. Stat. Mech. P06009 (2010)
18. Fermi, E., Pasta, J., Ulam, S.: Los Alamos Reports (LA-1940) (1955)
19. Leoncini, X., Verga, A., Ruffo, S.: Hamiltonian dynamics and the phase transition of the xy model. Phys. Rev. E **57**(6), 6377 (1998)
20. Van den Berg, T.L.: Systèmes avec interactions à longue portée. Master's thesis, Université Paris VII (2008)
21. de Buyl, P., Mukamel, D., Ruffo, S.: Self-consistent steady states in Hamiltonian mean field dynamics. Phys. Rev. E **84**, 061151 (2010). http://arxiv.org/abs/1012.2594v1; http://arxiv.org/pdf/1012.2594v1
22. Zaslavsky, G.M.: The Physics of Chaos in Hamiltonian Systems, 2nd edn. Imperial College Press, London (2007)
23. Barré, J., Bouchet, F., Ruffo, S., Dauxois, T., Yamaguchi, Y.: Stability criteria of the Vlasov equation and quasi-stationary states of the HMF model. Phys. A **337**, 36–66 (2004)
24. Bouchet, F., Dauxois, T.: Prediction of anomalous diffusion and algebraic relaxations for long-range interacting systems, using classical statistical mechanics. Phys. Rev. E **72**, 045103 (2005)
25. Julien, B., Freddy, B., Thierry, D., Stefano, R., Yoshiyuki, Y.: The Vlasov equation and the Hamiltonian mean-field model. Physica. A **365**, 177–183 (2006)
26. Barré, J., Olivetti, A., Yamaguchi, Y.Y.: Dynamics of perturbations around inhomogeneous backgrounds in the HMF model. J. Stat. Mech. **8**, 28 P08002 (2010)
27. Staniscia, F., Dauxois, T., Ninno, G.D., Ruffo, S., Bachelard, R.: Stability of inhomogeneous states in mean-field models with an external potential. J. Stat. Mech. P03022 (2011)

28. McLachlan, R.I., Atela, P.: The accuracy of symplectic integrators. Nonlinearity **5**, 541 (1992)
29. Latora, V., Rapisarda, A., Ruffo, S.: Lyapunov instability and finite size effects in a system with long-range forces. Phys. Rev. Lett. **80**(4), 692 (1998)
30. Firpo, M.C.: Analytic estimation of Lyapunov exponent in a mean-field model undergoing a phase transition. Phys. Rev. E **57**, 6599 (1998)
31. Benettin, G., Galgani, L., Strelcyn, J.M.: Kolmogorov entropy and numerical experiments. Phys. Rev. A **14**, 2338–2345 (1976)
32. Tsiganis, K., Anastasiadis, A., Varvoglis, H.: On the relation between the maximal LCN and the width of the stochastic layer in a driven pendulum. J. Phys. A: Math. Gen. **32**, 431 (1999)
33. Anteneodo, C., Tsallis, C.: Breakdown of the exponential sensitivity to initial conditions: role of the range of the interactions. Phys. Rev. Lett. **80**, 5313 (1998)
34. Tamarit, F., Anteneodo, C.: Rotators with long-range interactions: connection with the mean-field approximation. Phys. Rev. Lett. **84**(2), 208–211 (2000)
35. Campa, A., Giansanti, A., Moroni, D.: Canonical solution of classical magnetic models with long-range couplings. J. Phys. A Math. Gen. **36**, 6897 (2003)
36. Van den Berg, T.L., Fanelli, D., Leoncini, X.: Stationary states and fractional dynamics in systems with long range interactions. EPL **89**, 50010 (2010)
37. Campa, A., Giansanti, A., Moroni, D.: Metastable states in a class of long-range Hamiltonian systems. Phys. A **305**, 137 (2002)
38. Tarasov, V.E., Zaslavsky, G.M.: Fractional dynamics of systems with long-range interaction. Commun. Nonlinear Sci. Numer. Simul. (2006) **11**(8) 885–898 (2011)
39. Zaslavsky, G.M., Edelman, M., Tarasov, V.E.: Dynamics of the chain of forced oscillators with long-range interaction: From synchronization to chaos. Chaos **17**(4), 043124 (2007)
40. Afraimovich, V., Zaslavsky, G.M.: Space-time complexity in Hamiltonian dynamics. Chaos **13**(2), 519–532 (2003)
41. Chavanis, P.H.: Lynden-Bell and Tsallis distributions for the HMF model. Eur. Phys. J. B **53**(4), 487 (2006)
42. Bachelard, R., Antoniazzi, A., Chandre, C., Fanelli, D., Leoncini, X., Vittot, M.: Stabilizing the intensity of a wave amplified by a beam of particles. Eur. Phys. J. D **42**, 125–132 (2007)
43. Colson, W.: Theory of a free electron laser. Phys. Lett. A **59**, 187 (1976)
44. Casagrande, F., Bonifacio, R., Pellegrini, C.: Hamiltonian model of a free-electron laser. Opt. Commun. **61**, 55 (1987)
45. Bonifacio, R., De Salvo Souza, L.: Collective atomic recoil laser (CARL) optical gain without inversion by collective atomic recoil and self-bunching of two-level atoms. Nucl. Instrum. Meth. A **341**, 360 (1994)
46. Bonifacio, R., De Salvo Souza, L., Narducci, L. M., D'Angelo, E.J.: Exponential gain and self-bunching in a collective atomic recoil laser. Phys. Rev. A **50**, 1716 (1994)
47. Turchi, A.: Dynamics and statistics of systems with long range interactions: Application to 1-dimensional toy-models. Ph.D. thesis, Aix-Marseille Université and Univesita Degli Studi di Firenze (2012)
48. de Nigris, S.: Hamiltonian Dynamics of XY rotators model interacting on a Small World Network. Master's thesis, Aix-Marseille Université (2011)

Reducing the Sequential Dynamics of Excitatory Neural Networks to Synaptic Cellular Automata

V. I. Nekorkin, A. S. Dmitrichev and D. V. Kasatkin

Abstract We present a new approach for the description and analysis of sequential dynamics of excitatory neural networks. It is based on the reduction of dynamics of networks to the dynamics of cellular automata (CA) on the graph of connections. The attractors of the CA determine the different regimes of sequential dynamics of the original neural network. We illustrate our approach through Morris–Lecar and Hodgkin–Huxley neural networks.

1 Introduction

The neural systems comprised of neurons and glial cells [11] are known to exhibit a large variety of electrical activity. To study mechanisms of formation of different neural activities the approaches based on the dynamical systems paradigm are widely used [4, 5, 7, 8, 18, 21].

Neurophysiological experiments [9, 16, 23] have indicated that some neural processes (e.g., processes related to different cognitive tasks—memory, attention, psychomotor coordination, etc.) are accompanied by transient short-time activity of individual neurons or small groups of neurons. In such a process, a sequence of activity phases of different neurons emerges successively in time. It was shown within the dynamical systems framework [1, 3, 12, 20, 21] that this behavior is related to the existence of a collection of metastable invariant sets joined by heteroclinic trajectories in the phase space (the heteroclinic network) and so, can be thought of as a process of successive switchings among these metastable sets. There are some models in which the whole collection of metastable sets represented by either saddle

V. I. Nekorkin (✉) · A. S. Dmitrichev · D.V. Kasatkin
Nonlinear Dynamics Department, Institute of Applied Physics of the Russian Academy of Sciences, 46 Ul'yanov Street, 603950, Nizhny Novgorod, Russia,
e-mail: vnekorkin@neuron.appl.sci-nnov.ru

A. S. Dmitrichev
e-mail: admitry@neuron.appl.sci-nnov.ru

D.V. Kasatkin
e-mail: kasatkin@neuron.appl.sci-nnov.ru

H. González-Aguilar, E. Ugalde (eds.), *Nonlinear Dynamics New Directions,*
Nonlinear Systems and Complexity 12, DOI 10.1007/978-3-319-09864-7_5

equilibrium points [1, 20, 21] or saddle limit cycles [3] and the network of possible transitions between them can be rigorously established. However, sequential activity is not always directly related to the existence of a heteroclinic network. In [19] it was established that networks of class 2 excitable neurons coupled by excitatory synapses can demonstrate a variety of sequential activity regimes which are characterized by successive firing of neurons in the form of bursts (bunches of spikes) and formed by means of dynamical bifurcations. In such cases, in order to answer the main question of sequential dynamics—in which order neurons become activated—one needs to use a mathematical apparatus different from the heteroclinic channels technique.

Recently in [24] an approach for the study of neural networks has been proposed. It consists in reducing a given network to a discrete model. In this model [10], each neuron is represented by a finite number of states and there are rules which determine how a neuron goes from one state to another. However, the approach has some limitations. It is based essentially on a specific character of dynamics of neurons. Indeed, the neurons are assumed to be relaxational. In this case, each neuron can be in one of the three consecutive phases: active phase, when a neuron can excite other ones, a refractory phase, when a neuron is non-responsive to an action of the other ones, and rest phase, when a neuron can be excited (activated) by the other ones. The duration of the refractory phase is assumed to be a multiple of the duration of the active phase. Thus the duration of the active phase is considered as a discretization time step. The interaction between neurons is taken into account in the following way. If a neuron receives an excitatory input, the excitation occurs instantaneously. On the other hand, if a neuron receives inhibitory input, then it becomes excited due to the post-inhibitory rebound only when the inhibition ends. Moreover, the approach can be rigorously applied only to excitatory–inhibitory networks. In [2] the examples of application of the approach to specific biophysical models are presented.

Unlike [2, 24] here we offer an approach for analyzing the sequential dynamics of excitatory neural networks. It consists in reducing continuous dynamics of neural networks to a discrete dynamical systems in the form of a cellular automaton (CA) on the graph of connections. In the reduction, the main role is played by the dynamics of synapses but not by the specific features of neurons. In fact, the CA represents a network of synapses with a finite number of states which alternate each other according to some fixed rules. To determine the rules one needs to study only the responses of an individual synapse onto actions of neighboring (in graph of connections) synapses through corresponding neurons. As a result, the numerical integration of the whole system of ordinary differential equations (ODEs) is not needed. Moreover, since the form of the neuron responses is not important, the approach is applicable to a broad set of networks including those consisting of neurons, which possess the neural excitability property (neurons of the class 2 excitability in the terminology of Izhikevich[8]). We demonstrate our approach on the examples of Morris–Lecar and Hodgkin–Huxley neurons coupled by excitatory synapses with a short-term plasticity property.

The chapter is organized as follows. In Sect. 2 based on some general properties of synaptic and neuron dynamics we explicitly derive a cellular automaton for an

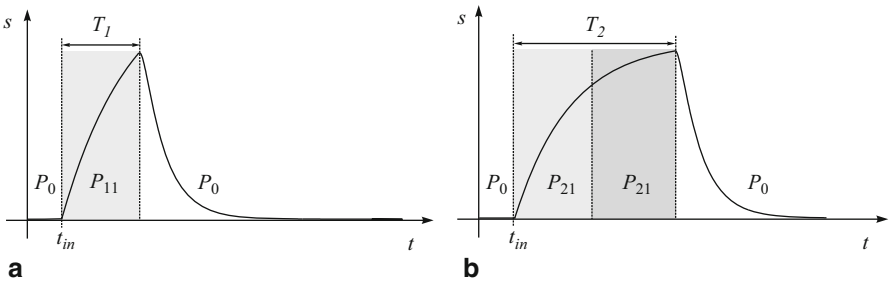

Fig. 1 Qualitative waveforms of synaptic conductance $s(t)$ corresponding to fast (**a**) and slow (**b**) synaptic responses ($T_2 \simeq 2T_1$). Symbols P_0, P_{11}, P_{21}, P_{22} signify the discrete states of a synapse (see below, for details)

arbitrary excitatory network neural network. In Sect. 3 we consider two concrete examples of excitatory neural networks, show how to build cellular automata for them, and then analyze their sequential dynamics. In Sect. 4 we formulate the main scheme of application of the approach. Section 5 is devoted to the concluding remarks.

2 Derivation of a Cellular Automata

Here we derive a cellular automaton for an arbitrary neural network consisting of N neurons with class excitability 2 coupled by excitatory synapses. First of all let us make some remarks and assumptions about the architecture of the network and dynamical properties of neurons and synapses.

Remark (r1). In [19] it was shown that a class 2 neuron under the application of excitatory synaptic current has the following dynamical behavior. It is at rest state when synaptic current is absent (the conductance is zero). On the other hand, when the synaptic conductance overcomes some threshold value which is close to its maximum, a neuron starts firing of spikes. The firing of spikes continues until the synaptic conductance is above the threshold. Then a neuron returns back to its rest state. *Thus the time course of synaptic conductance completely determines the dynamics of postsynaptic neuron.* Note that the firing of spikes triggers the processes of activation of next synaptic couplings.

Remark (r2). From neurophysiologic experiments it follows that a synapse possess refractory property, i.e., a synapse is nonsensitive to the presynaptic stimulation when it is active.

For our purposes we also assume that:

Assumption (a1). A synapse possesses short-term plasticity property [27], i.e., it has two types of responses (waveforms of synaptic conductance $s(t)$, see Fig. 1) depending on the presynaptic neurons activity—fast (Fig. 1a) and slow (Fig. 1b) ones which are distinguished by the characteristic rise times (T_2 and T_1) of the synaptic conductance. Such behavior may be caused, for instance, by the competition of presynaptic facilitation and postsynaptic desensitization processes [14, 25, 26].

Assumption (a2). There is a "resonance" relation between the value T_2 for the slow response and T_1 for the fast one such that $T_2 = 2T_1$.

Assumption (a3). The temporal intervals of generation of spikes are relatively short with respect to the characteristic timescales of evolution of the synaptic conductance.

Next we show that these properties allow one to reduce continuous dynamics of the network to a discrete one in the form of cellular automaton on the graph of synaptic connections.

Graph of connections. Let us first define directed graph $G =< Q_G, K_G >$. It has N vertices Q_G=$\{Q_1, Q_2, \ldots, Q_N\}$ which signify the synapses of the network. The set K_G=$\{K_1, K_2, \ldots, K_N\}$ reflects the architecture of the connections in the network. Each K_i is a collection of indices such that $j \in K_i$ if and only if there is a connection from the j-th synapse of the network to the i-th synapse through the j-th neuron. In the graph collection K_i defines a set of arrows started at the vertices $j \in K_i$ and ended at i. This possibility follows from the property (*r1*).

Discrete states of a synapse. We will define discrete states of a synapse according to the behavior of the s-variable describing its dynamics. Here we use the assumptions (*a1*) and (*a2*). We say that the i-th synapse is in the state $\psi_i(s_i)$ that is equal to:

- P_{11} if $s_i(t)$ undergoes the fast response and $s_i'(t) > 0$ (see Fig. 1a);
- P_{21} if $s_i(t)$ undergoes the response of the slow type, $s_i'(t) > 0$ and $t_{in} \le t \le T_1 + t_{in}$, where $s_i(t_{in}) = 0$, $s_i'(t_{in}) > 0$, i.e., $s_i(t)$ starts growing at the instant of time t_{in} (see Fig. 1b);
- P_{22} if $s_i(t)$ again undergoes the response of the slow type and $s_i'(t) > 0$, but $T_1 + t_{in} \le t \le 2T_1 + t_{in}$;
- P_0 if it is not in one of the previous states, i.e., either it is in the equilibrium state $s_i(t) = 0$ or $s_i'(t) < 0$ in both the slow and fast cases (see Fig. 1).

Thus, we have replaced the continuous description of the behavior of the i-th synapse in terms of $s_i(t)$ by a discrete description in terms of $\psi_i = \psi_i(s_i)$. The set of values of ψ_i, $i = 1, \ldots, N$, is the collection of the symbols $\mathcal{P} = \{P_0, P_{11}, P_{21}, P_{22}\}$. For the sake of convenience we identify P_0 with 0, P_{11} with 1, P_{21} with 2, and P_{22} with 3, so $\mathcal{P} = \{0, 1, 2, 3\}$. We will use both notations below.

The rules of CA. Now we define the rules of evolution in time of ψ_i, i.e., the rules of a CA. They can be formulated on the basis of properties (*r1*), (*r2*), and (*a3*).

(*i*) If i-th synapse at the instant of time t is in the state P_0 ($\psi_i(s_i(t)) = P_0$), and there is $j \in K_i$ such that $\psi_j(s_j(t)) = P_{11}$ or $\psi_j(s_j(t)) = P_{22}$ then it will be excited at the instant $t + T_1$, i.e., $\psi_i(s_i(t + T_1)) = P_{11}$ or $\psi_i(s_i(t + T_1)) = P_{21}$ depending on the values of threshold constants θ_{ji}.

(*ii*) If i-th synapse at the instant of time t is in the state P_{21}, i.e., $\psi_i(s_i(t)) = P_{21}$, then $\psi_i(s_i(t + T_1)) = P_{22}$, independently of other synapses. Moreover, the P_{21}-synapse cannot excite another synapse.

(*iii*) If $\psi_i(s_i(t)) = P_{11}$ or $\psi_i(s_i(t)) = P_{22}$, then $\psi_i(s_i(t + T_1)) = P_0$, independently of the states of other synapses.

(*iv*) Because of the existence of the refractory period, the synapses in the states P_{11}, P_{21}, P_{22} do not feel the action of other synapses.

Table 1 Synaptic dynamics rules. (Rules F_i of CA)

ψ_i / $\psi_j, j \in K_i$	P_0	P_{11}	P_{21}	P_{22}
$\forall j \in K_i, \psi_j = P_0$ or $\psi_j = P_{21}$	P_0	P_0	P_{22}	P_0
$\exists j \in K_i$, such that $\psi_j = P_{11}$ or $\psi_j = P_{22}$	P_{11} or P_{21} depending on θ_{ji}	P_0	P_{22}	P_0

These statements imply that for the fixed i the state $\psi_i(s_i(t+T_1))$ at the instant $t+T_1$ is uniquely determined by: the state $\psi_i(s_i(t))$ at the previous instant of time t; the states of the j-th synapse, $j \in K_i$, at the instant of time t; the values of the threshold constants θ_{ji}, $j \in K_i$. Hence,

$$\psi_i(s_i(t+T_1)) = F_i(\psi_i(s_i(t)), \{\psi_j(s_j(t))\}, \{\theta_{ji}\}, j \in K_i), \tag{1}$$

where F_i is a function determined by the statements (i)–(iv). The relation (1) is a synaptic CA determined on the graph of connections G. In Table 1 we summarize the rules of the CA. In what follows we identify $\psi_i(s_i(t))$ with the symbol ψ_i and $\psi_i(s_i(t+T_1))$ with the symbol $\overline{\psi_i}$.

Let us clarify how to use the table. If, for example, ψ_i=P_{11} and ψ_j=P_0, $j \in K_i$, then $\overline{\psi_i} = P_0$; but if $\psi_i = P_{21}$, $\psi_j = P_{21}$, $j \in K_i$, then $\overline{\psi_i} = P_{22}$.

Finally, if we fix the values of thresholds θ_{ji} the rules of the CA take the following form:

$$\overline{\psi_i} = F_i(\psi_i, \{\psi_j\}, j \in K_i), \tag{2}$$

where $\overline{\psi_i}, \psi_i \in \mathcal{P}$.

3 Building the Cellular Automaton by Examples

Here we illustrate building of cellular automata for two specific excitatory neural networks.

3.1 A Network of Synaptically Coupled Morris–Lecar Neurons

Let us start with the network of Morris–Lecar neurons [17] coupled by excitatory synapses with short-term plasticity property which has the architecture shown on Fig. 2. The dynamics of such a network is described by the following system of ODEs:

$$C\frac{dv_i}{dt} = -g_L(v_i - v_L) - g_{Ca}M_\infty(v_i)(v_i - v_{Ca}) - g_K n_i(v_i - v_K) + I_i^{ext} - g_{syn}s_i(v_i - v_{rev}), \tag{3}$$

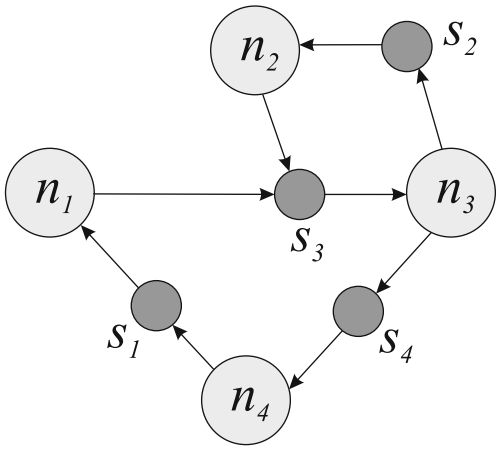

Fig. 2 The architecture of Morris–Lecar neural network. Here n_i and s_i signify the neurons and synapses respectively

$$\frac{dn_i}{dt} = \frac{n_\infty(v_i) - n_i}{\tau_n(v_i)}, \tag{4}$$

$$\frac{dr_i}{dt} = f_1(r_i) - s_i - k_1, \tag{5}$$

$$\frac{ds_i}{dt} = \varepsilon(f_{2i} - s_i - k_2). \tag{6}$$

The variables v_i, n_i characterize the membrane potential and the activation of the potassium ion channels of the i-th neuron ($i = 1, \ldots, 4$), C is the membrane capacitance. The terms at the RHS of Eq. (3) describe the currents flowing through the cell membrane of a neuron. The first three terms determine the leakage, the calcium, and the potassium ionic currents, respectively, g_L, g_{Ca}, g_K are the maximal conductances, v_L, v_{Ca}, v_K are the equilibrium (reverse) potentials for the corresponding ion channels, and $M_\infty(v)$, $n_\infty(v)$, $\tau_n(v)$ are the stationary states of the activation levels and the characteristic relaxation time respectively depending on the membrane potential by the sigmoid law:

$$M_\infty(v) = 0.5\left[1 + \tanh\left(\frac{v - v^{(1)}}{v^{(2)}}\right)\right],$$

$$n_\infty(v) = 0.5\left[1 + \tanh\left(\frac{v - v^{(3)}}{v^{(4)}}\right)\right],$$

$$\tau_n(v) = \left[\phi \cosh\left(\frac{v - v^{(3)}}{2v^{(4)}}\right)\right]^{-1},$$

where $v^{(1)} = -0.01$, $v^{(2)} = 0.15$, $v^{(3)} = 0$, $v^{(4)} = 0.3$, $\phi = 1$. The term I_i^{ext} is an external current. The last term at the RHS of Eq. (3) determines the synaptic current emerging as a result of action of other neurons on the i-th neuron by chemical

synapse, where g_{syn} is the maximum synaptic conductance, v_{rev} is synaptic reversal potential, and variable s_i corresponds to the fraction of open synaptic channels. To describe a short-term plasticity property, we introduced a phenomenological model of synapse in the form of a system of Eqs. (5) and (6). In Eq. (5), $f_1(r)$ is piecewise linear (PWL) continuous function which resembles the shape of a polynomial of fifth degree:

$$f_1(r) = \begin{cases} -\gamma_1 r - A(1+\sigma_1), & r \leqslant -x_0 \\ \gamma_2 r, & -x_0 < r \leqslant x_0 \\ -\gamma_3 r + A(1+\sigma_3), & x_0 < r \leqslant x_1 \\ \gamma_4 r - A(1+\sigma_4), & x_1 < r \leqslant x_2 \\ -\gamma_5 r + A(1+\sigma_5), & r > x_2 \end{cases} \tag{7}$$

where

$$\sigma_1 = \frac{\gamma_1}{\gamma_2}, \sigma_3 = \frac{\gamma_3}{\gamma_2}, \sigma_4 = \frac{\gamma_4}{\gamma_2} + 2\frac{\gamma_4}{\gamma_3}, \sigma_5 = \frac{\gamma_5}{\gamma_2} + 2\gamma_5\left(\frac{1}{\gamma_4} + \frac{1}{\gamma_3}\right),$$
$$x_0 = \frac{A}{\gamma_2}, x_1 = A\left(\frac{1}{\gamma_2} + \frac{2}{\gamma_3}\right), x_2 = A\left(\frac{1}{\gamma_2} + \frac{2}{\gamma_3} + \frac{2}{\gamma_4}\right)$$

with $A = 2/3$, $\gamma_1 = 0.1$, $\gamma_2 = 1.136$, $\gamma_3 = 5$, $\gamma_4 = 41.113$, $\gamma_5 = 20$.

In Eq. (6), f_{2i} is monotonically increasing continuous PWL function:

$$f_{2i} = \begin{cases} [\alpha + \mu\zeta_i\chi_i]r_i, & r_i < 0 \\ \beta r_i, & r_i \geqslant 0 \end{cases} \tag{8}$$

where $\chi_i = \sum_{\substack{j=1, \\ j\neq i}}^{N} H(v_j - \theta_{ji})$, $\zeta_i = H(\theta_{ref} - s_i)$ and $H(x) = 1/(1+\exp(-x/1000))$ is a smooth approximation of the Heaviside step function. The term χ_i describes an action of presynaptic neurons on the synapse of i-th neuron. Parameters θ_{ji} characterize the initial instants of activation of synaptic processes caused by input signals, i.e., the synaptic activation thresholds. The thresholds θ_{12}, θ_{14}, θ_{21}, θ_{24}, θ_{31}, θ_{42}, θ_{43} are set to 2 to conform to the architecture, while other ones, for definiteness, are chosen as follows: $\theta_{13} = \theta_{23} = \theta_{32} = -0.03$, $\theta_{34} = 0.0$, $\theta_{41} = -0.02$. The term ζ_i accounts for the refractory property of a synapse. It is equal to 1 only while the synapse is not activated ($s_i < \theta_{ref}$).

Note that special design of nonlinear functions (7) and (8) as well as relaxational behavior of Eqs. (5) and (6) provide fulfillment of conditions (*a1*) and (*a2*). Indeed for $\mu = 0$, i.e., in absence of external influence, any trajectory of the system consists of slow (in a vicinity of stable manifold of slow motions corresponding to falling parts of the curve $s = f_1(r) - k_1$) and fast ($s \approx const$). There are three branches of stable manifolds of slow motions. One of them lies in the half plane $r < 0$.

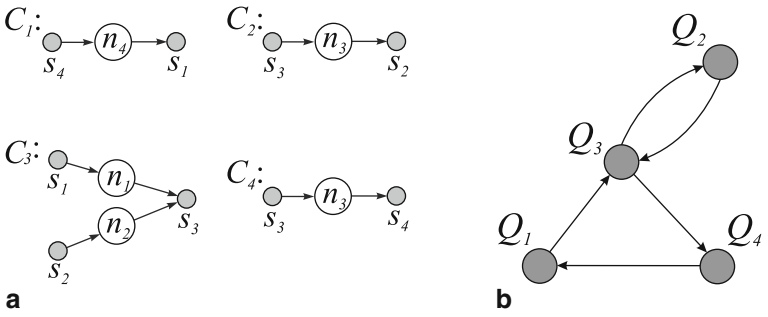

Fig. 3 Elementary clusters of the network (**a**) and corresponding graph of connection $G =< \{Q_i\}, \{K_i\}, i = \overline{1,4} >$ (with $K_1 = \{4\}$, $K_2 = \{3\}$, $K_3 = \{1,2\}$, $K_4 = \{3\}$) (**b**)

The evolution of the system along this branch corresponds to inactivation phase of synaptic coupling. Two other branches lie in the half plane $r > 0$. The evolution of the system along each of these branches corresponds to a certain scenario of activation (response) of synaptic coupling. The choice of one of the two branches depends on the strength of presynaptic stimulation (waveform of $\chi_i(t)$). Note also that PWL form of functions (7) and (8) is chosen only for the simplicity of analysis. These functions can be replaced by their smooth analogs without any major influences on the dynamics of a synaptic model.

In numerical simulations we use the following values of parameters for Morris–Lecar neuron:

$$C = 1.4, g_L = 0.1, g_{Ca} = 1.1, g_K = 2, v_L = -0.5, v_{Ca} = 1, \\ v_K = -0.7, I_i^{ext} = 0.13, g_{syn} = 0.0409, v_{rev} = 0.5, \tag{9}$$

and for synapse:

$$\alpha = 0.2, \beta = 2, k_1 = -0.616, k_2 = -0.216, \varepsilon = 0.005, \mu = 2.3, \theta_{ref} = 0.01. \tag{10}$$

The parameters of the neuron are chosen so that it is at rest in the absence of synaptic current. The choice of the v_{rev}-value corresponds to the case of excitatory synaptic coupling.

To build the cellular automaton the graph of connections must be constructed. For this purpose we single out the elementary clusters of the neural network. Each cluster C_i is defined as part of the network including the i-th and j-th synapses coupled with the i-th one through j-th neurons. It is easy to see from the architecture of the network (see Fig. 2) that it contains only four elementary clusters: C_1–C_4, which are shown on Fig. 3a. Based on the structure of each elementary cluster one can construct the graph of connections G shown in Fig. 3b.

Next one needs to specify the rules F_i for the CA. For this purpose we determine the responses of the clusters, i.e., for each cluster C_i, we find the responses of the i-th

Table 2 The rules $\overline{\psi_1} = F_1(\psi_1, \psi_4)$

ψ_1 / ψ_4	P_0	P_{11}	P_{21}	P_{22}
P_0	P_0	P_0	P_{22}	P_0
P_{11}	P_{11}	P_0	P_{22}	P_0
P_{21}	P_0	P_0	P_{22}	P_0
P_{22}	P_{11}	P_0	P_{22}	P_0

Table 3 The rules $\overline{\psi_2} = F_2(\psi_2, \psi_3)$

ψ_2 / ψ_3	P_0	P_{11}	P_{21}	P_{22}
P_0	P_0	P_0	P_{22}	P_0
P_{11}	P_{11}	P_0	P_{22}	P_0
P_{21}	P_0	P_0	P_{22}	P_0
P_{22}	P_{11}	P_0	P_{22}	P_0

synapse caused by the different (fast and slow) actions of the j-th synapse through the j-th neuron, $j \in K_i$. It is implied that a collective action of groups of several j-th synapses also has to be studied if K_i consists of more than one element.

Elementary cluster C_1. From the structure of the elementary cluster C_1 it follows that the state of the synapse s_1 depends only on the state of the synapse s_4 ($K_1 = \{4\}$). Numerical study shows that the response of the synapse s_1 (while it is in the state P_0) to the action of the synapse s_4 is always of minimal time scale T_1, independently of the state (P_{11} or P_{22}) of s_4, i.e., $F_1(P_0, P_{11}|P_{22}) = P_{11}$. In Table 2 full description of the rules F_1 defining transitions of synapse s_1 from one state to another is presented.

Elementary cluster C_2. The state of the synapse s_2 depends only on the state of the synapse s_3 (i.e., $K_2 = \{3\}$). The response of the synapse s_2 (while it is in the state P_0) to the action of the synapse s_3 is always of minimal time scale T_1, independently of the state of s_3. The corresponding rules are shown in Table 3.

Elementary cluster C_3. From the structure of the elementary cluster C_3 it is easy to see that the state of the synapse s_3 depends on the states of the synapses s_1 and s_2 (i.e., $K_1 = \{1, 2\}$). Numerical study shows that the response of s_3 (while it is in the state P_0) is always of the minimal time scale T_1, independently of the states of s_1 and s_2, i.e., $F_3(P_0, P_{11}|P_{22}, P_{11}|P_{22}) = P_{11}$. From here we obtain the rules presented in Table 4.

Elementary cluster C_4. The state of the synapse s_4 depends only on the state of the synapse s_3 (i.e., $K_4 = \{3\}$). The response of the synapse s_4 (while it is in the state P_0) to the action of the synapse s_3 is always of the double time scale T_2, independently of the state of s_3, i.e., $F_4(P_0, P_{11}|P_{22}) = P_{21}$. The corresponding rules are shown in Table 5.

Thus, Tables 2, 3, 4, and 5 give us the full description of the rules $F_i, i = 1, \ldots, 4$, of the CA. Using these rules one may study its dynamics. We remind that we denote the states of synapses by numbers: $P_0 \to 0$, $P_{11} \to 1$, $P_{21} \to 2$, $P_{22} \to 3$. The CA

Table 4 The rules $\overline{\psi_3} = F_3(\psi_3, \psi_1, \psi_2)$

ψ_3 / ψ_1/ψ_2	P_0	P_{11}	P_{21}	P_{22}
P_0/P_0	P_0	P_0	P_{22}	P_0
P_{11}/P_0	P_{11}	P_0	P_{22}	P_0
P_{21}/P_0	P_0	P_0	P_{22}	P_0
P_{22}/P_0	P_{11}	P_0	P_{22}	P_0
P_0/P_{11}	P_{11}	P_0	P_{22}	P_0
P_{11}/P_{11}	P_{11}	P_0	P_{22}	P_0
P_{21}/P_{11}	P_{11}	P_0	P_{22}	P_0
P_{22}/P_{11}	P_{11}	P_0	P_{22}	P_0
P_0/P_{21}	P_0	P_0	P_{22}	P_0
P_{11}/P_{21}	P_{11}	P_0	P_{22}	P_0
P_{21}/P_{21}	P_0	P_0	P_{22}	P_0
P_{22}/P_{21}	P_{11}	P_0	P_{22}	P_0
P_0/P_{22}	P_{11}	P_0	P_{22}	P_0
P_{11}/P_{22}	P_{11}	P_0	P_{22}	P_0
P_{21}/P_{22}	P_{11}	P_0	P_{22}	P_0
P_{22}/P_{22}	P_{11}	P_0	P_{22}	P_0

Table 5 The rules $\overline{\psi_4} = F_4(\psi_4, \psi_3)$

ψ_4 / ψ_3	P_0	P_{11}	P_{21}	P_{22}
P_0	P_0	P_0	P_{22}	P_0
P_{11}	P_{21}	P_0	P_{22}	P_0
P_{21}	P_0	P_0	P_{22}	P_0
P_{22}	P_{21}	P_0	P_{22}	P_0

has two attractors: A_0 and A_1. The attractor A_0 is the fixed point (0000). A fragment of the basin of A_0 is shown in Fig. 4a. Such a form of the illustration is convenient and has been used before (see, for instance [3, 24]). We see that if all elements of the network is activated then all of them come to the rest state P_0. The attractor A_1 is the periodic trajectory (0010) $\rightarrow$ (0102) $\rightarrow$ (0013) $\rightarrow$ (1100) $\rightarrow$ (0010). A part of the basin of A_1 is shown on Fig. 4b. The periodic points in the attractor are marked by the grey color.

According to the main property of cellular automata on finite graphs, every trajectory is eventually periodic and the attractors are periodic orbits. It is important to know the order in which elements become excited. For that, it is convenient to describe the motion on an attractor in the form of a spatio-temporal diagram or an unfolding, i.e., in the following way. We construct a figure in the plane with the horizontal axis corresponding to the discrete time (episodes) and with the vertical axis

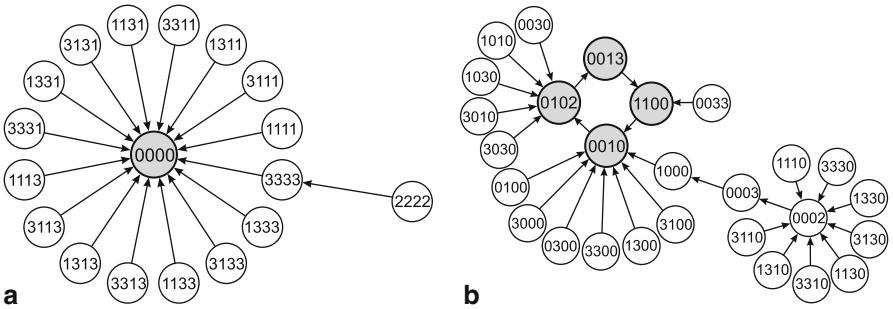

Fig. 4 Parts of the basins of (**a**) the fixed point A_0 and (**b**) the periodic attractor A_1

corresponding to the synapse number. Then, if i-th synapse in k-th temporal episode is active, i.e., it is in one of the states P_{11}, $P_{21,}$ or P_{22} ($\psi_i(k) \neq 0$), corresponding rectangle is marked by the black color. On the other hand, if i-th synapse in k-th episode is silent, i.e., it is in the state P_0 ($\psi_i(k) = 0$), corresponding rectangle is marked by the white color. We note that spatio-temporal diagrams (unfoldings) for a CA were used before (see, for instance [2, 3, 24]).

The unfolding for A_0 is trivial—no elements are excited. The unfolding for A_1 is shown on Fig. 5. The unfoldings of CA describe, in fact, the regimes of sequential activation of synapses of a neural network. However, they allow to ascertain the regimes of sequential activation of neurons of the network as well. Indeed, it is well known that a neuron fires the spikes when corresponding synaptic conductance overcomes some threshold value close to maximal conductance. In our case, it corresponds to narrow time windows in the vicinity of transitions of synapses from the state P_{11} (or P_{22}) to P_0 (or similarly to the narrow regions in the vicinity of transitions from black to white rectangles on unfoldings). From the unfolding corresponding to A_1 it is easy to obtain the following order of firings of neurons: $1, 2 \rightarrow 3 \rightarrow 2 \rightarrow 3, 4$ and so on.

For the confirmation of the validity of these results we have performed the direct numerical study of the original system (3)–(6) with architecture shown in Fig. 2. Results of numerics are presented in Fig. 6. The unfoldings of synaptic dynamics were constructed in the following way. There were considered the rectangles $D_i(a, b)$, $i = 1, 2, 3, 4$ on the plane with the horizontal axis corresponding to the time and vertical axis corresponding to the synapse number. The height of $D_i(a, b)$ is 1, the width is $(b - a)$, the lower-left corner has coordinates (a, i), and it is black if the synapse i is active at the instant t ($s_i'(t) > 0$), $a < t < b$—see Fig. 6a. Comparing the unfoldings of the CA and of the network, one may verify that the CA describes adequately sequential dynamics of the network.

One can see that while the process of the activation of synapses (Fig. 6a, b) is in the good correspondence with the unfolding for the CA (Fig. 5) it is not fully periodic. This is related to the fact that the resonance condition $T_2 = 2T_1$ is satisfied only with some (nonzero) accuracy. Nevertheless, first of all, the spacial order of

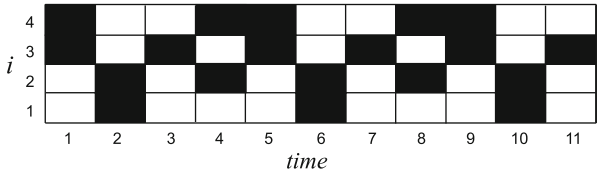

Fig. 5 Unfolding for the periodic attractor A_1 of CA

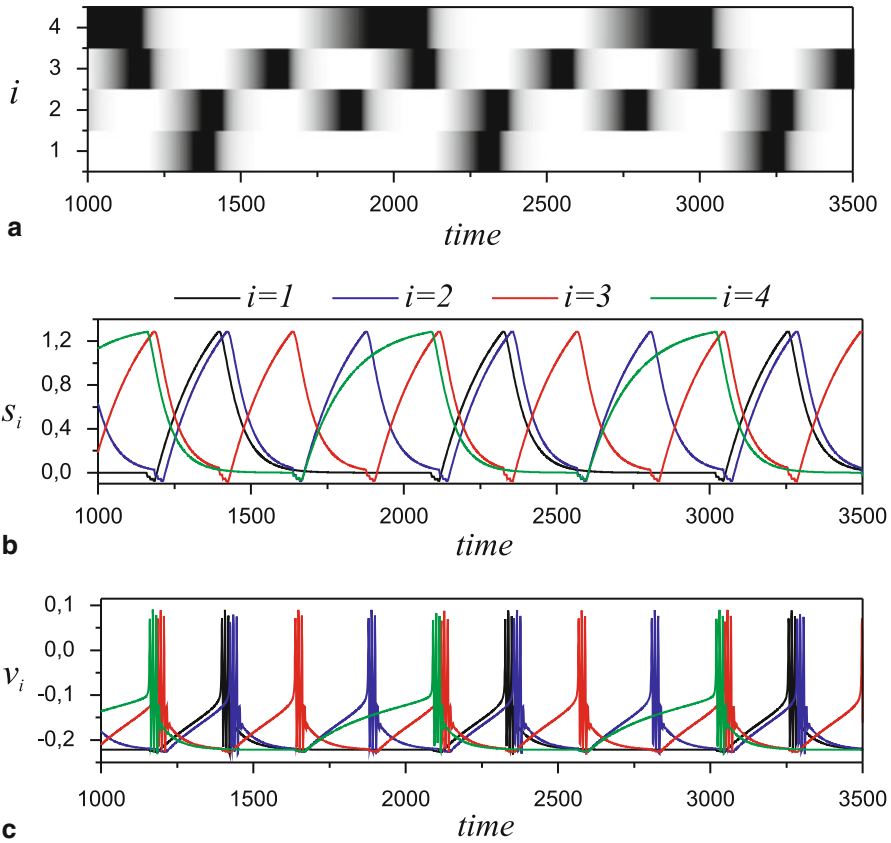

Fig. 6 Unfolding and realizations for established regime in the Morris–Lecar network: **a** unfolding; **b** realizations for synapses; **c** realizations for neurons. The parameters are defined by (9) and (10). The values of threshold constants are: $\theta_{13} = \theta_{23} = \theta_{32} = -0.03$, $\theta_{34} = 0.0$, $\theta_{41} = -0.02$. All other thresholds are set to 2

activation of synapses is exactly the same as for the CA, and, secondly, temporal intervals of activation are approximately the same as for the CA up to the scaling factor T_1.

In Fig. 6c the change of membrane potentials for different neurons is presented. The temporal intervals of oscillatory activity and the rest of neurons occur in the order prescribed by the unfolding for synapses. The number of spikes might be different

for different neurons and different times of observation, since it depends on the state of full network. Nevertheless, on an average the activation of the neuron network also occurs at the instants which are multiples of the same time scale T_1 (see Fig. 6c).

3.2 A Network of Synaptically Coupled Hodgkin–Huxley (HH) Neurons

Now we consider the network of Hodgkin–Huxley neurons [6] coupled by excitatory synapses with short-term plasticity property (the system (5), (6)) which has the architecture shown in Fig. 7a. The network is given by following system of ODE:

$$C\frac{dv_i}{dt} = I_i^{ext} - g_L(v_i - v_L) - g_{Na}m_i^3h_i(v_i - v_{Na}) - \tag{11}$$
$$- g_K n_i^4(v_i + v_K) - g_{syn}s_i(v_i - v_{rev}),$$
$$\frac{dx_i}{dt} = \frac{x_\infty(v_i) - x_i}{\tau_x(v_i)}, \tag{12}$$
$$\frac{dr_i}{dt} = f_1(r_i) - s_i - k_1, \tag{13}$$
$$\frac{ds_i}{dt} = \varepsilon(f_{2i} - s_i - k_2). \tag{14}$$

Eqs. (11) and (12) describe dynamics of membrane potential v_i and gating variable $x_i = m_i, h_i, n_i$, respectively ($i = 1, \ldots, 4$). The terms at the RHS of Eq. (11) describe correspondingly the external, the leakage, the sodium, the potassium, and the synaptic currents flowing through the cell membrane of the i-th neuron. We borrow the equilibrium function $x_\infty(v_i)$ and the characteristic relaxation time $\tau_x(v_i)$ for each ionic current from [5]. The thresholds θ_{12}, θ_{14}, θ_{21}, θ_{23}, θ_{24}, θ_{31}, θ_{42}, θ_{43} are set to 200 to conform to the architecture, while other ones, for definiteness, are chosen as follows: $\theta_{13} = 20$, $\theta_{32} = 10$, $\theta_{34} = 20$, and $\theta_{41} = 50$.

In numerical simulations for Hodgkin–Huxley neuron we use the following values of parameters:

$$C = 1, g_L = 0.3, g_{Na} = 120, g_K = 36, v_L = 10.613, v_{Na} = 115, \tag{15}$$
$$v_K = -12, I_i^{ext} = 6, g_{syn} = 0.066, v_{rev} = 150.$$

The parameters for synapse are defined by (10).

From the architecture of the network one can establish that it has four elementary clusters: $C_1 = \{4 \to 1\}$, $C_2 = \{3 \to 2\}$, $C_3 = \{1 \to 3\}$, $C_4 = \{3 \to 4\}$. Numerical study of the responses related to all clusters allow us to specify the rules F_i for the CA: $F_1(P_0, P_{11}|P_{22}) = P_{21}$, $F_2(P_0, P_{11}|P_{22}) = P_{11}$, $F_3(P_0, P_{11}|P_{22}) = P_{21}$, and $F_4(P_0, P_{11}|P_{22}) = P_{21}$. By using these rules one can see that the CA has the only nontrivial attractor A_3 that is the periodic trajectory (2000) $\to$ (3000) $\to$ (0020) $\to$ (0030) $\to$ (0102) $\to$ (0003) $\to$ (2000). In Fig. 7b a part of the basin of

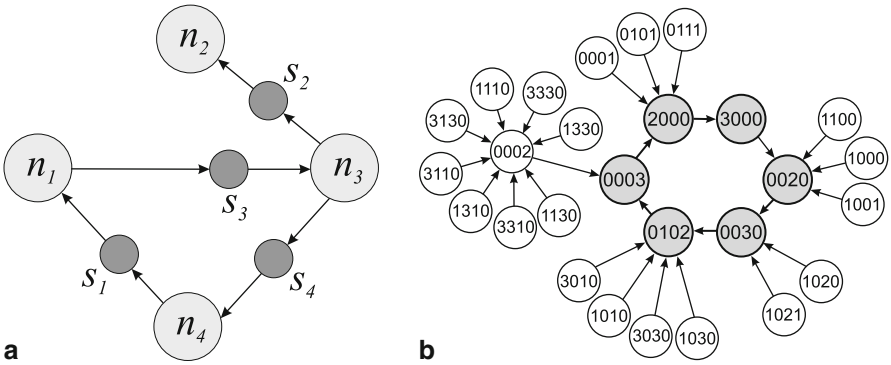

Fig. 7 **a** The architecture of Hodgkin–Huxley neural network. **b** A part of the basin of the periodic attractor A_3

A_3 is shown (the periodic points in the attractor are marked by the grey color). The unfolding of the attractor A_3 is depicted in Fig. 8a which predicts the following order of firings of neurons: $1 \rightarrow 3 \rightarrow 2 \rightarrow 4$ and so on. For comparison the waveforms of synaptic conductances and membrane potentials corresponding to established sequential regime in the Hodgkin–Huxley network are shown in Figs. 8b, c.

4 The Main Scheme of Application of the Approach

On the basis of aforementioned results an approach to study the sequential dynamics of excitatory neural networks can be formulated as follows:

1. Single out the elementary clusters of the neural network and construct the graph of connections $G =< Q_G, K_G >$ (see Sect. 2). The cluster C_i $(i = 1, \ldots, N)$ is defined as part of the network including the i-th and j-th synapses coupled with the $i-$th one through j-th neurons.
2. Determine the responses of each cluster. In other words, for each $i = 1, \ldots, N$, find the responses of the i-th synapse caused by the different (fast and slow) actions of the j-th synapse through the j-th neuron, $j \in K_i$. It is implied that a collective action of groups of several j-th synapses also has to be studied (if K_i consists of more than one element).
3. Using the responses, define the rules of the CA according to Table 1.
4. Study dynamics of CA, find its attractors and unfoldings (or spatio-temporal diagrams, see below) related to them.
5. Describe regimes of sequential dynamics of the original neural network.

Note that in the case of identical thresholds the clusters of the same architecture produce the same responses. Thus, for networks with identical thresholds the number of the studied cases on step 2 (and complexity of CA rules) coincides with the number of different clusters, independently of the size of a network. For example, in a network

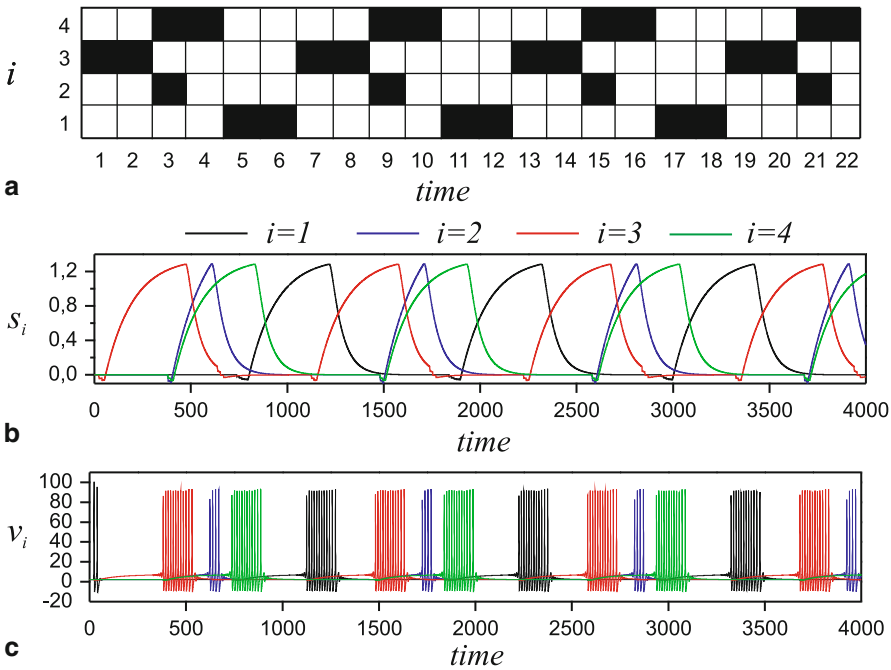

Fig. 8 **a** Unfolding for the periodic attractor A_3 of CA. The realizations for **b** synapses and **c** neurons corresponding to established regime in the Hodgkin–Huxley network. The parameters are defined by (15) and (10). The values of threshold constants are: $\theta_{13} = 20$, $\theta_{32} = 10$, $\theta_{34} = 20$, and $\theta_{41} = 50$. All other thresholds are set to 200

with maximum M synaptic connections per neuron taking into account the synaptic dynamics (two different synaptical responses) the number of studied cases is equal to $M(M + 3)/2$.

5 Conclusion

We have shown that under some conditions the continuous sequential dynamics of excitatory neural network can be reduced to the dynamics of a synaptic CA. Note that it adequately describes "turn on/turn off" behavior of the synapses as well as neurons of the network. The reduction is based on the dynamics of synapses but not on the specific features of neurons. Indeed, the internal dynamics of the neurons may be very complex and even chaotic. Thus, the approach is applicable to a broad set of excitatory neural networks. We have presented examples of its application to analysis of two different excitatory neural networks. Another advantage of our approach is that the numerical integration of the whole system of ODEs is not needed. In fact, the approach requires to study only the responses of an individual synapse onto actions of neighboring (in graph of connections) synapses through corresponding neurons.

It is worth to mention also that the description of network behavior on the base synaptic dynamics is, in fact, caused by the character of neural coupling by itself. In the recently published works [13, 15, 22], it was experimentally shown that relatively small number of so-called strong synaptic connections brings the main contribution in the dynamics of large neural networks. In many neural networks [22], there exists a "skeleton of stronger connections in a sea of weaker ones".

Acknowledgement The authors thank Prof. Valentin Afraimovich for discussion on dynamics of cellular automata. The authors acknowledge financial support from RFBR (Grant Nos. 13-02-00858, 14-02-31873)

References

1. Afraimovich, V.S., Zhigulin, V.P., Rabinovich, M.I.: On the origin of reproducible sequential activity in neural circuits. Chaos **14**, 1123 (2004)
2. Ahn, S., Smith, B.H., Borisyuk, A., Terman, D.: Analyzing neuronal networks using discrete-time dynamics. Phys. D **239**, 515 (2010)
3. Ashwin, P., Orosz, G., Wordsworth, J., Townley, S.: SIAM J. Appl. Dyn. Syst. **6**, 728 (2007)
4. Courbage, M., Nekorkin, V.I.: Map based models in neurodynamics. Int. J. Bifurc. Chaos. **20**, 1631 (2010)
5. Ermentrout, G.B., Terman, D.H.: Foundations of Neuroscience. Springer, New York(2010)
6. Hodgkin, A.L., Huxley, A.F.: A quantitative description of membrane current and its application to conduction and excitation in nerve. J. Physiol. **117**, 500 (1952)
7. Ibarz, B., Casado, J.M., Sanjuan, M.A.F.: Map-based models in neuronal dynamics. Phys. Rep. **501**, 1 (2011)
8. Izhikevich, E.: Dynamical Systems in Neuroscience. MIT Press, Cambridge (2007)
9. Jones, L.M., Fontanini, A., Sadacca, B.F., et al.: Natural stimuli evoke dynamics sequences of states in sensory cortical ensembles. Proc. Natl. Acad. Sci. U S A **104**, 18772 (2007)
10. Just, W., Ahn, S., Terman, D.: Minimal attractors in digraph system models of neuronal networks. Phys. D **237**, 3186 (2008)
11. Kandel, E.R., Schwartz, J.H., Jessell, T.H.: Principles of Neural Science. Prentice-Hall, London (1991)
12. Komarov, M.A., Osipov, G.V., Suykens, J.A.K., Rabinovich, M.I.: Numerical studies of slow rtythms emergence in neural microcircuits: Bifurcations and stability. Chaos **19**, 015107 (2009)
13. Koulakov, A.A., Hromadka, T., Zador, A.M.: Correlated connectivity and the distribution of firing rates in the neocortex. J. Neurosci. **29**, 3685 (2009)
14. Lee, C.-C.J., Anton, M., Poon, C.-S., McRae, G.J.: A kinetic model unifying presynaptic short-term facilitation and depression. J. Comput. Neurosci. **26**, 459 (2009)
15. Lefort, S., Tomm, C., Floyd Sarria, J.C., Peterson, C.C.H.: The excitatory neuronal network of the C2 barrel column in mouse primary somatosensory cortex. Neuron **61**, 301 (2009)
16. Mazur, O., Laurent, G.: Transient dynamics versus fixed point in odor representations by locust antennal lobe projection neurons. Neuron **48**, 661 (2005)
17. Morris, C., Lecar, H.: Voltage oscillations in the barnacle giant muscle fiber. Biophys. J. **35**, 193 (1981)
18. Nekorkin, V.I.: Nonlinear oscillations and waves in neurodynamics. Physics-Uspekhi. Adv. Phys. Sci. **51**, 295 (2008)
19. Nekorkin, V.I., Kasatkin, D.V., Dmitrichev, A.S.: Transient dynamics in a small ensemble of synaptically coupled Morris-Lecar neurons. Radiophys. Quantum Electron. **53**, 45 (2010)
20. Rabinovich, M.I., Varona, P.: Robust transient dynamics and brain functions. Front. Comput. Neurosci. **5**, 1 (2011)

21. Rabinovich, M.I., Varona, P., Selverston, A.I., Abarbanel, H.D.I.: Dynamical principles in neuroscience. Rev. Mod. Phys. **78**, 1213 (2006)
22. Song, S., Sjostrom, P.J., Reigl, M., et al.: Highly nonrandom features of synaptic connectivity in local cortical circuits. PLoS Biol. **3**, 0507 (2005)
23. Stopfer, M., Jayaraman, V., Laurent, G.: Intensity versus identity coding in an olfactory system. Neuron **39**, 991 (2003)
24. Terman, D., Ahn, S., Wang, X., Just, W.:Reducing neuronal networks to discrete dynamics. Physica D **237**, 324 (2008)
25. Trommershauser, J., Zippelius, A.: Biophysical model of a single synaptic connection: Transmission properties are determined by the cooperation of pre- and postsynaptic mechanisms. Neurocomputing **38–40**, 65 (2001)
26. Wong, A.Y.C., Graham, B.P., Billups, B., Forsythe, I.D.: Distinguishing between presynaptic and postsynaptic machanisms of short-term depression during action potential trains. J. Neurosci. **23**, 4868 (2003)
27. Zucker, R.S., Regehr, W.G.: Short-term synaptic plasticity. Annu. Rev. Physiol. **64**, 355 (2002)

Synchronization of Delayed-Feedback Semiconductor Lasers and Its Application in Optical Communication

Alexander N. Pisarchik and Flavio R. Ruiz-Oliveras

Abstract Semiconductor lasers with optical injection or delayed feedback have been widely studied because of their potential applications in optical communication using chaos synchronization. The delayed feedback through an external cavity or mirror enriches the laser dynamics so that different bifurcations (saddle-node, Hopf, period-doubling, torus, and crisis) arise when the coupling strength and/or delay time are varied. Recent research works on coupled semiconductor lasers have examined various mechanisms for their synchronization that may be useful to design optical communication networks. When the coupled lasers behave in a chaotic manner, different synchronization types can be achieved ranging from lag and phase synchronization to a completely synchronized motion. The route to synchronization of these lasers in a bistability domain displays a series of bifurcations with respect to the coupling strength. Complete chaos synchronization between the master and the slave lasers has been used to send information using the chaotic carrier. The message is encrypted in the chaotic output of the laser in the transmitter and then recovered by comparing with the chaotic output of the laser in the receiver. In the current chapter, a novel method of optical communication based on the combination of complete and generalized synchronization of chaotic semiconductor lasers is described.

1 Introduction

We currently live in the era of information, when societies, commerce, government, and private institutions require secure and fast communication. With the growing demand of electronic commerce, society in general has the need to keep its information safe while traveling through the network at high speeds. With the actual existence of the fiber optics network, semiconductor lasers are ideal candidates to build such communication systems.

In communication systems based on chaos synchronization [3, 26], information is are embedded within a chaotic carrier in a transmitter and recovered in a receiver

A. N. Pisarchik (✉) · F. R. Ruiz-Oliveras
Centro de Investigaciones en Optica, Loma del Bosque 115,
Lomas del Campestre, Leon, Guanajuato, Mexico
e-mail: apisarch@cio.mx

H. González-Aguilar, E. Ugalde (eds.), *Nonlinear Dynamics New Directions,*
Nonlinear Systems and Complexity 12, DOI 10.1007/978-3-319-09864-7_6

upon synchronization with the former. Due to their high relaxation oscillation frequencies (around tens of gigahertz) and direct comparability with existing optical fiber communication technology, semiconductor lasers have attracted much attention [22], especially after successive experiments with the Athens' fiber networks [2]. Delayed feedback or coupling in these lasers [12, 18] results in chaotic oscillations with a large information entropy. The performance of these communication systems largely depends on the quality of chaos synchronization, i.e., the synchronization error should be minimized. Depending on a particular application of chaotic communication, different encoding and decoding schemes, such as chaos masking, chaos shift keying, and chaos modulation have been developed [26].

In this chapter, we review different encryption schemes used in communication systems based on synchronization of chaotic semiconductor lasers. First, we describe a simple model which simulates dynamics of a solitary semiconductor laser with delayed feedback, and then we extend this model to a dual-cavity semiconductor laser. Finally, we analyze synchronization of two semiconductor lasers coupled in a master–slave configuration and characterize the system performance for optical communication.

2 Semiconductor Laser Model

The active media of an ordinary semiconductor laser is in the junction of the *n*- and *p*-type semiconductor materials. Since these lasers belong to class-B lasers [1] in which the polarization decay rate is much faster than the decay rates of the electric field and population inversion, their dynamics is an asymptotically stable fixed point resulting in a continuous wave (cw) laser emission. Usually, the dynamics of ordinary semiconductor lasers is regulated by two differential equations, one for the electric field and another one for nonequilibrium carriers.

2.1 Semiconductor Laser with Optical Feedback

Technically, optical feedback can be easily realized by injecting the laser radiation back into the laser cavity after its reflection from an external mirror, as shown in Fig. 1. The delayed optical feedback in a semiconductor laser induces an additional degree of freedom that enriches its dynamics so that intensity oscillations can be possible [28].

By varying the parameters of the external cavity, i.e., the reflectivity of the external mirror and the distance between the mirror and the laser facet, different dynamical regimes (cw, periodic, quasiperiodic, chaotic, and low frequency fluctuations) can be obtained [4]. The adequate model for a semiconductor laser with delayed optical feedback was developed by Lang and Kobayashi [6, 12]:

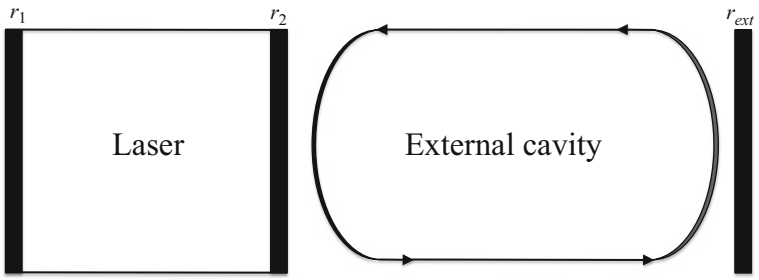

Fig. 1 Semiconductor laser with an external cavity. r_1, r_2 are the laser facet reflectivities and r_{ext} is the reflectivity of an external mirror that causes delayed optical feedback

$$\begin{aligned}
\dot{E}(t) &= (1 + j\alpha)\left(\frac{gN(t) - N_0}{1 + s|E(t)|^2} - \frac{1}{\tau_p}\right) E(t) + \kappa E(t - \tau)\exp(-i\phi) \\
\dot{N}(t) &= \frac{I}{e} - \frac{N(t)}{\tau_n} - \frac{g(N(t) - N_0)}{1 + s|E(t)|^2}|E(t)|^2 \\
\kappa &= \frac{1 - r_2^2}{\tau_d}\frac{r_{ext}}{r_2},
\end{aligned} \tag{1}$$

where $E(t)$ is the amplitude of the slow varying complex electric field, $|E(t)|^2 = P$ is the optical power or intensity in terms of the number of photons, $N(t)$ is the carrier number, α is the linewidth enhancement factor, g is the gain parameter, N_0 is the carrier number at transparency, s is the gain saturation coefficient, τ_p is the photon lifetime, κ is the feedback parameter, τ is the external cavity round trip time, $\varphi = \omega\tau$ is the phase due to the external cavity, ω is the free running laser frequency, I is the bias current (at the first laser threshold $I_{th} = 14.7$ mA), e is the elementary charge, τ_n is the carrier lifetime, and τ_d is the semiconductor laser cavity round trip time. Typical parameter values [15, 27] are present in Table 1.

Since the laser dynamics is regulated by the parameters of the external cavity, τ, ϕ, and κ are varied to obtain different dynamical regimes. The feedback parameter κ is given in per nanosecond (for reference, $\kappa = 10\ \text{ns}^{-1}$ corresponds to a 0.3 % reflectivity of the external mirror and $\tau = 1$ ns in a 15-cm external cavity filled with air).

The bifurcation diagram of the laser peak intensity shown in Fig. 2 demonstrates a period-doubling route to chaos in the external cavity semiconductor laser when the cavity length (feedback time) is increased. Both the phase $\phi = 0$ and the feedback strength $\kappa = 10\ \text{ns}^{-1}$ are kept constant. One can see that depending on the length of the external cavity, one can obtain either fix point (FP), period 1 (P1), period 2 (P2), period 3 (P3), period 4 (P4), quasiperiodicity (QP), or chaos (CH). If the external cavity length is small enough, the laser works in a cw regime marked as FP on the bifurcation diagram. When $\tau = 0.071$ ns, a Hopf bifurcation (HP) appears and the laser begins to oscillate in a P1 regime. For larger τ, two period-doubling bifurcations are observed, the first one at $\tau \approx 0.09$ ns, where P1 is transformed to P2; and the second one at $\tau \approx 0.095$ ns, where P2 changes to P4. A torus bifurcation (T) results in

Table 1 Typical parameter values used in the Lang–Kobayashi model

Parameter	Value
α	3
g	1.5×10^{-8} ps^{-1}
N_0	1.5×10^{8}
s	10^{-8}
τ_p	2 ps
τ_n	2 ns
e	1.6×10^{-19} C
τ_d	6.6 ps
r_2^2	0.3
I	29 mA

quasiperiodicity and then chaos arises as τ is further increased. At $\tau = 0.111$ ns, the chaotic attractor undergoes crisis, that gives rise to a P3 attractor born in a saddle-node bifurcation. Finally, the P3 undergoes a new cascade of period-doubling bifurcations terminated in chaos.

The power spectra in Fig. 3 illustrate how the laser dynamics changes with τ. Figure 3a shows the power spectrum for the P1 regime at $\tau = 0.08$. The oscillation frequency is around $f_m = 6$ GHz, that corresponds to the relaxation oscillation frequency of the semiconductor laser without an external cavity. Figure 3b shows the power spectrum of the P2 regime when $\tau = 0.092$. The relaxation oscillation frequency appears again together with its subharmonic frequency $f_m/2 = 3$ GHz. The power spectrum of the P3 window at $\tau = 0.112$ ns is shown in Fig. 3c. One can also see f_m and its subharmonic frequencies $f_m/3 = 2$ GHz and $2f_m/3 = 4$ GHz. At $\tau = 0.096$ ns, when P4 appears, the corresponding subharmonic frequencies $f_m/4$, $f_m/2$, and $3f_m/4$ emerge in the spectrum, as seen in Fig. 3d. The power spectrum of the QP regime at $\tau = 0.097$ ns is shown in Fig. 3e. In this regime, three frequencies

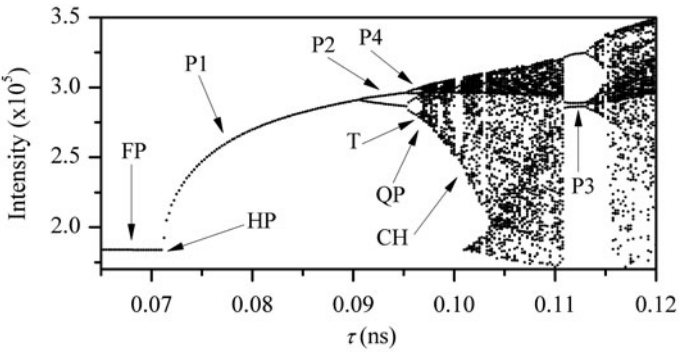

Fig. 2 Bifurcation diagram of laser peak intensity with respect to external cavity round trip time

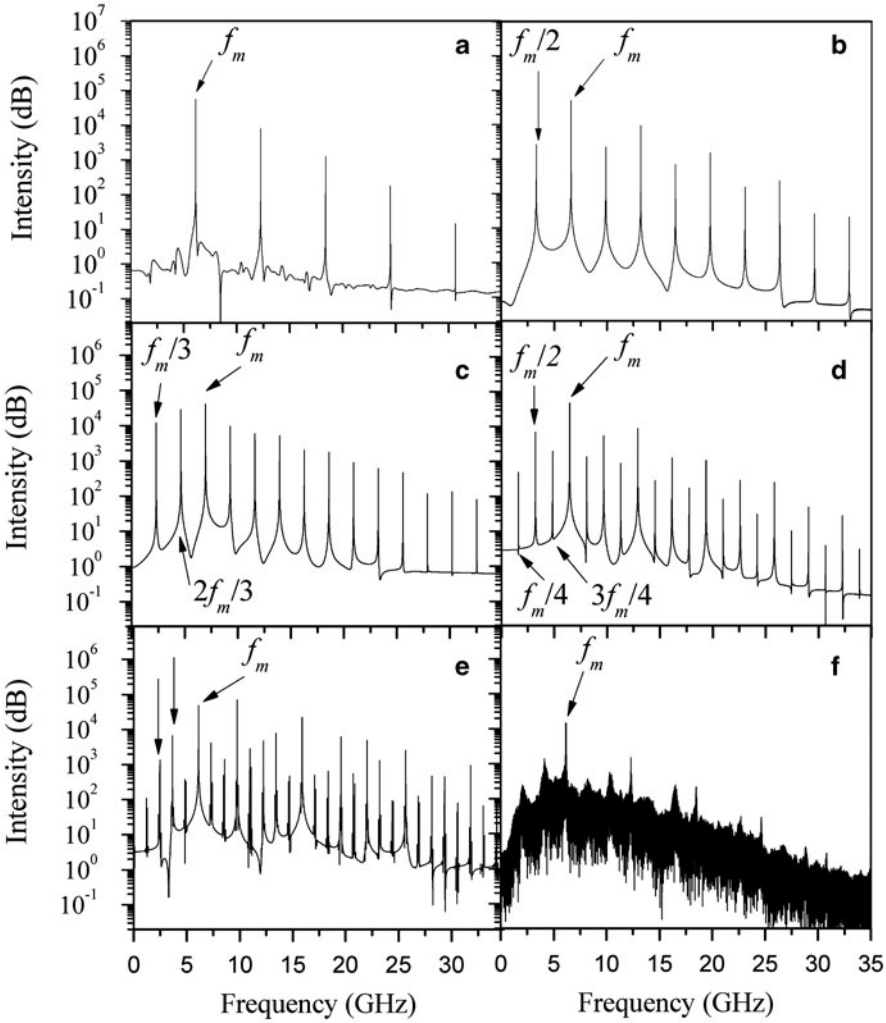

Fig. 3 Power spectra of **a** period-1, **b** period-2, **c** period-3, **d** period-4, **e** quasiperiodic, and **f** chaotic regimes. f_m is the relaxation oscillation frequency of the solitary laser

exist and the ratios between f_m and these frequencies are irrational numbers. The frequencies marked by the arrows in Fig. 3e are 2.47 and 3.654 GHz, and the ratios are $f_m/2.47 = 2.42914\ldots$ and $f_m/3.654 = 1.64203\ldots$. Figure 3f shows the broad band spectrum of the chaotic regime at $\tau = 0.105$ ns with the dominant frequency at f_m.

A semiconductor laser with an external cavity, similar to many other complex dynamical systems, such as electronic circuits, turbulent flows, etc. [10, 14], exhibits the coexistence of attractors [19]. In a multistability range, a particular attractor can be searched by changing initial conditions. Figure 4 shows two examples of the bifurcation diagrams of the laser peak intensity constructed by varying initial

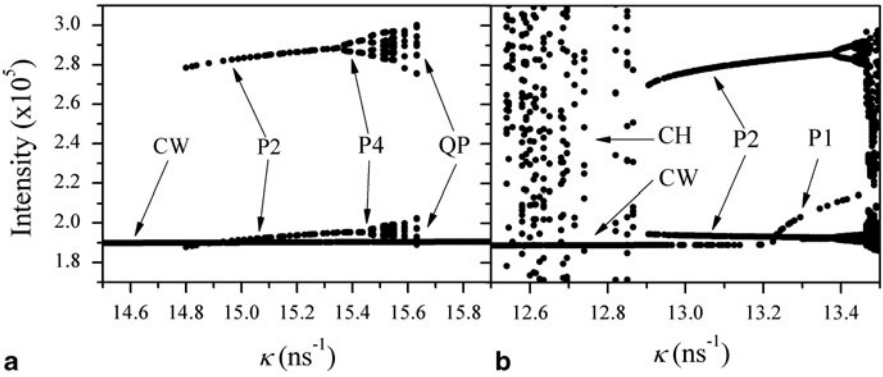

Fig. 4 Bifurcation diagrams of laser peak intensity with feedback strength κ as a control parameter for **a** $\phi = 0$ and $\tau = 0.2$ ns and **b** $\phi = \pi$ and $\tau = 0.4$ ns. The diagrams are obtained by varying initial conditions. The coexistence of different periodic regimes with CW and chaos is seen

conditions and using the continuation (branch tracing) method [21]. The regions of the coexistence of FP (CW) with P2, P4, QP, and chaos, and the regions of the coexistence of P1 with P2 and chaos can be clearly distinguished in these diagrams.

For better visualization, the dynamical states of the semiconductor laser with delayed optical feedback are plotted in the space of the control parameters κ, τ, and ϕ [19]. Figure 5a shows the state diagram in the parameter space of the feedback strength κ and the external round trip time τ, with $\phi = m\pi$ and $m = 0, 2, 4, \ldots$. Figure 5b shows the dynamical regimes in the parameter space of ϕ and τ for $\kappa = 25$ ns^{-1} and Fig. 5c in the parameter space of κ and ϕ for $\tau = 0.25$ ns. The black, yellow, blue, red, and white regions correspond, respectively, to FP, P1, P2, P3, QP, and chaos. One can see that the dynamics of the external-cavity semiconductor laser repeats every 2π. For small feedback strengths ($\kappa < 7.5$), the dynamics has a regular behavior (FP and periodic orbits) and for larger feedback strengths ($\kappa > 7.5$), it is QP or chaotic. The boundaries between black and yellow regions are Hopf bifurcations, between yellow and blue regions are period-doubling bifurcations, and the boundaries between the white regions and any color regions are either crisis or torus bifurcations.

2.2 *Semiconductor Laser with Two Optical Feedbacks*

A second external cavity can be added to the semiconductor laser to stabilize its output [16–18]. The advantage of this technique is that the position and reflectivity of the second mirror do not have to be very accurate. Figure 6 shows the optical scheme for the semiconductor laser with two external cavities, where r_1 and r_2 are the laser facet reflectivities, and r_3 and r_4 are the reflectivities of the external mirrors in the external cavities. The Lang–Kobayashi model is now given as

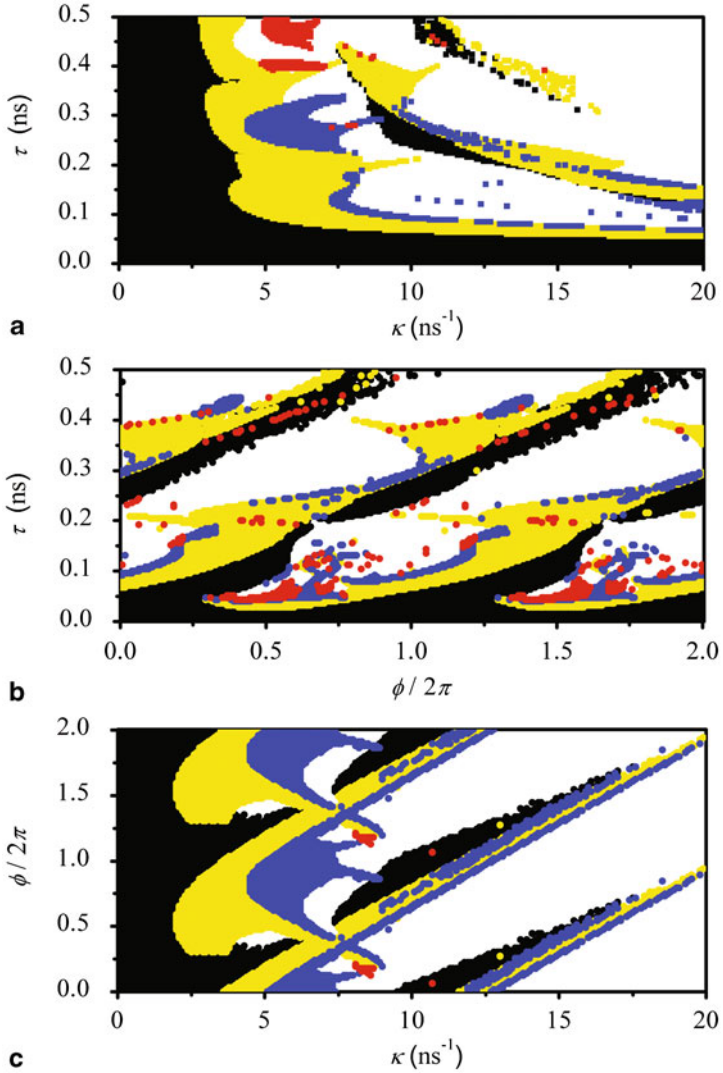

Fig. 5 State diagrams in parameter spaces of **a** κ and τ for $\phi = 0$, **b** ϕ and τ for $\kappa = 10\,\mathrm{ns}^{-1}$, and **c** κ and ϕ for $\tau = 0.25$ ns. The *black*, *yellow*, *blue*, *red*, and *white* regions indicate, respectively, FP, P1, P2, P3, QP, and chaotic regimes

$$\dot{E}(t) = (1 + j\alpha)\left(\frac{gN(t) - N_0}{1 + s|E(t)|^2} - \frac{1}{\tau_p}\right)E(t) + \kappa_1 E(t - \tau_1)\exp(-i\phi_1) + \kappa_2 E(t - \tau_2)\exp(-i\phi_2),$$
$$\dot{N}(t) = \frac{I}{e} - \frac{N(t)}{\tau_n} - \frac{g(N(t) - N_0)}{(1 + s|E(t)|^2)}|E(t)|^2, \tag{2}$$

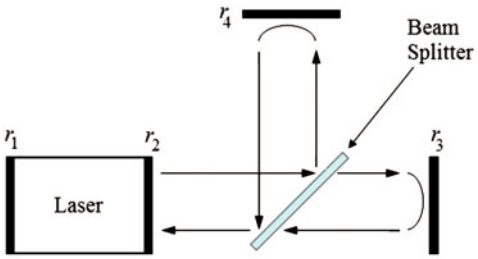

Fig. 6 Optical scheme of a semiconductor laser with two external cavities

where $\kappa_{1,2}$, $\tau_{1,2}$, and $\phi_{1,2}$ are the feedback parameter, cavity round trip time, and the phases of the first and second external cavities.

For this particular case, the phases of each cavity given as $\phi_{1,2} = \omega\tau_{1,2}$ are not kept independent and are related to the lengths of their corresponding external cavity. The bifurcation diagram of the laser peak intensity with respect to the ratio τ_2/τ_1 is shown in Fig. 7a. The round trip time of the first external cavity is kept constant at $\tau_1 = 0.22$ ns. The feedback strengths for both cavities are the same, $\kappa_{1,2} = 25\ \text{ns}^{-1}$. In the region where $\tau_2/\tau_1 < 0.4$, the dynamics is very sensitive to the ratio between the external round trip times. The enlarged part of the bifurcation diagram for $\tau_2/\tau_1 < 0.4$ is shown in Fig. 7b. A number of bifurcations, such as torus, inverse torus, crisis, Hopf, and inverse Hopf bifurcations are present. In the region near $\tau_2/\tau_1 = 1$, a chaotic window exists.

As in the case of the laser with a single external cavity, the state diagram in the two-dimensional parameter space of the external cavity round trip times τ_2/τ_1, and the ratio of feedback strengths κ_2/κ_1 yields much better representation of the overall dynamics of the laser with two external cavities. This diagram is shown in Fig. 8. The parameters of the first external cavity are fixed to $\tau_1 = 0.22$ ns and $\kappa_1 = 25\ \text{ns}^{-1}$. The color nomenclature is the same as used before.

In Fig. 8, one can distinguish the phase-locking regions, where the frequencies of two coupled oscillators are of some rational multiples of each other. The combined locked motion then becomes periodic, and the locking regions called Arnold tongues are observed. When the frequencies are not rational multiples of each other, the behavior is either quasiperiodic or chaotic. The Arnold tongues correspond to either the steady state (black regions) or periodic regimes (yellow, blue, and red). Within these regions, the phases of the two external cavities are locked, so that the laser evolves into the stable steady state or periodic regimes. The minima of the tongues occur when $\tau_2/\tau_1 = 1/4, 1/2, 3/4, \ldots$. It is remarkable that the diagram is almost symmetric around $\tau_2/\tau_1 = 1$. The asymmetry that may appear is due to multistability in the phase-locked regions. The addition of the second cavity can stabilize the laser dynamics [7]. It is clearly seen in Fig. 8 that the area corresponding to the stabilized dynamics (black region) is greater than any other region.

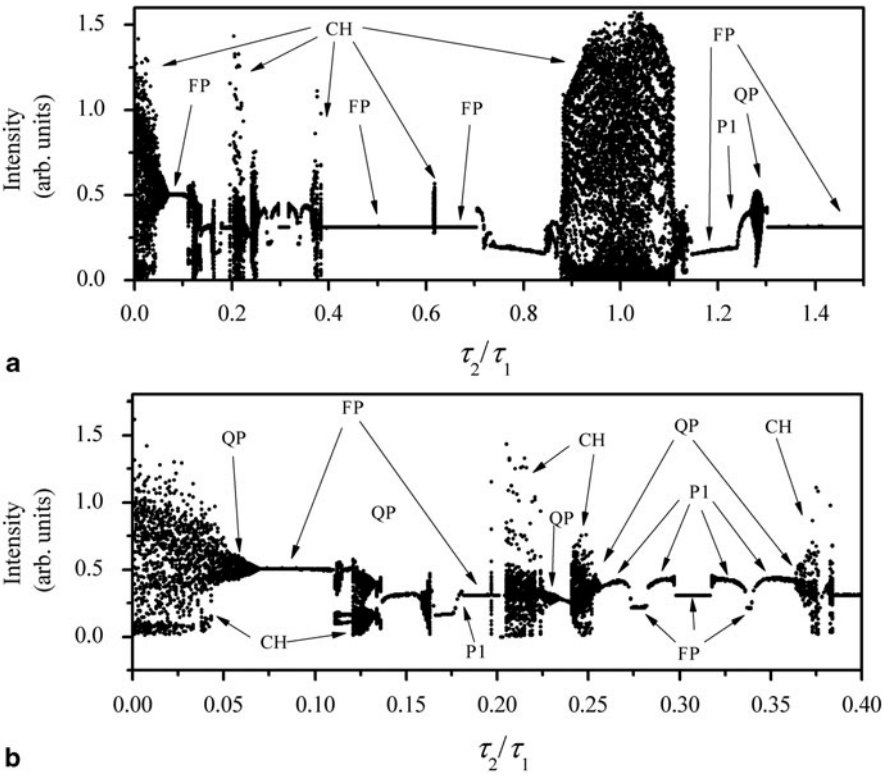

Fig. 7 Bifurcation diagram of peak laser intensity with respect to τ_2/τ_1. $\tau_1 = 0.22\,\text{ns}$, $\kappa_{1,2} = 25\,\text{ns}^{-1}$

3 Coupled Semiconductor Lasers

One of the simplest ways to synchronize two semiconductor lasers is to inject the output radiation of one laser into another. The laser whose signal is being injected is called *master laser* (ML), while the laser which receives the external radiation from ML is called *slave laser* (SL). Figure 9 represents a general optical scheme of two semiconductor lasers, each with external feedback, coupled in a master–slave configuration.

The dynamics of ML is described by Eq. (1). The optical injection from ML has to be added to the equation for the electric field of SL. When the laser optical frequencies are matched, the equation for a slow varying complex field of SL is written as

$$\dot{E}_s(t) = (1 + j\alpha)\left(\frac{gN_s(t) - N_0}{1 + s|E_s(t)|^2} - \frac{1}{\tau_p}\right)E_s(t) + \kappa E_s(t - \tau)\exp(-i\phi) + \gamma E_m(t),$$

$$\gamma = \eta\frac{\sqrt{1 - r^2}}{\tau_d r}, \tag{3}$$

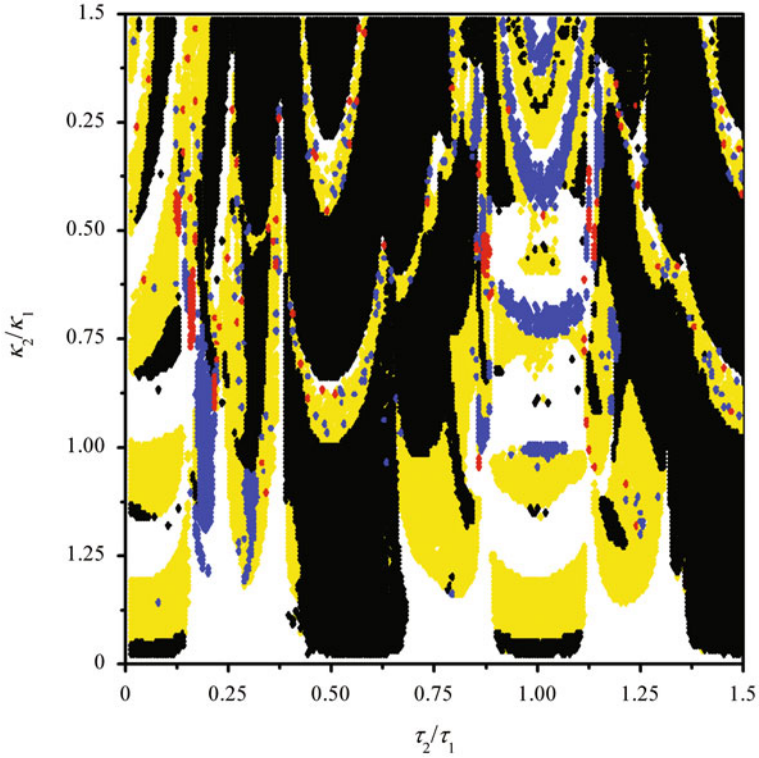

Fig. 8 State diagram in parameter space of τ_2/τ_1 and κ_2/κ_1 for $\tau_1 = 0.22$ ns and $\kappa_1 = 25$ ns^{-1}

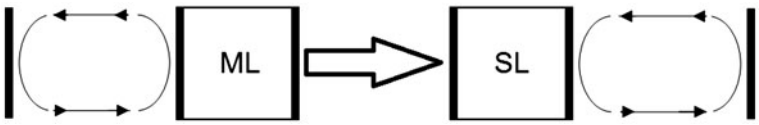

Fig. 9 Master-slave laser configuration to obtain synchronization

where the subscripts m and s stand for ML and SL, γ is the coupling parameter, η is the loss different than that introduced by the laser facet, and r is the laser facet reflectivity. The other parameters are the same as in Eq. (1). The coupling parameter η is given in per nanosecond. $\gamma = 50$ ns^{-1} corresponds to the case when approximately 22 % of the ML power is injected into SL.

3.1 Synchronization of Unidirectionally Coupled Lasers

During the last two decades, synchronization of different lasers, e.g., CO_2 [11, 25], fiber [29], and semiconductor [12], has been extensively studied. Semiconductor lasers have caught a special attention for communication because their relaxation oscillation frequencies are very high (around several gigahertz), which is approximately four orders of magnitude higher than relaxation oscillation frequencies of gas, solid-state, and fiber lasers. Several papers were devoted to synchronization of two coupled chaotic semiconductor lasers with external cavities (see, for instance, [8, 9, 13, 23]).

To measure synchronization between two lasers, one can use the cross-correlation function defined as [24]:

$$C(t) = \frac{\langle P_m(t)P_s(t-t') - \overline{P_m}\,\overline{P_s}\rangle}{\sigma_m \sigma_s}, \tag{4}$$

where $\langle \cdots \rangle$ stands for the time average and $\overline{P_m}$, $\overline{P_s}$, σ_m, and σ_s are the means and standard deviations of the ML and SL powers, respectively. The cross-correlation takes a value between 0 (no synchronization) and 1 (complete synchronization).

When ML and SL are in a chaotic regime and the coupling is low, the phase trajectories evolve independently. Figure 10a shows the ML vs. SL intensities for $\gamma = 5\ \text{ns}^{-1}$. For this case, the cross-correlation is close to zero. When the coupling between the lasers is strong enough ($\gamma = 70\ \text{ns}^{-1}$), complete synchronization takes place, as shown in Fig. 10b. Figure 10c shows the cross-correlation as a function of the coupling γ. To obtain complete synchronization, the lasers should be identical.

3.2 Synchronization of Multistable Lasers

As was already mentioned in Sect. 2, a semiconductor laser with delayed optical feedback exhibits the coexistence of attractors at certain parameters. Therefore, synchronization of two coupled lasers is not only dependent on the coupling strength but also on the initial conditions.

Here, we will show how two coupled semiconductor lasers with coexisting attractors are synchronized. First, we consider the lasers in which a stable steady state and chaotic attractor coexist. The parameters are the same as the ones used above for Fig. 4b. When the feedback strength is set to $\kappa = 12.7\ \text{ns}^{-1}$, the coexistence of FP with P1, P2, P4, and chaos, and the coexistence of P1 with P2 attractors are observed. Figure 11 shows the bifurcation diagram of the SL peak intensity (black squares) when ML is in a cw regime. One can see that the cw injection from ML stabilizes either a fixed point or a periodic orbit in the chaotic SL. As the coupling is increased, a series of Hopf bifurcations (at $\gamma = 4.5\ \text{ns}^{-1}$ and $\gamma = 19.75\ \text{ns}^{-1}$) appears giving rise to a periodic orbit, whose frequency (red and blue squares) depends on the coupling. One of the frequencies (red squares) is close to the laser relaxation

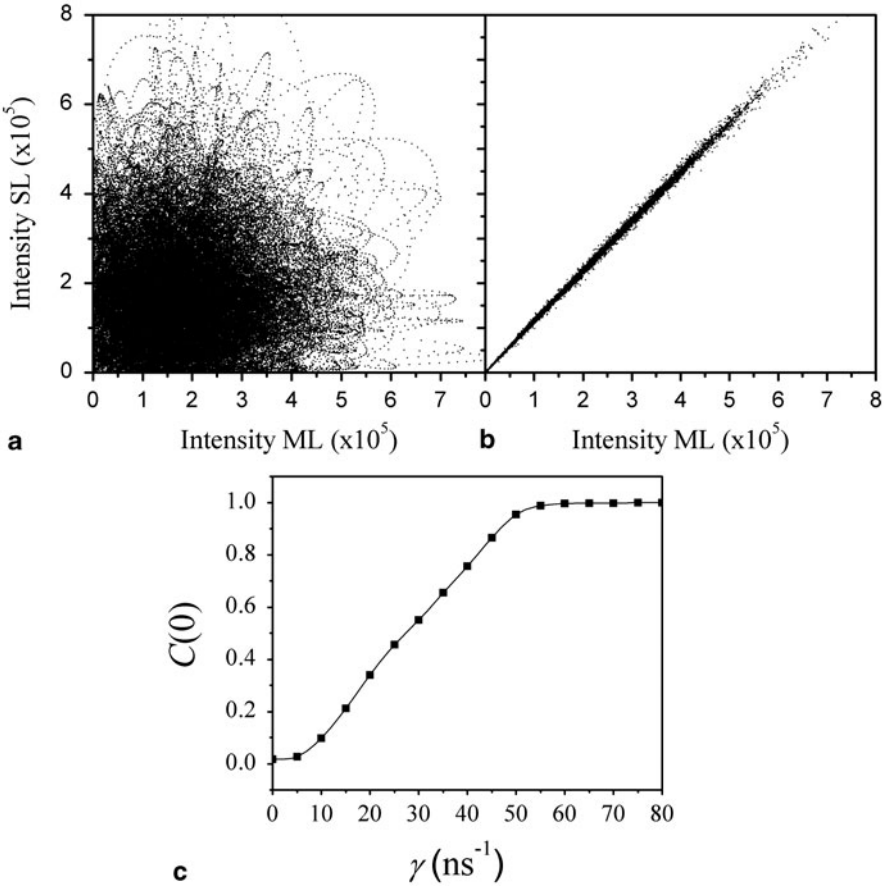

Fig. 10 Phase space plots of **a** master vs. slave laser for $\gamma = 5$ ns^{-1}, **b** master vs. slave laser for $\gamma = 70$ ns^{-1}, and **c** cross-correlation vs. coupling γ

oscillation frequency ($f_m = 6$ GHz), while another frequency (blue squares) is much higher (about 4 GHz more) than the first one. The coexistence of two attractors (periodic orbit and fixed point) in SL is observed between two vertical lines in Fig. 11. At $\gamma = 44$ ns^{-1}, an inverse Hopf bifurcation (IHP) arises, and for larger γ, only the cw regime remains. In a certain way, for a strong coupling, we can say that ML and SL are "synchronized," since both end up having the same dynamics.

Now, let ML be in a chaotic regime while SL initially is in a stable steady state (cw). For this case, already for a very small coupling, SL behaves chaotic and the cross-correlation between the laser intensities increases as γ is increased. The behavior is the same as for the monostable lasers shown in Fig. 10c, when both lasers are chaotic.

Next, we turn to the bistability region, where a cw regime coexists with a periodic orbit. When the feedback is set to $\kappa = 15.1$ ns^{-1} and other parameters are the same as for Fig. 4a, we observe the coexistence of cw and P2. First, we consider the case

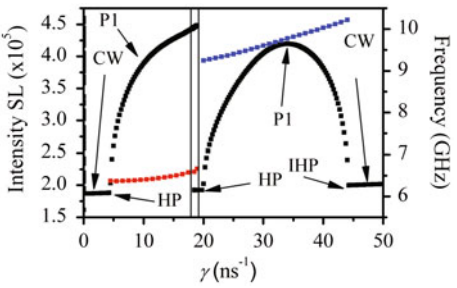

Fig. 11 Bifurcation diagram of SL peak intensity (*black squares*) and oscillation frequency (*red* and *blue squares*) as functions of coupling parameter γ, when ML is in a cw regime

when ML is in the P2 regime, while SL being uncoupled is in a cw regime. For this case, the SL dynamics is very rich. Figure 12a, b show respectively the bifurcation diagram of the SL peak intensity and the cross-correlation between ML and SL. The chaotic regime switches to a quasiperiodic one at $\gamma \approx 13$ ns^{-1}. At $\gamma \approx 47$ ns^{-1}, an inverse torus bifurcation appears leading to P2 and complete synchronization between the lasers. From Fig. 12b, one can see that the cross-correlation resembles the dynamics. The lowest correlation is observed when SL is chaotic. Then, as the coupling is increased, the correlation grows up when the laser switches to a quasiperiodic regime. After that, the correlation decreases, but it remains higher than in the chaotic regime. Finally, for a very strong coupling, SL is synchronized with ML to the period 2.

Finally, we consider the case when ML is in a cw regime and SL initially in a period 2. Figure 13 shows the bifurcation diagram of the SL peak intensity (black squares) and the oscillation frequency (red squares) as functions of the coupling parameter γ. The injection of the cw radiation into the periodically oscillating SL induces a fixed point already at a very low coupling. As γ is increased, a periodic orbit is born in a Hopf bifurcation at $\gamma \approx 7$ ns^{-1} and dead in an inverse Hopf bifurcation at $\gamma \approx 43$ ns^{-1}. One can see that this case resembles the previous case, when ML

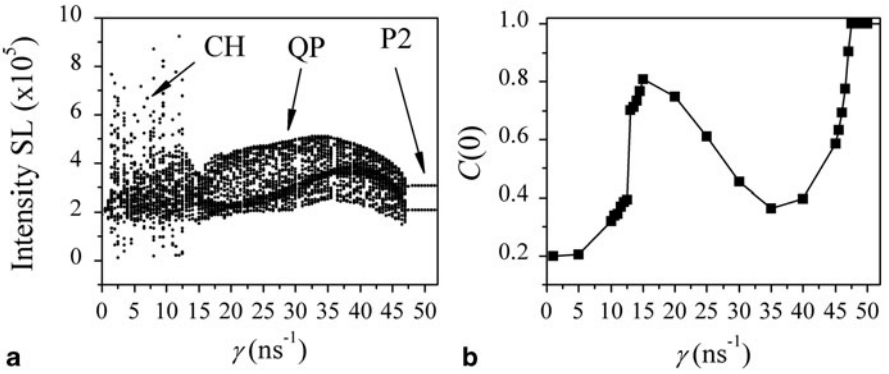

Fig. 12 **a** Bifurcation diagram of SL peak intensity. **b** Cross-correlation between ML and SL as functions of coupling parameter γ, when ML is in period 2 and SL initially in cw

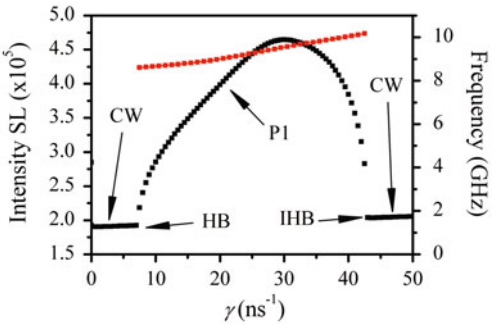

Fig. 13 Bifurcation diagram of SL peak intensity (*black squares*) and frequency of induced periodic orbit (*red squares*) as functions of γ, when ML is in cw and SL initially in period 2

was in cw and SL in a chaotic regime. In general, when there is a coupling between the lasers, the ML dynamics will dictate the SL's overall behavior. When a periodic orbit and chaos coexist and ML initially is in the periodic state, the SL dynamics is very similar to that shown in Fig. 12. On the other hand, when ML is chaotic, SL becomes also chaotic and at a strong enough coupling, the lasers are completely synchronized. It should be noted that when the lasers are monostable and both stay in a cw regime being uncoupled, the dynamical behavior of the coupled system is similar to that shown in Figs. 11 and 13.

4 Communication with Chaotic Semiconductor Lasers

A general communication system contains a transmitter and a receiver. The transmitter is in charge of modulating a signal into a series of bits, which can be sent to the receiver. The important application of chaotic synchronization to communication is that information may be sent using a chaotic carrier that allows signal encryption in a wide frequency range. In this case, both the transmitter and the receiver generate chaotic waveforms. A message is added to the chaotic output of the transmitter to be recovered after the filtering in the receiver, which must be synchronized with the transmitter. Figure 14 illustrates how this scheme works.

4.1 Encryption Schemes

Among many encoding and decoding schemes, here we consider only three most popular schemes commonly used in communication systems based on chaotic synchronization. These are chaotic modulation, chaotic masking, and shift keying.

4.1.1 Chaotic Modulation

Chaotic modulation resembles the typical amplitude modulation (AM). The message is added by modulating the emitter's chaotic carrier according to the following expression:

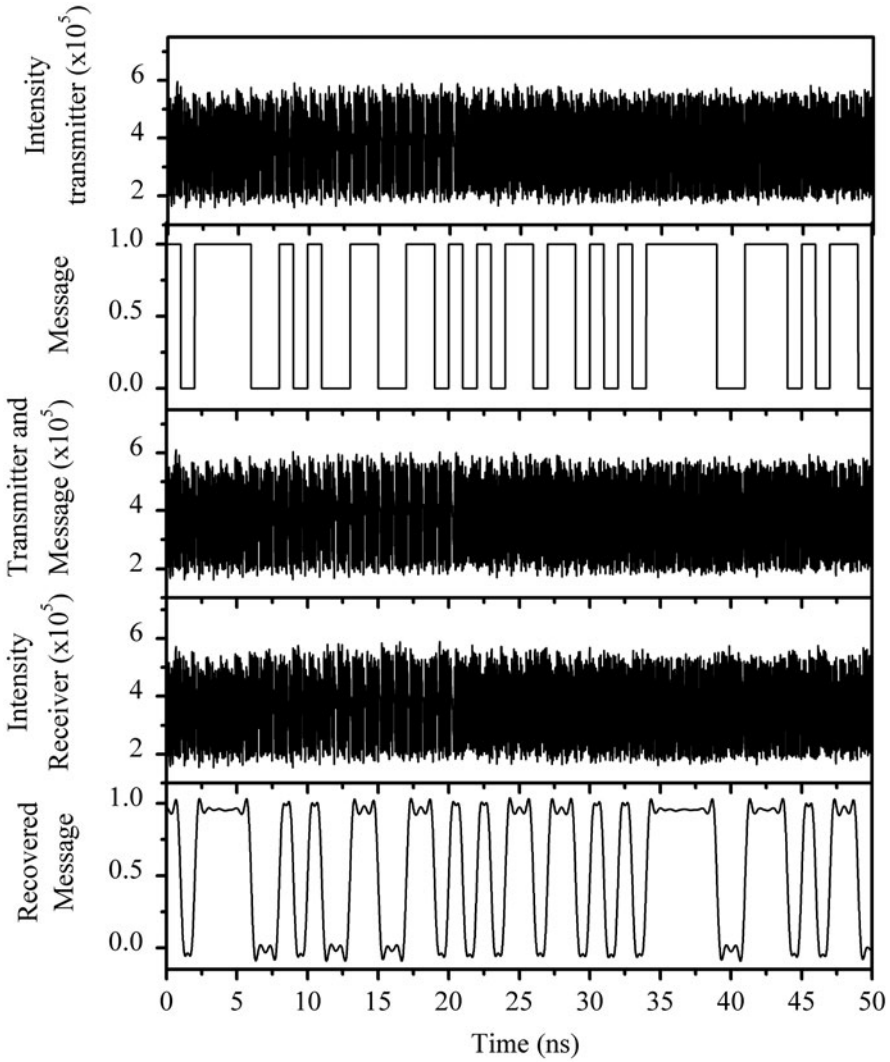

Fig. 14 Encoding and decoding a message using chaotic carrier

$$M(t) = (1 - \epsilon m(t))P_t(t). \tag{5}$$

Here, ϵ is the amplitude of the encoded message, $m(t)$ is the message itself, and $P_t(t)$ is the transmitter laser intensity. In this scheme, the message $m(t)$ and the intensity $P_t(t)$ have the same phase. Since the transmitter laser is synchronized with the receiver laser, the message is recovered as follows:

$$m_r(t) = \frac{1}{\epsilon}\left(1 - \frac{M(t)}{P_r(t)}\right). \tag{6}$$

Here, $P_r(t)$ is the receiver laser intensity and $m_r(t)$ is the recovered message.

4.1.2 Chaotic Masking

For chaotic masking, the message is just added to the intensity of the transmitter laser as

$$M(t) = P_t + \epsilon m(t). \tag{7}$$

To recover the message, one needs to subtract the intensity of the receiver laser from the incoming signal from the transmitter as follows:

$$m_r(t) = \frac{M(t) - P_r(t)}{\epsilon}. \tag{8}$$

4.1.3 Chaotic Shift Keying

Chaotic shift keying refers to the scheme when the signal is added to the transmitter itself, but not to the outcoming signal from it. This can be done by adding the message to the pump current of the transmitter laser as

$$I(t) = I + \epsilon m(t), \tag{9}$$

where I is the constant pump current. To recover the message, one just needs to subtract the intensity of the transmitter laser from that of the receiver laser as follows:

$$m_r(t) = P_t(t) - P_r(t). \tag{10}$$

4.2 One-Channel Communication Scheme

4.2.1 Scheme Description

A one-channel communication scheme consists of ML or a transmitter and SL or a receiver, both operating in a chaotic regime. The message is encrypted into the chaotic output of ML. To recover the message, SL needs to be synchronized with ML. Figure 15a shows the scheme used for both chaotic modulation and chaotic masking while Fig. 15b displays the scheme for shift keying.

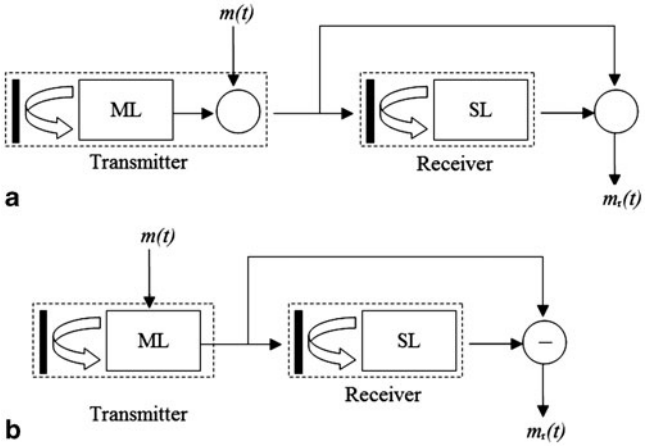

Fig. 15 Schemes for **a** chaotic modulation and chaotic masking, and **b** shift keying

4.2.2 Communication Quality

There are several methods to analyze the quality of a recovered signal. One of them is the eye diagram [20] which consists of splitting up the message into a series of fixed intervals, which then are shifted and overlapped, as shown in Fig. 16. This is the easy way to concentrate all message bits in a small time interval.

Another measure for quantitative estimation of communication quality is the Q-factor given as [5]

$$Q = \frac{S_1 - S_0}{\sigma_1 + \sigma_0}, \tag{11}$$

where S_1 and S_0 are the average optical intensities of bits "1" and " 0," and σ_1 and σ_0 are the corresponding standard deviations.

Figure 17 shows the Q-factor of a transmitted message of 1 Gbs^{-1} as a function of the coupling between the transmitter and the receiver using chaotic modulation. The blue and green curves correspond to the message amplitudes which lead to 2 and 4 % modulation of the chaotic carrier, respectively. For good transmission, the eye diagram of the recovered message should be clean. This requires $Q \geq 10$. Figure 18 shows the eye diagrams corresponding to different Q-factors.

4.2.3 Synchronization

The quantitative measure of synchronization is the synchronization error $\langle e \rangle$

$$e = \left\langle \sqrt{(P_m(t) - P_s(t))^2} \right\rangle, \tag{12}$$

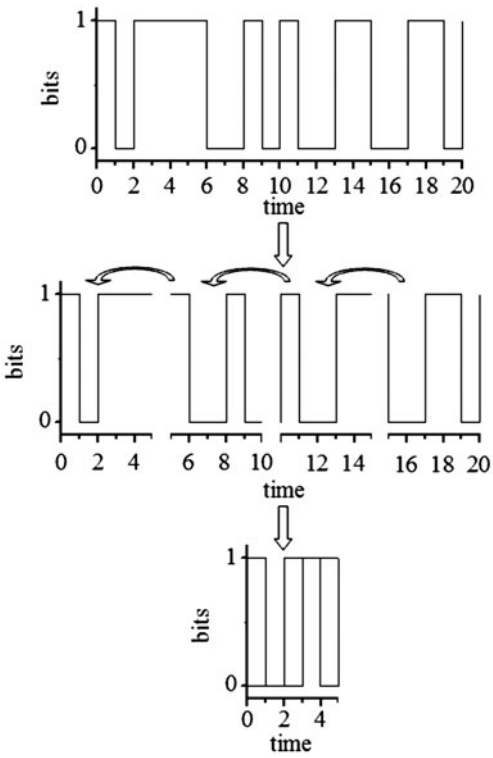

Fig. 16 Forming eye diagram from a message by splitting it into a series of 5 bits

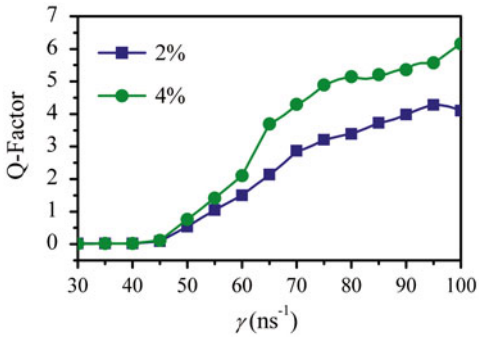

Fig. 17 Q-factor as a function of coupling γ using chaotic modulation

where P_m and P_s are the ML and SL intensities and $\langle \cdots \rangle$ stands for the time average. One of the reasons why a message cannot be recovered with a good quality is the fact that the synchronization error between the transmitter and the receiver increases when the message is added. This is because the message itself acts as an external perturbation to the system.

Figure 19 shows how the mean synchronization error increases for different encryption schemes when the message is added to the transmitter. The mean synchronization error is normalized to 1 (1 indicates that there is no synchronization).

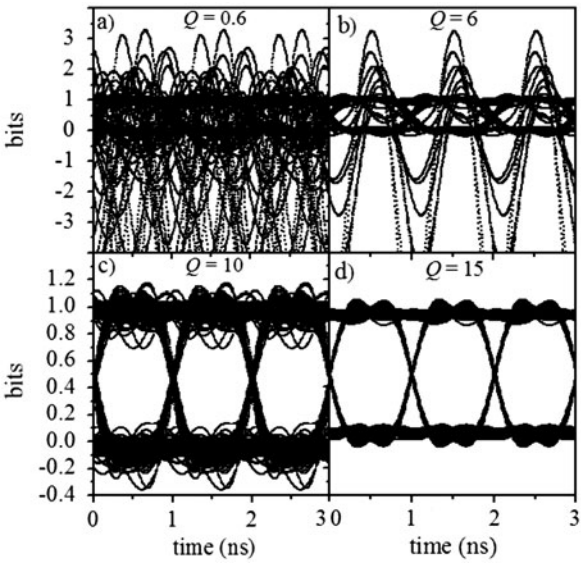

Fig. 18 Eye diagrams and corresponding Q-factors. The diagrams are clean when $Q \geq 10$

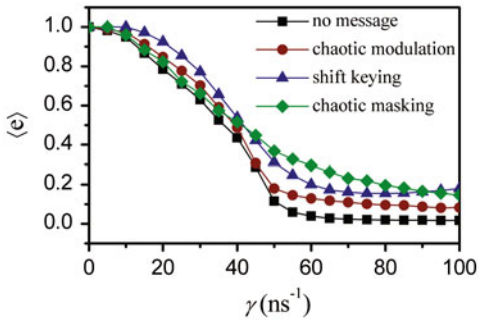

Fig. 19 Mean synchronization error between transmitter and receiver lasers

The black curve with squares in Fig. 19 indicates the mean synchronization error when no message is added. It is seen that when $\gamma \approx 60$ ns^{-1}, $\langle e \rangle$ is very close to zero, which means complete synchronization. When the message is added, the mean synchronization error increases for all encryption methods. For chaotic modulation (brown curve and circles), the increment is not so strong, as for chaotic shift keying (blue curve and triangles) and chaotic masking (green diamonds).

4.3 Two-Channel Communication Scheme

4.3.1 Scheme Description

To avoid an increasing synchronization error when the message is added, a two-channel communication system is used. This system consists of a transmitter and

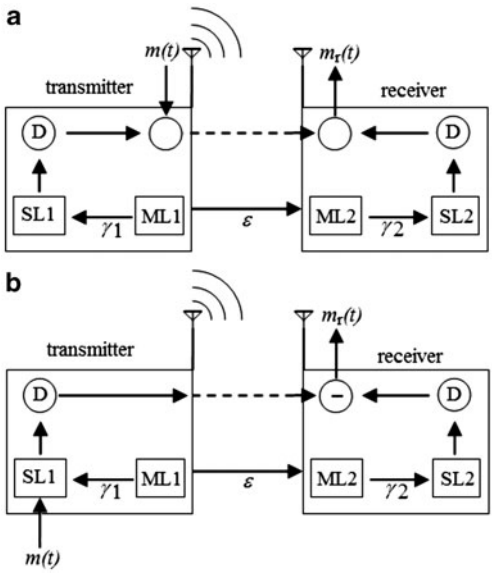

Fig. 20 Scheme of a two-channel communication system for **a** chaotic masking and modulation and **b** shift keying.

a receiver, each one containing a master–slave pair. Figure 20a shows a scheme of this system for both chaotic masking and modulation and Fig. 20b for shift keying. The master laser (ML1) in the transmitter has the same characteristics as the master laser (ML2) in the receiver and ε is the coupling strength between these two lasers. Since these two lasers are identical, complete synchronization can be achieved with an appropriate coupling. The slave laser (SL1) in the transmitter has the same characteristics as the slave laser (SL2) in the receiver, i.e., they are identical. However, the master laser (ML1) and the slave laser (SL1) in the transmitter have different characteristics, that means that complete synchronization is not possible and only generalized synchronization can be obtained. The same is for the receiver, where ML2 and SL2 have different characteristics and only generalized synchronization can be obtained. Therefore, the signals transmitted through channels 1 and 2 are different. $\gamma 1$ is the coupling strength between ML1 and SL1 in the receiver and $\gamma 2$ is the coupling between ML2 and SL2 in the receiver.

4.3.2 Cross-Correlation and Synchronization

Since ML1 and ML2 are completely synchronized, SL1 and SL2 are also completely synchronized because of the existence of generalized synchronization between ML1 (ML2) and SL1 (SL2) lasers in the transmitter and in the receiver. Because SL1 and SL2 are completely synchronized, a message added to SL1 can be recovered in the receiver by comparing SL1 and SL2. In the scheme in Fig. 20, the lasers' outputs are detected by a detector D. Once the optical signal is digitalized, the message is added to the electric signal (for the cases of chaotic masking and modulation) and then

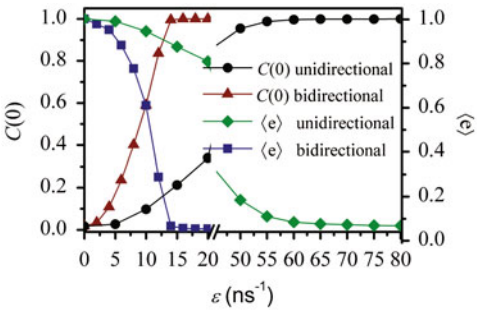

Fig. 21 Cross-correlation and mean synchronization error between ML1 and ML2 as functions of coupling ϵ. The *black circles* and *green diamonds* correspond to unidirectional coupling and the *brown triangles* and *blue squares* squares to bidirectional coupling

transmitted through an antenna in the transmitter. Then, the message is received by an antenna in the receiver and the electric signals from SL1 and SL2 are compared. The communication can be completely optical if the message is added directly to the SL1 output, and sent to the receiver via an optical fiber. Then, the waveform of SL2 is compared with that of SL1.

The parameters of the external cavities of ML1 (ML2) and SL1 (SL2) are set different to achieve generalized synchronization between them. For both ML1 and ML2, the feedback strength is $\kappa_m = 25\ \text{ns}^{-1}$ and the external round trip time is $\tau_m = 1$ ns. For both SL1 and SL2, the feedback strength is $\kappa_m = 20\ \text{ns}^{-1}$ and the external round trip time is $\tau_m = 0.5$ ns. Another advantage of the two-channel scheme is that bidirectional coupling between ML1 and ML2 is possible without loss of security. Bidirectional coupling between the MLs will lead to a lower mean synchronization error, and therefore, synchronization between SL1 and SL2 will be better.

The cross-correlation and the mean synchronization error between ML1 and ML2 as functions of their coupling ϵ, for the cases of unidirectional and bidirectional coupling, are shown in Fig. 21. The black circles and the green diamonds correspond to the cross-correlation and the mean synchronization error for unidirectional coupling, while the brown triangles and the blue squares for bidirectional coupling. When the coupling is bidirectional, a smaller coupling strength ϵ between ML1 and ML2 is required to obtain complete synchronization. Even though the cross-correlation $C(0) \approx 1$, when $\epsilon > 16\ \text{ns}^{-1}$ for bidirectional and $\varepsilon > 60\ \text{ns}^{-1}$ for unidirectional coupling, the mean synchronization error for bidirectional coupling is $\langle e \rangle < 0.005$ and for unidirectional coupling is $\langle e \rangle < 0.025$.

Figure 22 shows the cross-correlation and the mean synchronization error between ML1 and SL1 as functions of the coupling ($\gamma 1$) between them. Similar behavior is observed for the lasers in the receiver, ML2, and SL2. One can see that complete synchronization can never be achieved for $\gamma 1 = 100\ \text{ns}^{-1}$, where the cross-correlation (green squares) $C(0) \approx 0.84$, and the mean synchronization error (blue triangles) $\langle e \rangle \approx 0.39$. The same results are found for unidirectional and bidirectional coupling.

Figure 23 shows the cross-correlation and the mean synchronization error between SL1 and SL2 as functions of the coupling strength between ML1 and SL1 and between ML2 and SL2. These coupling strengths, $\gamma 1$ and $\gamma 2$, are varied equally. For the case of unidirectional coupling, the coupling strength between ML1 and ML2 is

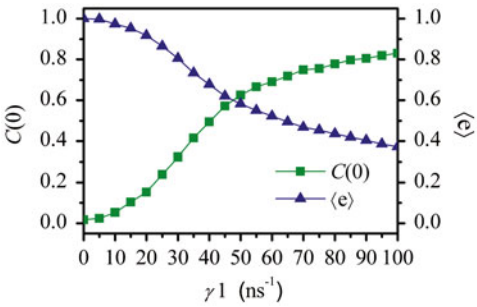

Fig. 22 Cross-correlation (*green squares*) and mean synchronization error (*blue triangles*) as functions of coupling $\gamma 1$ between ML1 and SL1

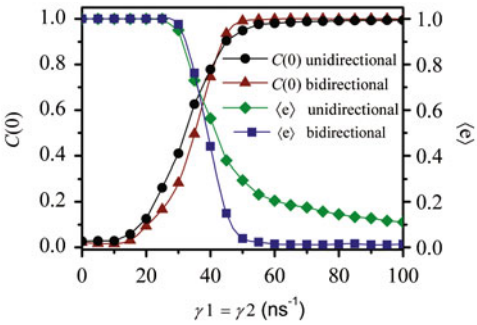

Fig. 23 Cross-correlation and mean synchronization error between SL1 and SL2 as functions of coupling $\gamma 1$ and $\gamma 2$. The *black circles* and *green diamonds* correspond to unidirectional coupling and the *brown triangles* and *blue squares* to bidirectional coupling

set to $\varepsilon = 80\ \text{ns}^{-1}$ and for bidirectional coupling, it is set to $\varepsilon = 16\ \text{ns}^{-1}$. The brown curve with triangles and the blue curve with squares correspond, respectively, to the cross-correlation and the mean synchronization error for the case of bidirectional coupling between ML1 and ML2. The black curve with circles and the green curve with diamonds correspond, respectively, to the cross-correlation and the mean synchronization error for the case of unidirectional coupling between ML1 and ML2. For the case of bidirectional coupling, the synchronization error between SL1 and SL2 is $\langle e \rangle < 0.01$.

4.3.3 Communication Quality

Now, we analyze the quality of message transmission using the two-channel scheme. Figure 24 shows how the Q-factor depends on the coupling parameter between ML1 (ML2) and SL1 (SL2) when the coupling strengths $\gamma 1$ and $\gamma 2$ are equally varied. For the case of unidirectional coupling, the coupling strength between ML1 and ML2 is set to $\varepsilon = 80\ \text{ns}^{-1}$ and for bidirectional coupling to $\varepsilon = 16\ \text{ns}^{-1}$. Figure 24a corresponds to chaotic masking, i.e., the message is added to the output signal of SL1 in the transmitter. The green curve with diamonds (unidirectional coupling) and brown curve with squares (bidirectional coupling) correspond to a 1 Gbs^{-1} transmission rate, while the black curve with circles (unidirectional coupling) and blues curve with triangles (bidirectional coupling) to a 5 Gbs^{-1} transmission rate.

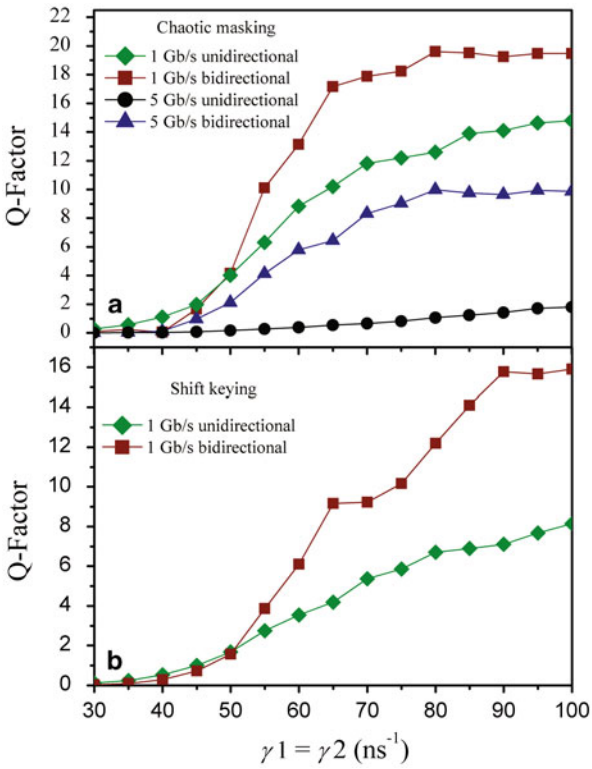

Fig. 24 Q-factors. **a** Chaotic masking. The *brown curve with squares* (bidirectional coupling) and the *green curve with diamonds* (unidirectional coupling) correspond to a 1 Gbs^{-1} transmission rate. The *blue curve with triangles* (bidirectional coupling) and the *black curve with circles* (unidirectional coupling) correspond to a 5 Gbs^{-1} transmission rate. **b** Shift keying. The *brown curve with squares* (bidirectional coupling) and the *green curve with diamonds* (unidirectional coupling) correspond to a 1 Gbs^{-1} transmission rate

One can see that for bidirectional coupling, a 5 Gbs^{-1} transmission rate is possible, since $Q \approx 10$ when $\gamma 1 = \gamma 2 > 80\ ns^{-1}$.

The Q-factor for shift keying is shown in Fig. 24b. In this case, the message is added to the pump current of SL1 in the transmitter. The brown curve with squares corresponds to a 1 Gbs^{-1} transmission using bidirectional coupling between ML1 and ML2 and the green curve with squares to the case of unidirectional coupling. One can see that a good quality of transmission is only possible using bidirectional coupling. For this case, a 5 Gbs^{-1} transmission is not possible, since $Q < 2$ for both unidirectional and bidirectional coupling. For the two-channel scheme, chaotic modulation is not possible because of very low Q-factors.

4.3.4 Robustness to Parameter Mismatch

To check the robustness of this system to a parameter mismatch between the transmitter and the receiver, we keep the coupling between ML1 and SL1 constant ($\gamma 1 = 80\ ns^{-1}$) and vary the coupling between ML2 and SL2 ($60 \leq \gamma 2 \leq 100\ ns^{-1}$). This mismatch in the coupling parameters causes a difference between the cross-correlation of the lasers in the transmitter and in the receiver. This difference affects

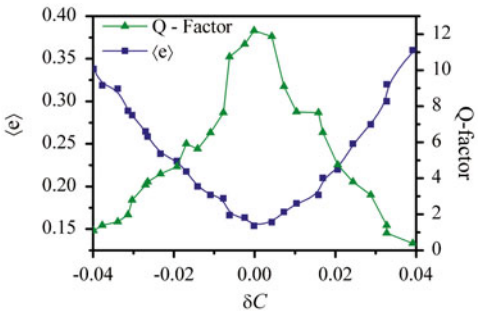

Fig. 25 Mean synchronization error (*blue squares*) and Q-factor (*green triangles*) as functions of δC for unidirectional coupling using chaotic masking at a 1 Gbs^{-1} transmission rate

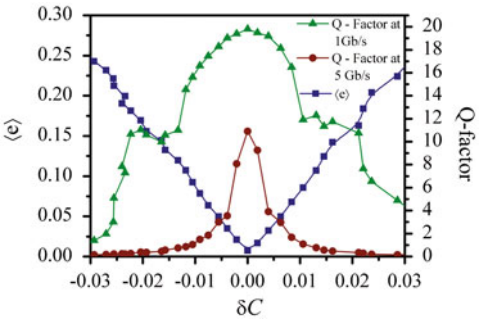

Fig. 26 Mean synchronization error (*blue squares*) and Q-factor at 1 Gbs^{-1} (*green triangles*) and 5 Gbs^{-1} (*brown circles*) as functions of δC for bidirectional coupling using chaotic masking

synchronization between SL1 and SL2, thus changing the quality of the transmitted message. In the following equation, we will show how the mean synchronization error and the Q-factor depend on the difference between the cross-correlations of the lasers in the transmitter and the receiver:

$$\delta C = C_T - C_R. \tag{13}$$

Here, C_T and C_R are the cross-correlations between ML1 and SL1 and between ML2 and SL2. For $\gamma 1 = 80\ \text{ns}^{-1}$, the cross-correlation between ML1 and SL1 is $C_T = 0.7781$. Figure 25 shows the mean synchronization error (blue squares) and Q-factor (green triangles) at a 1 Gbs^{-1} transmission rate for unidirectional coupling between ML1 and ML2 ($\epsilon = 80\ \text{ns}^{-1}$) when chaotic masking is used. As was mentioned above, a good transmission is obtained when $Q \geq 10$, that corresponds to a mismatch of $|\gamma 1 - \gamma 2| \leq 2\ \text{ns}^{-1}$.

Figure 26 shows the mean synchronization error (blue squares) and Q-factor at a 1 (green triangles) and 5 Gbs^{-1} (brown circles) transmission rates for bidirectional coupling between ML1 and ML2 ($\varepsilon = 16\ \text{ns}^{-1}$) using chaotic masking. While at the 1 Gbs^{-1} transmission rate, a mismatch of $|\gamma 1 - \gamma 2| \leq 12\ \text{ns}^{-1}$ is possible to ensure a good transmission, at the 5 Gbs^{-1} transmission rate, no parameter mismatch is allowed. From this figure, it is also clear why the 5 Gbs^{-1} transmission rate is only possible for bidirectional coupling, but not for unidirectional coupling. In the case

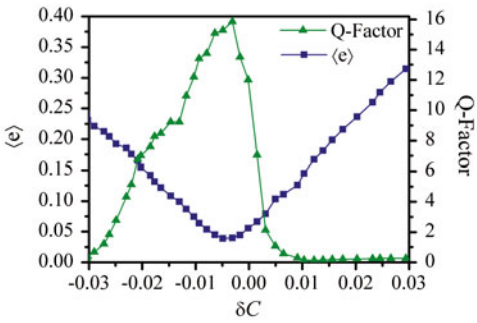

Fig. 27 Mean synchronization error (*blue squares*) and Q-factor (*green triangles*) as functions of δC for bidirectional coupling using shift keying

of bidirectional coupling, the mean synchronization error is $\langle e \rangle < 0.01$ when there is no parameter mismatch ($\delta C = 0$), and for unidirectional coupling, $\langle e \rangle > 0.15$.

Next, consider the case when shift keying is used. Figure 27 shows the mean synchronization error (blue squares) and Q-factor (green triangles) at a 1 Gbs^{-1} transmission rate for bidirectional coupling between ML1 and ML2 ($\varepsilon = 16\ \text{ns}^{-1}$). One can see that a good transmission is possible when $0 < \gamma 1 - \gamma 2 < 9\ \text{ns}^{-1}$. The curves are not symmetric around $\delta C = 0$, as in the previous cases, because when the message is added to the pump current of SL1, there already exists a parameter mismatch when the bits "1" are being added to the system. This mismatch in the pump currents is then compensated by the mismatch between the couplings $\gamma 1$ and $\gamma 2$, so that the curves of the mean synchronization error and Q-factor are shifted with respect to δC. Similar results are obtained when a mismatch exists between other parameters.

5 Conclusion

In this short review, we have described the behavior of coupled semiconductor lasers with delayed feedback. Their rich dynamics implies important advantages for application in optical communication. This still remains a hot research topic—tens of articles and several patents appear every year. We believe that future trends in this direction will be focused on the development of new optical communication systems based on different types of synchronization, the implementation of laser networks, and the prominent use of exciting dynamical behaviors of complex systems, such as chaos and multistability.

Acknowledgements This work was supported by Consejo Nacional de Ciencia y Tecnologia of Mexico (Project No. 100429).

References

1. Arecchi, F.T., Lippi, G.L., Puccioni, G.P., Tredicce, J.R.: Deterministic chaos in laser with injected signal. Opt. Commun. **51**, 308–314 (1984)
2. Argyris, A., Syvridis, D., Larger, L., Annovazzi–Lodi, V., Colet, P., Fischer, I., García-Ojalvo, J., Mirasso, C.R., Pesquera, L., Shore, K.A.: Chaos-based communications at high bit rates using commercial fibreoptic links. Nature **438**, 343–346 (2005)
3. Aswin, P.: Synchronization from chaos. Nature **422**, 384–385 (2003)
4. Jesper, M., Bjarne, T., Jannik, M.: Chaos in semiconductor laser with optical feedback: Theory and experiment. IEEE J. Quantum Electron. **28**(1), 93–108 (1992)
5. Kanakidis, K., Argyris, A., Syvridis, D.: Performance characterization of high-bit-rate optical chaotic communication systems in a back to back configuration. J. Lightwave Technol. **21**(3), 750–758 (2003)
6. Lang, R., Kobayashi, K.: External optical feedback effects on semiconductor injection laser properties. IEEE J. Quantum Electron. **16**(3), 347–355 (1980)
7. Liu, Y., Ohtsubo, J.: Dynamics and chaos stabilization of semiconductor lasers with optical feedback from an interferometer. IEEE J. Quantum Electron. **33**(7), 1163–1169 (1997)
8. Liu, Y., Takiguchi, Y., Davis, P., Aida, T., Saito, S., Liu, J.M.: Experimental observation of complete chaos synchronization in semiconductor lasers. IEEE J. Quantum Electron. **80**(23), 4306–4308 (2002)
9. Locquet, A., Massoller, C., Mégret, P., Blondel, M.: Comparison of two types of synchronization of external-cavity semiconductor lasers. Opt. Lett. **27**, 31–33 (2002)
10. Maurer, J., Libchaber, L.: Effect of the Prandtl number on the onset of turbulence in liquid 4He. J. Phys. Lett. **21**(4), 515–518 (1980)
11. Meucci, R., Salvadori, F., Ivanchenko, M.V., Naimee, K.A., Zhous, C., Arecchi, F.T., Boccaletti, S., Kurths, J.: Synchronization of spontaneous bursting in a CO_2 laser. Phys. Rev. E Stat. Nonlin. Soft Matter Phys. **74**, 066207 (2006)
12. Mirasso, C.R., Colet, P., Fernandez, P.G.: Synchronization of chaotic semiconductor lasers: Application to encoded communications. IEEE Photon. Technol. Lett. **8**(2), 299–301 (1996)
13. Murakami, A.: Synchronization of chaos due to linear response in optically driven semiconductor lasers. Phys. Rev. E Stat. Nonlin. Soft Matter Phys. **65**, 056617 (2002)
14. Ravalet, F., Marié, L., Chiffaudel, A., Daviaud, F.: Multistability and memory effect in a highly turbulent flow: Experimental evidence of a global bifurcation. Phys. Rev. Lett. **93**, 164501 (2004)
15. Revuelta, J., Mirasso, C.R., Colet, P., Pesquera, L.: Criteria for synchronization of coupled chaotic external-cavity semiconductor lasers. IEEE Photon. Technol. Lett. **14**(2), 140–142 (2002)
16. Rogister, F., Mégret, P., Deparis, O., Blondel, M., Erneux, T.: Suppression of low-frequency fluctuations and stabilization of a semiconductor laser subjected to optical feedback from a double cavity: Theoretical results. Opt. Lett. **24**, 1218–1220 (1999)
17. Rogister, F., Sukow, D.W., Gavrielidis, A., Mégret, P., Deparis, O., Blondel, M.: Experimental demonstration of suppression of low-frequency fluctuations and stabilization of an external cavity diode. Opt. Lett. **25**, 808–810 (2000)
18. Ruiz-Oliveras, F.R., Pisarchik, A.N.: Phase-locking phenomenon in a semiconductor laser with external cavities. Opt. Exp. **14**, 12859–12867 (2006)
19. Ruiz-Oliveras, F.R., Pisarchik, A.N.: Synchronization of semiconductor lasers with coexisting attractors. Phys. Rev. E Stat. Nonlin. Soft Matter Phys. **79**, 016202 (2009)
20. Ruiz-Oliveras, F.R., Soriano, M.C., Colet, P., Mirasso, C.R.: Information encoding and decoding using unidirectionally coupled chaotic semiconductor lasers subject to filtered optical feedback. IEEE J. Quantum Electron. **45**(8), 962–968 (2009)
21. Seydel, R.: From Equilibrium to Chaos: Practical Bifurcation and Stability. Elsevier, New York (1988)

22. Shore, K.A., Spencer, P.S., Pierce, I.: Synchronization of chaotic semiconductor lasers. In: Pisarchik, A.N. (ed.) Recent Advances in Laser Dynamics: Control and Synchronization, pp. 79–104. Research Singpost, Kerala (2008)
23. Sivaprakasam, S., Spencer, P.S., Rees, P., Shore, K.A.: Regimes of chaotic synchronization in external-cavity laser diodes. IEEE J. Quantum Electron. **38**(9), 1155–1161 (2002)
24. Soriano, M.C., Ruiz-Oliveras, F.R., Colet, P., Mirasso, C.R.: Synchronization properties of coupled semiconductor lasers subject to filtered optical feedback. Phys. Rev. E Stat. Nonlin. Soft Matter Phys. **78**, 046218 (2008)
25. Tanii, K., Tohei, T., Sugawara, T., Tachikawa, M., Shimizu, T.: Two different routes to chaos in a two-mode CO_2 laser with saturable absorber. Phys. Rev. E Stat. Nonlin. Soft Matter Phys. **59**, 1600–1604 (1999)
26. Tang, S., Chen, H.F., Liu, J.M.: Performance of synchronized chaotic optical communication systems. In: Larson, L.E., Liu, J.M., Tsimring, L.S. (eds.) Digital Communications Using Chaos and Nonlinear Dynamics, Series: Institute for Nonlinear Science, pp. 341–378. Springer, New York (2006)
27. Vicente, R., Dauden, J., Colet, P., Toral, R.: Analysis and characterization of the hyperchaos generated by a semiconductor laser subject to a delayed feedback loop. IEEE J. Quantum Electron. **41**(4), 541–548 (2005)
28. Weiss, C.O., Vilaseca, R.: Dynamics of Lasers. VCH, Weinheim (1991)
29. Zhou, P., Chen, Z., Wang, X., Li, X., Liu, Z., Xu, X., Hou, J., Jiang, Z.: Synchronization and coherent combining of two pulsed fiber lasers. Chin. Opt. Lett. **6**, 523–525 (2000)

Transient Dynamics on the Edge of Stability

Irma Tristan and Mikhail Rabinovich

Abstract Here we propose, on the basis of the winnerless competition (WLC) principle, which induces robust transient dynamics in open complex networks, and whose geometrical image in phase space is a heteroclinic sequence, to study the behavior of complex multiagent systems such as brain or ecological food networks that present transient dynamics in a network with active elements whose equilibria are in multidimensional unstable manifolds. In particular, we introduce and study numerically a characteristic of sequential transient dynamics, an uncertainty function that measures the level of nonreproducibility of generalized heteroclinic channels. For a Lotka–Volterra-type model, we describe the behavior of uncertainty functions and its dependence on parameters of the system. We analyze the probability to get a heteroclinic chain with fixed uncertainty and its dependence on the number of saddles of the chain and the number of elements in the network.

1 Introduction

A dynamical complex system consists of many coupled (interacting) dynamical units forming global modes in their collective behavior. The connectivity and the type of interaction among units are very important for the cooperative dynamics. When we consider multiagent, open, nonlinear complex systems that are influenced by inward (source), and outward (sink) information fluxes along with an external driving source, the standard approach in the analysis of such systems are based on the asymptotic behavior, when all transient modes vanish. The transient behavior is merely treated as an irregularity during which the system is presumed to be immature for accurate computation. Despite the advantages of this traditional treatment, like

I. Tristan (✉)
Instituto de Investigacion en Comunicacion Optica,
Universidad Autonoma de San Luis Potosi, Karakorum 1470,
Lomas 4a 78210, San Luis Potosi, Mexico
e-mail: tristan.irma@gmail.com

M. Rabinovich
BioCircuits Institute, University of California San Diego,
9500 Gilman Drive, La Jolla CA 92093-0402, USA
e-mail: mrabinovich@ucsd.edu

H. González-Aguilar, E. Ugalde (eds.), *Nonlinear Dynamics New Directions,*
Nonlinear Systems and Complexity 12, DOI 10.1007/978-3-319-09864-7_7

a rich variety of methods available for locating and manipulating the attractors, this view overlooks the possibility that a balance encountered along the dynamics might not be the terminal state. Transitions among multiple metastable states are common in complex systems of nature. Then, even when the traditional paradigm for understanding the processing of neural sequences is computation with attractors [7, 8, 10, 21], a sequential behavior is transient, and thus new approaches are needed to describe this kind of neural activity. For example, in the field of neuroscience, the execution of many cognitive functions such as sequential learning, short-term memory, and decision making involves a transient dynamical process as well as any dynamical mechanism underlying cognitive processes have to be reproducible in all experiments in similar environmental conditions and, at the same time, they must be sensitive to changing internal and external information [17]. With a similar discussion, in the field of ecology, dynamical principles have been used to design their models and experiments since the days of Lotka, Volterra, and Gause. Nowadays, the methods of nonlinear dynamics have become the main tool for the analysis of evolution of ecological systems. Traditionally, ecological theory is mostly interested in the asymptotic states of limit sets of the food web and their stability (see, for example, [4, 19]); however, in complex ecological models, competition often does not lead to simple attractors, instead it demonstrates sequential activity.

The generation and control of informational sequences and their reorganization or reshaping is one of the most intriguing subjects for disciplines such as neuroscience and the theory of autonomous intelligent systems, among others. In spite of the diversity of sequential activities of sensory, odor, and cognitive neural systems, they have many similarities from the dynamical point of view [17]. A complex system operates in a sequence of transient phases, each leading to a metastable equilibrium, which can be viewed as a temporary leader (or winner) that maintains the balance until the beginning of the next transition. Therefore, the modeling problem of such systems has two facets: (i) organization of the phase space that characterizes the chain of metastable states and the transients regimes connecting them; and (ii) the amount of time that the system spends in the vicinity of a metastable state. The former determines the setup for the sequential activity, the direction, and the strength of information exchange. Thus, one necessary condition on the predictability of complex network dynamics is to learn how tight or loose the interactions are. The latter depends on environmental conditions or intrinsic dynamics embedded in the temporary winner. This assigns a critical role for noise in processes and in subprocesses operating at different scales in the complex system hierarchy.

Prototype dynamical models that are widely accepted in computational neuroscience [13, 22] and ecology [11, 20] have been shown to exhibit a transient winnerless competition (WLC) [1, 3, 15, 16] for a fairly broad range of parameters. These experimental results allow us to suppose that it is precisely the competition between different agents or cognitive states that results in typical sequential behavior. A new biologically inspired concept of sequence processing based on the WLC principle and on transient but stable heteroclinic sequences (SHSs) was introduced in 2004; see for instance [1, 17, 18]. As far as transient behaviour is concerned, there were no adequate mathematical models for it, in particular, of sequential activity that

occurs in many neural circuits until a few years ago, when the concepts of SHS and stable heteroclinic channel (SHC) were presented [1, 18]. These are not attractors, but behave like them in a considerable period of time during the evolution of the dynamical system. This new mathematical object, as studied in [1, 18], opens the possibility of the modeling of transient sequential activity in neural circuits and other networks of active elements as a more accurate mathematical image of this behavior.

In this chapter we investigate the generalized Lottka–Volterra model (GLVM) for the case of a generalized heteroclinic channel (GHC) containing saddles with multidimensional unstable manifolds with one leading direction. This is the case that corresponds to the edge of heteroclinic channel stability.

2 The Model

We consider a system of ordinary differential equations

$$\dot{x} = X(x), \qquad x \in \mathbb{R}^d, \tag{1}$$

where the vector field X is C^2-smooth. We assume that the system (1) has N equilibria $Q_1, Q_2, \ldots, Q_N$, such that each Q_i is a hyperbolic point of saddle type with one-dimensional unstable manifold $W^u_{Q_i}$, which consists of Q_i and two "separatrices," the connected components of $W^u_{Q_i} \setminus Q_i$ which we denote by Γ_i^+ and Γ_i^-. This manifold corresponds to the positive eigenvalue of the linearization of system (1) at Q_i, i.e., that of $\mathcal{D}X|_{Q_i}$. We assume also that

$$\Gamma_i^+ \subset W^s_{Q_{i+1}}, \tag{2}$$

where $W^s_{Q_{i+1}}$ is the stable manifold of Q_{i+1}.

Definition 1 The set $\Gamma := \cup_{i=1}^{N} Q_i \cup_{i=1}^{N-1} \Gamma_i^+$ is called the heteroclinic sequence (HS). Denote by $\lambda_1^{(i)}, \ldots, \lambda_d^{(i)}$ the eigenvalues of the matrix $\mathcal{D}X|_{Q_i}$.

By the assumption above, one of the eigenvalues is positive. Without loss of generality one can assume that they are ordered in such a way that

$$\lambda_1^{(i)} > 0 > Re\ \lambda_2^{(i)} \geq \cdots \geq Re\ \lambda_d^{(i)}. \tag{3}$$

The number

$$\nu_i = \frac{-Re\ \lambda_2^{(i)}}{\lambda_1^{(i)}}$$

is called the saddle value.

If $\nu_i > 1$, then the compression along the stable manifolds dominates the stretching along the one-dimensional unstable manifold, this is referred to as a dissipative saddle. If all saddles in the heteroclinic chain are dissipative, then the trajectories in their vicinity cannot escape from the chain, providing stability.

Definition 2 The heteroclinic sequence Γ is called an SHS if

$$\nu_i > 1, \qquad i = 1, \ldots, N. \tag{4}$$

The conditions (4) are the frame that determine the inequalities for the stability of the SHS for the specific dynamical model, for example, the Lotka–Volterra (LV) type models [1, 2].

Recent results of work with the LV model have shown that the requirements for the system parameters to accomplish SHS stability became harder and harder to be effective with the increasing number of saddles in the heteroclinic chain [6]. In particular, a long enough heteroclinic chain became unstable for any finite parameter values while information transduction and processing became unpredictable.

In this chapter we introduce and study a quantitative characteristic of such an unpredictability, i.e., an uncertainty function. The dynamical mechanism of unpredictability is caused by a non-one-dimensionality of unstable separatrices that can destroy the reproducibility of the sequence. According to this we introduce a new dynamical object for complex systems with WLC dynamics, i.e., heteroclinic tree, a sequence with many branches.

2.1 SHS for Saddles with Multidimensional Unstable Manifolds

We consider the system (1) and assume that it has N equilibria $Q_1, Q_2, \ldots, Q_N$, such that each Q_i is a hyperbolic, saddle-type point as described in the Introduction, with possibly multidimensional unstable manifold but with one-dimensional strongly unstable manifold $W^u_{Q_i}$, which consists of Q_i and two "separatrices," denoted by Γ_i^+ and Γ_i^- as described previously. This manifold corresponds to the maximal positive eigenvalue of the linearization of system (1) at Q_i, i.e., that of $\mathcal{D}X|_{Q_i}$. We make the analogous assumption (2) where $W^s_{Q_{i+1}}$ is the stable manifold of Q_{i+1}.

Definition 3 The set $\Gamma := \cup_{i=1}^{N} Q_i \cup_{i=1}^{N-1} \Gamma_i^+$ is called the heteroclinic sequence (HS). Denote by $\lambda_1^{(i)}, \ldots, \lambda_d^{(i)}$ the eigenvalues of the matrix $\mathcal{D}X|_{Q_i}$.

By the assumption above, at least one of the eigenvalues is positive. Without loss of generality one can assume that they are ordered in such a way that

$$\lambda_1^{(i)} > \cdots \geq Re\ \lambda_{m_i}^{(i)} > 0 > Re\ \lambda_{m_i+1}^{(i)} \geq \cdots \geq Re\ \lambda_d^{(i)}. \tag{5}$$

The saddle value is

$$\nu_i = \frac{-Re\ \lambda_{m_i+1}^{(i)}}{\lambda_1^{(i)}}.$$

The one-dimensional strongly stable manifold corresponds to the eigendirection related to $\lambda_1^{(i)}$. Such manifold exists and is at least C^1-smooth [9].

The heteroclinic sequence, Γ, is called a generalized heteroclinic sequence (GHS) if $\nu_i > 1, i = 1, \ldots, N$.

For $m_i = 1$ this definition coincides with the definition of SHS in [1]. If $m_i = 1$ the conditions imply stability of Γ, in the sense that every trajectory started at a point in the vicinity of Q_1 remains in a neighborhood of Γ until it comes into the neighborhood of Q_N. In fact, the motion along this trajectory can be treated as a sequence of switchings between the equilibria Q_i, $i = 1, 2, \ldots, N$. If $m_i > 1$ then some amount of stability remains feasible even if we subject the system (1) to the action of a small noise as we see below.

Of course, the condition $\Gamma_i^+ \subset W^s_{Q_{i+1}}$ indicates the fact that the system (1) is not structurally stable and can only be realized either for exceptional values of parameters or for systems of a special form. As an example of such a system one may consider the LV model that under some conditions on its parameters will possess GHS.

2.2 Uncertainty Functions

We introduce now the quantitative characteristics of such a behavior that measures the level of nonreproducibility of dynamics in a neighborhood of a GHS.

Let us consider a system (1) having a GHS consisting of the saddles Q_i, $i = 1, \ldots, N$, and heteroclinic orbits joining their vicinities. It is useful to introduce a characteristic that measures the level of unpredictability for orbits in a neighborhood of a GHS. One can do it as follows.

Let $V(\epsilon, \delta)$ be a neighborhood of the GHS consisting of balls of radius ϵ around the saddles united with *tunnels* of size ϵ around separatrices joining these saddles. Let us fix the value of ϵ. Given a randomly chosen initial point x_0 in a δ neighborhood of Q_1 let $p_k(\delta)$ denote the probability to stay in $V(\epsilon, \delta)$ until the neighborhood of the last saddle Q_N for the trajectory starting at x_0. In other words $p_k(\delta)$ measures the possibility of the occurrence of k successive saddles in the collection $Q_1 \ldots Q_N$.

Definition 4 The quantity

$$u_k(\delta) = 1 - p_k(\delta)$$

is said to be an uncertainty function for the given GHS.

2.3 LV-Type Model

We will study a transient multiagent competition in the framework of the following form of a Lotka–Volterra model (LVM):

$$\frac{da_i}{dt} = a_i \left[\sigma_i(\mathbf{E}) + \eta_i(t) - \sum_j^n \rho_{ij} a_j \right]. \tag{6}$$

An SHS arises due to strict conditions on the system (1). In the case of the LVM, one such constraint is that the average activity of the elements in the network is

positive definite ($a_i \geq 0$), since the trajectories can never go through the invariant hyperplanes $a_j = 0$ and the inequalities that frame the relationship between σ_i and ρ_j in order to satisfy the conditions $\nu_i > 1$.

Here each $a_i(t)$ represents the average level of activity of the ith element; $\rho_{ij} \geq 0$ is the interaction strength between elements i and j; $\sigma_i(\mathbf{E})$ is the growth rate for the average level of activity of element i that depends on the environmental parameter $\mathbf{E}$ (σ_i/ρ_{ii} is the overall carrying capacity of element i in the absence of the other elements); η_i is the level of environmental noise. The product $a_i\big[\sigma_i(\mathbf{E}) + \eta_i(t)\big]$ determines the interaction of the element i with the environment. We will consider a nonsymmetrical interaction between the elements in the network, $\rho_{ij} \neq \rho_{ji}$. The role of nonsymmetry in the inhibition as a result of the interaction between the elements in the network has been discussed previously in [15].

The phase space of the system (6) is bounded by the manifolds $\{a_i = 0\}$, which are included in the phase space.

Let us focus on the region in the control parameter space, where, in the absence of noise, all nontrivial equilibria (fixed points) $a_i^0 = \sigma_i/\rho_{ii} > 0$, $a_j^0 = 0$, $j \neq i$, on the a_i-axis are saddles. Without loss of generality we may assume that $\rho_{ii} = 1$. In this region long multiactivity transients may exist. The necessary conditions for these are the following: for each increment i, i.e., among the eigenvalues of the matrix of the linearized system at the equilibrium $(0 \cdots 0\ \sigma_i\ 0 \cdots 0)$, there is at least one positive: $\sigma_j - \rho_{ji}\sigma_i > 0$.

Each saddle has one- or m_i-dimensional unstable separatrix (manifold), $m_i < N - 2$, where N is the number of saddles in the chain, as opposed to n, the number of element in the network. The unstable separatrix connects the previous saddle with the next one (or the saddle with a stable equilibrium). For multiagent system competition, the existence of heteroclinic sequences (that consist of saddles and heteroclinic trajectories connecting them) in the phase space is structurally stable in the class of LVM and a very general phenomenon.

2.4 GHS in the LVM in the Absence of Noise

We are dealing now with the system (6) in the case of $\eta_i(t) = 0$, $i = 1, \ldots, N$ and look for the conditions under which the system has a GHS consisting of saddles $Q_k = (0, \ldots, 0, \sigma_{i_k}, 0, \ldots, 0)$ linked by heteroclinic trajectories, $k = 1, \ldots, N \leq n$.

Selection of Saddles The saddles Q_k have the following increments (eigenvalues of the linearized system at Q_k): $\sigma_j - \rho_{ji_k}\sigma_{i_k}$, $j \neq i_k$, and $-\sigma_{i_k}$ [1].

The saddles $Q_k = (0, \ldots, 0, \sigma_{i_k}, 0, \ldots, 0)$, $k = 2, \ldots, N$ are selected in such a way that: there are $m_{i_k} - 1$ positive eigenvalues, $m_{i_k} > 1$, one of them is maximal, and the rest, are negative. Then the following inequalities hold

$$\sigma_{i_{k+1}} - \rho_{i_{k+1}i_k}\sigma_{i_k} > \sigma_{i_{k+1}^{(2)}} - \rho_{i_{k+1}^{(2)}i_k}\sigma_{i_k} >> \cdots > \sigma_{\beta_{k+1}} - \rho_{\beta_{k+1}i_k}\sigma_{i_k} > 0, \qquad (7)$$

where $\beta_{k+1} = i_{k+1}^{m_{i_k}-1}$, and the other eigenvalues are negative.

We recall now the conditions [12] under which the system (6) has GHS.

Heteroclinic Connections To assure that there is a heteroclinic orbit $\Gamma_{i_{k-1}i_k}$ joining Q_{k-1} and Q_k, the following condition has to be satisfied

$$1 - \rho_{i_{k-1}i_k}\rho_{i_k i_{k-1}} \neq 0. \tag{8}$$

This orbit belongs to the plane $P_{i_{k-1}i_k} = \cap_{j\neq i_{k-1},i_k}^{n}\{a_j = 0\}$, where the point Q_k has a one-dimensional strongly unstable direction (indicated by i_{k+1}). This fact can be shown in the same way as for one-dimensional unstable direction [1]. Indeed, the restriction of (6) on the plane $P_{i_{k-1}i_k}$ has the form that is independent of the dimension of the unstable manifold.

Leading Directions Under the following conditions

$$-\sigma_{i_k} < \sigma_{i_{k-1}} - \rho_{i_{k-1}i_k}\sigma_{i_k} < 0, \tag{9}$$

and

$$\sigma_i - \rho_{i_k}\sigma_{i_k} < \sigma_{i_{k-1}} - \rho_{i_{k-1}i_k}\sigma_{i_k}, \tag{10}$$

the separatrix $\Gamma_{i_{k-1}i_k}$ comes to Q_k following a leading direction, transversal to the a_{i_k}-axis on the plane $P_{i_{k-1}i_k}$. To prove it, we use the same arguments as in [1].

Dissipativity of Saddles The saddle value

$$\nu_{i_k} = \frac{\rho_{i_{k-1}i_k}\sigma_{i_k} - \sigma_{i_{k-1}}}{\sigma_{i_{k+1}} - \rho_{i_{k+1}i_k}\sigma_{i_k}}, \tag{11}$$

is defined for every saddle Q_k. We assume that

$$\nu_{i_k} > 1,\ k = 1, \ldots, N. \tag{12}$$

It means that every saddle Q_k is "dissipative."

Under the conditions (7)–(12) the system (6) in the absence of noise has a GHS [12], containing the collection $\{Q_k\}$ of the saddles.

Given a randomly chosen initial point in a small δ-neighborhood of Q_{i_0} let $p_k(\delta)$ be the probability to perform a successive switching among saddles $Q_{i_m}, Q_{i_{m+1}}, \ldots, Q_{i_{m+k-1}}$, $m \geq 0$, $m + k - 1 \leq N$, by the orbit going through this initial point. Then

$$u_k(\delta) = 1 - p_k(\delta)$$

will be the uncertainty function for the given GHS.

In other words, $p_k(\delta)$ shows us the level of reproducibility of k successive saddles in the ordered collection $Q_{i_0}, \ldots, Q_{i_N}$. As we mentioned, for SHS, $p_k(\delta) = 1$, $k = 0, \ldots, N - 1$. So, provided that δ, a set of initial points and the size ϵ of the heteroclinic channel, i.e., the distance from the point on a trajectory performing the switching between saddle to the corresponding heteroclinic trajectory belonging to the GHS, are chosen in a right way, there is no uncertainty, $u_k(\delta) = 0$. But for GHS, the situation is nontrivial as one can see from the computer modeling.

3 Numerical Results

To perform calculations according to the definition of $u_k(\delta)$, one must fix δ, and a set of initial points. Also it is important to check how $u_k(\delta)$ depends on parameters of the system.

3.1 Prescribed Sequence

We first consider values of parameters for which a heteroclinic sequence is prescribed as in [2]. When choosing the nonmaximal positive eigenvalues, we impose the additional restriction $i^{(2)}_{k+2} \neq i^{(2)}_{k+1}$; see [2] for details. We analyze first the case of GHS containing saddles with one-dimensional unstable manifolds in the system (6), which is the case of SHS, with $n = 25$, $N = 8$, and multiplicative noise of level 1×10^{-4}. The expected sequence is $i_k = 2, 4, 6, 8, 10, 12, 14, 16$.

As the first step, let us choose the following values of δ: $1e-5, 1e-4, 1e-3, 1e-2, 1e-1, 1, 10$ and $\epsilon = 1.0$, the radius of the heteroclinic channel, so when the system evolves within this distance of an equilibrium we account it as part of the sequence. For each value of δ we have performed one experiment consisting of 100 sets of 100 simulations each studying the dynamics of the LVM, where the integration was performed by using the Milstein integration scheme [14]. For each set of 100 simulations: we have chosen the parameters in the following way: (i) the connectivity matrix (ρ_{ij}) is assumed to have diagonal entries all equal to 1; and since we have a prescribed sequence, the rest of the values will be generated as described in Sect. 2.4; (ii) the growth rates σ_i were set to be random numbers taken uniformly from the interval $(5, 10)$, with a variation smaller than $\pm 5e-4$. For every simulation (among 100 in a given set) initial conditions for $a_i(t)$ were set randomly but uniformly from $(0, \frac{\delta}{\sqrt{n}})$, except for $a_0(0)$, which was set to equal $\sigma_0 + \delta s$ where s is a random number taken uniformly from the interval $(-0.5,0.5)$.

We defined x_k as the number of cases for which it was possible to find a segment of length $k, k = 0, \ldots, N$, of the prescribed sequence within each set of 100 simulations. The uncertainty function is defined as follows: given a value of δ let $u_k(\delta) = \frac{s-x_k}{s}$, for $k = 0, \ldots, N$ where s is the number of simulations in each trial. We will average this number for all sets of simulations and denote it by $\overline{u}_k(\delta)$.

In Fig. 1, for each value of δ, we present the average reproducibility in a form of a column. Each color is related to the occurrence of the corresponding number of elements in the sequence: the blue one corresponds to the full reproducibility (eight elements); the red one, to seven elements; the green one, to six elements; the purple one, to five elements, the turquoise one, to four elements; the orange one, to three elements; the light blue one, to two elements; the pink one, to one element; and the light green one to no appearance of elements. We observe that when the system starts evolving with initial conditions within the ball of radius δ and $\delta \leq \epsilon$ around the first saddle in the expected GHS, the average reproducibility for a segment of the

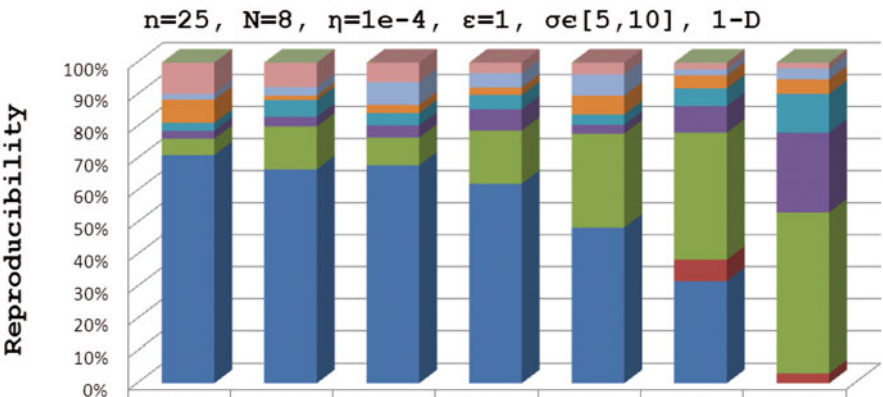

	δ = 1e-5	δ = 1e-4	δ = 1e-3	δ = 1e-2	δ = 1e-1	δ = 1	δ = 10
0 saddles	0.00	0.00	0.00	0.00	0.00	0.03	0.01
1 saddle	9.74	7.62	6.10	3.35	3.67	2.06	1.81
2 saddles	1.85	2.74	7.12	4.47	6.66	1.90	3.42
3 saddles	7.23	1.37	2.57	2.28	5.90	4.07	4.52
4 saddles	2.52	5.18	3.81	4.47	3.20	5.53	12.13
5 saddles	2.46	3.03	3.86	6.67	2.76	8.28	24.91
6 saddles	5.08	13.42	8.63	16.59	29.32	39.70	50.12
7 saddles	0.00	0.02	0.00	0.00	0.00	6.71	3.08
8 saddles	71.12	66.62	67.91	62.17	48.49	31.72	0.00

Fig. 1 Reproducibility for the case of GHS containing saddles with one-dimensional unstable manifolds, corresponding to $n = 25$, $N = 8$, $\eta = 1e-4$, $\epsilon = 1.0$, $\delta = 1e-5, 1e-4, 1e-3, 1e-2, 1e-1, 1, 10$ and $\boldsymbol{\sigma} \in [5, 10]$

sequence with length 6 or larger is at least 75.81 %. For the case when starting at the ball of radius δ and $\epsilon < \delta$ we observe that we have a reproducibility of 53.2 % for a segment of the sequence with length 6 or larger even when the complete sequence is not followed since the first saddle is skipped, but then retaking the sequence from the following steps (saddles). Still, we get 78.11 % of reproducibility for at least the last five elements of the sequence.

Figure 2 shows the uncertainty function corresponding to δ values ranging from $1e^{-5}$ to 10. In this graph we represent the function of uncertainty in series corresponding to different values of δ. We find that when $\delta \leq \epsilon$, $\overline{u}_6(\delta) \lesssim 0.238$ and $\overline{u}_8(\delta) \lesssim 0.683$. Additionally, when $\epsilon < \delta$, $\overline{u}_6(\delta) \lesssim 0.468$ and $\overline{u}_8(\delta) = 1.000$. As δ decreases, $\overline{u}_i(\delta)$, $i = 0, \ldots, N$ decreases as well, and for $\delta \lesssim 1e-3$, $\overline{u}_8(\delta) \lesssim 0.335$. It is interesting that for the sequence with length smaller than 6, the uncertainty increases approximately linearly but jumps up when the sequence length is 7 saddles.

We repeated the same experiment for the case of GHS with two-dimensional unstable manifolds in the system (6), with the same exact parameters. The results follow.

In Fig. 3, for each value of δ, we present the average reproducibility in a form of a column. Each color is related to the occurrence of the corresponding number

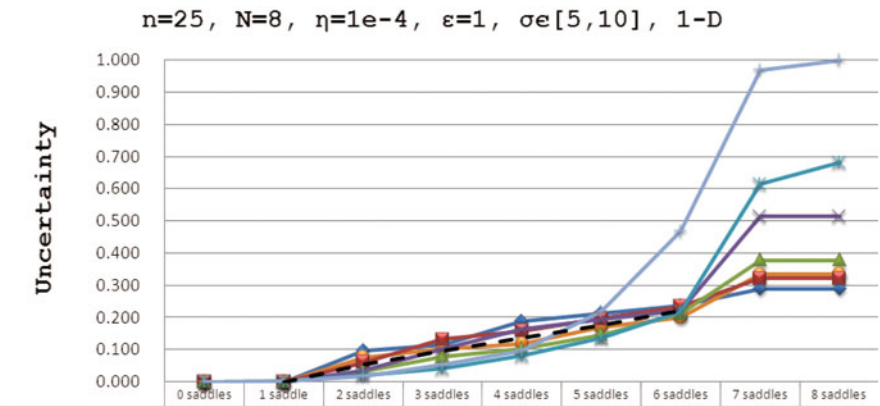

	0 saddles	1 saddle	2 saddles	3 saddles	4 saddles	5 saddles	6 saddles	7 saddles	8 saddles
δ = 1e-5	0.000	0.000	0.097	0.116	0.188	0.213	0.238	0.289	0.289
δ = 1e-4	0.000	0.000	0.076	0.104	0.117	0.169	0.199	0.334	0.334
δ = 1e-3	0.000	0.000	0.061	0.132	0.158	0.196	0.235	0.321	0.321
δ = 1e-2	0.000	0.000	0.033	0.078	0.101	0.146	0.212	0.378	0.378
δ = 1e-1	0.000	0.000	0.037	0.103	0.162	0.194	0.222	0.515	0.515
δ = 1	0.000	0.000	0.021	0.040	0.081	0.136	0.219	0.616	0.683
δ = 10	0.000	0.000	0.018	0.052	0.098	0.219	0.468	0.969	1.000
Average uncertainty		0.000	0.054	0.096	0.135	0.176	0.221		

Fig. 2 Uncertainty functions for the case of GHS containing saddles with one-dimensional unstable manifolds, corresponding to $n = 25$, $N = 8$, $\eta = 1e-4$, $\epsilon = 1.0$, $\delta = 1e-5, 1e-4, 1e-3, 1e-2, 1e-1, 1, 10$ and $\boldsymbol{\sigma} \in [5, 10]$. One sees that the average uncertainty function grows, in fact, approximately linearly and slowly with an approximate slope of 0.043 from $N = 1$ to $N = 6$ and then undergoes an abrupt increasing (compare with [5])

of elements in the sequence as in Fig. 1. This time, when the system starts evolving with initial conditions within the ball of radius δ and $\delta \leq \epsilon$, the reproducibility for a segment of the sequence with length 6 or larger is at least 63.02 %, which is 12.79 % less than in the first experiment. But when the system starts its evolution within the ball of radius δ and $\epsilon < \delta$ we observe that its reproducibility is 45.45 % for a segment of the sequence with length 6 or larger even when the complete sequence does not follow because it skips the first saddle, but then retakes the sequence from the following steps. Here, the reproducibility is 70.86 % for at least the last five elements of the sequence, which is only 7.25 % less than in the first experiment.

In Fig. 4, as in Fig. 2, we represent the function of uncertainty in series corresponding to a different value of δ and we find out that when $\delta \leq \epsilon$, $\overline{u}_6(\delta) \lesssim 0.370$ and $\overline{u}_8(\delta) \lesssim 0.821$. Meanwhile, when $\epsilon < \delta$, $\overline{u}_6(\delta) \lesssim 0.546$ and $\overline{u}_8(\delta) = 0.994$.

As δ decreases, $\overline{u}_i(\delta)$, $i = 0, \ldots, N$ decreases as well, and for $\delta \lesssim 1e-3$, $\overline{u}_8(\delta) \lesssim 0.362$, which has increased only 0.017 from the case of a SHC for the same values of δ.

It is important to note, with respect to the experiments described here, that even though the average reproducibility for the complete set of realizations is not so close to 100 %, there are many individual trials in which we observe full reproducibility. As we use the median of the frequency of reproducibility within trials, we understand

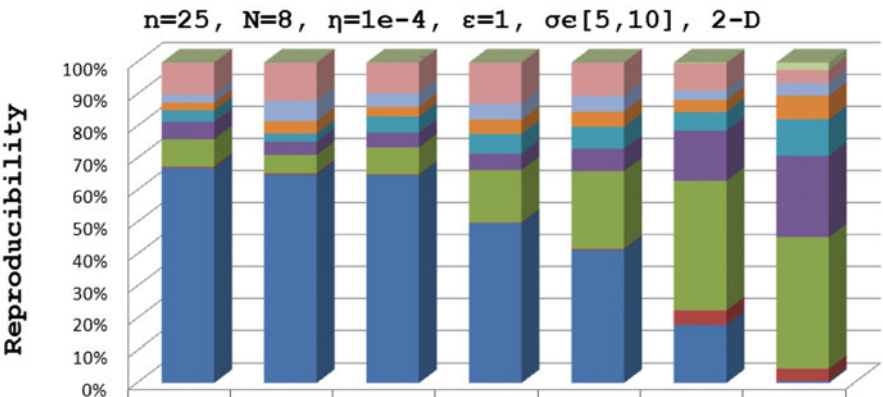

	δ = 1e-5	δ = 1e-4	δ = 1e-3	δ = 1e-2	δ = 1e-1	δ = 1	δ = 10
0 saddles	0.00	0.00	0.00	0.00	0.00	0.29	2.31
1 saddle	9.98	11.88	9.51	12.83	10.44	8.38	4.08
2 saddles	2.56	6.40	4.31	5.03	4.95	3.04	4.05
3 saddles	2.45	3.95	3.05	4.47	4.70	3.75	7.30
4 saddles	3.55	2.51	4.99	6.15	6.85	5.89	11.40
5 saddles	5.43	4.19	4.71	5.16	7.04	15.63	25.41
6 saddles	8.57	5.69	8.32	16.32	24.25	40.53	40.96
7 saddles	0.41	0.35	0.24	0.23	0.28	4.56	3.88
8 saddles	67.05	65.03	64.87	49.81	41.49	17.93	0.61

Fig. 3 Reproducibility for the case of GHS containing saddles with two-dimensional unstable manifolds, corresponding to $n = 25$, $N = 8$, $\eta = 1e-4$, $\epsilon = 1.0$, $\delta = 1e-5, 1e-4, 1e-3, 1e-2, 1e-1, 1, 10$ and $\boldsymbol{\sigma} \in [5, 10]$

that the average reproducibility could be misleading into think that the GHS is not as reproducible as it actually is.

In Fig. 5, we present the median of the frequency of the reproducibility against different values of δ for each of the 100 trials. Here we juxtapose series corresponding in the case of SHS (blue series) and a series corresponding in the case of GHS (red series). We observe that if δ is significantly smaller than ϵ, then for the case of SHS the sequence is reproduced completely most of the times in most of the trials, meanwhile for the case of GHS containing saddles with two-dimensional unstable manifolds, even though the sequence is reproduced completely most of the times, it is not usual to get 100 % reproducibility within trials. So the GHS reproducibility shows a stronger dependence on δ, unlike the SHS case, unless $\epsilon < \delta$, where GHS and SHS reproducibility yields a similar behavior.

In summary:

(i) When the system starts its evolution in a δ-vicinity around the first saddle of the sequence for δ small enough, there is a very low rate of unpredictability, even compared with the case of a SHS, since the difference between them is significantly low. Nevertheless, the difference increases with δ, until it exceeds

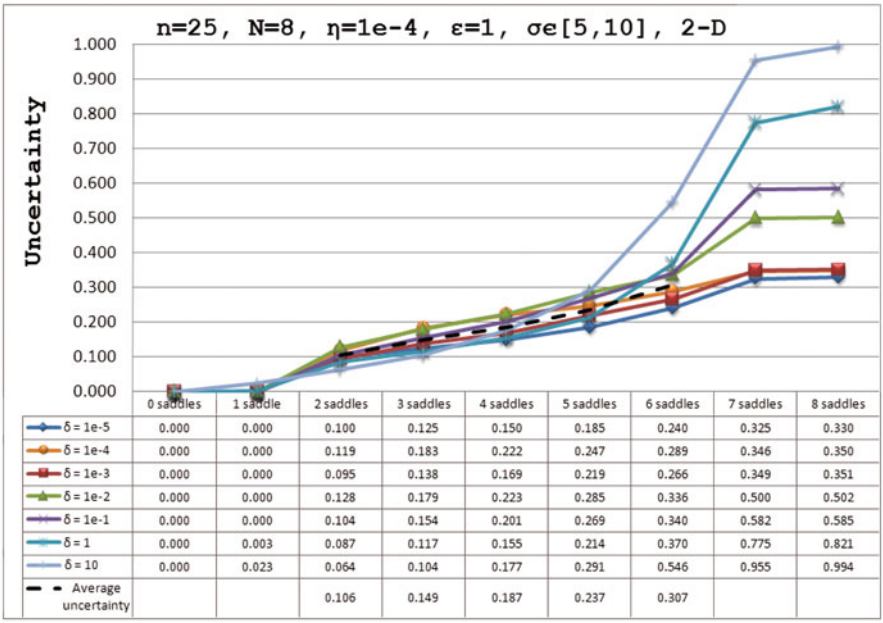

	0 saddles	1 saddle	2 saddles	3 saddles	4 saddles	5 saddles	6 saddles	7 saddles	8 saddles
δ = 1e-5	0.000	0.000	0.100	0.125	0.150	0.185	0.240	0.325	0.330
δ = 1e-4	0.000	0.000	0.119	0.183	0.222	0.247	0.289	0.346	0.350
δ = 1e-3	0.000	0.000	0.095	0.138	0.169	0.219	0.266	0.349	0.351
δ = 1e-2	0.000	0.000	0.128	0.179	0.223	0.285	0.336	0.500	0.502
δ = 1e-1	0.000	0.000	0.104	0.154	0.201	0.269	0.340	0.582	0.585
δ = 1	0.000	0.003	0.087	0.117	0.155	0.214	0.370	0.775	0.821
δ = 10	0.000	0.023	0.064	0.104	0.177	0.291	0.546	0.955	0.994
Average uncertainty			0.106	0.149	0.187	0.237	0.307		

Fig. 4 Uncertainty functions for the case of GHS containing saddles with two-dimensional unstable manifolds, corresponding to $n = 25$, $N = 8$, $\eta = 1e-4$, $\epsilon = 1.0$, $\delta = 1e-5, 1e-4, 1e-3, 1e-2, 1e-1, 1, 10$ and $\boldsymbol{\sigma} \in [5, 10]$. Here one sees, similarly to Fig. 2, that the average uncertainty function grows approximately linearly and slowly with an approximate slope of 0.049 from $N = 2$ to $N = 6$ and then undergoes an abrupt increasing (see [5])

the predetermined size of the heteroclinic channel ϵ. The behavior of the uncertainty functions for the both cases becomes similar again. The occurrence of at least five of eight saddles in sequence is preserved with an uncertainty below 0.220 for the case of SHS and below 0.292 for the case of GHS.

(ii) The main qualitative observation we obtained here is that the longer the sequence of saddles, the greater the uncertainty function is. This is in agreement with the following: it is well known that the length of the sequence of the informational items that a human is able to keep is about 7 or less [5, 6].

(iii) It is interesting to remark that the multidimensionality factor is precisely the cause of a stronger dependence on the initial conditions when it comes to the full reproducibility of the sequence when $\delta < \epsilon$ as seen in Fig. 5, but as δ increases and gets greater than ϵ the behavior becomes similar and retakes the heteroclinic sequence later on (in spite of the size of δ).

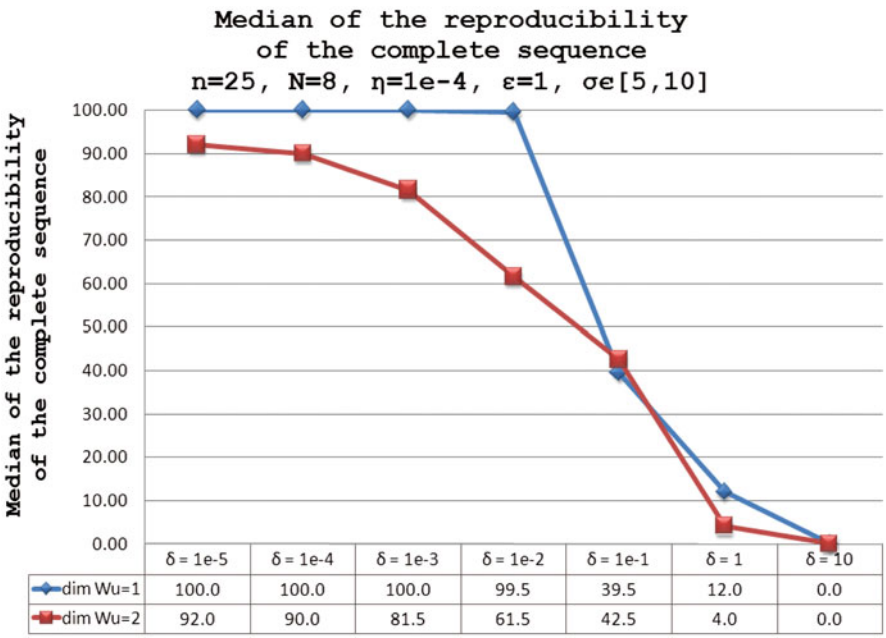

Fig. 5 Experiment corresponding to $n = 25$, $N = 8$, $\eta = 1e-4$, $\epsilon = 1.0$, $\delta = 1e-5, 1e-4, 1e-3, 1e-2, 1e-1, 1, 10$ and $\boldsymbol{\sigma} \in [5, 10]$

3.2 *Uncertainty Functions for the Case of GHS Containing Saddles with Arbitrary Multidimensional Unstable Manifolds*

Complementary to the study we made in Sect. 3.1, we consider now the case of GHS also containing saddles with multidimensional unstable manifolds. Here, we do not prescribe the sequence as we did for Sect. 3.1. The dimension of the unstable manifolds of the saddles is not fixed.

To perform calculations according to the definition of $u_k(\delta)$, we must choose δ, and a set of initial points. Differing from the previous performance, we do not have a prescribed sequence, the system is free to evolve according to the set of parameters and there is no expected order in the GHS. The GHS contains saddles with multidimensional unstable manifolds and we are interested in studying the behavior of the system as the number of elements in the network increases.

Our experiment considers the following values for the number of elements of the network $n = 10, 20, 30, 40, 50, 60, 70, 80, 90, 100$, as well as the following parameters: $\eta = 1e - 4$, $\delta = 1e - 3$, and $\epsilon = 0.5$. The time for the evolution of the system was fixed: $T = 100$. As before, for each value of n we performed 100 sets of 100 simulations each of the dynamics of the LVM, where the integration was performed by using the Milstein integration scheme [14]. For each set of 100

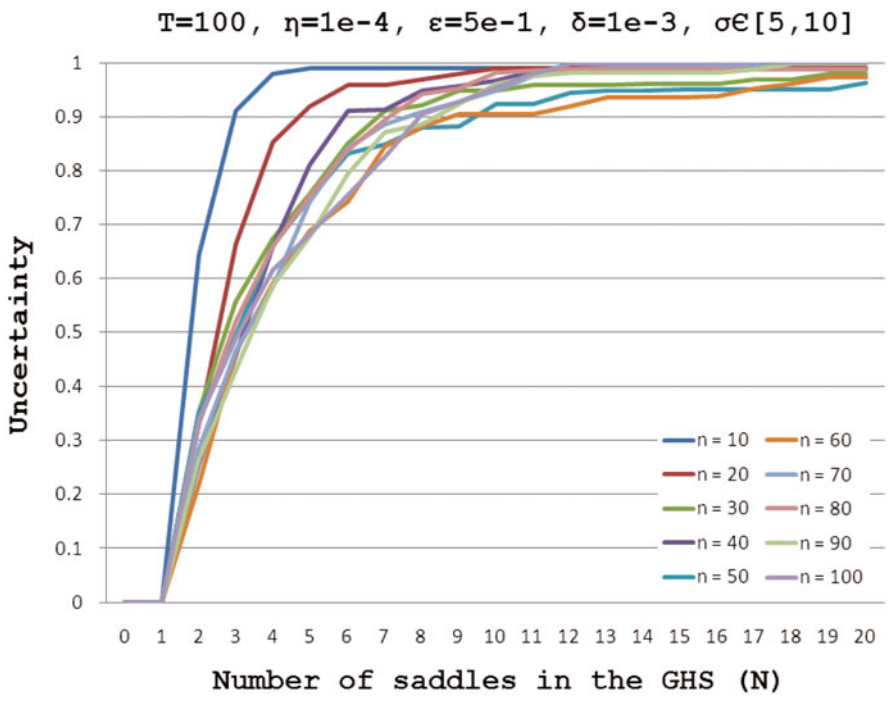

Fig. 6 Uncertainty functions for the case of GHS containing saddles with multidimensional unstable manifolds, corresponding to $n = 10, 20, 30, 40, 50, 60, 70, 80, 90, 100$, $\eta = 1e-4$, $\epsilon = 0.5$, $\delta = 1e-3$ and $\boldsymbol{\sigma} \in [5, 10]$

simulations: (i) the connectivity matrix (ρ_{ij}) is assumed to have diagonal entries all equal to 1, and since we do not have a prescribed sequence, the rest of the values are set to be random numbers taken uniformly from the interval $(1 \times 10^{-10}, 20)$ with a variation smaller than $\pm 10^{-4}$, (ii) the growth rates σ_i were set to be random numbers taken uniformly from the interval $(5, 10)$, with a variation smaller than $\pm 5e-4$. For every simulation (among 100 in a given set) initial conditions for $a_i(t)$ were set randomly but uniformly from $(0, \frac{\delta}{\sqrt{n}})$, with the exception of $a_0(0)$, which was set to equal $\sigma_0 + \delta s$ (where s is a random number taken uniformly from the interval $(-0.5, 0.5)$).

The system is expected to evolve in a direction corresponding to the maximal positive increment at each saddle as we described in the Sect. 3.1. If it did not evolve in this manner the simulation was terminated.

Unlike Sect. 3.1, x_k is defined as the number of times that the GHS had length k, $k = 0, \ldots, N$ within each set of 100 simulations. The uncertainty function is defined as follows: given a value of δ let $u_k(\delta) = \frac{s - x_k}{s}$, for $k = 0, \ldots, N$ where s is the number of simulations in each trial. We will average this number for all sets of simulations and denote it by $\overline{u}_k(\delta)$. Seldom were there sets for which the length was atypically large. Those sets were removed when calculating $\overline{u}_k(\delta)$.

In Fig. 6, the graph of the uncertainty function is shown. In this graph we present the function of uncertainty in series corresponding to different values of n. We find out that except for $n = 10, 20$, $\overline{u}_3(\delta) \lesssim 0.558$; and except for $n = 10$, $\overline{u}_2(\delta) \lesssim 0.364$. Also, we would like to point out that the behavior for $n > 20$ is not essentially different for each value of n. We have the qualitative observation that the larger the number of elements in the network the greater the function of uncertainty is. The difference comes to be less remarkable as n increases.

The average number of nodes involved in GHS for our experiment as well as the median of this number is illustrated in Fig. 7. For both quantities we find that there is an accelerated growing rate of the quantities when $n \lesssim 30$ compared to the rate of growing for $n > 30$, going from a growing rate of 0.0830 to one of 0.0178 for the average number of nodes, and from 0.0948 to 0.0172 for the median number of nodes. Again, we presume that this behavior is influenced by the time available for the system to evolve.

Based on the previous observation, we presume a similar behavior for the average length of the GHS (taking into account that some saddles may be visited more than once during heteroclinic switching); for the set of simulations of the dynamics of the LVM increasing in a rate of 0.0524 from $n = 10$ to $n = 60$ and becoming less than 0.006 for $n > 60$ because of our decision to fix the time available for the evolution of the system, see Fig. 8.

The average dimension of the unstable manifold W^u at each saddle in the GHS for every simulation of the LVM is shown in Fig. 9. It is evident that this quantity is approximately linearly dependent on the number of elements in the network in a rate of 0.0389. The greater the number of elements, then the greater the probability to meet in the sequence with a saddle with multidimensional unstable manifold.

Its evolution in a δ-vicinity around the first saddle of the sequence for δ small enough, we had a very low rate of predictability for our model with a GHS compared with the case of prescribed order. It is also interesting to remark that this rate of uncertainty for $\overline{u}_3(\delta)$ is unchanged even when n increases.

4 Conclusions

There are two different ways for a heteroclinic channel to lose its stability: (i) the stretching of a phase volume along the sequence became larger than compressing, or (ii) the unstable separatrix of a saddle became multidimensional. In this chapter we have considered the second scenario, which in our opinion is the most typical for complex multiagent networks like the brain or an ecological food web. We have shown that in complex networks, in spite of the multidimensionality of saddles unstable manifold, some amount of order along transients remains to be feasible: many trajectories follow a strongly unstable direction and the probability to indicate a generalized heteroclinic sequence is high enough.

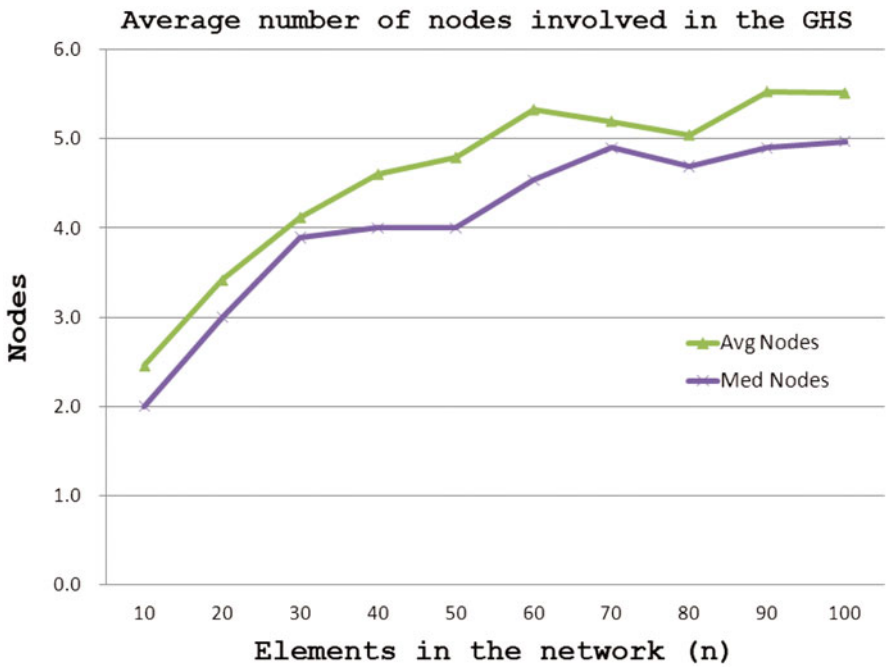

Fig. 7 Average number of nodes involved in GHS for the experiment described for $n = 10, 20, 30, 40, 50, 60, 70, 80, 90, 100$, $\eta = 1e-4$, $\epsilon = 0.5$, $\delta = 1e-3$, $T = 100$

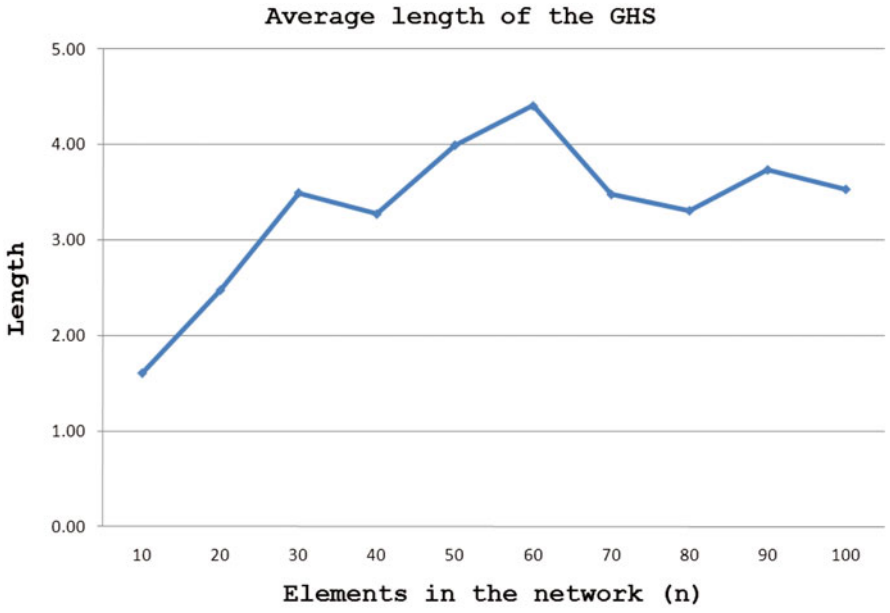

Fig. 8 Average length of the GHS for the experiment described for $n = 10, 20, 30, 40, 50, 60, 70, 80, 90, 100$, $\eta = 1e-4$, $\epsilon = 0.5$, $\delta = 1e-3$, $T = 100$

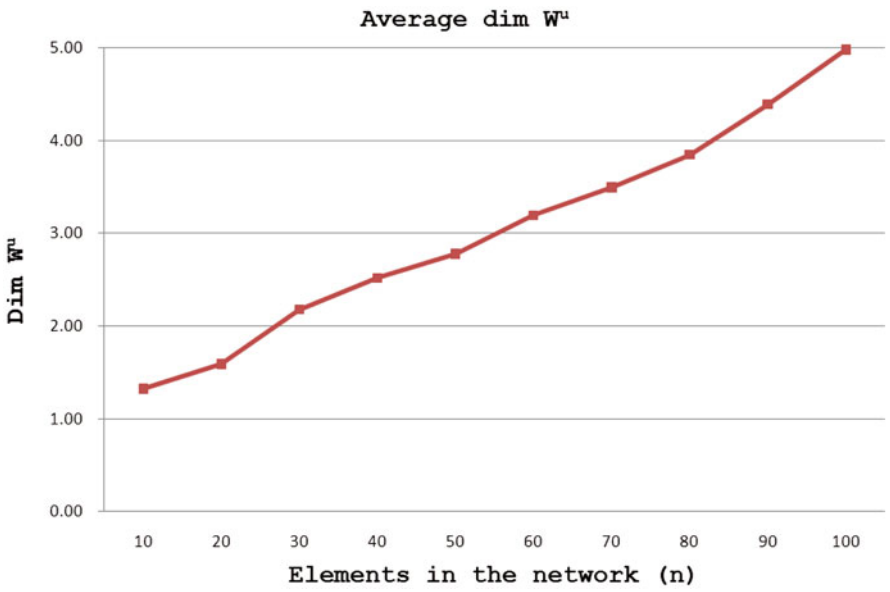

Fig. 9 Average dimension of the unstable manifold W^u at each saddle in the GHS described for $n = 10, 20, 30, 40, 50, 60, 70, 80, 90, 100$, $\eta = 1e-4$, $\epsilon = 0.5$, $\delta = 1e-3$, $T = 100$

Acknowledgements We thank Valentin Afraimovich for many constructive discussions and suggestions that helped us to make this piece of research stronger. I.T. acknowledges support by CONACYT. M.R. was supported by US Naval Research by grant ONR N00014-1-0741.

References

1. Afraimovich, V., Zhigulin, V., Rabinovich, M.: On the origin of reproducible sequential activity in neural circuits. Chaos (An Interdisciplinary Journal of Nonlinear Science) **14**, 1123 (2004)
2. Afraimovich, V., Tristan, I., Huerta, R., Rabinovich, M.: Winnerless competition principle and prediction of the transient dynamics in a Lotka–Volterra model. Chaos (An Interdisciplinary Journal of Nonlinear Science) **18**, 043103 (2008)
3. Ashwin, P., Timme, M.: Nonlinear dynamics: When instability makes sense. Nature **436**(7047), 36–37 (2005)
4. Bastolla, U., Lässig, M., Manrubia, S., Valleriani, A.: Biodiversity in model ecosystems, I: Coexistence conditions for competing species. J. Theor. Biol. **235**(4), 521–530 (2005)
5. Bick, C., Rabinovich, M.: Dynamical origin of the effective storage capacity in the brain's working memory. Phys. Rev. Lett. **103**(21), 218101 (2009)
6. Bick, C., Rabinovich, M.: On the occurrence of stable heteroclinic channels in Lotka-Volterra models. Dyn. Syst. **25**(1), 97–110 (2010)
7. Doboli, S., Minai, A., Best, P.: Latent attractors: A model for context-dependent place representations in the hippocampus. Neural Comput. **12**(5), 1009–1043 (2000)
8. Hertz, J., Krogh, A., Palmer, R.: Introduction to the Theory of Neural Computation. Perseus Books Group, Cambridge (1991)
9. Hirsh, M., Pugh, C., Shub, M.: Invariant Manifolds (Lecture Notes in Mathematics, vol. 583) (1977)

10. Hopfield, J.: Neural networks and physical systems with emergent collective computational abilities. Proc. Natl. Acad. Sci. U S A **79**(8), 2554–2558 (1982)
11. Lotka, A.: Elements of Physical Biology. Williams & Wilkins company, Baltimore (1925)
12. Muezzinoglu, M., Tristan, I., Huerta, R., Afraimovich, V., Rabinovich, M.: Transients versus attractors in complex networks. Int. J. Bifurcat. Chaos **20**(6), 1–23 (2010)
13. Nowotny, T., Rabinovich, M.: Dynamical origin of independent spiking and bursting activity in neural microcircuits. Phys. Rev. Lett. **98**(12), 128106 (2007)
14. Øksendal, B.: Stochastic Differential Equations: An Introduction With Applications. Springer, Berlin-Heidelberg (2003)
15. Rabinovich, M., Volkovskii, A., Lecanda, P., Huerta, R., Abarbanel, H., Laurent, G.: Dynamical encoding by networks of competing neuron groups: Winnerless competition. Phys. Rev. Lett. **87**(6), 68102 (2001)
16. Rabinovich, M., Huerta, R., Varona, P.: Heteroclinic synchronization: Ultrasubharmonic locking. Phys. Rev. Lett. **96**(1), 14101 (2006)
17. Rabinovich, M., Huerta, R., Varona, P., Afraimovich, V.: Generation and reshaping of sequences in neural systems. Biol. Cybern. **95**(6), 519–536 (2006)
18. Rabinovich, M., Huerta, R., Varona, P., Afraimovich, V.: Transient cognitive dynamics, metastability, and decision making. PLoS Comput. Biol. **4**(5) (2008)
19. Toro, M., Aracil, J.: Qualitative analysis of system dynamics ecological models. Syst. Dyn. Rev. **4**(1–2), 56–80 (2006)
20. Volterra, V.: Variations and fluctuations of the number of individuals in animal species living together. ICES J. Mar. Sci. **3**(1), 3 (1928)
21. Waugh, F., Marcus, C., Westervelt, R.: Fixed-point attractors in analog neural computation. Phys. Rev. Lett. **64**(16), 1986–1989 (1990)
22. Wilson, H., Cowan, J.: A mathematical theory of the functional dynamics of cortical and thalamic nervous tissue. Biol. Cybern. **13**(2), 55–80 (1973)

Phase Control of Chaotic Maps

Sijo K. Joseph and Miguel A. F. Sanjuán

Abstract The phase control is a well-known control method that has been typically applied to periodically driven dynamical systems. Its application allows controlling them through the phase difference between the forcing term and another harmonic perturbation. In the current chapter, we focus on the application of this control method to maps. In particular, we analyze two paradigmatic maps: the bouncing ball map and the Hénon map. As a result, we observe that the application of the phase control can suppress or enhance the chaotic behavior on them. We also analyze the crisis induced intermittency in the bouncing ball map when the phase of the control signal is varied. Finally, the scaling behavior of the average Lyapunov exponents near the phase induced crisis is studied. Future applications of the phase control method are also discussed.

1 Introduction

The important characteristic of a chaotic dynamical system is the exponential sensitivity to the initial conditions. Even arbitrary close trajectories diverge with time at a finite distance, thus the long term predictions are impossible. This is what is known as the butterfly effect as concocted by Philip Merilees "Does the flap of a butterfly's wings in Brazil set off a tornado in Texas?" If that is true, our natural counter question is, what happens when another butterfly flaps its wings, will the effect get canceled? Our answer is yes.

One of the pioneering methods of chaos control, the OGY controlling chaos method [19], is based on the fact that a very small variation of a system parameter, by means of a feedback, can transform a chaotic trajectory into a periodic one and vice versa.

S. K. Joseph (✉) · M. A. F. Sanjuán
Nonlinear Dynamics, Chaos and Complex Systems Group, Departamento de Física,
Universidad Rey Juan Carlos, Tulipán s/n, 28933 Móstoles, Madrid, Spain
e-mail: sijo.joseph@urjc.es

M. A. F. Sanjuán
e-mail: miguel.sanjuan@urjc.es

H. González-Aguilar, E. Ugalde (eds.), *Nonlinear Dynamics New Directions,*
Nonlinear Systems and Complexity 12, DOI 10.1007/978-3-319-09864-7_8

The idea that chaos could be controlled, instead of chaos could not be forecasted, gave rise to an explosive interest to researchers. Despite numerous publications in this field, only a few strict facts were established, while many issues remained open. In view of the wide scope of possible applications, this area is of interest both to the dynamical systems theorists and control engineers [1, 7, 27].

1.1 Phase Control Method

Chaos control methods are usually classified within two main categories depending on how they interact with the chaotic system. The first category corresponds to feedback methods, which are aimed to stabilize one of the stable orbits that lie in the chaotic attractor by applying small perturbations that depend on the time-varying state of the system. The experimental implementation of the feedback methods is hard to achieve since it demands a fast response to the time variation of the system state. For this reason, nonfeedback methods have appeared more useful in many practical cases. The nonfeedback methods allow to switch between different dynamical behaviors by applying either parameter perturbations or external forcing signals that do not depend on the current state of the system [3, 14, 21].

Here, we focus on a nonfeedback control technique called phase control method [27]. This technique has been used to control the chaotic behavior of a Duffing oscillator [25], to control intermittencies [26], and to avoid escapes in a nonlinear oscillator [22], among others. Similar ideas have been also applied in the context of Josephson junctions [4, 5] and population dynamics in theoretical ecology [10].

Nonfeedback methods have been mainly used to suppress chaos in periodically driven dynamical systems:

$$\dot{\mathbf{x}} = \mathbf{f}(\mathbf{x},\mathbf{p}) + \mathbf{F}\cos(\omega t), \tag{1}$$

where $\mathbf{x}, \mathbf{f}$, and $\mathbf{F}$ are vectors of the m-dimensional phase space, and p is the parameter vector of the system. The main idea of these nonfeedback methods is to apply a harmonic perturbation either to some of the parameters of the system

$$\dot{\mathbf{x}} = \mathbf{f}(\mathbf{x}, p_i(1 + \epsilon\cos(r\omega t + \phi)), p_j) + \mathbf{F}\cos(\omega t) \tag{2}$$

for $j = 1 \ldots n$ being $j \neq i$, or as an external additional forcing to the system,

$$\dot{\mathbf{x}} = \mathbf{f}(\mathbf{x}, \mathbf{p}) + \mathbf{F}\cos(\omega t) + \epsilon\mathbf{u}\cos(r\omega t + \phi). \tag{3}$$

Here, $\mathbf{u}$ is conveniently chosen as a unitary vector, r determines the ratio between the frequency of the forcing and the natural frequency of the system, and ϕ is the phase difference between the natural oscillation and the forcing signal.

In resonant parametric perturbation methods, the numerical and experimental explorations have been essentially focused on the role played by the perturbation amplitude ϵ and the resonance condition r, but the role of the phase difference ϕ has

hardly been explored. However, it is observed that the phase difference ϕ between the periodic forcing and the perturbation has certain influence on the dynamical behavior of the system. The type of control based on varying the phase difference ϕ in search of a desired dynamical behavior is known as the phase control technique.

2 Dissipative Maps

In dissipative maps the phase space volume is not conserved. The phase space volume shrinks as time proceeds. Hence the value of the Jacobian is less than one. In area-preserving maps, the value of the Jacobian is unity, and we cannot observe a definite chaotic attractor. However in a dissipative map, we can observe a definite chaotic attractor. We are going to study two different dissipative chaotic maps called the dissipative bouncing ball map and the Hénon map which are two simple paradigmatic models of dissipative maps.

2.1 Bouncing Ball Map

An acceleration mechanism of cosmic ray particles interacting with the time-dependent magnetic field was proposed by Enrico Fermi in 1949 [6]. This phenomenon was explained later in terms of a simple classical model by Stanislaw Ulam [24]. Afterward, this model became popular as the Fermi–Ulam model [17] and several modified versions were proposed over the years because of its interesting dynamical properties [2, 16]. Among the different models, the simplest one that displays chaotic behavior is the system with one ball bouncing on a vibrating table under the action of gravity. This is widely known as the bouncing ball system [11, 13].

In the simple bouncing ball model, a ball bounces on a sinusoidally vibrating table under the action of gravity. The evolution of the bouncing ball system is a mix of continuous and discrete evolution. In between the collisions, the evolution of the system is continuous but it is discontinuous at the time of collision. Using this property, we can easily make a discrete map of the system by analyzing the impact time series. Let $X(t)$ be the position of the ball with respect to the ground reference frame, then the series $X(t_0), X(t_1), X(t_2), \ldots, X(t_n)$ represents the impact time position series of the ball.

Next, we follow the derivation of the bouncing ball map as it was introduced in Ref. [11]. Let $\bar{V}_k$ be the velocity of the ball with respect to the fixed reference frame, just after the impact time t_k and $\bar{V}_k^{'}$ be the velocity just before the impact time t_k. The nature of the impact is relevant, so that if the impact between table and the ball is inelastic, we have

$$\bar{V}_k = -\alpha \bar{V}_k^{'}, \tag{4}$$

where α is the coefficient of restitution $0 < \alpha \leq 1$. When $\alpha = 1$, the collision is completely elastic. We are interested in the quantities which are in the ground frame

of reference. Considering the $k+1$ collision, consequently we will get

$$\bar{V}_{k+1} = -\alpha \bar{V}_{k+1}^{'}, \tag{5}$$

$$\bar{V}_{k+1} = V_{k+1} - U_{k+1}, \tag{6}$$

$$\bar{V}_{k+1}^{'} = V_{k+1}^{'} - U_{k+1}, \tag{7}$$

where U_{k+1} is the velocity of the vibrating table at the $(k+1)$th collision. Substituting Eqs. (6) and (7) in Eq. (5), we get

$$V_{k+1} - U_{k+1} = -\alpha(V_{k+1}^{'} - U_{k+1}),$$

$$V_{k+1} = (1+\alpha)U_{k+1} - \alpha V_{k+1}^{'}. \tag{8}$$

The variable t represents the instantaneous time between two adjacent collisions ($t_k \leq t \leq t_{k+1}$), where t_k is the time of the kth impact on the table and t_{k+1} is the time of the $(k+1)$th impact. Let $X(t)$ be the vertical position of the ball in the ground frame of reference, then according to Newton's law, the instantaneous position of the ball is given by

$$X(t) = X_k + V_k(t - t_k) - \frac{g}{2}(t - t_k)^2 \tag{9}$$

and the velocity of the table is given by

$$V_{k+1} = \frac{dX}{dt}|_{t=t_{k+1}}. \tag{10}$$

Now we can compute the impact velocity equation. The table position is given by $s(t) = A\sin(\omega t + \theta_0)$, so that our table velocity is given by

$$U_{k+1} = \frac{ds}{dt}|_{t=t_{k+1}}. \tag{11}$$

The instantaneous distance between the table and the ball is given by $d(t) = x(t) - s(t)$. We can find the impact time by solving $d(t_{k+1}) = 0$ since an impact occurs when the distance between the table and the ball goes to zero. Therefore

$$X_k + V_k(t_{k+1} - t_k) - \frac{1}{2}g(t_{k+1} - t_k)^2 - A\sin(\omega t_{k+1} + \theta_0) = 0. \tag{12}$$

The above equation is called the time recurrence equation. If we substitute $U_k = A\omega\cos(\omega t_k + \theta_0)$ and $V_{k+1}^{'} = V_k - g(t_{k+1} - t_k)$ in Eq. (8), we can obtain Eq. (13), which is the recurrence velocity equation

$$V_{k+1} = (1+\alpha)A\omega\cos(\omega t_{k+1} + \theta_0) - \alpha[V_k - g(t_{k+1} - t_k)]. \tag{13}$$

The complete recurrence equations are given by

$$X_k + V_k(t_{k+1} - t_k) - \frac{1}{2}g(t_{k+1} - t_k)^2 - A\sin(\omega t_{k+1} + \theta_0) = 0, \tag{14}$$

$$V_{k+1} = (1+\alpha)A\omega\cos(\omega t_{k+1} + \theta_0) - \alpha[V_k - g(t_{k+1} - t_k)]. \tag{15}$$

These are the exact time and velocity recurrence equations, respectively. But one of them is explicit and another one is implicit. Since we want to construct a nonlinear map out of these equations, we need both equations to be explicit. To solve this problem, we make use of an approximation called the high bounce approximation.

2.1.1 High Bounce Approximation

In this approximation, we assume that the bouncing height of the ball is large compared with the vibration of the table. Thus, we say that the velocity of the ball simply change its sign for the $(k+1)$th collision, therefore

$$V'_{k+1} = -V_k. \tag{16}$$

Using the equation of motion we have,

$$V'_{k+1} = V_k - g(t_{k+1} - t_k). \tag{17}$$

Substituting Eq. (16) in Eq. (17) we have,

$$t_{k+1} = t_k + \frac{2V_k}{g}. \tag{18}$$

Thus the approximated explicit recurrence equations are given by

$$\begin{aligned} t_{k+1} &= t_k + \frac{2V_k}{g}, \\ V_{k+1} &= (1+\alpha)A\omega\cos(\omega t + \theta_0) - \alpha[V_k - g(t_{k+1} - t_k)]. \end{aligned} \tag{19}$$

If we transform Eqs. (18) and (19) to make them dimensionless by changing variables as $x_k = \omega t_k + \theta_0$, $y_k = (2\omega/g)V_k$, and $\beta = (2\omega^2 A/g)(1+\alpha)$ we get,

$$\begin{aligned} x_{k+1} &= x_k + y_k \\ y_{k+1} &= \beta\cos x_{k+1} - \alpha[y_k - 2(x_{k+1} - x_k)]. \end{aligned} \tag{20}$$

If we substitute the phase equation $x_{k+1} = x_k + y_k$ in Eq. (20), we get the complete approximated explicit recurrence equations, which are given by,

$$\begin{aligned} x_{n+1} &= x_n + y_n \\ y_{n+1} &= \alpha y_n + \beta\cos(x_n + y_n). \end{aligned} \tag{21}$$

Here x is associated with the time interval between collisions and y is associated with the velocity of the ball just after the impact. Here α is the coefficient of restitution and β is related to the frequency and amplitude of the table. The Jacobian matrix of a two-dimensional map is defined by

$$J = \frac{\partial(x_{i+1}, y_{i+1})}{\partial(x_i, y_i)}, \tag{22}$$

so that the Jacobian matrix of the bouncing ball map is given by,

$$J = \begin{bmatrix} 1 & 1 \\ \beta S & \alpha + \beta S \end{bmatrix},$$

where $S = \sin(x_k + y_k)$. In order to calculate the dissipation effect, let us take the determinant of the Jacobian matrix, which is given by,

$$|J| = \begin{vmatrix} 1 & 1 \\ \beta \sin(x_k + y_k) & \alpha + \beta \sin(x_k + y_k) \end{vmatrix}$$

So that,

$$|J| = \alpha. \tag{23}$$

Here in the dissipative bouncing ball model, we are considering the inelastic collisions of the ball with the table. Hence the energy is not conserved. The energy loss is determined by the dissipation coefficient α. Hence, it is evident that α is the dissipation coefficient, so here, α gives the measure of the contraction of phase space.

The eigenvalues of the Jacobian matrix are given by,

$$\Lambda^2 - \Lambda\ Tr(J) + |J| = 0, \tag{24}$$

where $Tr(J)$ means the trace of the matrix J. Thus, by solving this equation, we get

$$\Lambda = \frac{1}{2}\left[(1 + \alpha + \beta S) \pm \sqrt{(1 + \alpha + \beta S)^2 - 4\alpha}\right], \tag{25}$$

where $S = \sin(x_k + y_k)$ and Λ are the local Lyapunov exponents. The global Lyapunov exponents are defined as,

$$\lambda_j = \lim_{n\to\infty} \frac{1}{n} \ln|\Lambda_j|, \quad j = 1, 2, \tag{26}$$

where Λ_j are the eigenvalues of $M = \prod_{i=1}^{n} J_i(x_i, y_i)$. If the value of λ_j is positive, then the phase space trajectories diverge exponentially, which in turn gives the chaotic behavior in the system.

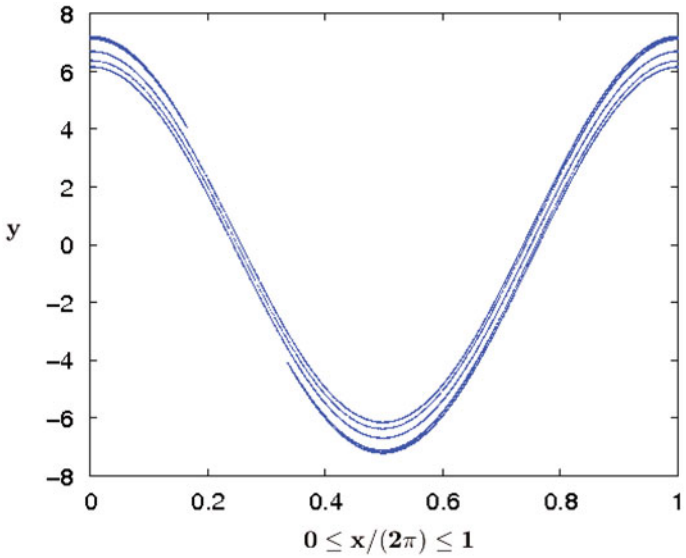

Fig. 1 The figure shows the chaotic attractor of the dissipative bouncing ball map. Here we have taken the parameter values $\alpha = 0.1$ and $\beta = 6.56$

Since the bouncing ball system is dissipative, there exists a chaotic attractor, which is shown in Fig. 1. Here the width of the attractor depends on the dissipation coefficient α. If the value of α is close to zero, the width of the attractor is minimum and the width is maximum when the value of the alpha is close to unity. If the value of the dissipation coefficient α reaches unity, then the specific chaotic attractor vanishes and the system shows a sort of Hamiltonian chaos.

2.1.2 Standard Map

If the coefficient of restitution is unity, then the dissipative bouncing ball map reduces to the standard map,

$$\begin{aligned} x_{n+1} &= x_n + y_n \\ y_{n+1} &= y_n + \beta \cos(x_n + y_n). \end{aligned} \tag{27}$$

This is an area-preserving map since the determinant of the Jacobian matrix is unity. This is one of the important chaotic maps also studied in connection with the kicked rotor.

2.2 Hénon Map

The Lorenz system consists of a system of three first-order ordinary differential equations whose solutions for an appropriate choice of parameters tend toward a strange attractor called the Lorenz attractor. Hénon's original idea was to replace these first-order ordinary differential equations by a simple two-dimensional map which shows the same properties of the Lorenz system.

We are going to consider Hénon's original derivation of the map [12]. Consider a region elongated along the x axis. We begin the folding by

$$T^{'} : x^{'} = x,\ y^{'} = y + 1 - ax^2. \tag{28}$$

We complete the folding by a contraction along the x axis,

$$T^{''} : x^{''} = bx^{'},\ y^{''} = y^{'}. \tag{29}$$

Finally we come back to the orientation along the x axis by,

$$T^{'''} : x^{'''} = y^{''},\ y^{'''} = x^{''}. \tag{30}$$

The final map will be defined as the product $T = T^{'''}T^{''}T^{'}$. If we write (x_n, y_n) for (x, y) and (x_{n+1}, y_{n+1}) for $(x^{'''}, y^{'''})$, then we have,

$$\begin{aligned} x_{n+1} &= y_n + 1 - ax_n^2 \\ y_{n+1} &= bx_n. \end{aligned} \tag{31}$$

The above map is called the Hénon map, but we use a slightly different version of the Hénon map, which is given by,

$$\begin{aligned} x_{n+1} &= A + By_n - x_n^2 \\ y_{n+1} &= x_n. \end{aligned} \tag{32}$$

This is one of the paradigmatic examples of discrete dynamical systems that exhibit chaotic behavior, where A and B are the parameters of the map. The Jacobian of the map is given by

$$|J| = \begin{vmatrix} -2x_n & B \\ 1 & 0 \end{vmatrix}$$

so that,

$$|J| = -B. \tag{33}$$

This makes that $-B$ is a measure of the contraction of the phase space.

The chaotic attractor for the Hénon map is shown in Fig. 2.

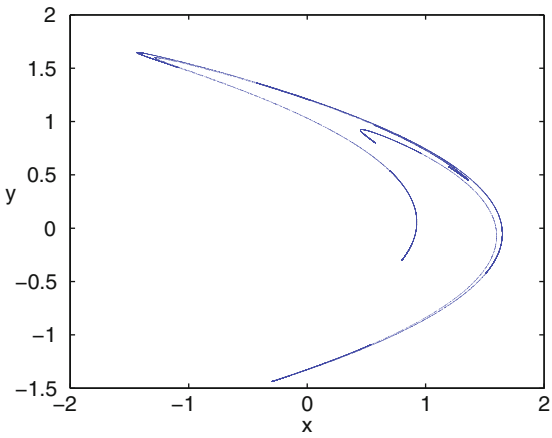

Fig. 2 The figure shows the chaotic attractor for the Hénon map. Here we take the parameter values $A = 1.3$ and $B = 0.285$

3 Phase Control of Chaos

Now we are going to apply the phase control method on nonlinear chaotic maps such as the dissipative bouncing ball map and the Hénon map. The key idea of the phase control method is to apply a harmonic external perturbation to one of the variables of the map. It is possible to control chaos in the system by simply tuning the phase of the external perturbation.

3.1 Control of Chaos in the Bouncing Ball Map

We apply the phase control method on the bouncing ball map Eq. (21), by adding an external harmonic perturbation to the parameter β. Finally, the equation used for the numerical exploration of our technique reads

$$\begin{aligned} x_{n+1} &= x_n + y_n \\ y_{n+1} &= \alpha y_n + \beta(1 + \epsilon \sin(2\pi r n + \phi)) \cdot \\ &\quad \times \cos(x_n + y_n), \end{aligned} \tag{34}$$

where ϵ, ϕ, and r are used as free parameters and $\alpha = 0.1$ is fixed. When the forcing amplitude ϵ is zero, this map reduces to the simple bouncing ball map.

One of the key ideas of this control technique consists of assuming that the external perturbation is of small amplitude, so that once we may fix r and for a considerably small value of parameter ϵ, we may use only ϕ as a free parameter to control the system. Physically it means that we are adding an external small sinusoidal perturbation to the table frequency and changing only the phase of the applied control signal.

In order to analyze the effect of the phase control on the bouncing ball system, first we have to observe the dynamics of the system without the control.

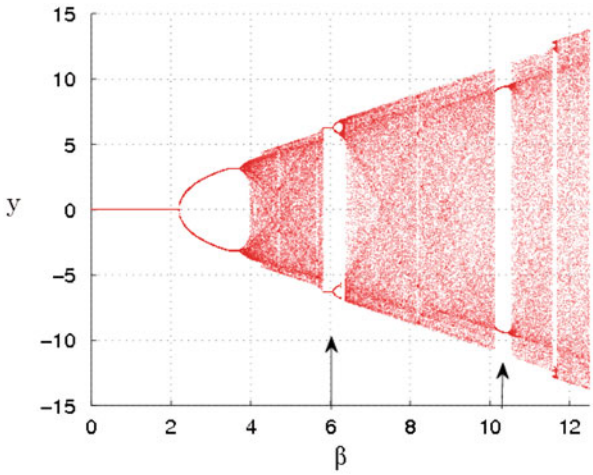

Fig. 3 The figure shows the bifurcation diagram of the bouncing ball system by varying the parameter β. Here we can observe two wide periodic windows at $\beta = 6$ and at $\beta = 10.3$

We have analyzed the bifurcation diagram of the unperturbed bouncing ball system by changing the value of parameter β. This is shown in the Fig. 3, where we can see some regions of chaotic behavior and some periodic windows. For example, the one centered at $\beta = 6$ and other at $\beta = 10.3$. By applying our phase control method, it is possible to change the behavior of the system from chaotic to periodic and vice versa. Thus, we simply start with parameter values which give chaotic dynamics in the unperturbed bouncing ball system. In order to evaluate in a detailed way the role of ϵ and ϕ, we calculate the largest Lyapunov exponent over every point in a 200×200 grid in the rectangle of the parameter plane $0.02 \leq \epsilon \leq 0.07$, $0 \leq \phi \leq 2\pi$, fixing r for each computation, which is shown in Fig. 4. We consider that the perturbation acting on the system is small, and consequently this requires small values of ϵ. As we are searching for areas in the parameter plane where the transition between chaotic and regular motion takes place, we take care of transient states by waiting for a sufficiently long time to fix the corresponding stable regime. We plot the results of several integer and half integer r values. The black and white color associated with each point in the (ϵ, ϕ) plane indicates the sign of the largest Lyapunov exponent. If it is greater than zero (white region), then the dynamics is chaotic and if it is less than zero (black region), then the system shows a regular periodic behavior.

Figure 4 shows that there exist wide regions of the (ϵ, ϕ) plane where λ is smaller than zero, and therefore, chaos is suppressed. We note that the controlled regions, far from having a trivial or irregular shape, present a symmetry that depends on the parity of the r parameter. The system has π symmetry when r is an odd multiple of 0.5 and 2π symmetry when r takes even multiples of 0.5. The most interesting feature is the role of the phase ϕ in selecting the final state of the system. From Fig. 4a, we can see that we have a periodic behavior for the parameter values at $\phi = \pi/2$ and $\epsilon = 0.03$, so that we fix these values and search for the system behavior. Thus, we have plotted the bifurcation diagram in Fig. 5 by fixing $\phi = \pi/2, \epsilon = 0.03$, and $\alpha = 0.1$. It

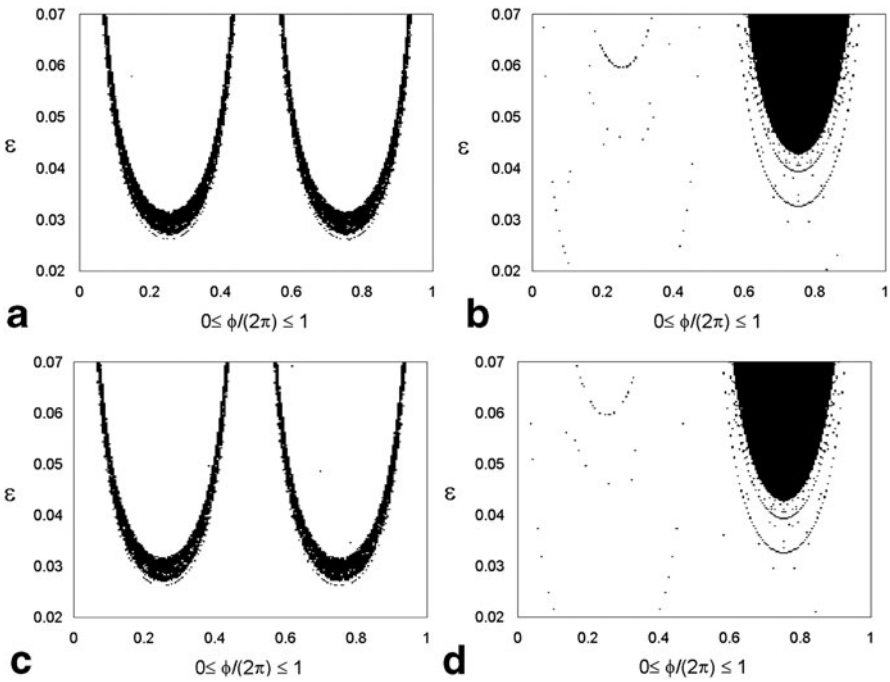

Fig. 4 The figure shows the sign of the largest Lyapunov exponent λ computed at every point of a 200×200 grid of (ϵ, ϕ) values. The range of variation is $0 \leq \phi \leq 2\pi, 0.02 \leq \epsilon \leq 0.07$ for different values of the resonant condition. **a** $r = 0.5$. **b** $r = 1.0$. **c** $r = 1.5$. **d** $r = 2.0$. The Lyapunov exponent is negative in the black regions. These regions have a structure that follows the expected symmetry around $\phi = \pi$ when r is an odd multiple of 0.5 and the trivial symmetry around $\phi = 2\pi$ for an even multiple of 0.5. We set the parameters $\beta = 6.56$, $\alpha = 0.1$

is observed that by a proper choice of the frequency of the controlling signal and a suitable phase difference ϕ, it is possible to avoid chaos in the bouncing ball system.

We can observe other interesting phenomena like the appearance as well as the disappearance of periodic windows in the bifurcation diagram. Next, we compare the bifurcation diagram without the perturbation (Fig. 3) with the bifurcation diagram when the perturbation is applied (Fig. 5). Thus we can observe that in Fig. 5, a new periodic window arises around $\beta = 4$, and at the same time, we can observe that the periodic window centered at $\beta = 10.3$ vanishes. This interesting phenomenon is particularly useful to generate as well as suppress chaos in a dynamical system. If we operate our system near the parameter range, where new periodic windows arise when a periodic perturbation is applied, we can easily control chaos. If the system is operating in a periodic window which vanishes under the action of the periodic perturbation, then we can generate chaos in the system. In this way, we can switch the system behavior from chaotic to periodic and vice versa.

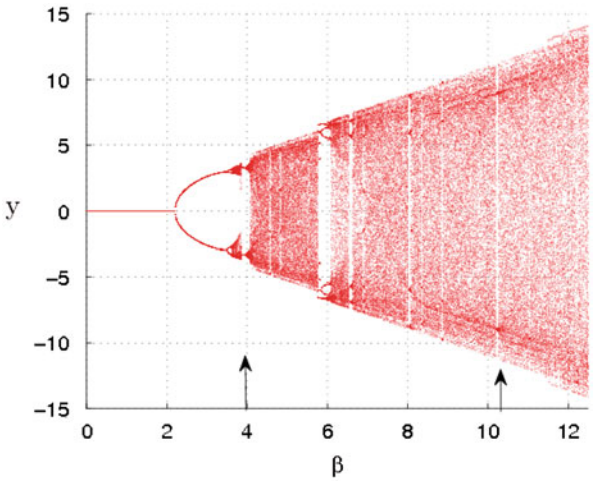

Fig. 5 The figure shows the bifurcation diagram of the bouncing ball system when the phase control is applied. On the y axis we have the velocity of the bouncing ball. We see that a new periodic window arises under perturbation when $\beta = 4$, and at the same time, the periodic window centered at $\beta = 10.3$ disappears. Here the perturbation parameters are taken as $\alpha = 0.1$, $r = 0.5$, $\epsilon = 0.03$, and $\phi = \pi/2$

3.2 *Control of Chaos in the Hénon Map*

In order to apply our phase control technique in the Hénon map Eq. (21), we add a harmonic perturbation $\epsilon \sin(2\pi rn + \phi)$ to the parameter B. Finally the equation used for the numerical exploration of the technique reads

$$\begin{aligned} x_{n+1} &= A + B(1 + \epsilon \sin(2\pi rn + \phi))y_n - x_n^2 \\ y_{n+1} &= x_n. \end{aligned} \tag{35}$$

In order to suppress chaos, we have to search for the suitable ϵ, ϕ values in the Eq. (35). To analyze the effect of phase control on the Hénon map, we simply start with parameter values for which there is chaotic dynamics in the unperturbed Hénon map (Fig. 6).

Afterward, to evaluate in a detailed way the role of ϵ and ϕ, we calculate the largest Lyapunov exponent over every point in a 200×200 grid in the rectangle of the parameter plane $0.003 \leq \epsilon \leq 0.006$, $0 \leq \phi \leq 2\pi$, fixing r for each computation, which is shown in Fig. 7. Note that as we explained before, we consider that the perturbation acting on the system is small, and consequently, this requires small values of ϵ.

As we are searching for areas in the parameter plane where the transition between chaotic and regular motion takes place, we take care of transient states by waiting for a sufficiently long time to fix the corresponding stable regime. We plot the results of several integer and half integer r values. The black and white color associated with each point in the (ϵ, ϕ) plane indicates the sign of the largest Lyapunov exponent. If it is greater than zero (white region), then the dynamics is chaotic and if it is less than zero (black region), then the system shows a regular periodic behavior.

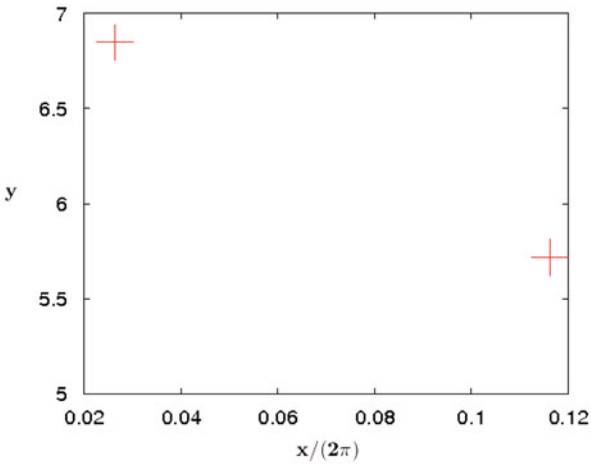

Fig. 6 The figure shows the period two attractor in the phase space of the bouncing ball system when the periodic perturbation is applied. When the periodic perturbation is absent, the bouncing ball map shows a chaotic attractor which is shown in Fig. 1. Here we take the parameter values $\alpha = 0.1, \beta = 6.56, \epsilon = 0.03, r = 0.5$, and $\phi = 1.57$

Figure 7 shows that there exist wide regions of the (ϵ, ϕ) plane where λ is smaller than zero, and therefore chaos is suppressed. The control regions, far from having a trivial or irregular shape, present a symmetry that depends on the parity of the r parameter. The most interesting feature is the role of the phase ϕ in selecting the final state of the system. From Fig. 7a, we can see that we have a periodic behavior for the parameter values at $\phi = \pi/2$ and $\epsilon = 0.00475$, so that we fix these values and search for the system behavior. Thus, we have plotted the phase space diagram in Fig. 8 by fixing $A = 1.3, B = 0.285, \phi = \pi/2,$ and $\epsilon = 0.00475$. Here we can see that the chaotic Hénon attractor (shown in Fig. 2) turned into an orbit of period 14 (shown in Fig. 8). As a result, it is possible to avoid chaos in the Hénon map by a proper choice of the phase difference ϕ.

4 Phase-Dependent Intermittency and Crisis

When the control parameter is modified, a chaotic attractor can touch an unstable periodic orbit inside its basin of attraction, and a sudden expansion of the chaotic attractor is observed. This phenomenon is called an interior crisis [8]. Beyond the crisis, the system preserves a memory of the former situation, thus a fraction of the time is spent in the region corresponding to the precrisis attractor, and during the rest of the time, excursions around the formerly unstable periodic orbit take place. This behavior is known as crisis-induced intermittency. Before the crisis, such excursions cannot take place unless noise or an external perturbation induces them. We show that the intermittency at an interior crisis can be controlled by our phase control method. We give a numerical evidence that if we choose a proper parameter value, it can be used to enhance the crisis. An experimental and theoretical study of phase control of intermittency was already tested successfully in a laser system by Zambrano et al. [26].

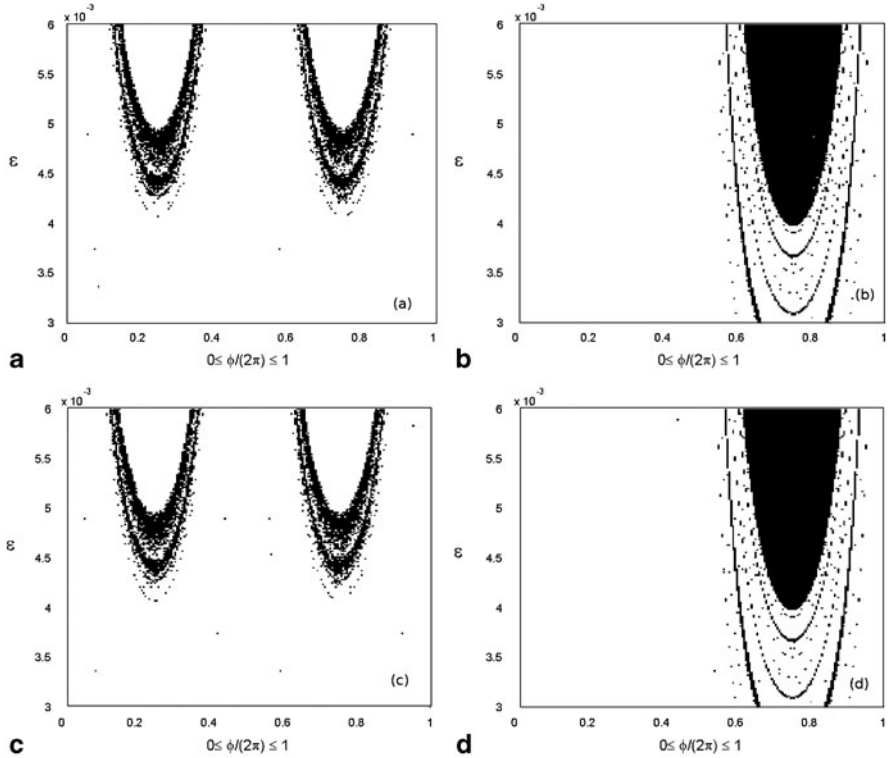

Fig. 7 The figure shows the sign of the largest Lyapunov exponent λ computed at every point of a 200×200 grid of (ϵ, ϕ) values. The range of variation is $0 \leq \phi \leq 2\pi, 0.003 \leq \epsilon \leq 0.006$ for different values of the resonant condition: **a** $r = 0.5$. **b** $r = 1.0$. **c** $r = 1.5$. **d** $r = 2.0$. The Lyapunov exponent is negative in the *black regions*. These regions have a structure that follows the expected symmetry around $\phi = \pi$ when r is an odd multiple of 0.5 and the trivial symmetry around $\phi = 2\pi$ for an even multiple of 0.5. Here we take $A = 1.3$ and $B = 0.285$

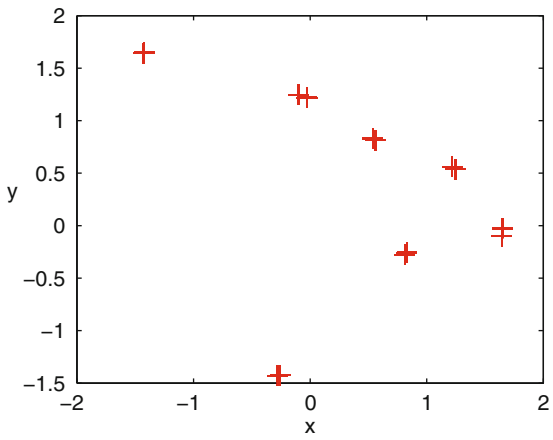

Fig. 8 The figure shows the period 14 attractor when the external periodic perturbation is applied. When the external perturbation is absent, the system shows a chaotic attractor which is shown in Fig. 2. Here we take the parameter values $A = 1.3$, $B = 0.285$, $\epsilon = 0.00475$, $\phi = \pi/2$, and $r = 0.5$

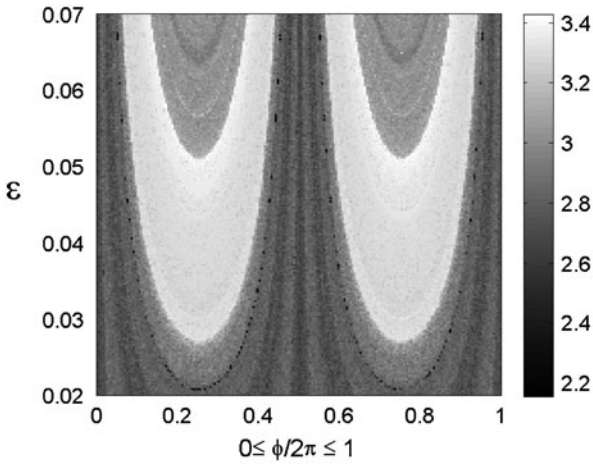

Fig. 9 The figure shows the average value of the relative maxima of the velocity, $< H >$, computed at every point of a 200×200 grid of (ϵ, ϕ) values in the region $0 \leq \phi \leq 2\pi, 0.02 \leq \epsilon \leq 0.07$ for the perturbed bouncing ball map. The *white region* shows the sudden expansion in the attractor. Here we set the parameters $\alpha = 0.1$, $\beta = 4.05$, and $r = 0.5$.

4.1 Intermittency in the Bouncing Ball Map

In order to analyze the effect of the phase ϕ and the forcing amplitude ϵ on the crisis, we scan over the possible ϕ and ϵ values to determine the region where the crisis is induced. A good indicator to discriminate between the different dynamical states of the system for different values of the parameter is

$$< H >=< \max(y_n) >|_{y_n > y_0}, \tag{36}$$

where $< H >$ gives the average value of the maximum of the time series of y_n. In other words, $< H >$ is the average value of the relative maximum velocity of the bouncing ball just after the impact. The value of y_0 is chosen in such a way that $< H >$ enables us to distinguish between the chaos and the intermittent regime. In the numerical simulations, we have observed that taking $y_0 = 10^{-6}$, that is, neglecting only extremely small peaks of the signal, is sufficient for this discrimination.

In Fig. 9, the wide symmetrical white regions show that there is an expansion in the attractor. But that exists only for some specific values of the parameters. We can see that there is a range of phase values (white regions) that give a sudden expansion in the attractor, which in turn, leads to intermittency. There exists a symmetry in the phase value of the applied signal which induces the internal crisis in the system. This can be explained in terms of the symmetry of the map under the transformation $\phi \to \phi + \pi/2$. This symmetry depends on the frequency ratio r. In order to gain a deeper insight into the role of ϕ in nonlinear systems, we study the effect of phase on the perturbed map close to an interior crisis. From Fig. 10a and b, we can observe the sudden expansion of the attractor. Actually, the dense points in the enlarged attractor give the attractor in the precrisis regime and the enlarged dotted region gives the intermittency, as can be observed in Fig. 10. The dotted region gives the leaking trajectories from one piece of the attractor to another, and the phase change enhances the crisis in the system which in turn induces intermittency.

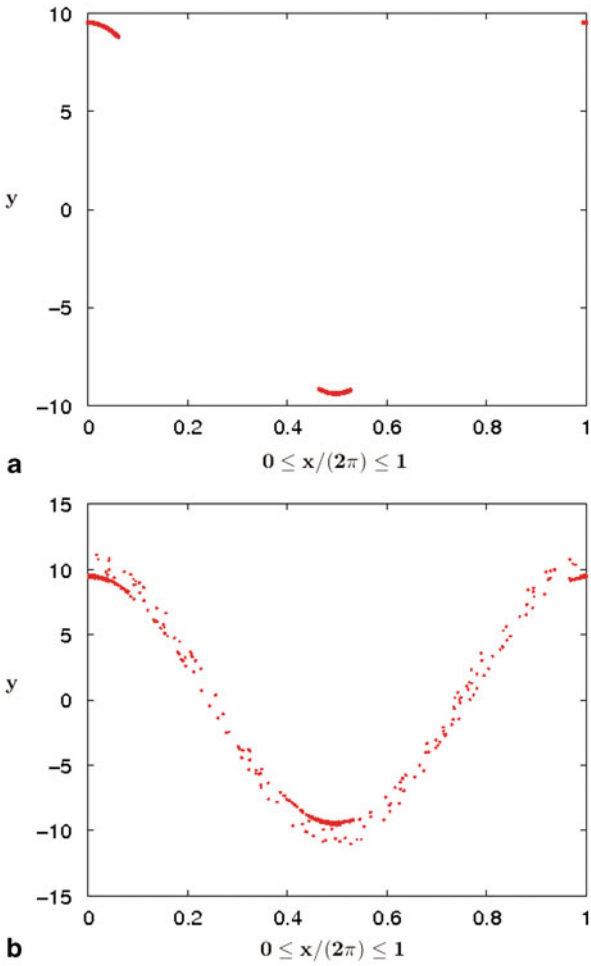

Fig. 10 **a** The chaotic three-piece attractor just before ($\phi = 0.27650$) the interior crisis. **b** The enlarged attractor just after interior crisis ($\phi = 0.27660$). Thus the system has an interior crisis at $\phi_c \approx 0.27655$. The *dense points* in the enlarged attractor give the attractor in the precrisis regime and the *enlarged dotted region* gives the intermittency. Here we fix $\alpha = 0.1$, $\beta = 10.4$, and $\epsilon = 0.03$

One of the interesting aspects to study is the scaling property of the phase close to the critical point after the occurrence of the crisis. In this postcrisis regime, the dynamics describing the evolution of the system is intermittent. A scaling law for the mean time that a chaotic orbit spends in the region of the precrisis attractor ($< \tau >$), as the control parameter (ϕ), is varied and has been proposed by Grebogi et al. [9]. It is found that $< \tau >$ decreases according to the scaling relation $< \tau > \sim \mid \phi - \phi_c \mid^{-\gamma}$ where γ is the scaling exponent describing the scaling of $< \tau >$ with a parameter ϕ. The behavior of the Lyapunov exponents near the crisis point for the dissipative standard map had been studied by B. Pompe and R. W. Leven [20]. According to them, the increase of the largest Lyapunov exponent near the crisis is a consequence of the rapid growth of the transition probability. Thus, we can say that the mean time that a chaotic orbit spends in the region $< \tau >$ is inversely proportional to

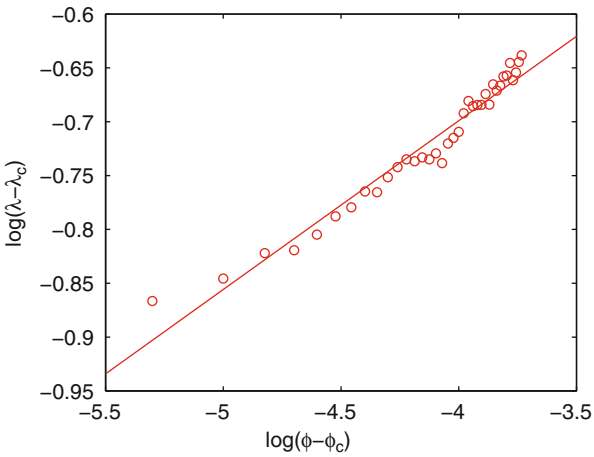

Fig. 11 The figure shows the graph of the $\log(\lambda - \lambda_c)$ vs. $\log(\phi - \phi_c)$. The slope of the linear best fit yields the value of the scaling exponent $\gamma = 0.15$ with a norm of residuals 0.07. Here the phase of the control signal gives the same scaling behavior like a normal parameter. We vary ϕ from 0.276615 to 0.276800 with an increment of 5×10^{-6}

the Lyapunov exponents. In other words, the size of the attractor is related to the Lyapunov exponent via the Kaplan–Yorke dimension. Thus the new scaling equation reads,

$$\lambda(\phi) - \lambda(\phi_c) \sim \mid \phi - \phi_c \mid^{\gamma} . \tag{37}$$

In our case as we know, the phase can enhance the crisis. Thus we analyze the validity of the scaling law of averaged Lyapunov exponent vs. the phase of the applied signal near the crisis regime. Behavior of the Lyapunov exponents near the crisis regime has been studied by several authors [18, 23]. Here, we calculate the average Lyapunov exponents using 10^2 initial conditions calculated over an orbit length of 10^4 iterations. The slope of the linear best fit gives the value of the scaling exponent $\gamma = 0.15$ with the norm of residuals 0.07 (Fig. 11).

5 Concluding Remarks and Future Applications

The phase control method is a chaos control technique which has been successfully applied to periodically driven dynamical systems. The method has been successful in controlling diverse phenomena, including chaotic behavior, escaping dynamics, intermittent behavior, among others, through the phase difference between the forcing term and another harmonic perturbation. We have focused our attention here into the application of this control method to maps. And in particular, we have analyzed two paradigmatic maps: the bouncing ball map and the Hénon map. As a result, we observe with the help of extensive numerical simulations that the application of the phase control can suppress or enhance the chaotic behavior on them. In essence, an appropriate choice of the phase ϕ can lead the system from a chaotic state to a periodic state. Through an extensive exploration of the parameter space, we have

explored zones of chaos suppression for different values of ϵ and ϕ, detecting some interesting patterns. This pattern preserves certain kind of symmetry in the bouncing ball map as well as the Hénon map. We have observed a strong effect of the phase of the control signal in suppressing and generating chaotic behavior in the bouncing ball map and the Hénon map. Another aspect that we have also analyzed is the effect of the phase in inducing the intermittent behavior near a crisis in the bouncing ball map. Our analysis shows that the phase actually may help to enhance the size of the attractor and to contribute to the crisis-induced phenomenon in the bouncing ball map. Finally, we have analyzed the scaling behavior of the crisis in the bouncing ball map by varying the phase. In summary, we have shown that the phase control method is a useful and interesting method for dissipative maps, through which we are able to suppress and generate chaos and control the intermittency in chaotic system close to a crisis, among other effects.

The results we have shown are of a general nature since we have used as models, some paradigmatic maps. Obviously, the same ideas are useful to any other map of similar characteristics. Modeling with maps is very common in nonlinear dynamics and applications. Seasonal effects in theoretical ecology can be modeled through a periodic environmental forcing. These kind of problems are widely used in modeling, and by simply tuning the phase difference between two periodic forcings, the dynamics of the system can be controlled [10]. By changing the phase difference in the driving fields of the Josephson junction, the chaotic dynamics of the system can be controlled as shown in Ref. [4]. A recent review on map-based neuron models [15] has been published where neuron models are described with maps. These ideas of chaos control on maps can be certainly applied to these kind of map-based neuron models. Since the phase control method is already been successfully applied on diverse models describing several fields, it can be easily extended to other fields as well. We believe that the application and implementation of this control method can be helpful and useful in many different situations where a map is used to describe the system dynamics.

Acknowledgements This work was supported by the Spanish Ministry of Science and Innovation under Project No. FIS2013-40653-P.

References

1. Andrievskii, B.R., Fradkov, A.L.: Control of chaos: Methods and applications. II. Applications. Autom. Remote Control **65**, 505–533 (2004)
2. Brahic, H.: Numerical study of a simple dynamical system. 1. The associated plane area-preserving mapping. Astron. Astrophys. **12**, 98–110 (1971)
3. Braiman, Y., Goldhirsch, I.: Taming chaotic dynamics with weak periodic perturbations. Phys. Rev. Lett. **66**, 2545–2548 (1991)
4. Chitra, R.N., Kuriakose, V.C.: Dynamics of coupled Josephson junctions under the influence of applied fields. Phys. Lett. A **365**, 284–289 (2007)
5. Chitra, R.N., Kuriakose, V.C.: Phase effects on synchronization by dynamical relaying in delay-coupled systems. Chaos **18**, Art. 023129 (2008)

6. Fermi, E.: On the origin of the cosmic radiation. Phys. Rev. **75**, 1169–1174 (1949)
7. Fradkov, A.L., Evans, R.J.: Control of chaos: Methods and applications in engineering. Annu. Rev. Control **29**, 33–56 (2005)
8. Grebogi, C., Ott, E., Yorke, J.A.: Crises, sudden changes in chaotic attractors, and transient chaos. Phys. D **7**, 181–200 (1983)
9. Grebogi, C., Ott, E., Romeiras, F., Yorke, J.A.: Critical exponents for crisis-induced intermittency. Phys. Rev. A **36**, 5365–5380 (1987)
10. Greenman, J.V., Pasour, V.B.: Phase control of resonant systems: Interference, chaos and high periodicity. J. Theor. Biol. **278**, 74–86 (2011)
11. Guckenheimer, J., Holmes, P.: Nonlinear Oscillations, Dynamical Systems, and Bifurcations of Vector Fields. Applied Mathematical Sciences, vol. 42. Springer, New York (1983)
12. Hénon, M.: A two-dimensional mapping with a strange attractor. Commun. Math. Phys. **50**, 69–77 (1976)
13. Holmes, P.J.: The dynamics of repeated impacts with a sinusoidally vibrating table. J. Sound Vib. **84**, 173–189 (1982)
14. Hsu, R.R., Su, H.T., Chern, J.L., Chen, C.C.: Conditions to control chaotic dynamics by weak periodic perturbation. Phys. Rev. Lett. **78**, 2936–2939 (1997)
15. Ibarz, B., Casado, J.M., Sanjuán, M.A.F.: Map-based models in neuronal dynamics. Phys. Rep. **501**, 1–74 (2011)
16. Leonel, E.D., McClintock, P.V.E.: Effect of a frictional force on the Fermi–Ulam model. J. Phys. A: Math. Gen. **39**, 11399–11415 (2006)
17. Lieberman, M.A., Lichtenberg, A.J.: Stochastic and adiabatic behavior of particles accelerated by periodic forces. Phys. Rev. A **5**, 1852–1866 (1972)
18. Mehra, V., Ramaswamy, R.: Maximal Lyapunov exponent at crises. Phys. Rev. E **53**, 3420–3424 (1996)
19. Ott, E., Grebogi, C., Yorke, J.A.: Controlling chaos. Phys. Rev. Lett. **64**, 1196–1199 (1990)
20. Pompe, B., Leven, R.W.: Behaviour of Lyapunov exponents near crisis points in the dissipative standard map. Phys. Scr. **38**, 651–656 (1988)
21. Sanjuán, M.A.F.: Using nonharmonic forcing to switch the periodicity in nonlinear systems. Phys. Rev. E **58**, 4377–4382 (1998)
22. Seoane, J.M., Zambrano, S., Euzzor, S., Meucci, R., Arecchi, F.T., Sanjuán, M.A.F.: Avoiding escapes in open dynamical systems using phase control. Phys. Rev. E **78**, Art. 016205 (2008)
23. Stynes, D., Hanan, W.G., Pouryahya, S., Heffernan, D.M.: Scaling relations and critical exponents for two dimensional two parameter maps. Eur. Phys. J. B **77**, 469–478 (2010)
24. Ulam, S.M.: On some statistical properties of dynamical systems. In: Cam, L.M.L., Neyman, J., Scott, E. (eds.) Proceedings of the Fourth Berkeley Symposium on Mathematical Statistics and Probability (University of California, Berkeley, 20 June–30 July 1960), vol. 3, pp. 315–320. University of California Press, Berkeley (1961)
25. Zambrano, S., Brugioni, S., Allaria, E., Leyva, I., Meucci, R., Sanjuán, M.A.F., Arecchi, F.T.: Numerical and experimental exploration of phase control of chaos. Chaos **16**, Art. 013111 (2006)
26. Zambrano, S., Mariño, I.P., Salvadori, F., Meucci, R., Sanjuán, M.A.F., Arecchi, F.T.: Phase control of intermittency in dynamical systems. Phys. Rev. E **74**, 016202 (2006)
27. Zambrano, S., Seoane, J.M., Mariño, I.P., Sanjuán, M.A.F., Meucci, R.: Phase Control in Nonlinear Systems, Chap. 6, pp. 147–188. World Scientific, Singapore (2010)

Voltage Interval Mappings for an Elliptic Bursting Model

Jeremy Wojcik and Andrey Shilnikov

Abstract We employed Poincaré return mappings for a parameter interval to an exemplary elliptic bursting model, the FitzHugh–Nagumo–Rinzel model. Using the interval mappings, we were able to examine in detail the bifurcations that underlie the complex activity transitions between: tonic spiking and bursting, bursting and mixed-mode oscillations, and finally, mixed-mode oscillations and quiescence in the FitzHugh–Nagumo–Rinzel model. We illustrate the wealth of information, qualitative and quantitative, that was derived from the Poincaré mappings, for the neuronal models and for similar (electro) chemical systems.

1 Introduction

The class of elliptic bursting models is rich and can be found in diverse scientific studies, ranging from biological systems [37] to chemical processes such as the Belousov–Zhabotinky reaction [2]. Transitions between activity states for elliptic bursting models is not common knowledge. Often in the sciences, specialization leads to discoveries that remain unknown in other branches of science; the recent reincarnation of mixed-mode oscillations (MMO) in neuroscience, for example. In neuroscience, transitions in activity revolve around a changing membrane potential and specific changes in potential may instigate the onset of a seizure in the case of epilepsy or determine muscle reactions in response to stimulus. The class of elliptic bursting models needs a more general treatment that can span multiple disciplines. We propose a case study of the phenomenological FitzHugh–Nagumo–Rinzel model in order to investigate the mechanisms for state transitions in dynamic behavior.

J. Wojcik (✉)
Applied Technology Associates, 1300 Britt St. SE, Albuquerque,
NM 87123, USA
e-mail: wojcik.jeremy@gmail.com

A. Shilnikov
Department of Computational Mathematics and Cybernetics,
Lobachevsky State University of Nizhni Novgorod, Nizhni Novgorod, Russia
e-mail: ashilnikov@gsu.edu

H. González-Aguilar, E. Ugalde (eds.), *Nonlinear Dynamics New Directions,*
Nonlinear Systems and Complexity 12, DOI 10.1007/978-3-319-09864-7_9

Bursting represents direct evidence of multiple time scale dynamics of a model. Deterministic modeling of bursting models was originally proposed and done within a framework of three-dimensional, slow–fast dynamical systems. Geometric configurations of models of bursting neurons were pioneered by Rinzel [29, 30] and enhanced in [5, 16]. The proposed configurations are all based on the geometrically comprehensive dissection approach or the time scale separation, which has become the primary tool in mathematical neuroscience. The topology of the slow-motion manifolds is essential to the geometric understanding of dynamics. Through the use of geometric methods of the slow–fast dissection, where the slowest variable of the model is treated as a control parameter, it is possible to detect and follow the manifolds made of branches of equilibria and limit cycles in the fast subsystem. Dynamics of a slow–fast system are determined by, and centered around, the attracting sections of the slow-motion manifolds [3, 26, 28, 36].

The slow–fast dissection approach works exceptionally well for a multiple time scale model, provided the model is far from a bifurcation in the singular limit. On the other hand, a bifurcation describing a transition between activities may occur from reciprocal interactions involving the slow and fast dynamics of the model. Such slow–fast interactions may lead to the emergence of distinct dynamical phenomena and bifurcations that can occur only in the full model, but not in either subsystem of the model. As such, the slow–fast dissection fails at the transition where the solution is no longer constrained to stay near the slow-motion manifold, or when the time scale of the dynamics of the fast subsystem slows to that of the slow system, near the homoclinic and saddle node bifurcations, for example.

Transformative bifurcations of repetitive oscillations, such as bursting, are most adequately described by Poincaré mappings [34], which allow for global bifurcation analysis. Time series-based Poincaré mappings have been heavily employed for examinations of voltage oscillatory activities in a multitude of applied sciences [1, 12, 18], despite their limitation due to sparseness. Often, feasible reductions to mappings of the slowest variable can be achieved through the aforementioned dissection tool in the singular limit [15, 24, 32, 34]. However, this method often fails for elliptic bursters since no single valued mapping for the slow variable can be derived for the particular slow motion manifold.

In this chapter, we refine and expound on the technique of creating a family of one-dimensional mappings, proposed in [6–8], for the leech heart interneuron, into the class of elliptic models of endogenously bursting neurons. We will show that a plethora of information, both qualitative and quantitative, can be derived from the mappings to thoroughly describe the bifurcations as such a model undergoes transformations. We also demonstrate the power of deriving not only individual mappings, but the additional benefits of having the entire family of mappings created from an elliptic bursting model.

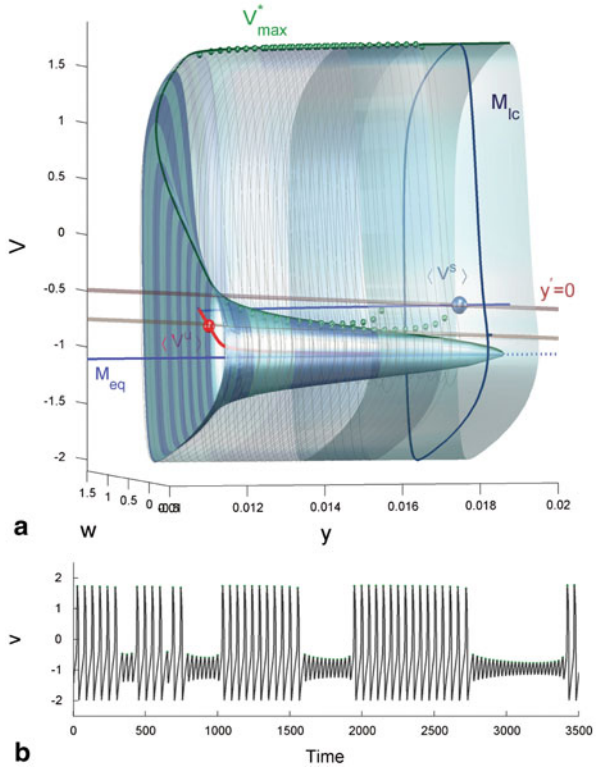

Fig. 1 **a** Topology of the tonic spiking, M_{lc}, and quiescent, M_{eq} manifolds. *Solid and dashed branches* of M_{eq} are made of stable and unstable equilibria of the model, respectively. The space curve, labeled by V^*_{max} (*in green*), corresponds to the v-maximal coordinates of the periodic orbits composing M_{lc}. An intersection point of $y' = 0$ with M_{eq} is an equilibrium state of (1). Shown in *gray* is the bursting trajectory traced by the phase point: the number of spikes per burst is the same as the number of turns the phase point makes around M_{lc}. Spikes are interrupted by the periods of quiescence when the phase point follows M_{eq} after it falls from M_{lc} near the fold. **b** A voltage trace for $c = -0.67$ displaying the voltage evolution in time as the phase point travels around the slow motion manifolds

2 FitzHugh–Nagumo–Rinzel Model

We introduce the exemplary phenomenological elliptic bursting model, the FitzHugh–Nagumo–Rinzel model. The model exhibits all necessary traits for the class of elliptic bursters: the time series form elliptic shaped bursts and oscillations begin through an Andronov–Hopf bifurcation and end in a saddle-node bifurcation. The model exhibits several types of oscillations, including: constant high-amplitude oscillatory behavior (tonic spiking), bursting, low-amplitude oscillations, and MMO. The mathematical FitzHugh–Nagumo–Rinzel model of the elliptic burster is given

by the following system of equations with a single cubic nonlinear term:

$$\begin{aligned} v' &= v - v^3/3 - w + y + I, \\ w' &= \delta(0.7 + v - 0.8\, w), \\ y' &= \mu(c - y - v); \end{aligned} \tag{1}$$

here we fix $\delta = 0.08$, $I = 0.3125$ is an applied external current, and $\mu = 0.002$ is a small parameter determining the pace of the slow y-variable. The slow variable, y, becomes frozen in the singular limit, $\mu = 0$. We employ c as the primary bifurcation parameter of the model, variations of which elevate/lower the slow nullcline given by $y' = 0$. The last equation is held geometrically in a plane given by $v = y - c$ in the three-dimensional phase space of the model, see Fig. 1. The two fast equations in (1) describe a relaxation oscillator in a plane, provided δ is small. The fast subsystem exhibits either tonic spiking oscillations or quiescence for different values of y corresponding to a stable limit cycle and a stable equilibrium state, respectively. The periodic oscillations in the fast subsystem are caused by a hysteresis induced by the cubic nonlinearity in the first "voltage" equation of the model.

Figure 1a presents a three-dimensional view of the slow-motion manifolds in the phase space of the FitzHugh–Nagumo–Rinzel model. The tonic spiking manifold M_{lc} is composed of the limit cycles for the model (1), both stable (outer) and unstable (inner) sections. The fold on M_{lc} corresponds to a saddle-node bifurcation, where the stable and unstable branches merge. The vertex, where the unstable branch of M_{lc} collapses at M_{eq}, corresponds to a subcritical Andronov–Hopf bifurcation. The manifold M_{eq} is the space curve made from equilibria of the model. The intersection of the plane, $y' = 0$ with the manifold, determines the location of the existing equilibrium state for a given value of the bifurcation parameter c: stable (saddle-focus) if located before (after) the Andronov–Hopf bifurcation point on the solid (dashed) segment of M_{eq}. The plane, $y' = 0$, called the slow nullcline, above (below) which the y-component of a solution of the model increases (decreases). The plane moves in the three-dimensional phase space as the control parameter c is varied. When the slow nullcline cuts through the solid segment of M_{eq}, the model enters a quiescent phase corresponding to a stable equilibrium state. Raising the plane to intersect the unstable (inner) cone-shaped portion of M_{lc} makes the equilibrium state unstable through the Andronov–Hopf bifurcation, which is subcritical in the singular limit, but becomes supercritical at a given value of the small parameter $\varepsilon = 0.002$, see Fig. 1a. Continuing to raise the slow nullcline by increasing c gives rise to bursting represented by solutions following and repeatedly switching between M_{eq} and M_{lc}. Bursting occurs in the model (1) whenever the quiescent M_{eq} and spiking M_{lc} manifolds contain no attractors, i.e., neither a stable equilibrium state nor a stable periodic orbit exist. The number of complete revolutions, or "windings," of the phase point around M_{lc} corresponds to the number of spikes per burst. The larger the number of revolutions the longer the active phase of the neuron lasts. Spike trains are interrupted by periods of quiescence while the phase point follows the branch M_{eq}, onto which the phase point falls from M_{lc} near the fold; see Fig. 1. The length of the quiescent period, as well as the delay of the stability loss (determined mainly, but

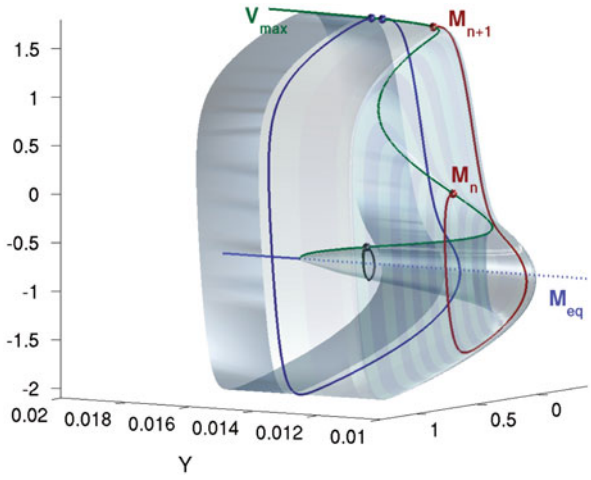

Fig. 2 Three sample orbits demonstrating the construction of the return mapping T: $M_n \to M_{n+1}$ defined for the points of the cross-section V_{max} on the manifold M_{lc}. Singling out the v-coordinates of the points gives pairs (V_n, V_{n+1}) constituting the voltage interval mapping at a given parameter, c

not entirely, by the small parameter μ) begins after the phase point passes through the subcritical Andronov–Hopf bifurcation onto the unstable section of M_{eq}. Further increase of the bifurcation parameter, c, moves the slow nullcline up so that it cuts through the stable cylinder-shaped section of the manifold M_{lc} far from the fold. This gives rise to a stable periodic orbit corresponding to tonic spiking oscillations in the model.

3 Voltage Interval Mappings

Methods of the global bifurcation theory are organically suited for examinations of recurrent dynamics such as tonic spiking, bursting, and subthreshold oscillations [10, 20], as well as their transformations. The core of the method is a reduction to, and derivation of, a low dimensional Poincaré return mapping with an accompanying analysis of the limit solutions: fixed, periodic, and homoclinic orbits each representing various oscillations in the original model and referenced therein. It is customary that such a mapping is sampled from time series, such as identification of voltage maxima, minima, or interspike intervals [11]; see Fig. 1b. A drawback of a mapping generated by time series is sparseness as the construction algorithm reveals only a single periodic attractor of a model, unless the latter demonstrates chaotic or mixing dynamics producing a large set of densely wandering points. Chaos may also be evoked by small noise whenever the dynamics of the model are sensitively vulnerable to small perturbations that do not substantially reshape intrinsic properties of the autonomous model [8, 35]. Small noise, however, can make the solutions of the model wander thus revealing the mapping graph.

A computer-assisted method for constructing a complete family of Poincaré mappings for an interval of membrane potentials was proposed in [6] following [31].

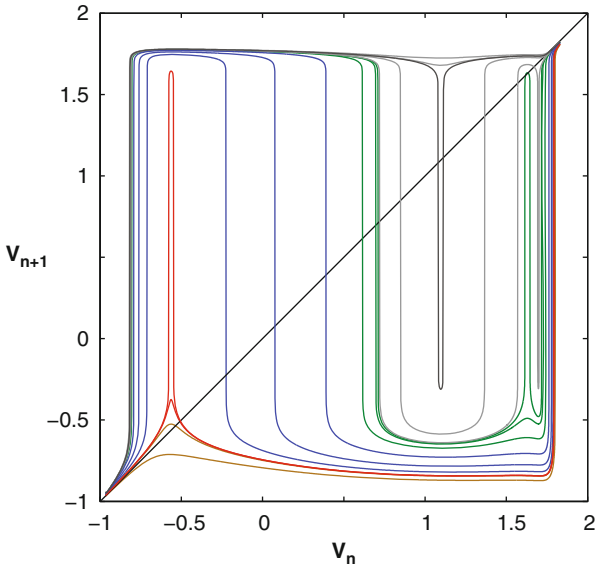

Fig. 3 Coarse sampling of the c-parameter family of the Poincaré return mappings $T : V_n \to V_{n+1}$ for the FitzHugh–Nagumo–Rinzel model at $\mu = 0.002$ as c decreases from $c = -0.55$ through $c = -1$. The *gray* mappings correspond to the dominating tonic spiking activity in the model. The *green* mappings show the model transitioning from tonic spiking to bursting. The *blue* mappings correspond to the bursting behavior in the model. The *red* mappings show the transition from bursting into quiescence. The *orange* mappings correspond to the quiescence in the model. An intersection point of a mapping graph with the bisectrix is a fixed point, $v^\star$, of the mapping. The stability of the fixed point is determined by the slope of the mapping graph, i.e., it is stable if $|T'(v^\star)| < 1$. Nearly vertical slopes of graph sections are due to an exponentially fast rate of instability of solutions (limit cycles) of the fast subsystem compared to the slow component of the dynamics of the model

Having a family of such mappings we are able to elaborate on various bifurcations of periodic orbits, examine bistability of coexisting tonic spiking and bursting, and detect the separating unstable sets that are the organizing centers of complex dynamics in any model. Examination of the mappings will help us make qualitative predictions about transitions *before* the transitions occur in models.

By construction, the mapping T takes the space curve $\mathrm{V}^*_{\mathrm{max}}$ into itself after a single revolution around the manifold M_{lc} (Fig. 2), i.e., $T : \mathrm{V_n} \to \mathrm{V_{n+1}}$. This technique allows for the creation of a Poincaré return mapping; taking an interval of the voltage values into itself. The found set of matching pairs $(\mathrm{V_n}, \mathrm{V_{n+1}})$ constitutes the graph of the Poincaré mapping for a selected parameter value c. Provided the number of paired coordinates is sufficiently large and by applying a standard spline interpolation we are able to iterate trajectories of the mapping, compute Lyapunov exponents, evaluate the Schwarzian derivative, extract kneading invariants for the topological entropy, and determine many other quantities.

Varying the parameter, c, we are able to obtain a dense family that covers all behaviors, bifurcations, and transitions of the model (1). A family of the mappings for the parameter c varied within the range $[-1, -0.55]$ is shown in Fig. 3. Indeed,

for the sake of visibility, this figure depicts a sampling of mappings that indicate evolutionary tendencies of the model. A thorough examination of the family allows us to foresee changes in model dynamics. A family of mappings allows us to analyze all the bifurcations whether stable or unstable fixed and periodic orbits including homoclinic and heteroclinic orbits and bifurcations. By following the mapping graph we can predict a value of the parameter at which the corresponding periodic orbit will lose stability or vanish, for example, giving rise to bursting from tonic spiking.

A fixed point, $v^\star$, is discerned from the mapping as an intersection of the graph with the bisectrix. Visually we determine the stability of the fixed point by the slope of the graph at the fixed point. If the slope of the graph is less than 1 in absolute value, the point is stable. When the absolute value of the slope of the graph at the fixed point is greater than 1, the fixed point is unstable. Alternatively, stability may be determined from forward iterates of an initial point in the neighborhood of the fixed point which converges to the fixed point.

4 Qualitative Analysis of Mappings

The family of mappings given in Fig. 3 allows for global evolutionary tendencies of the model (1) to be qualitatively analyzed. One can first see that the flat mappings in gray have a single fixed point corresponding to the tonic spiking state. The green mappings show the actual transition and saddle-node bifurcation after which we have regular bursting patterns, seen in the blue mappings. We also see the other unstable fixed point clearly moving to the lower corner. The red mappings indicate the transition from bursting to quiescence, as the fixed point changes stability.

A major benefit of using the voltage interval mapping is that we are able to understand transitions between the activity states of the model by analyzing and comparing the bifurcations between the states. Activity transitions commonly occur in a slow–fast model near the bifurcations of the fast subsystem where the description of dynamics in the singular limit is no longer accurate because of the failure of (or interpretation of) the slow–fast dissection paradigm. This happens, for example, when the two-dimensional fast subsystem of the model (1) is close to a saddle-node bifurcation (near the fold on the tonic spiking manifold M_{lc}) where the fast dynamics slow to the time scale of the slow subsystem. Such an interaction may cause new and peculiar phenomena such as torus formation and subsequent breakdown near the fold on the spiking manifold [21, 33]. We now turn our attention to a more thorough analysis of the individual mappings.

4.1 Transition from Tonic Spiking to Bursting

We begin where the model is firmly in the tonic spiking regime at $c = -0.594355$. Tonic spiking is caused by the presence of a stable periodic orbit located far from the fold on the manifold M_{lc} (Fig. 1). The only v-maximum of this orbit corresponds

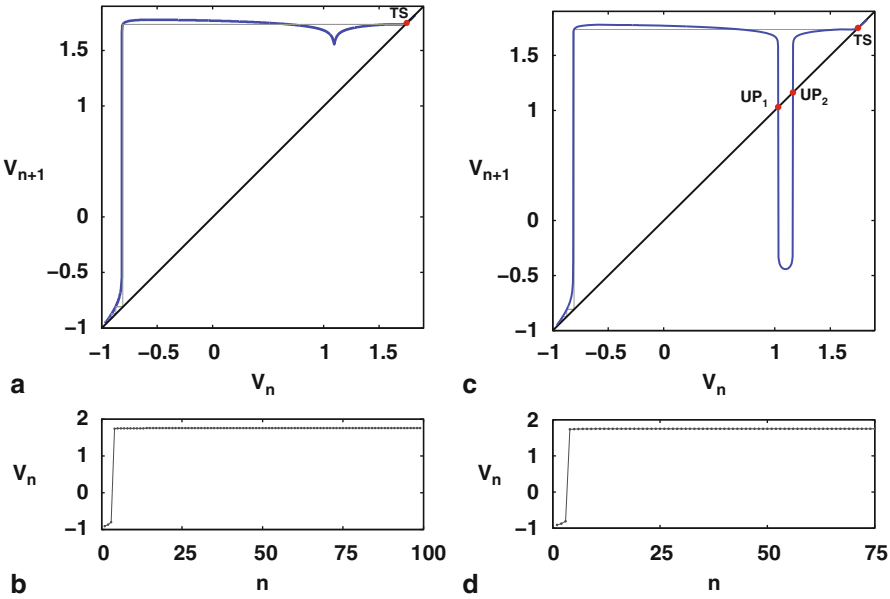

Fig. 4 **a** Poincaré return mapping for the parameter, $c = -0.594255$. We see a single fixed point, *TS*, corresponding to continuous large amplitude oscillations. We also see a *cusp* which insinuates a possible change in the mapping shape. **b** A maximal "time" series obtained from iterating the mapping, n times. **c** Return mapping for $c = -0.595$. We see the *cusp* has enlarged and intersected the identity line creating two additional fixed points, UP_1 and UP_2. The two fixed points are clearly unstable. **d** There is no indication in the maximal trace, or model dynamics, that would indicate the formation of these fixed points

to a stable fixed point, labeled TS in Fig. 4a. The flat section of the mapping graph adjoining the stable fixed point clearly indicates a rapid convergence to the point in the v-direction, as shown by the trace in inset, Fig. 4b. Here the slope of the mapping reflects the exponential instability (stability) of the quiescent (tonic spiking) branch, made of unstable equilibria and stable limit cycles of the fast subsystem of the model.

The formation of the cusp is an indication of a change in dynamics for the mapping. Thus the mapping insinuates a transition in dynamics of the model (1) prior to occupance. Note that the maximal voltage trace provides no indication of any eminent transition in the model's behavior. The mapping in Fig. 4a, b, taken for the parameter $c = -0.595$, clearly illustrates that after the cusp has dropped below the bisectrix, two additional fixed points, UP_1 and UP_2, are created. UP_1 and UP_2 have emerged through a preceding fold or saddle-node bifurcation taking place at some intermediate parameter value between $c = -0.594255$ and $c = -0.595$. Again, let us stress that the singular limit of the model at $\mu = 0$ gives a single saddle-node bifurcation through which the tonic spiking periodic orbit looses stability after it reaches the fold on the tonic spiking manifold. We point out that, for an instant, the model becomes bistable right after the saddle-node bifurcation in Fig. 4 leading to the emergence of another stable fixed point with an extremely narrow basin of attraction. Here, as before the hyperbolic tonic spiking fixed point, TS, dominates the dynamics of the model.

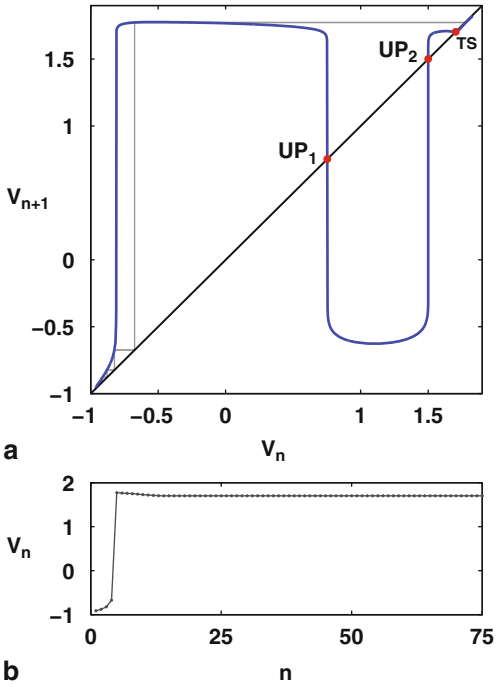

Fig. 5 **a** Varying the parameter further to $c = -0.615$ we find the unstable fixed point UP_2 has moved closer to the stable fixed point, *TS*. The other unstable fixed point UP_1 remains in approximately the same location. **b** Again the maximal trace shows no indication of any change in dynamics

Figure 5a demonstrates that, as the parameter is decreased further to $c = -0.615$, the gap between the new fixed points widens as the point UP_2 moves toward the stable tonic spiking point, TS, indicating a possible saddle-node bifurcation is eminent. Through this saddle-node bifurcation, these fixed points merge and annihilate each other; thereby terminate the tonic spiking activity in the FitzHugh–Nagumo–Rinzel model. Before that happens however, several bifurcations involving the fixed point, TS, drastically reshape the dynamics of the model. First, the multiplier becomes negative around $c = -0.619$, which is the first indication of an impending period-doubling cascade. This is confirmed by the mapping at $c = -0.6193$ in Fig. 6a, b, and c showing that the fixed point has become unstable through the supercritical period-doubling bifurcation. Furthermore, the dynamics of the mapping is directly mimicked in the full model behavior; see Fig 6d.

The newly born period-2 orbit becomes the new tonic spiking attractor of the mapping. Observe from the voltage trace in Fig. 6b the long transient bursting behavior thus indicating that boundaries of the attraction basin of the period-2 orbit become fractal. Next, the model approaches bursting onset. Correspondingly, the FitzHugh–Nagumo–Rinzel model starts generating chaotic trains of bursts with randomly alternating numbers of spikes per burst. The number of spikes depends on how close the trajectory of the mapping comes to the unstable (spiraling out) fixed point, TS, that is used to represent the tonic spiking activity. Each spike train is interrupted by a single quiescent period. The unstable point, UP_1, corresponds to a

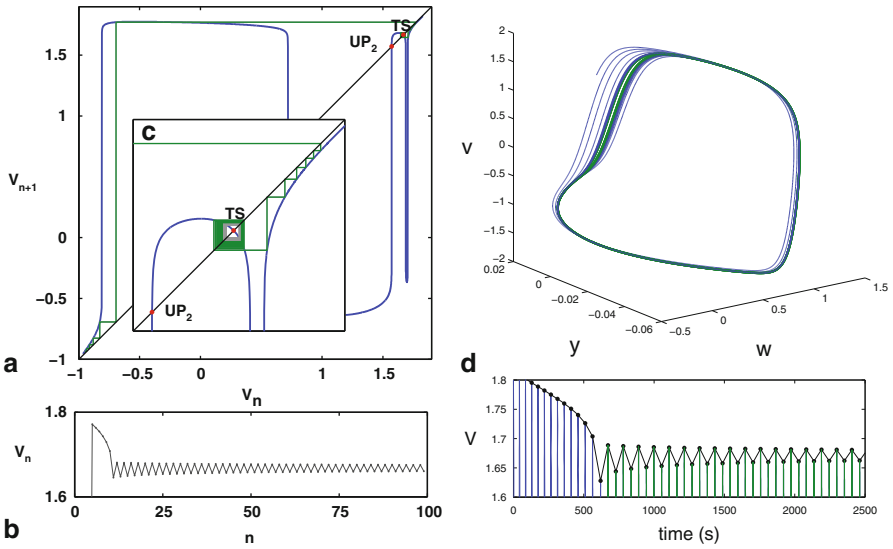

Fig. 6 **a** Poincaré mapping at $c = -0.6193$ and the voltage trace in **b** both demonstrate chaotic bursting transients. **c** Enlargement of the *right top corner* of the mapping shows that the tonic spiking fixed point has lost the stability through a supercritical period-doubling bifurcation. The new born period-2 orbit is a new attractor of the mapping, as confirmed by the *zigzagging* voltage trace represented in **b**. **d** The same dynamics found directly from integrating the model. We find after a short transient (*blue*) the model dynamics converge to a period-2 orbit (*green*) as indicated from the mapping **a**

saddle periodic orbit of the model that is located on the unstable, cone-shaped section of the tonic spiking manifold M_{lc} in Fig. 1. Recall that this saddle periodic orbit is repelling in the fast variables and stable in the slow variable.

By comparing Figs. 4, 5, 6, and 7 one could not foresee that the secondary saddle-node bifurcation eliminating the tonic spiking fixed point TS, or corresponding round stable periodic orbit on the manifold M_{lc} would be preceded by a dramatic concavity change in the mapping shape, causing a forward and inverse cascade of period doubling bifurcations right before the tonic spiking orbit TS. The corresponding fixed point, TS, becomes stable again through a reverse sequence of period doubling bifurcations before annihilating through the secondary saddle-node bifurcation. However, the basin of attraction becomes so thin that bursting begins to dominate the bi-stable dynamics of the model. Note that the bursting behavior becomes regular as the phase points pass through the upper section of the mapping tangent to the bisectrix. The number of iterates that the orbit makes here determine the duration of the tonic spiking phase of bursting and is followed by a quiescence period initially comprising a single iterate of the phase point to the right of the threshold UP_1. The evolution of bursting into MMO and on to subthreshold oscillations will be discussed in the next section.

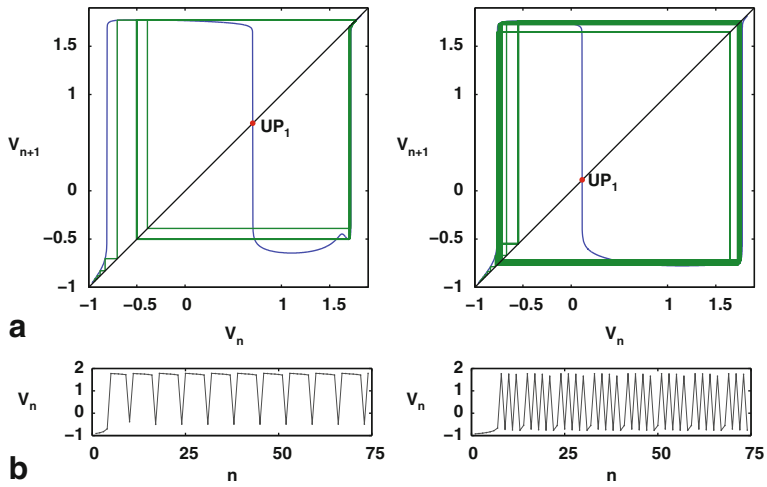

Fig. 7 **a** Periodic bursting with five spikes in the Poincaré interval mapping for the FitzHugh–Nagumo–Rinzel model at $c = -0.6215$. The single unstable fixed point UP_1 separates the tonic spiking section of the mapping from the quiescent or subthreshold section (*left*). The number of iterates of the phase point adequately defines the ordinal type of bursting **b**. Note a presence of a small hump around ($V_0 = 1.6$, $V_1 = -0.5$) which is an echo of the saddle-node bifurcation. **c** Poincaré return mapping at $c = -0.75$. Here we find a burst pattern of three spikes followed by two small amplitude oscillations. The mappings are able to capture all the bursting patterns exhibited by the model

4.2 From Bursting to Mixed-Mode Oscillations and Quiescence

The disappearance of the tonic spiking orbit, TS, accords with the onset of regular bursting in the mapping and in the model (1). In the mapping, a bursting orbit is comprised of iterates on the tonic spiking and quiescent sections separated by the unstable threshold fixed point, UP_1, of the mapping in Fig. 7. The shape of the graph undergoes a significant change reflecting the change in dynamics. The fixed points in the upper right section of the mapping disappear through a saddle-node bifurcation. One of the features of the saddle-node is the bifurcation memory: the phase point continues to linger near a phantom of the disappeared saddle-node. The mapping near the bisectrix can generate a large number of iterates before the phase points diverge toward the quiescent phase. The larger the number of iterates near the bisectrix corresponds to a longer tonic spiking phase of bursting. Figure 7 demonstrates how the durations of the phases change along with a change in the mapping shape: from a single quiescent iterate to the left of the threshold, UP_1, to a single tonic-spiking iterate corresponding to a bursting orbit with a single large spike in the model.

The transition from bursting to quiescence in the model is not monotone because the regular dynamics may be sparked by episodes of chaos. Such subthreshold chaos in the corresponding mapping at $c = -0.9041$ is demonstrated in Fig. 8a. This phenomena is labeled MMO because the small amplitude subthreshold oscillations

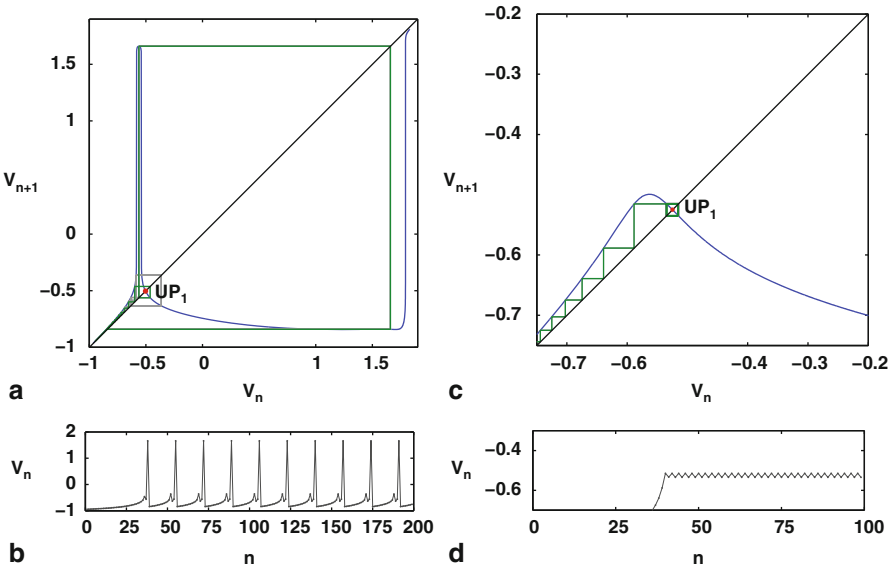

Fig. 8 **a** Chaotic MMO and bursting in the mapping at $c = -0.904$ caused by the complex recurrent behavior around the unstable fixed point UP_1. **b** Subthreshold oscillations are disrupted sporadically by large and intermediate magnitude spikes thereby destroying the rhythmic bursting in the model. **c** Poincaré return mapping for the FitzHugh–Nagumo–Rinzel model shows no bursting but complex subthreshold period-2 oscillations at $c = -0.908$. **d** After the peak in the mapping decreases in amplitude, high amplitude spikes become impossible. Here, chaos is caused by homoclinic orbits to the unstable fixed point UP_1, just prior to this figure

are sporadically interrupted by larger spikes (inset b). Use of the mapping makes the explanation of the phenomena in elliptic bursters particularly clear. In Fig. 8a, after the mapping (or the model) fires a spike, the phase point is reinjected close to the threshold point, UP_1, from where it spirals away to make another cycle of bursting. Note that the number of iterates of the phase point around UP_1 may vary after each spiking episode. This gives rise to solutions that are called bi-asymptotic or homoclinic orbits to the unstable fixed point UP_1. The occupancy of such a homoclinic orbit to a repelling fixed point is the generic property of a one-dimensional non-invertible mapping [25], since the point of a homoclinic orbit might have two pre-images. Note that the number of forward iterates of a homoclinic point may be finite in a non-invertible mapping, because the phase point might not converge, but merely jump onto the unstable fixed point after being reinjected. However, the number of backward iterates of the homoclinic point is infinite, because the repelling fixed point becomes an attractor for an inverse mapping in restriction to the local section of the unimodal mapping; see Fig. 8a, b. The presence of a single homoclinic orbit leads to the abundance of other emergent homoclinics [13] via a homoclinic explosion [34].

A small decrease of the bifurcation parameter causes a rapid change in the shape of the mapping, as depicted in Fig. 8c, d. The sharp peak near the threshold becomes

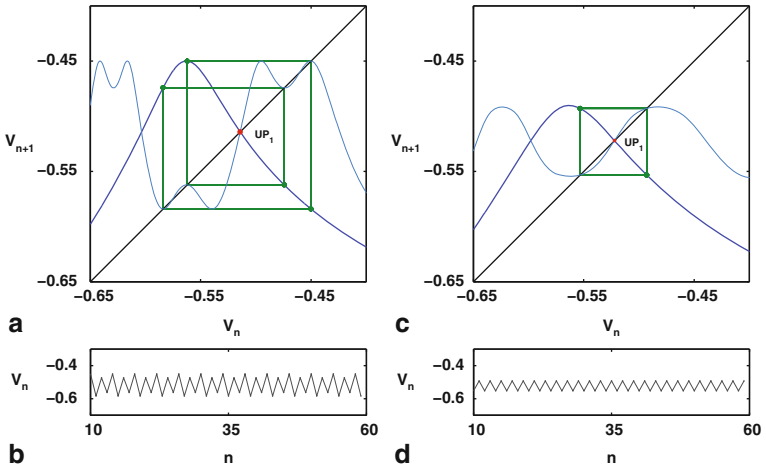

Fig. 9 **a** and **c** Show stable period-4 and period-2 orbits (*green*) of the interval mapping at $c = -0.906$ and $c = -0.9075$. Shown in *light-blue* are the corresponding mappings T^4 and T^2 of degrees four and two with four and two stable fixed points correspondingly. The traces of the orbits are shown in insets **b** and **d**

lower so that the mapping can no longer generate large amplitude spikes. As the parameter is decreased further, the unstable fixed point, UP_1, becomes stable through a reverse period-doubling cascade. The last two stages of the cascade are depicted in Fig. 9. Insets a and c of the figure show stable period-4 and period-2 orbits, and their traces in insets b and d, as the parameter c is decreased from -0.906 to -0.9075. Here we demonstrate another ability of the interval mappings derived directly from the flow. In addition to the original mapping, T, in Fig. 9 we see two superimposed mappings, T^2 and T^4, (shown in light blue) of degrees two and four respectively. The four points of periodic orbit in inset a corresponds to the four fixed points of the fourth degree mapping T^4 at $c = -0.9075$, whereas the period-2 orbit in c correspond to two new fixed points of the mapping T^2 in c at $c = -0.9075$. We see clearly that both periodic orbits are indeed stable because of the slopes of the mappings at the fixed points on the bisectrix. Using the mappings of higher degrees we can evaluate the critical moments at which the period-2 and period-4 orbits are about to bifurcate. We point out that a period-doubling cascade, beginning with a limit cycle near the Hopf-initiated canard toward subthreshold chaos has been recently reported in slow–fast systems [38, 39].

Decreasing c further, the period-2 orbit collapses into the fixed point, UP_1, which becomes stable. The multiplier, first negative becomes positive but is still less than one in the absolute value. In terms of the model, this means that the periodic orbit collapses into a saddle-focus through the subcritical Andronov–Hopf bifurcation. After that, the equilibrium state, located at the intersection of the manifold M_{eq} with the slow-nullcline (plane) in Fig. 1, becomes stable and the model goes into

quiescence for parameter values smaller then $c = -0.97$. The stable equilibrium state corresponds to the fixed point, Q, which is the global attractor in the mapping.

5 Quantitative Features of Mappings: Kneadings

In this section we discuss a quantitative property of the interval mappings for the dynamics of the model (1). In particular, we carry out the examination of complex dynamics with the use of calculus-based and calculus-free tools such as Lyapunov exponents and kneading invariants for the symbolic description of MMOs.

Chaos may be quantitatively measured by a Lyapunov exponent. The Lyapunov exponent is evaluated for the one-dimensional mappings as follows:

$$\lambda = \lim_{N \to +\infty} \frac{1}{N} \sum_{i=1}^{N} \log |T'(v_i)|, \tag{2}$$

where $T'(v_i)$ is the slope (derivative) of the mapping at the current iterate v_i corresponding to the ith step for $i = 0, \ldots, N$. Note that, by construction, the mapping graph is a polygonal and to accurately evaluate the derivatives in (5) we used a cubic spline. The Lyapunov exponent, λ, yields a lower bound for the topological entropy $h(T)$ [19]; serving as a measure of chaos in a model. The Lyapunov exponent values $\lambda \simeq 0.24$ and $\lambda \simeq 0.58$, found for the interval mappings at $c = -0.9041$ and $c = -0.90476$, respectively, show that chaos is developed more in the case of subthreshold oscillations than for MMOs.

The topological entropy may also be evaluated though a symbolic description of the dynamics of the mapping that require no calculus-based tools. The curious reader is referred to [14, 23] for the in-depth and practical overviews of the kneading invariants, while below we will merely touch the relevant aspects of the theory. For unimodal mappings of an interval into itself with a single critical point, v_c, like for the case $c = -0.90476$, we need only to follow the forward iterates of the critical point to generate the *unsigned kneading sequence* $\kappa(v_c) = \{\kappa_n(v_c)\}$ defined on $\{-1, +1\}$ by the following rule:

$$\kappa_n(v_q) = \begin{cases} +1, & \text{if } T^n(v_c) < v_c \\ -1, & \text{if } T^n(v_c) > v_c; \end{cases} \tag{3}$$

here $T^n(v_c)$ is the nth iterate of the critical point v_c.

The kneading invariant of the unimodal mapping is a series of the *signed kneadings* $\{\tilde{\kappa}_n\}$ of the critical point, which are defined through the unsigned kneadings, κ_i, as follows:

$$\tilde{\kappa}_n = \prod_{i=1}^{n} \kappa_i, \tag{4}$$

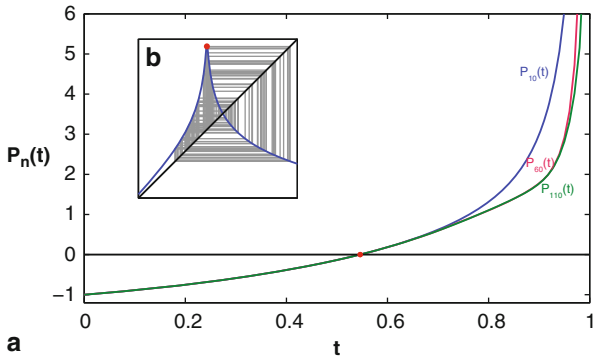

Fig. 10 **a** Graphs of the three polynomials, $P_{10}(t)$, $P_{60}(t)$, and $P_{110}(t)$ defined on the unit interval, and generated through the series of the signed kneadings at $c = -0.90476$. Inset **b** shows the corresponding interval mapping. The iterates of the critical point, v_c, determine the symbolic dynamics for the unsigned kneading symbols: -1 if the phase point lands on the decreasing section of the mapping graph to the right of the critical point, and $+1$ if it lands to the increasing section of the mapping, which is to the left of the critical point

or, recursively:

$$\tilde{\kappa}_i = \kappa_i \, \tilde{\kappa}_{i-1}, \qquad i = 2, 3, \ldots . \tag{5}$$

Next we construct a formal power series;

$$P(t) = \sum_{i=0}^{\infty} \tilde{\kappa}_i \, t^i . \tag{6}$$

The smallest zero, t^* (if any), of the series within an interval $t \in (0, 1)$ defines the topological entropy, $h(T) = \ln(1/t^*)$. The sequence of the signed kneadings, truncated to the first ten terms, $\{-+++-++++-+\}$ for the mapping in Fig. 10b, generates the polynomial $P_{10}(t) = -1 + t + t^2 + t^3 - t^4 + t^5 + t^6 + t^7 - t^8 + t^9$. The single zero of $P_{10}(t)$ at $t^* \approx 0.544779$ yields a close estimate for the topological entropy $h(T) \approx 0.6073745$, see Fig. 10a.

The advantage of an approach based on the kneading invariant to quantify chaos is that evaluation of the topological entropy does not involve numerical calculus for such equationless interval mappings, but relies on the mixing properties of the dynamics instead. Moreover, it requires relatively few forward iterates of the critical point to compute the entropy accurately, as the polynomial graphs in Fig. 10 suggest. Besides yielding the quantitative information such as the topological entropy, the symbolic description based on the kneading invariants provide qualitative information for identifying the corresponding Farey sequences describing the MMOs in terms of the numbers of subthreshold and tonic spiking oscillations.

6 Discussion

We present a case study for an in-depth examination of the bifurcations that take place at activity transitions between tonic spiking, bursting, and MMOs in the FitzHugh–Nagumo–Rinzel model. The analysis is accomplished through the reduction to a single-parameter family of equationless Poincaré return mappings for an interval of the "voltage" variable. We stress that these mappings are *models* themselves for evaluating the complex dynamics of the full three-dimensional model. Nevertheless, the dynamics of the single accumulative variable, v, reflects the cooperative dynamics of other variables in the model. The reduction is feasible since the model is a slow–fast system and, hence, possesses a two-dimensional, slow-motion tonic-spiking manifold around which the oscillatory solutions of the models linger. We have specifically concentrated on the dynamics of the voltage [7, 8], as it is typically the only measurable, and thus comparable, variable in experimental studies in neuroscience and physical chemistry.

It is evident that no one-dimensional return mapping of the interval is intended to detect a torus in the phase plane, whereas the pointwise mappings generated by a forward time series of the voltage can identify the torus formation in the phase space. Note that the torus has a canard-like nature, that is the torus exists within a narrow parameter window. A torus formation in a three-dimensional model with two slow variables near the fold was reported also in [17]. Another parallel of the FitzHugh–Nagumo–Rinzel model with electrochemical systems, including the Belousov–Zhabotinky reaction, is that the latter also demonstrates a quasiperiodic regime [2]. The emergence of the torus near the fold of the tonic spiking manifold first described in [9, 33] has turned out to be a generic phenomenon observed recently in several plausible models [22], including a model for the Purkinje cells [4, 21], and in a hair cell model [27].

A minor drawback of the approach is a small detuning offset in parameter values at which the model and the mapping have nearly the same dynamics, matching orbits, or undergo the same bifurcations. This is caused by the fact that a one-dimensional mapping for a single voltage variable does not fully encompass the dynamics of other, major and minor, variables of the corresponding model. In general, most features of a dissipative model with a negative divergence of the vector field that results in a strong contraction of the phase volumes, are adequately modeled by a one-dimensional Poincaré mapping. However, this is not true when such a contraction is no longer in place, for example, when the divergence becomes sign-alternating. There are two such places near the manifold M_{lc} in the model (1): one is near the fold, the second is close to the cone-shaped tip. The sign alternating near the tip of the cone is where the model has an equilibrium state of the saddle-focus type with a pair of complex conjugate eigenvalues with a small positive real part and a real negative eigenvalue due to the Andronov–Hopf bifurcation and the smallness of ε.

The algorithm for interval mapping construction has two stages. First, one needs to identify the tonic spiking manifold in the phase space of the slow–fast neuron model in question. This is accomplished by either using the geometric dissection method, or

the parameter continuation technique. The more accurately and completely the first stage is performed the more natural and smooth these numerically derived mappings will be. The second stage is to build the mappings for a range of parameter values. The analysis of such mappings lets one identify not only attractors, but more importantly, the unstable sets including fixed, periodic, and homoclinic orbits, which are known to be the globally organizing centers governing the dynamics of any model. In addition, having computationally smooth mappings allows one to create symbolic descriptions for dynamics, compute kneading invariants, evaluate Schwarzian derivatives, etc., as well as estimate other quantities measuring the degree of complexity for the trajectory behavior like Lyapunov exponents and topological entropy.

Our computational method allows us to thoroughly describe the bifurcations that the model (1) undergoes while transitioning between states: from tonic spiking to bursting and then to quiescence. Taken individually, each mapping offers only a glimpse into the system behavior. However, with an entire family of mappings we obtain deep insight into the evolution of the model's dynamics though the interplay and bifurcations of the fixed points and periodic orbits. This allows for not only the description of bifurcations post factum, but to predict the changes in the dynamics of the model under consideration before they actually occur. For additional analysis on elliptic bursters including torus formation, we refer the reader to [37].

Acknowledgments This work was supported by the NSF grant DMS-1009591, the RFFI grant 11-01-00001, the RSF grant 14-41-00044 and by the MESRF grant 02.B.49.21.003.

References

1. Albahadily, F., Ringland, J., Schell, M.: Mixed-mode oscillations in an electrochemical system. I. A Farey sequence which does not occur on a torus. J. Chem. Phys. **90**(2), 813–822 (1989)
2. Argoul, F., Roux, J.: Quasiperiodicity in chemistry: An experimental path in the neighbourhood of a codimension-two bifurcation. Phys. Lett. A **108**(8), 426–430 (1985)
3. Arnold, V., Afraimovich, V., Ilyashenko, Y., Shilnikov, L.: Bifurcation theory. In: Arnold, V. (ed.) Dynamical Systems. Encyclopaedia of Mathematical Sciences, vol. V. Springer, Berlin (1994)
4. Benes, N., Barry, A., Kaper, T., Kramer, M., Burke, J.: An elementary model of torus canards. Chaos **21**, 023131 (2011)
5. Bertram, R., Butte, M., Kiemel, T., Sherman, A.: Topological and phenomenological classification of bursting oscillations. Bull. Math. Biol. **57**(3), 413–439 (1995) (PM:7728115)
6. Channell, P., Cymbalyuk, G., Shilnikov, A.: Applications of the Poincaré mapping technique to analysis of neuronal dynamics. Neurocomputing **70**, 10–12 (2007)
7. Channell, P., Cymbalyuk, G., Shilnikov, A.: Origin of bursting through homoclinic spike adding in a neuron model. Phys. Rev. Lett. **98**(13), Art. 134101 (2007) (PM:17501202)
8. Channell, P., Fuwape, I., Neiman, A., Shilnikov, A.: Variability of bursting patterns in a neuron model in the presence of noise. J. Comput. Neurosci. **27**(3), 527–542 (2009). doi:10.1007/s10827-009-0167-1. http://dx.doi.org/10.1007/s10827-009-0167-1
9. Cymbalyuk, G., Shilnikov, A.: Coexistence of tonic spiking oscillations in a leech neuron model. J. Comput. Neurosci. **18**(3), 255–263 (2005). doi:10.1007/s10827-005-0354-7. http://dx.doi.org/10.1007/s10827-005-0354-7

10. Doi, J., Kumagai, S.: Generation of very slow neuronal rhythms and chaos near the hopf bifurcation in single neuron models. J. Comput. Neurosci. **19**(3), 325–356 (2005). doi:10.1007/s10827-005-2895-1. http://dx.doi.org/10.1007/s10827-005-2895-1
11. Gaspard, M.K.P., Sluyters, J.: Mixed-mode oscillations and incomplete homoclinic scenarios to a saddle-focus in the indium/thiocyanate electrochemical oscillator. J. Chem. Phys. **97**(11), 8250–8260 (1992)
12. Gaspard, P., Wang, X.: Homoclinic orbits and mixed-mode oscillations in far-from-equilibrium. J. Stat. Phys. **48**(1/2), 151–199 (1987)
13. Gavrilov, N., Shilnikov, L.: On three-dimensional dynamical systems close to systems with a structurally unstable homoclinic curve. Math. USSR-Sb. **17**(3), 467–485 (1972)
14. Glendinning, P., Hall, T.: Zeros of the kneading invariant and topological entropy for Lorenz maps. Nonlinearity **9**, 999–1014 (1996)
15. Griffiths, R., Pernarowski, M.: Return map characterizations for a model of bursting with two slow variables. SIAM J. Appl. Math. **66**(6), 1917–1948 (2006)
16. Guckenheimer, J.: Towards a global theory of singularly perturbed systems. In: Broer, H.W., van Gils, S.A., Hoveijn, F., Takens, F. (eds.) Nonlinear Dynamical Systems and Chaos. Progress in Nonlinear Differential Equations and Their Applications, vol. 19, pp. 214–225 (1996)
17. Guckenheimer, J.: Singular Hopf bifurcation in systems with two slow variables. SIAM J. Appl. Dyn. Syst. **7**(4), 1355–1377 (2008)
18. Hudson, J., Marinko, D.: An experimental study of multiple peak periodic and nonperiodic oscillations in the Belousov–Zhabotinskii reaction. J. Chem. Phys. **71**(4), 1600–1606 (1979)
19. Katok, A.: Lyapunov exponents, entropy and periodic orbits for diffeomorphisms. Publ. Math. IHES **51**, 137–173 (1980)
20. Koper, M., Gaspard, P.: Mixed-mode oscillations and incomplete homoclinic scenarios to a saddle-focus in the indium/thiocyanate electricochemical oscillators. J. Chem. Phys. **97**(11), 8250–8260 (1992)
21. Kramer, M., Traub, R., Kopell, N.: New dynamics in cerebellar Purkinje cells: Torus canards. Phys. Rev. Lett. **101**(6), Art. 068103 (2008)
22. Kuznetsov, A., Kuznetsov, S., Stankevich, N.: A simple autonomous quasiperiodic self-oscillator. Commun. Nonlinear Sci. Numer. Simul. **15**, 1676–1681 (2010)
23. Li, M.C., Malkin, M.: Smooth symmetric and Lorenz models for unimodal maps. Int. J. Bifurc. Chaos **13**(11), 3353–3371 (2003)
24. Medvedev, G.: Transition to bursting via deterministic chaos. Phys. Rev. Lett. **97**, Art. 048102 (2006)
25. Mira, C.: Chaotic Dynamics from the One-Dimensional Endomorphism to the Two-Dimensional Diffeomorphism. World Scientific, Singapore (1987)
26. Mischenko, E., Kolesov, Y., Kolesov, A., Rozov, N.: Asymptotic Methods in Singularly Perturbed Systems. Monographs in Contemporary Mathematics. Consultants Bureau, New York (1994)
27. Neiman, A., Dierkes, K., Lindner, B., Shilnikov, A.: Spontaneous voltage oscillations and response dynamics of a Hodgkin-Huxley type model of sensory hair cells. J. Math. Neurosci. **1**(11) (2011)
28. Neishtadt, A.I.: On delayed stability loss under dynamical bifurcations I. Differ. Equ. **23**, 1385–1390 (1988)
29. Rinzel, J.: A formal classification of bursting mechanisms in excitable systems. In: Gleason, A.M. (ed.) Proceedings of the International Congress of Mathematics, pp. 1578–1593. AMS, Providence (1987)
30. Rinzel, J., Lee, Y.S.: Dissection of a model for neuronal parabolic bursting. J. Math. Biol. **25**(6), 653–675 (1987)
31. Shilnikov, A.: On bifurcations of the Lorenz attractor in the Shimizu–Morioka model. Phys. D **62**(1–4), 338–346 (1993)
32. Shilnikov, A., Kolomiets, M.: Methods of the qualitative theory for the Hindmarsh–Rose model: A case study. A tutorial. Int. J. Bifurc. Chaos **18**(7), 1–32 (2008)

33. Shilnikov, A., Rulkov, N.: Origin of chaos in a two-dimensional map modelling spiking-bursting neural activity. Int. J. Bifurc. Chaos **13**(11), 3325–3340 (2003)
34. Shilnikov, L., Shilnikov, A., Turaev, D., Chua, L.: Methods of Qualitative Theory in Nonlinear Dynamics, vols. 1 and 2. World Scientific, Singapore (1998, 2001)
35. Su, J., Rubin, J., Terman, D.: Effects of noise on elliptic bursters. Nonlinearity **17**, 133–157 (2004)
36. Tikhonov, A.: On the dependence of solutions of differential equations from a small parameter. Mat. Sb. **22**(64), 193–204 (1948)
37. Wojcik, J., Shilnikov, A.: Voltage interval mappings for activity transitions in neuron models for elliptic bursters. Phys. D **240**, 1164–1180 (2011)
38. Zaks, M.: On chaotic subthreshold oscillations in a simple neuronal model. Math. Model. Nat. Phenom. **6**(1), 1–14 (2011)
39. Zaks, M.A., Sailer, X., Schimansky-Geier, L., Neiman, A.B.: Noise induced complexity: From subthreshold oscillations to spiking in coupled excitable systems. Chaos **15**(2), Art. 26117 (2005). doi:10.1063/1.1886386. http://dx.doi.org/10.1063/1.1886386

Levenshtein's Distance for Measuring Lexical Evolution Rates

Filippo Petroni, Maurizio Serva and Dimitri Volchenkov

Abstract The relationships between languages molded by extremely complex social, cultural and political factors are assessed by an automated method, in which the distance between languages is estimated by the average normalized Levenshtein distance between words from the list of 200 meanings maximally resistant to change. A sequential process of language classification described by random walks on the matrix of lexical distances allows to represent complex relationships between languages geometrically, in terms of distances and angles. We have tested the method on a sample of 50 Indo-European and 50 Austronesian languages. The geometric representations of language taxonomy allow for making accurate interfaces on the most significant events of human history by tracing changes in language families through time. The Anatolian and Kurgan hypothesis of the Indo-European origin and the "express train" model of the Polynesian origin are thoroughly discussed.

1 Introduction

The evolution of languages goes on like to haploid evolution for asexual organisms, as evolving reproduction, mutation and extinction. Hypotheses concerning their relationships can be verified provided a distance between languages is evaluated from the lexical differences, in analogy with the genetic distance between species.

D. Volchenkov (✉)
Cognitive Interaction Technology—Center of Excellence, Universität Bielefeld,
Postfach 10 01 31, 33501 Bielefeld, Germany
e-mail: volchenk@physik.uni-bielefeld.de

M. Serva
Dipartimento di Matematica, Università dell'Aquila,
67010 L'Aquila, Italy
e-mail: serva@univaq.it

F. Petroni
Dipartimento di Scienze Economiche ed Aziendali Università di Cagliari V.le S. Ignazio,
17 09123 Cagliari Italy
e-mail: fpetroni@unica.it

H. González-Aguilar, E. Ugalde (eds.), *Nonlinear Dynamics New Directions,*
Nonlinear Systems and Complexity 12, DOI 10.1007/978-3-319-09864-7_10

The idea to assess the dissimilarity between languages using vocabulary, has its roots in the work of the French explorer Dumont D'Urville, who collected comparative lists of 115 basic terms from various languages during his voyages aboard the Astrolabe from 1826 to 1829 and introduced the idea of measuring the similarity between words with the same meaning in his work about the geographical division of the Pacific [1]. The method used by modern glottochronology developed by Swadesh [2] estimates the distance between languages from the percentage of shared *cognates* (words inferred to have a common historical origin) assuming that vocabularies change at a constant average rate. However, the identification of cognates is often a matter of sensibility and personal knowledge, as they do not necessarily look similar, so that the task of counting the number of cognate words shared by the two languages is difficult. For instance, the Spanish word *leche* and the Greek word *gala* are cognates. In fact, *leche* comes from the Latin *lac* with genitive form *lactis*, while the genitive form of *gala* is *galactos*. This identification became possible because of our historical records that are hardly available for languages of Central Africa, Australia or Polynesia. Moreover, the comparison of languages over a large vocabulary is only apparently more accurate, as many similar words rather carry information about complex social, cultural and political factors molding the extreme historical contacts, than about the actual language similarity. It is also worth a mention that languages belonging to the same family may not share many words in common, while languages of two distinct families may share many. For instance, Brahui spoken in Pakistan, Afghanistan and Iran is a Dravidian language accordingly to its syntactic structure, despite of 85 % of its vocabulary being Indo-European (IE). Eventually, the rates of lexical changes in words are all different, being probably related to the frequency of use of the associated meanings [3]; those words with a high rate of changes might be worthless for inferring the language relatedness.

Summarizing, the successful application of phylogenetic methods to language evolution requires:

1. A distance accumulating the differences in systematic sound correspondences between the realizations of individual meanings;
2. A well-adjusted input vocabulary exhibiting uniformly high stability of items, with respect to the defined distance;
3. A suitable agglomerative clustering technique that maps the matrix of lexical distances calculated over the optimized vocabulary into low-dimensional space of language groups;
4. A plausible hypothesis on the dynamical process of language evolution that evolves the obtained geometric representation of language taxonomy in time.

In our work, we consequently fulfill the outlined program and apply it to the study of the language evolution in the IE and Austronesian (AU) language families that allows us for making accurate inferences on the most significant events of human history by tracking changes in language families through time.

2 The Relations Among Languages Encoded in the Matrix of Lexical Distances

Complex relations between languages may be expressed in a numerical form with respect to many different features [4]. The standard Levenshtein (edit) distance accounting for the minimal number of insertions, deletions or substitutions of single letters needed to transform one word into the other has been introduced in information theory [5]. In our work, being guided by [6, 7], while comparing two words, w_1 and w_2, we use the edit distance divided by the number of characters of the *longer of the two*,

$$D\left(w_1, w_2\right) \;=\; \frac{\left\|w_1, w_2\right\|_L}{\max\left(\left|w_1\right|, \left|w_2\right|\right)} \tag{1}$$

where $\left\|w_1, w_2\right\|_L$ is the standard Levenshtein distance between the words w_1 and w_2, and $|w|$ is the number of characters in the word w. For instance, according to (1) the normalized Levenshtein distance between the orthographic realizations of the meaning *milk* in English and in German (*Milch*) equals $2/5$. Such a normalization seems natural since the deleted symbols from the longer word and the empty spaces added to the shorter word, then stand on an equal footing: the shorter word is supplied by a number of spaces to match the length of the longer one. The distance (1) is symmetric, $D\left(w_1, w_2\right) = D\left(w_2, w_1\right)$, and takes values between 0 and 1 for any two words, w_1 and w_2, so that $D\left(w, w\right) = 0$, and $D\left(w_1, w_2\right) = 1$ when all characters in these words are different. The normalized edit distance between the orthographic realizations of two words can be interpreted as the probability of mismatch between two characters picked from the words at random.

Given the short list $\mathcal{L}$ containing $|\mathcal{L}| = M$ meanings, we define the lexical distance between the two languages, l_1 and l_2, as the average of the normalized Levenshtein distance (1)—the smaller the result is, the more affine are the languages,

$$d\left(l_1, l_2\right) \;=\; \frac{1}{M} \cdot \sum_{\alpha \in \mathcal{L}} D\left(w_\alpha^{(l_1)}, w_\alpha^{(l_2)}\right), \tag{2}$$

where α is a meaning from the list $\mathcal{L}$, and $w_\alpha^{(l)}$ is its orthographic realization in the language l. The distance (2) is symmetric, $d(l_1, l_2) = d(l_2, l_1)$, $d(l, l) = 0$, and $d(l_1, l_2) = 1$ if and only if none of words of the $\mathcal{L}$ meanings in the language l_1 has any common character with those words in the language l_2. that is already improbable even over the short list of 200 meanings. The lexical distance (2) between two languages, l_1 and l_2, can be interpreted as the average probability to distinguish them by a mismatch between two characters randomly chosen from the orthographic realizations of $\mathcal{L}$. As a result, for the two samples of 50 languages selected from the IE and AU language families, we obtained the two symmetric 50×50 matrices; each matrix therefore contains 1225 independent entries. The phylogenetic trees from the lexical distance matrices (2) were constructed and discussed in [6, 7].

3 The Short List of Meanings and Its Stability

Following [8], we define the stability of the meaning α over a sample of N languages by

$$S(\alpha) = 1 - \frac{2}{N(N-1)} \sum_{l_i > l_j} D\left(w_\alpha^{(l_i)}, w_\alpha^{(l_j)}\right) \tag{3}$$

where the sum goes over all ordered pairs (l_i, l_j) of languages in the sample. With this definition, $S(\alpha)$ takes a value between 0 and 1. The sum in the RHS. of (3) is smaller for those words corresponding to meanings with a lower rate of lexical evolution, since they tend to remain more similar in two languages. Therefore, to a larger $S(\alpha)$ there corresponds a greater stability.

We computed the stability values for the 200 meanings according to the original choice of Swadesh [2] for the 50 language samples of both language families. The main source for the database for the IE group was the file prepared by Dyen et al. [9]. This database contains Swadesh's vocabulary with basic 200 meanings which seem maximally resistant to change, including borrowing [10], for 96 languages. The words are given there without diacritical symbols and adopted for using classic linguistic comparative methods to extract sets of cognates—words that can be related by consistent *sound* changes. Some words are missing in [9] but for our choice of 50 languages we have filled most of the gaps and corrected some errors by finding the words from Swadesh lists and from dictionaries freely available on the web. For the AU group, the huge database [11] has been used under the author's permission that we acknowledge. The AU database is adopted to reconstruct systematic *sound correspondences* between the languages in order to uncover historically related cognate forms and is under the permanent cleaning and development, with the assistance of linguistic experts correcting mistakes and improving the cognacy judgments. The lists in [11] contain more than 200 meanings that do not completely coincide with those in the original Swadesh list. For our choice of 50 AU languages, we have retained only those words which are included in the both data sets of [9] and of the original vocabulary [2, 9]. The resulting list has still many gaps due to missing words in the data set [11] and incomplete overlap between the list of [11] and the original Swadesh list [2, 9]. We have filled some of the gaps by finding the words from Swadesh's lists available on the web and by direct knowledge of the Malagasy language (by *M.S.*). We used the English alphabet (26 characters plus *space*) in our work to make the language data suitable for numerical processing. Those languages written in the different alphabets (i.e. Greek etc.) were already transliterated into English in [9]. In [11], many letter–diacritic combinations are used which we have replaced by the underlying letters, reducing again the set of characters to the standard English alphabet. Interestingly, the abolition of all diacritical symbols favouring a "simple" alphabet allowed us to obtain a reasonable result. The database modified by the authors is available [12]. Readers are welcome to modify, correct and add words to the database.

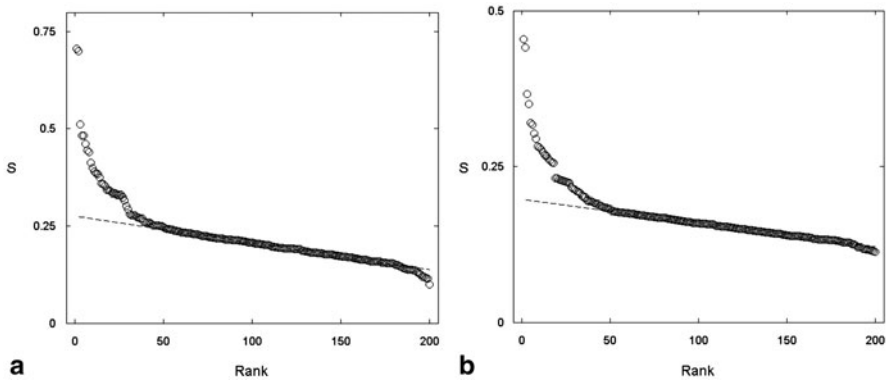

Fig. 1 Stability in a decreasing ranking for the 200 meanings over the 50 languages samples from the IE (**a**) and AU (**b**) language languages. The s*traight line* between position *51* and position *180* underlines the initial and final deviations from the linear behaviour

In Fig. 1, we have shown the plot of ranked stability values $S(\alpha)$ calculated for the 200 meanings in the short lists, for the IE and AU language groups in [13]. At the beginning the stability values drop rapidly; then, between the 50th position and the 180th, it decreases slowly and almost linearly with rank; finally at the end the stability drops again. This behaviour is not Gaussian, since high and low stability parts of the curve are not symmetric. The curve is fitted by a straight line to highlight the initial and final deviations from linearity. Clearly, one should keep all the meanings with higher information, take at least some of the most stable meanings in the linear part of the curve and exclude completely those meanings with lower information. The correlation coefficient between the stability index computed for the two groups is roughly 0.21 [13] suggesting that the stability of items in the short list depends strongly on the studied family. In order to understand whether the most stable terms in the two short lists show a large coincidence, we considered the first n items in the ranking list for both families, and we computed the number $m(n)$ of common items in the two lists. To underline the non-causal behaviour, $m(n)$ has to be compared with n^2/N, which is the average number of common items if one randomly chooses n items from any of the two lists. Then, it is natural to define $p(n)$ as $m(n)$ divided by n^2/N. If there is no relation between stability in the two families, $p(n)$ must be close to 1 for every n. The behaviour of $p(n)$ as a function of n can be seen in Fig. 2 indicating that indeed there is a non-trivial overlapping of the two lists of most stable n items since $p(n)$ is always larger than 1. This fact confirms the correlation between the two rankings, and also shows that this effect is strong only for small n ($n < 50$). For larger n, the overlapping is much closer to 1 and random coincidences prevail. This means that the most stable terms in the two lists are those that show a larger coincidence.

To give an example of the lists found with our approach, we show here a table of the 20 most stable items for the IE and AU language groups. Together with any of the items we report its stability record within the family.

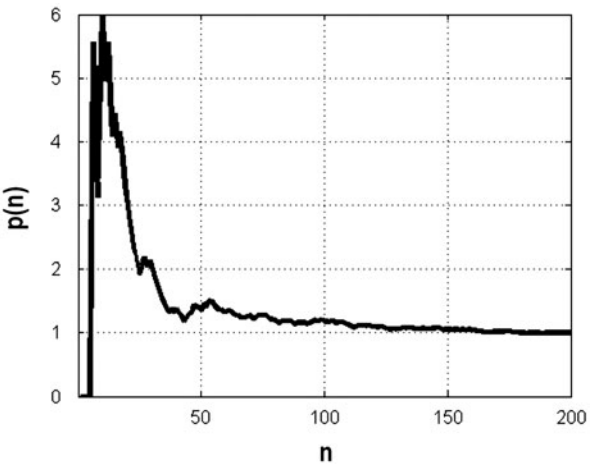

Fig. 2 The number of common items in the two lists of most stable n items obtained for the Austronesian and Indo-European families. The number is normalized by the random coincidence $n^2/200$

Table 1 The 20 most stable words for the Indo-European and Austronesian language families, with their stability values within the family

Indo-European	Stability	Austronesian	Stability
YOU	0.45395	EYE	0.70646
THREE	0.44102	FIVE	0.70089
MOTHER	0.36627	FATHER	0.51095
NOT	0.35033	DIE	0.48157
NEW	0.31961	STONE	0.48157
NOSE	0.3169	THREE	0.46087
FOUR	0.30226	TWO	0.44411
NIGHT	0.29403	LOUSE	0.43958
TWO	0.28214	ROAD	0.41217
NAME	0.27962	FOUR	0.39798
TOOTH	0.27677	HAND	0.38997
STAR	0.27269	NAME	0.38493
SALT	0.26792	LIVER	0.38375
DAY	0.26695	PUSH	0.37444
GRASS	0.26231	MOTHER	0.35821
SEA	0.25906	WE	0.35749
DIE	0.25602	EAT	0.3529
SUN	0.25535	STICK	0.34242
ONE	0.23093	I	0.34208
FEATHER	0.23055	VOMIT	0.33861

4 The Structural Component Analysis of Linguistic Data

Component analysis is a standard tool in diverse fields from neuroscience to computer graphics. It helps to reduce a complex data set to a lower dimension suitable for visual apprehension and to reveal its simplified structures. Independent component analysis (ICA) [14] and principal component analysis (PCA) [15] are widely used for separating a multivariate signal into additive subcomponents. However, it is clear that these standard techniques of component analysis have to be dramatically improved for any meaningful application on language data, as there is no reason to suggest neither that the directions of maximum variance recovered by the standard PCA method are good enough for identification of principal components in the linguistic data, nor that the language traits are statistically independent. Since all languages within a language family interact with each other and with the languages of other families in real time, it is obvious that any historical development in language cannot be described only in terms of pairwise interactions, but it reflects a genuine higher order influence among the different language groups. Generally speaking, the number of parameters describing all possible parallels we may observe between the linguistic data from the different languages would increase exponentially with the data sample size. The only hope to perform any useful data analysis in such a case relies upon a proper choice of features that re-expresses the data set to make all contributions from an asymptotically infinite number of parameters *convergent* to some non-parametric *kernel*.

It is important to mention that any symmetric matrix of lexical distances (2) uniquely determines a weighted undirected fully connected graph, in which vertices represent languages, and edges connecting them have weights equal to the relevant lexical distances between languages (2). Since the graph encoded by the matrix (2) is relatively small (of 50 vertices) and essentially not random, it is obviously out of the usual context of complex network theory. A suitable method for the structural component analysis (SCA) of networks (weighted graphs) by means of *random walks* (or Markov chains, in a more general context) has been formulated in [16–18]. Being a version of the *kernel PCA* method [19], it generalizes PCA to the case, where we are interested in principal components obtained by taking all higher-order correlations between data instances. The SCA method has been successfully applied to the analysis of language taxonomies in [20].

Let us note that there are infinitely many matrices that match all the structure of $d(l_i, l_j)$ and contain all the information about the relationships between languages estimated by means of the lexical distances (2). It is remarkable that all these matrices are related to each other by means of a linear transformation, which can be interpreted as a random walk,

$$T\left(l_i, l_j\right) \;=\; \Delta^{-1}\, d\left(l_i, l_j\right), \tag{4}$$

defined on the weighted undirected graph determined by the matrix of lexical distances $d(l_i, l_j)$, The diagonal matrix in (4) $\Delta = \mathrm{diag}(\delta_{l_1}, \delta_{l_2}, \ldots \delta_{l_N})$ contains the *cumulative* lexical distances $\delta_{l_i} = \sum_{j=1}^{N} d(l_i, l_j)$, for each language l_i. Diagonal elements of the matrix T are equal to zero, since $d\,(l_i, l_i) = 0$, for any language l_i.

The matrix (4) is a stochastic matrix, $\sum_{j=1}^{N} T(l_i, l_j) = 1$, being nothing else, but the normalized matrix of lexical distances (2). Random walks defined by the transition matrix (4) describe the statistics of a sequential process of language classification. Namely, while the elements of the matrix $T(l_i, l_j)$ evaluate the probability of successful differentiation of the language l_i provided the language l_j has been identified certainly, the elements of the squared matrix T^2, ascertain the successful differentiation of the language l_i from l_j through an intermediate language, the elements of the matrix T^3 give the probabilities to differentiate the language through two intermediate steps, and so on. The whole host of complex and indirect relationships between orthographic representations of the vocabulary meanings encoded in the matrix of lexical distances (2) is uncovered by the von Neumann series estimating the characteristic time of successful classification for any two languages in the database over a language family,

$$J\left(l_i, l_j\right) \;=\; \lim_{n\to\infty} \sum_{k=0}^{n} T^n\left(l_i, l_j\right) \;=\; \frac{1}{1-\mathbf{T}}. \tag{5}$$

The last equality in (5) is understood as the group generalized inverse [20], being a symmetric, positive semi-definite matrix which plays essentially the same role for the SCA, as the covariance matrix does for the usual PCA analysis. The standard goal of a component analysis (minimization of the data redundancy quantified by the off-diagonal elements of the kernel matrix) is readily achieved by solving an eigenvalue problem for the matrix $J(l_i, l_j)$. Each column vector q_k, which determines a direction where $\mathbf{J}$ acts as a simple rescaling, $\mathbf{J}q_k = \lambda_k q_k$, with some real eigenvalue $\lambda_k = 0$, is associated to the virtually independent trait in the matrix of lexical distances $d(l_i, l_j)$. Independent components $\{q_k\}$, $k = 1, \ldots N$, define an orthonormal basis in $\mathbb{R}^N$ which specifies each language l_i by N numerical coordinates, $l_i \to (q_{1,i}, q_{2,i}, \ldots q_{N,i})$. Languages that cast in the same mould in accordance with the N individual data features are revealed by geometric proximity in Euclidean space spanned by the eigenvectors $\{q_k\}$ that might be either exploited visually, or accounted analytically. The rank-ordering of data traits $\{q_k\}$, in accordance to their eigenvalues, $\lambda_0 = \lambda_1 < \lambda_2 = \ldots = \lambda_N$, provides us with the natural geometric framework for dimensionality reduction. At variance with the standard PCA analysis [15], where the largest eigenvalues of the covariance matrix are used in order to identify the principal components, while building language taxonomy, we are interested in detecting the groups of the most similar languages, with respect to the selected group of features. The components of maximal similarity are identified with the eigenvectors belonging to the smallest non-trivial eigenvalues. Since the minimal eigenvalue $\lambda_1 = 0$ corresponds to the vector of stationary distribution of random walks and thus contains no information about components, we have used the three consecutive components $(q_{2,i}, q_{3,i}, q_{4,i})$ as the three Cartesian coordinates of a language point $l_i(x, y, z)$ in order to build a three-dimensional geometric representation of language taxonomy. Points symbolizing different languages in space of the three major data traits are contiguous if the orthographic representations of the vocabulary meanings in these languages are similar.

5 Geometric Representation of the IE Family

Many language groups in the IE family had originated after the decline and fragmentation of territorially-extreme polities and in the course of migrations when dialects diverged within each local area and eventually evolved into individual languages. In Fig. 3, we have shown the three-dimensional geometric representation of 50 languages of the IE language family in space of its three major data traits detected in the matrix of lexical distances calculated over the Swadesh list of meanings. Due to the striking central symmetry of the representation, it is natural to describe the positions of language points l_i with the use of spherical coordinates,

$$r_i = \sqrt{q_{2,i}^2 + q_{3,i}^2 + q_{4,i}^2}, \quad \theta_i = \arccos\left(\frac{q_{4,i}}{r_i}\right), \quad \phi_i = \arctan\left(\frac{q_{3,i}}{q_{2,i}}\right), \qquad (6)$$

rather than the Cartesian system.

The principal components of the IE family reveal themselves in Fig. 3 by four well-separated spines representing the four biggest traditional IE language groups: Romance and Celtic, Germanic, Balto-Slavic, and Indo-Iranian. These groups are monophyletic and supported by the sharply localized distributions of the azimuth (φ) and inclination (zenith) angles (θ) over the languages shown in Fig. 4a and b, respectively.

The Greek, Romance, Celtic and Germanic languages form a class characterized by approximately the same azimuthal angle (Fig. 4a), thus belonging to one plane in the three-dimensional geometric representation shown in Fig. 3, while the Indo-Iranian, Balto-Slavic, Armenian and Albanian languages form another class, with respect to the inclination (zenith) angle (Fig. 4b).

It is remarkable that the division of IE languages with respect to the azimuthal and zenith angles evident from the geometric representation in Fig. 3 perfectly coincides with the well-known *centum-satem* isogloss of the IE language family (the terms are the reflexes of the IE numeral "100"), related to the evolution in the phonetically unstable palatovelar order [21]. The palatovelars merge with the velars in centum languages sharing the azimuth angle, while in satem languages observed at the same zenith angle the palatovelars shift to affricates and spirants. Although the satem–centum distinction was historically the first original dialect division of the IE languages [22], it is not accorded much significance by modern linguists as being just one of many other isoglosses crisscrossing all IE languages [23]. The basic phonetic distinction of the two language classes does not justify in itself the areal groupings of historical dialects, each characterized by some phonetic peculiarities indicating their independent developments. The appearance of the division similar to the centum–satem isogloss (based on phonetic changes only) may happen because of the systematic sound correspondences between the Swadesh words across the different languages of the same language family.

The projections of Albanian, Greek and Armenian languages onto the axes of the principal components of the IE family are rather small, as they occupy the centre of the diagram in Fig. 3. Being eloquently different from others, these languages can be

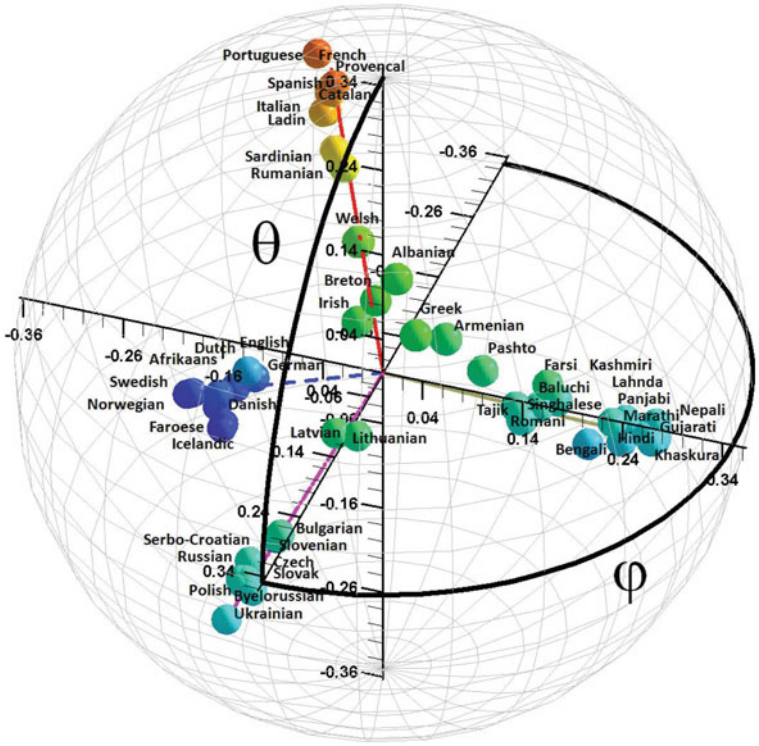

Fig. 3 The three-dimensional geometric representation of the Indo-European language family in space of the major data traits (q_2, q_3, q_4) colour coded. The *origin* of the graph indicates the centre of mass, $q_1 = \pi$, of the matrix of lexical distances $d(l_i, l_j)$, not the Proto-Indo-European language. Due to the central symmetry of representation, it is convenient to use the spherical coordinates to identify the positions of languages: the radius from the *centre* of the graph, the inclination angle θ and the azimuth angle φ

resolved with the use of some minor components $q_k, k > 3$. Remarkably, the Greek and Armenian languages always remain proximate confirming the Greeks' belief that their ancestors had come from Western Asia [24].

6 In Search of Lost Time

Geometric representations of language families can be conceived within the framework of various physical models that infer on the evolution of linguistic data traits. In traditional glottochronology [2], the time at which languages diverged is estimated on the assumption that the core lexicon of a language changes at a constant average rate. This assumption based on an analogy with the use of carbon dating for

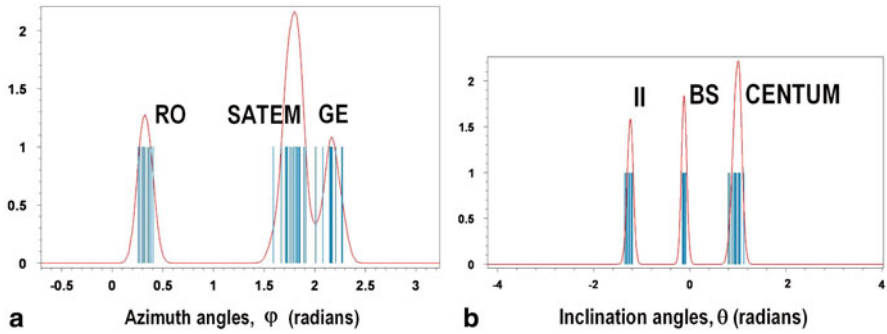

Fig. 4 a The kernel density estimates of the distributions of azimuthal angles in the three-dimensional geometric representation of 50 languages of the Indo-European language family, together with the absolute data frequencies. Romance (*RO*), Germanic (*GE*) and the satem languages (*SATEM*) are easily differentiated with respect to the azimuthal angles. **b** The kernel density estimates of the distributions of inclination (zenith) angles in the three-dimensional geometric representation of 50 languages of the Indo-European language family, together with the absolute data frequencies. Indo-Iranian (*II*), Balto-Slavic (*BS*), and the centum languages (*CENTUM*) are attested by the inclination (zenith) angles

measuring the age of organic materials was rejected by mainstream linguists, considering a language as a social phenomenon driven by unforeseeable sociohistorical events not stable over time. Indeed, mechanisms underlying evolution of dialects of a proto-language evolving into individual languages are very complex and hardly formalizable.

In our method based on the statistical evaluation of differences in the orthographic realizations of Swadesh's vocabulary, a complex nexus of processes behind the emergence and differentiation of dialects within each language group is described by the single degree of freedom, along the radial direction (see (6)) from the origin of the graph shown in Fig. 3, while the azimuthal (φ) and zenith (θ) angles are specified by a language group.

It is worth a mention that the distributions of languages along the radial direction are remarkably heterogeneous indicating that the rate of changes in the orthographic realizations of Swadesh's vocabulary was varying over time. Being ranked within the own language group and then plotted against their expected values under the normal probability distribution, the radial coordinates of languages in the geometrical representation, Fig. 3, show very good agreement with univariate normality, as seen from the normal probability plots in Fig. 5a–d.

The hypothesis of normality of these distributions can be justified by taking on that for a long time the divergence of orthographic representations of the core vocabulary was a *gradual* change accumulation process into which many small, independent innovations had emerged and contributed additively to the outgrowth of new languages. Perhaps, the orthographic changes arose due to the fixation of phonetic innovations developed in the course of long-lasting interactions with non-IE languages in areas of their intensive historical contacts.

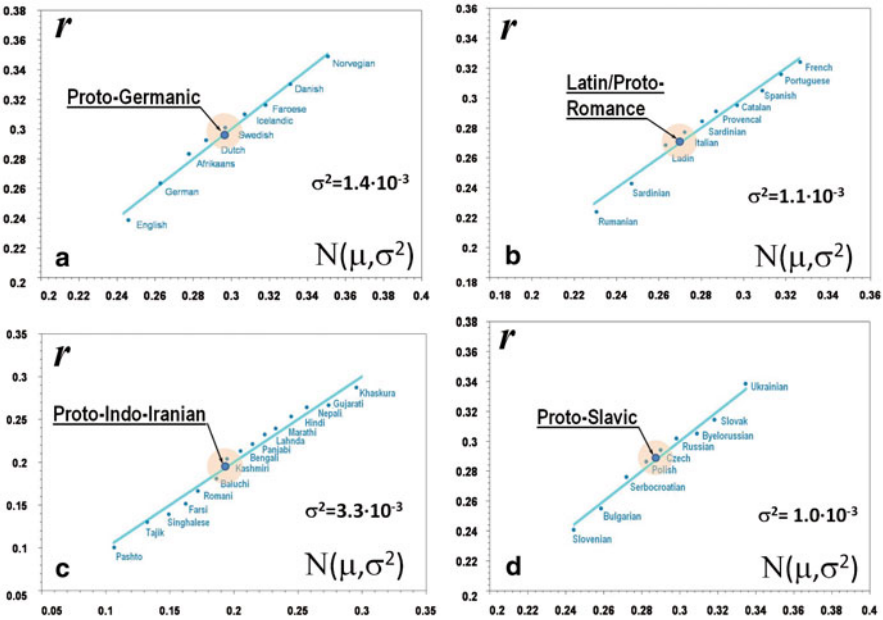

Fig. 5 The *panels A–D* show the normal probability plots fitting the distances r of language points from the centre of mass to univariate normality. The data points were ranked and then plotted against their expected values under normality, so that departures from linearity signify departures from normality. The values of variance are given for each language group. The expected locations of the proto-languages, together with the end points of the 95 % confidence intervals, are displayed on the normal plots by *circles*

In physics, the univariate normal distribution is closely related to the time evolution of a mass-density function $\rho(r,t)$ under homogeneous diffusion in one dimension,

$$\rho(r,t) \;=\; \frac{1}{2\pi\sigma^2}\cdot\exp\left(-\frac{(r-\mu)^2}{2\sigma^2}\right),$$

in which the mean value μ is interpreted as the coordinate of a point where all mass was initially concentrated, and variance $\sigma^2 \propto t$ grows linearly with time. If the distributions of languages along the radial coordinate of the geometric representation do fit to univariate normality for all language groups, then in the long run the value of variance in these distributions grew with time at some approximately constant rate. The constant increment rates of variance of radial positions of languages in the geometrical representation, Fig. 3, has nothing to do with the traditional glottochronological assumption about the steady borrowing rates of cognates [25]. It is also important to mention that the values of variance σ^2 calculated for the languages over the individual language groups (see Fig. 5a–d) do not correspond to physical time rather give a statistically consistent estimate of age for each language group.

In order to assess the pace of variance changes with physical time and calibrate our dating method, we have to use the historically attested events.

Although historical compendiums report us on grace, growth and glory succeeded by the decline and disintegration of polities in days of old, they do not tell us much about the simultaneous evolution in language. It is beyond doubt that massive population migrations and disintegrations of organized societies, both destabilizing the social norms governing behaviour, thoughts and social relationships can be taken on as the chronological anchors for the onset of language differentiation. However, the idealized assumption of a punctual *split* of a proto-language into a number of successor languages shared implicitly by virtually all phylogenetic models is problematic for a linguist well aware of the long-lasting and devious process by which a real language diverges [26]. We do not aspire to put dates on such a fuzzy process, rather consider language as a natural appliance for dating of those migrations and fragmentation happened during poorly documented periods in history.

While calibrating the dating mechanism in our model, we have used the four anchor events [27]:

1. The last Celtic migration (to the Balkans and Asia Minor) (by 300 BC)
2. The division of the Roman Empire (by 500 AD)
3. The migration of German tribes to the Danube River (by 100 AD)
4. The establishment of the Avars Khaganate (by 590 AD) overspreading Slavic people who did the bulk of the fighting across Europe

It is remarkable that a very slow variance pace of a millionth per year

$$\frac{t}{\sigma^2} = (1.367 \pm 0.002) \times 10^6 \tag{7}$$

is evaluated uniformly, with respect to all of the anchoring historical events mentioned above.

The time–variance ratio (7) deduced from the well attested events allows us to retrieve the probable dates for

1. The break-up of the Proto-Indo-Iranian continuum preceding 2400 BC, in a good agreement with the migration dates from the early Andronovo archaeological horizon [28]
2. The end of common Balto-Slavic history as early as by 1400 BC, in support of the recent glottochronological estimates [29] well agreed with the archaeological dating of Trziniec–Komarov culture, localized from Silesia to Central Ukraine
3. The separation of Indo-Aryans from Indo-Iranians by 400 BC, probably as a result of Aryan migration across India to Ceylon, as early as in 483 BC [30]
4. The division of Persian polity into a number of Iranian tribes migrated and settled in vast areas of Southeastern Europe, the Iranian plateau and Central Asia by 400 BC, shortly after the end of Greco–Persian wars [31].

7 Evidence for Proto-Indo-Europeans

The basic information about the Proto-Indo-Europeans arises out of the comparative linguistics of the IE languages. There were a number of proposals about early Indo-European origins so far. For instance, the *Kurgan* scenario postulating that the people of an archaeological "Kurgan culture" (early fourth millennium BC) in the Pontic steppe were the most likely speakers of the proto- IE language, is widely accepted [32]. The *Anatolian* hypothesis suggests a significantly older age of the IE proto-language as spoken in Neolithic Anatolia and associates the distribution of historical IE languages with the expansion of agriculture during the Neolithic revolution in the eighth and sixth millennia BC [22].

It is a subtle problem to trace back the diverging pathways of language evolution to a convergence in the IE proto-language since symmetry of the modern languages assessed by the statistical analysis of orthographic realizations of the core vocabulary mismatches that in ancient time. The major IE language groups have to be re-examined in order to ascertain the locations of the individual proto-languages as if they were extant. In our approach, we associate the mean μ of the normal distribution of languages belonging to the same language group along the radial coordinate r with the expected location of the group proto-language. Although we do not know what the exact values of means were, the sample means calculated over the several extant languages from each language group give us the appropriate estimators. There is a whole interval around each observed sample mean within which, the true mean of the whole group actually can take the value.

In order to target the locations of the five proto-languages (the Proto-Germanic, Latin, Proto-Celtic, Proto-Slavic, and Proto-Indo-Iranian) with the 95 % confidence level, we have supposed that variances of the radial coordinate calculated over the studied samples of languages are the appropriate estimators for the true variance values of the entire groups. The expected locations of the proto-languages, together with the end points of the 95 % confidence intervals, are displayed on the normal plots, in Fig. 5a–d. Let us note that we did not include the Baltic languages into the Slavic group when computing the Proto-Slavic centre point because these two groups exhibit different statistics, so that such an inclusion would dramatically reduce the confidence level for the expected locations of the proto-languages. Although the statistical behaviour of the proto-languages in the geometric representation of the IE family is not known, we assume that it can be formally described by the "diffusion scenario", as for the historical IE languages. Namely, we assume that the locations of the five proto-languages from a statistically determined central point fit to multivariate normality. Such a null hypothesis is subjected to further statistical testing, in which the chi-square distribution is used to test for goodness of fit of the observed distribution of the locations of the proto-languages to a theoretical one. The chi-square distribution with k degrees of freedom describes the distribution of a random variable $Q = \sum_{i=1}^{k} X_i^2$, where X_i are k independent, normally distributed random variables with mean 0 and variance 1.

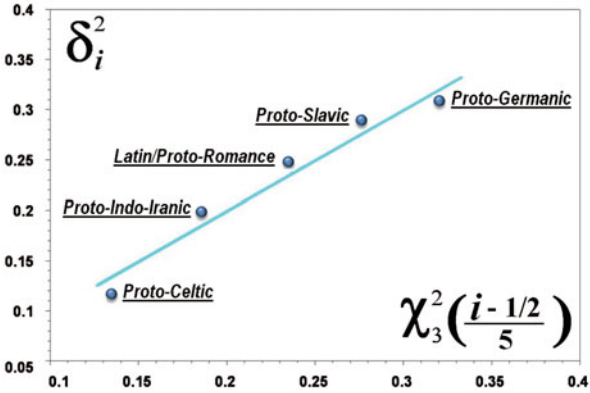

Fig. 6 The graphical test to check three-variate normality of the distribution of the distances δ_i of the five proto-languages from a statistically determined central point is presented by extending the notion of the normal probability plot. The integer parameter i specifies the number of degrees of freedom. The chi-square distribution is used to test for goodness of fit of the observed distribution: the departures from three-variant normality are indicated by departures from linearity

In Fig. 6, we have used a simple graphical test to check three-variate normality by extending the notion of the normal probability plot. The locations of proto-languages have been tested by comparing the goodness of fit of the scaled distances from the proto-languages to the central point (the mean over the sample of the five proto-languages) to their expected values under the chi-square distribution with three degrees of freedom. In the graphical test shown in Fig. 6, departures from three-variant normality are indicated by departures from linearity. Supposing that the underlying population of parent languages fits to multivariate normality, we conclude that the determinant of the sample variance–covariance matrix has to grow linearly with time. The use of the previously determined time–variance ratio (7) then dates the initial break-up of the Proto-Indo-Europeans back to 7000 BC pointing at the early Neolithic date, to say nothing about geography, in agreement with the Anatolian hypothesis of the early Indo-European origin [7, 21, 22, 24, 33].

The linguistic community estimates of dating for the proto-IE language lie between 4500 and 2500 BC, a later date than the Anatolian theory predicts. These estimations are primarily based on the reconstructed vocabulary (see [34] and references therein) suggesting a culture spanning the Early Bronze Age, with knowledge of the wheel, metalworking and the domestication of the horse and thus favouring the Kurgan hypothesis. It is worth a mention that none of these words are found in the Swadesh list encompassing the basic vocabulary related to agriculture that emerged perhaps with the spread of farming, during the Neolithic era. Furthermore, the detailed analysis of the terms uncovered a great incongruity between the terms found in the reconstructed proto-IE language and the cultural level met with in the Kurgans lack of agriculture [35]. Let us note that our dating (2400 BC) for the migration from the Andronovo archaeological horizon (see Sect. 6) and the early break-up of the proto-Indo-Iranian continuum estimated by means of the variance (see Fig. 5c) is

compatible with the Kurgan time frame. However, despite the Indo-Iranian group of languages being apparently the oldest among all other groups of the IE family, we cannot support the general claim of the Kurgan hypothesis, at least on the base of Swadesh's lexicon.

8 In Search of Polynesian Origins

The colonization of the Pacific Islands is still the recalcitrant problem in the history of human migrations, despite many explanatory models based on linguistic, genetic and archaeological evidences have been proposed in so far. The origins, relationships and migration chronology of Austronesian settlers have constituted the sustainable interest and continuing controversy for decades. The components probe for a sample of 50 AU languages immediately uncovers the both Formosan (F) and Malayo-Polynesian (MP) branches of the entire language family (see Fig. 7).

The distribution of azimuth angles shown in Fig. 8a identifies them as two monophyletic jets of languages that cast along either axis spanning the entire family plane. The clear geographic patterning is perhaps the most remarkable aspect of the geometric representation. It is also worth mentioning that the language groupings as recovered by the component analysis of lexical data reflect profound historical relationships between the different groups of AU population. For instance, the Malagasy language spoken in Madagascar casts in the same mould as the Maanyan language spoken by the Dayak tribe dwelling in forests of Southern Borneo and the Batak Toba language of North Sumatra spoken mostly west of Lake Toba.

Despite Malagasy sharing much of its basic vocabulary with the Maanyan language [36], many manifestations of Malagasy culture cannot be linked up with the culture of Dayak people: the Malagasy migration to East Africa presupposes highly developed construction and navigation skills with the use of out-rigger canoes typical of many Indonesian tribes which the Dayak people, however, do not have, also some of the Malagasy cultivations and crop species (such as wet rice) cannot be found among forest inhabitants. In contrast, some funeral rites (such as the second burial, *famadihana*) typical of the leading entities of the Madagascar highlands are essentially similar to those of Dayak people. A possible explanation is that population of the Dayak origin was brought to Madagascar as slaves by Malay seafarers [6]. As the Dayak speakers formed the majority in the initial settler group, in agreement with the genetic parental lineages found in Madagascar [37], their language could have constituted the core element of what later became Malagasy, while the language of the Malay dominators was almost suppressed, albeit its contribution is still recovered by the exploration of the leading traits on language data.

The AU language family forks at the northernmost tip of the Philippines, the Batanes Islands located about 190 km south of Taiwan (see Fig. 8b). On the distribution of azimuth angles shown in Fig. 8a, the Itbayaten language representing them in the studied sample is pretty close to the azimuth, $\varphi = 0$, bridging over the separating language family branches (Fig. 8b). By the way, the MP-offset descends from the

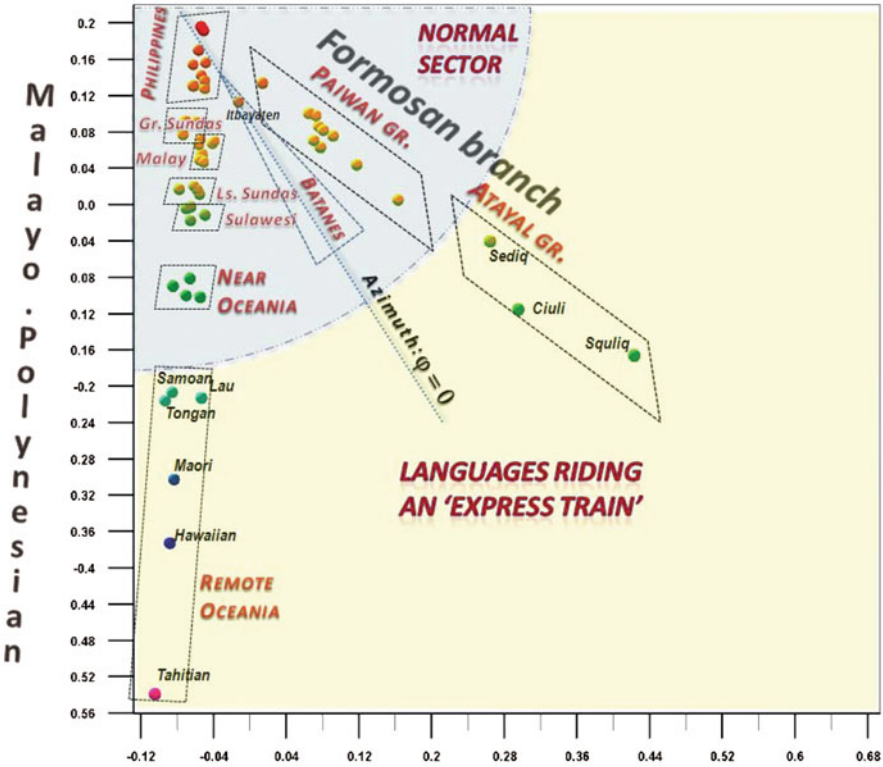

Fig. 7 The geometric representation of the 50 AU languages in space of the major data traits (q_2, q_3) shows the remarkable geographic patterning. It is convenient to use the polar coordinates: the radius from the centre of the graph, $r_i = \sqrt{q_{2,i}^2 + q_{3,i}^2}$, and the azimuth angle $\varphi = \arctan(\frac{q_{3,i}}{q_{2,i}})$, to identify the positions of languages. For languages in the "normal sector", the distribution of radial coordinates conforms to univariate normality. At variance with them, languages located at the distant margins of the AU family apparently follow the "express train" evolution model (see Sect. 9) The "normal sector" consists of the following languages: from Philippines, *Bontoc, Kankanay, Ilokano, Hanunoo, Cebuano, Tagalog, Pangasinan, Mansaka, Maranao*; from Great Sunda and Malay, *Malagasy, Maanyan, Ngaiu dayak, Toba batak, Bali, Malay, Iban, Sasak, Sunda, Javanese*; from Lesser Sunda and Sulawesi, *Sika, Kambera, Wolio, Baree, Buginese, Manggarai, Sangir, Makassar*; from Near Oceania, *Manam, Motu, Nggela, Mota*; of Paiwan group (Taiwan) *Pazeh, Thao, Puyuma, Paiwan, Bunun, Amis, Rukai, Siraya, Kavalan*

northern Philippines (the northern Luzon Island) and springs forth eastward through the Malay Archipelago across Melanesia culminating in Polynesia (Fig. 9); in accordance with the famous "express train" model of migrations peopled the Pacific [38]. In its turn, the F-branch embarks on the southwest coast of Taiwan and finds its way to the northern Syueshan Mountains inhabited by Atayal people that compose many ethnic groups with different languages, diverse customs and multiple identities. Evidently, both the offshoots derived their ancestry in Southeast Asia as strengthened by multiple archaeological records [38], but then evolved mostly independently from

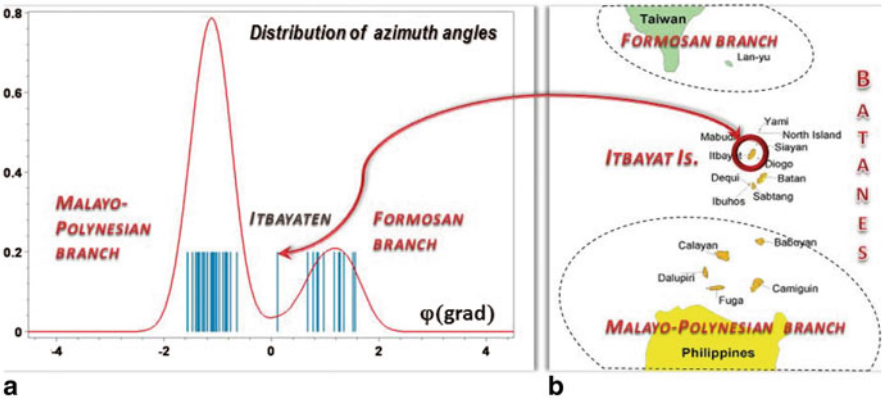

Fig. 8 **a** The distribution of azimuth angles in the geometric representation of the 50 AU languages shown in Fig. 7. **b** The Itbayaten language is pretty close to the azimuth, $\varphi = 0$, bridging over the language family branches lexically and geographically

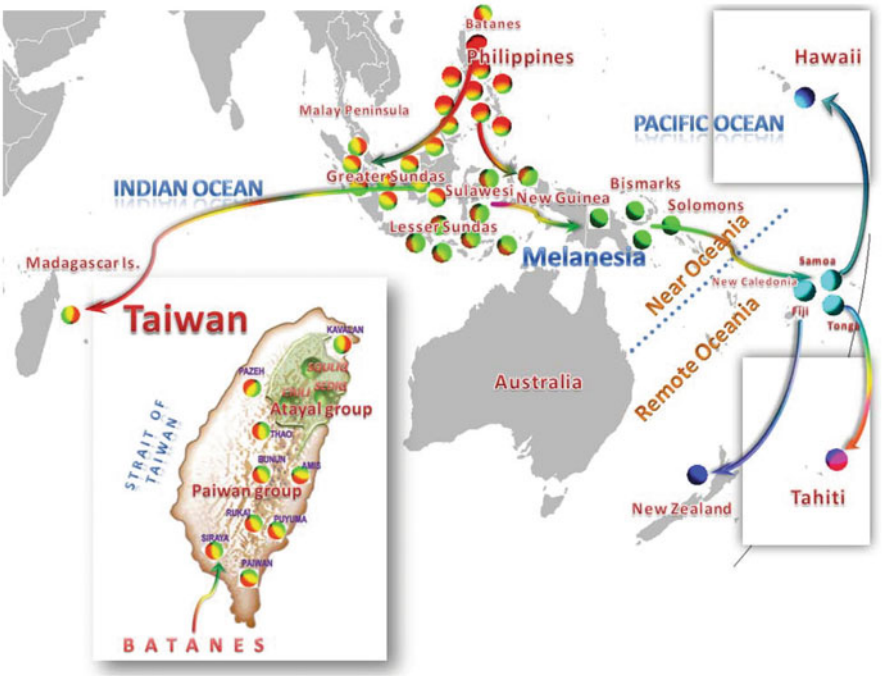

Fig. 9 The geometric representation of the 50 AU languages (Fig. 7) projected onto the geographic map uncovers the possible route of Austronesian migrations

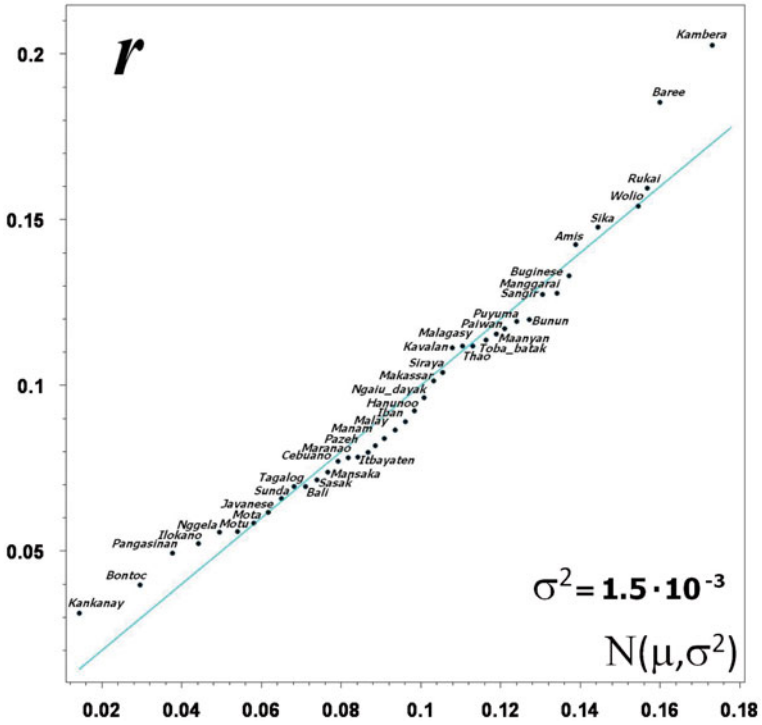

Fig. 10 The normal probability plot fitting the distances r of language points from the "centre of mass" of the geometrical representation of the AU language family to univariate normality. The data points for languages belonging to the "normal sector" shown in Fig. 7 were ranked and then plotted against their expected values under normality, so that departures from linearity signify departures from normality. The value of variance over all languages belonging to the "normal sector" is $\sigma^2 = 1.5 \times 10^{-3}$

each other, on evidence of the Y-chromosome haplotype spread over Taiwanese and Polynesian populations [39].

The distribution of languages spoken within Maritime Southeast Asia, Melanesia, Western Polynesia and of the Paiwan language group in Taiwan over the distances from the centre of the diagram representing the AU language family in Fig. 7 conforms to univariate normality (see Fig. 10) suggesting that an interaction sphere had existed encompassing the whole region, from the Philippines and Southern Indonesia through the Solomon Islands to Western Polynesia, where ideas and cultural traits were shared and spread as attested by trade [40, 41] and translocation of farm animals [42, 43] among shoreline communities.

Although the lack of documented historical events makes the use of the developed dating method difficult, we may suggest that variance evaluated over Swadesh's vocabulary forges ahead approximately at the same pace uniformly for all human societies involved in trading and exchange forming a singular cultural continuum.

Then, the time–age ratio (7) deduced from the previous chronological estimates for the IE family returns 550 AD if applied to the Austronesians as the likely break-up date of their cultural continuum, pretty well before 600–1200 AD while descendants from Melanesia settled in the distant apices of the Polynesian triangle as evidenced by archaeological records [44–46].

9 Austronesian Languages Riding an Express Train

The distributions of languages spoken in the islands of East Polynesia and of the Atayal language groups in Taiwan over the radial coordinate from the centre of the geometric representation shown in Fig. 7 break from normality, so that the general "diffusive scenario" of language evolution used previously for either of the chronological estimates is obviously inapplicable to them. For all purposes, the evolution of these extreme language subgroups cannot be viewed as driven by independent, petty events. Although the languages spoken in Remote Oceania clearly fit the general trait of the entire MP-branch, they seem to evolve without extensive contacts with Melanesian populations, perhaps because of a rapid movement of the ancestors of the Polynesians from South-East Asia as suggested by the "express train" model [38] consistent with the multiple evidences on comparatively reduced genetic variations among human groups in Remote Oceania [47–49].

In order to obtain reasonable chronological estimates, an alternative mechanism on evolutionary dynamics of the extreme language subgroups in space of traits of the AU language family should be reckoned with. The simplest "adiabatic" model entails that no words had been transferred to or from the languages riding the express train to Polynesia, so that the lexical distance among words of the most distanced languages tends to increase primarily due to random permutations, deletions or substitutions of phonemes in the words of their ancestor language. Under such circumstances the radial coordinate of a remote language riding an "express train" in the geometric representation (see Fig. 7) effectively quantifies the duration of its relative isolation from the Austronesian cultural continuum. Both of the early colonization of a secluded island by Melanesian seafarers and of the ahead of time migration of the indigenous people of Taiwan to highlands can be discerned by the excessively large values of the radial coordinates r of their languages. In Fig. 11, we have presented the log-linear plot, in which the radial coordinates of remote languages were ranked and then plotted against their expected values under the exponential distribution (shown by the dash-dotted line in Fig. 11).

The radial coordinates of the languages at the distant margins of the AU family diagram shown in Fig. 11 may be deduced as evolving in accordance with the simple differential equation

$$\dot{r} = ar \tag{8}$$

where $\dot{r}$ means the derivative of r with respect to isolation time, and $a > 0$ is some constant quantifying the rate of radial motion of a language riding the express

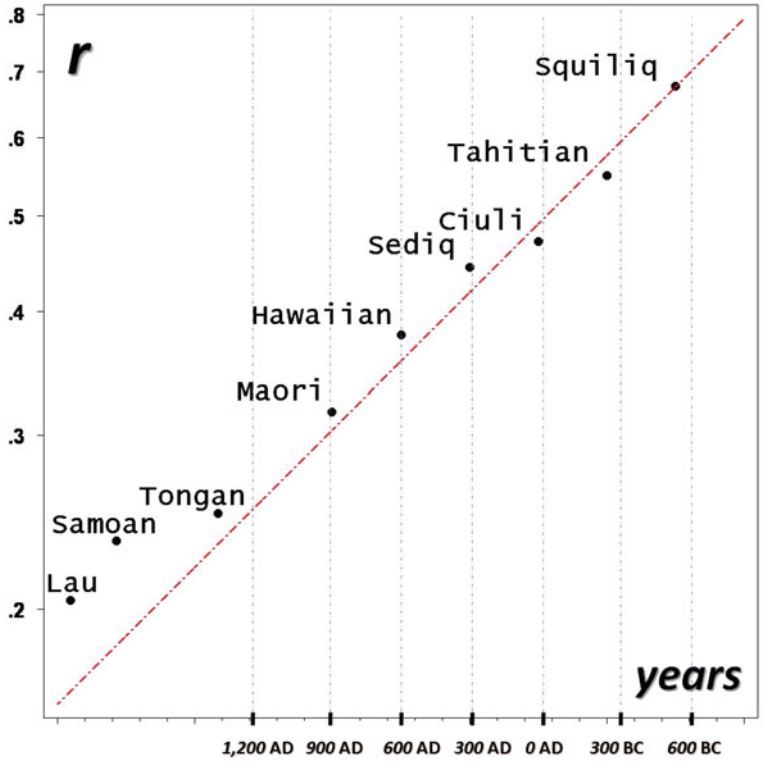

Fig. 11 The log-linear plot fitting the distances r to remote languages riding an "express train" in the geometric representation (see Fig. 7) to an exponential distribution. The radial coordinates of the languages were ranked and then plotted against their expected values under the exponential distribution. As usual, the departures from linearity signify departures from the tested distribution (given by the *dash-dotted line*)

train in space of the major traits of the AU family. In the proposed model of language evolution, it is suggested that in absence of contact borrowings the orthographic realizations of Swadesh's meanings would accumulate emergent variations in spellings, so that the radial coordinate indicating the divergence of a remote language from the rest of the group can grow unboundedly with isolation time.

A simple equation mathematically similar to (8) has been proposed by Swadesh [2] in order to describe the change of cognates in time, in the framework of the glottochronological approach. In our previous work [6], another similar equation has been suggested for the purpose of modeling the time evolution of normalized edit distances between languages. However, we have to emphasize that the statistical model (8) has a direct relation to neither the percentage of cognates (as in the traditional glottochronological approach), nor the edit distance itself.

Then the relative dates estimating the duration of relative isolation of the distant languages from the extensive contacts with other Austronesian languages can be

derived basing on the assumption (8) as

$$t_1 - t_2 = \frac{1}{a} \cdot \ln \frac{r_1}{r_2} \tag{9}$$

where $r_2 > r_1$ are the radial coordinates of the languages from the centre of the sample diagram shown in Fig. 7.

Tahiti located in the archipelago of Society Islands is the farmost point in the geometric representation of the Austronesian family and the foremost Austronesian settlement in the Remote Oceania attested as early as 300 BC [44], the date we placed the incipience of the Tahitian society. According to many archaeological reconstructions [44–46], descendants from West Polynesia had spread through East Polynesian archipelagos and settled in Hawaii by 600 AD and in New Zealand by 1000 AD testifying the earliest outset dates for the related languages. It is worth mentioning that all stride times between the offsets of these three Polynesian languages hold consistently the same rate

$$a = (4.27 \pm 0.01) \times 10^{-4} \tag{10}$$

affirming the validity of the "adiabatic" conjecture described above and allowing us to assign the estimated dates to the marks of the horizontal axis of the timing diagram presented in Fig. 11. The language divergence among Atayal people distributed throughout an area of rich topographical complexity is neatly organized by the myths of origin place, consanguine clans and geographical barriers that have lead to the formation of a unique concept of ethnicity remarkable for such a geographically small region as Taiwan. The complexity of the Atayal ethnic system and the difficulty of defining the ethnic borders hindered the classification of the Atayal regional groups and their dialects which has been continuously modified throughout the last century.

In our work, we follow the traditional classification [50] of the Atayal group into three branches based on their places of origin: Sediq (Sedek), Ciuli (Tseole) Atayal, and Squiliq (Sekilek) Atayal. In account with the standard lexicostatistic arguments [51], the Sediq dialect subgroup could have split off from the rest of the Atayal groups about 1600 years ago, as both the branches share up to a half of the cognates in the 200 words of basic vocabulary. This estimated date is very tentative in nature and calls for a thorough crosschecking. The Atayal people had been recognized as they had started to disperse to the northern part of Taiwan around 1750 AD [52]. Being formed as the isolated dialect subgroups in island interiors, they showed the greatest diversity in race, culture and social relations and sometimes considered each other as enemies and prime head hunting targets.

Given the same rate of random phonetic changes as derived for the Polynesian languages, the "adiabatic" model of language evolution returns the stride times of 1000 years between the Sediq dialect subgroup and Squiliq Atayal and of 860 years between the Ciuli and Squiliq Atayal languages. Consistently, Sediq is estimated to have branched off from the other Atayal languages 140 years before the main Atayal group split into two. The Squiliq subgroup had been attested during the latest migration of Atayal people, as late as 1820 AD [52]. Perhaps, a comprehensive study

of the Atayal dialects by their symmetry can shed light on the origins of the Atayal ethnic system and its history.

10 Conclusion

We have presented the new paradigm for the analysis of language phylogeny. The proposed method is fully automated; it avoids subjectivity since all results can be replicated by other scholars assuming that the database is the same. Furthermore, it allows for rapid comparison of items of a very large number of languages.

We applied here our method to the IE and AU families of languages considering 200 items lists of words according to the original choice of Swadesh. The output was a stability measure for all items computed separately for the two families. The ranking plots show that the two families behave in the same way, with the higher stability items deviating from the linear interpolation because of their very large values. We are convinced that this phenomenology we observe, both for IE and AU languages, should be a universal characteristic of stability distributions, common to all families. On the contrary, it turns out that the most stable items are not the same even if there is a positive correlation between the stability computed for IE and AU groups.

We evaluated the lexical distances between languages by means of the mean normalized edit distances between the orthographic realizations of Swadesh's meanings. Then, we considered an infinite sequential process of language classification described by random walks on the matrix of lexical distances. As a result, the relationships between languages belonging to one and the same language family are translated into distances and angles, in multi-dimensional Euclidean space. The derived geometric representations of language taxonomy are used in order to test the various statistical hypotheses about the evolution of languages.

Our method allows for making accurate inferences on the most significant events of human history by tracking changes in language families through time. Computational simplicity of the proposed method based primarily on linear algebra is its crucial advantage over previous approaches to the computational linguistic phylogeny that makes it an invaluable tool for the automatic analysis of both the languages and the large document data sets that helps to infer on relations between them in the context of human history. Recently, we have applied the developed method in order to investigate the detailed historical configuration of Malagasy dialects spoken on Madagascar [53].

Acknowledgements We profoundly thank R.D. Gray for the permission to use the Austronesian Basic Vocabulary Database [54] containing lexical items from languages spoken throughout the Pacific region.

References

1. D'Urville, D.: Sur les îles du Grand Océan. Bull. Soc. Goégr. **17**, 1–21 (1832)
2. Swadesh, M.: Lexicostatistic dating of prehistoric ethnic contacts. Proc. Am. Philos. Soc. **96**, 452–463 (1952)
3. Pagel, M., Atkinson, Q.D., Meadel, A.: Frequency of word-use predicts rates of lexical evolution throughout Indo-European history. Nature **449**, 717–720 (2007).
4. Nichols, J., Warnow, T.: Tutorial on computational linguistic phylogeny. Lang. Linguist. Compass **2**(5), 760–820 (2008)
5. Levenshtein, V.I.: Binary codes capable of correcting deletions, insertions and reversals. Sov. Phys. Dokl. **10**, 707–710 (1966)
6. Petroni, F., Serva, M.: Language distance and tree reconstruction. J. Stat. Mech. Theory Exp. **2008**, P08012 (2008)
7. Serva, M., Petroni, F.: Indo-European languages tree by Levenshtein distance. Europhys. Lett. **81**, 68005 (2008)
8. Petroni, F., Serva, M.: Lexical evolution rates derived from automated stability measures. J. Stat. Mech. **2010**, P03015 (2010)
9. Dyen, I., Kruskal, J., Black, P.: Comparative Indo-European Database collected by Isidore Dyen. http://www.wordgumbo.com/ie/cmp/iedata.txt. Copyright (C) 1997 by Isidore Dyen, Joseph Kruskal, and Paul Black. The file was last modified on Feb 5, 1997. Redistributable for academic, non-commercial purposes (1997)
10. McMahon, A., Heggarty, P., McMahon, R., Slaska, N.: Swadesh sublists and the benefits of borrowing: An Andean case study. Trans. Philol. Soc. **103**(2), 147–170 (2005)
11. Greenhill, S.J., Blust, R., Gray, R.D.: The Austronesian Basic Vocabulary Database: From Bioinformatics to Lexomics. Evol. Bioinform. **4**, 271. The Austronesian Basic Vocabulary Database. http://language.psy.auckland.ac.nz/austronesian (2008)
12. The database modified by the authors is publicly available on-line at http://univaq.it/∼serva /languages/languages.html
13. Petroni, F., Serva, M.: Automated words stability and languages phylogeny. J. Quant. Linguist. **18**(1), 53–62 (2011)
14. Hyvärinen, A., Karhunen, J., Oja, E.: Independent Component Analysis. Wiley, New York (2001)
15. Jolliffe, I.T.: Principal Component Analysis, 2nd ed. Springer Series in Statistics, vol. XXIX. Springer, New York (2002)
16. Blanchard, P., Volchenkov, D.: Intelligibility and first passage times in complex urban networks. Proc. R. Soc. A **464**, 2153–2167 (2008)
17. Blanchard, P., Volchenkov, D.: Mathematical Analysis of Urban Spatial Networks. Understanding Complex Systems, vol. XIV. Springer, Berlin (2009)
18. Volchenkov, D.: Random walks and flights over connected graphs and complex networks. In Communications in Nonlinear Science and Numerical Simulation. http://dx.doi.org/10.1016/j.cnsns.2010.02.016 (2010)
19. Schölkopf, B., Smola, A.J., Müller, K.-R.: Nonlinear component analysis as a kernel eigenvalue problem. Neural Comput. **10**, 1299–1319 (1998)
20. Blanchard, P., Petroni, F., Serva, M., Volchenkov, D.: Geometric representations of language taxonomies. Comput. Speech Lang. **25**(3), 679–699 (2011).
21. Gamkrelidze, T.V., Ivanov, V.V.: (1995) Indo-European and the Indo-Europeans: A Reconstruction and historical analysis of a proto-language and a proto-culture. Trends in Linguistics: Studies and Monographs, vol. 80. de Gruyter Berlin
22. Renfrew, C.: Archaeology and Language: The Puzzle of Indo-European Origins. Cambridge University Press, New York (1987)
23. Baldi, P.: The Foundations of Latin. Mouton de Gruyter Series Trends in Linguistics: Studies and Monographs, vol. 117. de Gruyter, Berlin (2002)
24. Gamkrelidze, T.V., Ivanov, V.V.: The early history of Indo-European languages. Sci. Am. **262**(3), 110–116 (1990)

25. Embelton, S.M.: Statistics in Historical Linguistics. Bochum, Brockmeyer (1986)
26. Heggarty, P.: Interdisciplinary indiscipline? Can phylogenetic methods meaningfully be applied to language data and to dating language? In: Forster&, P., Renfrew, C. (eds.) Phylogenetic Methods and the Prehistory of Languages, p. 183. McDonald Institute for Archaeological Research, Cambridge (2006)
27. Fouracre, P.: The New Cambridge Medieval History. Cambridge University Press (1995–2007)
28. Bryant, E.: The Quest for the Origins of Vedic Culture: The Indo-Aryan Migration Debate. Oxford University Press (2001)
29. Novotná, P., Blažek, V.: Glottochronolgy and its application to the Balto-Slavic languages. Baltistica **XLII**(2), 185–210 (2007)
30. Mcleod, J.: The History of India. Greenwood Publishing Group (2002)
31. Green, P.: The Greco-Persian Wars. University of California Press, Berkeley (1996)
32. Gimbutas, M.: Old Europe in the fifth millenium B.C.: The European situation on the arrival of Indo-Europeans. In: Polomé, E.C. (ed.) The Indo-Europeans in the Fourth and Third Millennia. Karoma Publishers, Ann Arbor (1982)
33. Renfrew, C.: Time depth, convergence theory, and innovation in proto-Indo-European. Proceedings of the conference languages in prehistoric Europe, p. 227, Eichstätt University, 4–6 October 1999, Heidelberg (2003)
34. Mallory, J.P.: In Search of the Indo-Europeans: Language, Archaeology, and Myth. Thames & Hudson, London (1991)
35. Krell, K.S.: Gimbutas' Kurgan-PIE homeland hypothesis: A linguistic critique. In: Blench, R., Spriggs, M. (eds.) Archaeology and Language, II, p. 267, London, Routledge (1998)
36. Dahl, O.C.: Avhandlinger utgitt av Egede-Instituttet **3**, 408, Arne Gimnes Forlag (1951)
37. Hurles, M.E., Sykes, B.C., Jobling, M.A., Forster, P.: The dual origins of the Malagasy in island Southeast Asia and East Africa: Evidence from maternal and paternal lineages. Am. J. Hum. Genet. **76**, 894 (2005)
38. Diamond, J.M.: Express train to Polynesia. Nature **336**, 307–308 (1988)
39. Su, B., et al.: Polynesian origins: Insights from the Y chromosome. Proc. Natl. Acad. Sci. U S A **97**(15), 8225–8228 (2000)
40. Bellwood, P., Koon, P.: Lapita colonists leave boats unburned! Antiquity **63**(240), 613–622 (1989)
41. Kirch, P.V.: The Lapita Peoples: Ancestors of the Oceanic World. Blackwell, Cambridge (1997)
42. Matisoo-Smith, E., Robins, J.H.: Origins and dispersals of Pacific peoples: Evidence from mtDNA phylogenies of the Pacific rat. Proc. Natl. Acad. Sci. U S A **101**(24), 9167–9172 (2004)
43. Larson, G., et al.: Phylogeny and ancient DNA of Sus provides insights into neolithic expansion in island Southeast Asia and Oceania. Proc. Natl. Acad. Sci. U S A **104**(12), 4834–4839 (2007)
44. Kirch, P.V.: On the road of the winds: An archaeological history of the Pacific islands before European contact. University of California Press, Berkley (2000)
45. Anderson, A., Sinoto, Y.: New radiocarbon ages for colonization sites in East Polynesia. Asian Perspect. **41**, 242–257 (2002)
46. Hurles, M.E., et al.: Untangling Pacific settlement: The edge of the knowable. Trends Ecol. Evol. **18**, 531–540 (2003)
47. Lum, J.K., Jorde, L.B., Schiefenhovel, W.: Affinities among Melanesians, Micronesians, and Polynesians: A neutral, biparental genetic perspective. Hum. Biol. **74**, 413–430 (2002)
48. Kayser, M., et al.: Melanesian and Asian origins of polynesians: mtDNA and Y chromosome gradients across the Pacific. Mol. Biol. Evol. **23**, 2234–2244 (2006)
49. Friedländer, J.S., et al.: Genetic structure of Pacific islanders. PLoS Genet. **4**(1), e19 (2008) (Public Library of Science)
50. Utsurikawa, N.: A Genealogical and Classificatory Study of the Formosan Native Tribes. Toko shoin, Tokyo (1935)
51. Li, P.J.: Types of lexical derivation of men's speech in Mayrinax. Bull. Inst. Hist. Philol. **54**(3) 1–18 (1983) (Academia Sinica)

52. Li, P.J.: The dispersal of The Formosan aborigines in Taiwan. Lang. Linguist. **2**(1), 271–278 (2001)
53. Volchenkov, D., Filippo, P., Maurizio, S., Søren, W.: Malagasy dialects and the peopling of madagascar, Journal of Royal Soc. Interface, p. 1–14, doi:10.1098/rsif.2011.0228 (2011)
54. The Austronesian Basic Vocabulary Database by R.D. Gray is publicly available on -line at http://language.psy.auckland.ac.nz/austronesian/